Improving Antibody-drug Conjugate Tumor Distribution and Efficacy Using Single-Cell Imaging and Multiscale Modeling

by

Cornelius Cilliers

A dissertation submitted in partial fulfillment
of the requirements for the degree of
Doctor of Philosophy
(Chemical Engineering)
in the University of Michigan
2018

Doctoral Committee:

Assistant Professor Greg M. Thurber, Chair
Professor Trachette Jackson
Associate Professor Sunitha Nagrath
Assistant Professor Fei Wen

Cornelius Cilliers

ccillier@umich.edu

ORCID ID: 0000-0001-5320-7994

Dedication

This dissertation is dedicated to

Nina

Mom and Dad

Acknowledgments

The work in this thesis would not have been possible without the unwavering support and encouragement of countless colleagues, friends, and family. I am fortunate and extremely grateful to have been surrounded by such talented and wonderful people.

First, I would like to thank my advisor Prof. Greg Thurber for his guidance, encouragement, and support throughout my five years here. His eagerness and passion for research was contagious and motivating when work was going well, while his patience and understanding helped reassure me when there were challenges. I appreciated his encouragement, approachability, and open-door policy because I knew I could always walk over and talk with him. Even on the days that I had several questions and would talk for significant amounts of time, it always felt like he was invested in helping me. I would also like to thank my committee members, Prof. Jackson, Prof. Nagrath, and Prof. Wen for their support and encouragement. I would also like to acknowledge the funding from the National Institute of Health, Eli Lilly, Takeda Pharmaceuticals, and Rackham Graduate School, which made my doctoral studies possible.

The Thurber lab has been a wonderful place to work and I am grateful for all the lab members who have helped me here. This includes Liang Zhang, Sumit Bhatnagar, Tejas Navaratna, Lydia Atangcho, Bruna Menezes, Eshita Khera, Ian Nessler, and Reggie Evans. All of you have contributed to this thesis through suggestions, discussion, and making our lab a great place to work. I especially want to thank Liang and Sumit for their hard work setting up the lab, developing protocols for the lab, training me on several instruments and techniques, and holding

my work to a high standard. I would also like to acknowledge the several outstanding undergraduates that have helped me with several projects, including Nikolas Christodolu, Hans Guo, and Jianshan Liao. I would also like to thank the Eniola and Wen labs for their helpful discussions, equipment, and lending supplies in times of great need.

Outside of the lab I have had the support of many close friends, including David Hietala, Mason Smith, Brett Hill, Trenton Wilke, Vikesh Chandrashekar, Nishanth Bharadwaj, Tomas Guerrero, and Douglas Dafler. From floating to fantasy football and everything in between, I've made many unforgettable memories with you all. I want to thank you for your friendship and for always being there to get me out of the lab and have fun.

I would like to thank my family for all their love and support. My parents have supported me at every stage throughout my life. Their support has opened so many opportunities for me and none of my accomplishments would have been possible without them. I would also like to thank my brother and sister who have always helped encourage me to set my goals high.

Finally, I want to thank my wonderful girlfriend Nina Gasbarro for all her love, support, patience, and encouragement. No matter how long or difficult my day was, you always knew how to cheer me up and make me smile. You have filled my life with laughter, love, and joy, and I love you so very much.

Table of Contents

Dedication ii

Acknowledgments iii

List of Figures ix

List of Tables xiii

List of Appendices xiv

Abstract xv

Chapter 1 Introduction 1

1.1 Antibody Therapy 1

1.2 Antibody Drug Conjugates (ADCs) 3

1.3 Antibody Heterogeneity in the Tumor 5

1.4 Near-infrared (NIR) Fluorescence Imaging 7

Chapter 2 Residualization Rates of Near Infrared Dyes for the Rational Design of Molecular Imaging Agents 9

2.1 Publication Information 9

2.2 Abstract 9

2.3 Background 10

2.4 Results 12
2.5 Discussion 16
2.6 Conclusion 20
2.7 Experimental Methods 20

Chapter 3 Tracking Antibody Distribution with Near-Infrared Fluorescent Dyes: Impact of Dye Structure and Degree of Labeling on Plasma Clearance 23
3.1 Publication Information 23
3.2 Abstract 23
3.3 Background 24
3.4 Results 27
3.5 Discussion 43
3.6 Conclusion 50
3.7 Experimental Methods 50

Chapter 4 Absolute Quantification of Protein Metabolism with Single Cell Resolution In Vivo Using Near-Infrared Ratio Imaging 55
4.1 Abstract 55
4.2 Background 55
4.3 Results 58
4.4 Discussion 68
4.5 Conclusions 73
4.6 Experimental Methods 74

Chapter 5 Multiscale Modeling of Antibody-Drug Conjugates: Connecting Tissue and Cellular Distribution to Whole Animal Pharmacokinetics and Potential Implications for Efficacy 79

5.1 Publication Information 79

5.2 Abstract 79

5.3 Background 80

5.4 Results 84

5.5 Discussion 106

5.6 Conclusion 115

5.7 Experimental Methods 115

Chapter 6 Improved Tumor Penetration and Single-Cell Targeting of Antibody Drug Conjugates Increases Anticancer Efficacy and Host Survival 119

6.1 Publication Information 119

6.2 Abstract 119

6.3 Background 120

6.4 Results 123

6.5 Discussion 142

6.6 Conclusion 149

6.7 Experimental Methods 150

Chapter 7 Concluding Remarks and Future Directions 156

7.1 Summary of Work 156

7.2 Future Work and Directions 159

7.3 Concluding Remarks 162

Appendices 165

References 187

List of Figures

Figure 1.1 Antibody-drug conjugate structure and mechanism of action. 3

Figure 2.1 Selected NIR Dye structures. 14

Figure 2.2 Confocal microscopy of A431 cells following surface labeling with antibody-dye conjugates. 15

Figure 2.3 Dye residualization quantification and PAMPA Assay. 16

Figure 3.1 Dye structures and relative size of dyes to antibody. 28

Figure 3.2 SDS-PAGE of antibody-dye conjugates and free dye. 29

Figure 3.3 Antibody-dye absorbance spectra. 30

Figure 3.4 Antibody-800CW conjugate plasma clearance. 32

Figure 3.5 Antibody-AF680 conjugate plasma clearance. 32

Figure 3.6 Absolute concentrations of antibody-dye conjugate plasma clearance. 33

Figure 3.7 SDS-PAGE of serum stability samples. 34

Figure 3.8 Antibody-dye conjugate serum stability. 34

Figure 3.9 Fluorescence SDS-PAGE of bevacizumab-dye conjugate blood samples. 35

Figure 3.10 Theoretical dye per antibody distribution and fluorescence contribution. 39

Figure 3.11 Fluorescence scan of whole organs. 40

Figure 3.12 Bevacizumab biodistribution at 0.3 DoL. 40

Figure 3.13 Fluorescence histology following injection of T-DM1-AF680. 42

Figure 3.14 Immunofluorescence histology of T-DM1-AF680 with antihuman Fc staining. 43

Figure 4.1 Dual label NIR fluorescence imaging technique concept. 59

Figure 4.2 Example absorbance spectra of dually labeled T-DM1. 59

Figure 4.3 *In vitro* flow cellular metabolism. 61

Figure 4.4 Plasma clearance for each agent over 24 hours. 62

Figure 4.5 *In vitro* confocal microscopy of dually labeled proteins. 63

Figure 4.6 NIR Fluorescence SDS-PAGE of dual labeled T-DM1. 64

Figure 4.7 Whole organ immunofluorescence histology. 65

Figure 4.8 *In vivo* cellular metabolism and distribution. 67

Figure 4.9 Whole animal imaging 24 hours post injection for each agent using the PerkinElmer In Vivo Imaging System (IVIS). 68

Figure 5.1 Multi-scale PBPK-Krogh cylinder model diagram. 85

Figure 5.2 Heterogeneous ADC distribution. 86

Figure 5.3 Normalized plasma clearance of trastuzumab and trastuzumab-AF680. 87

Figure 5.4 Distribution of unlabeled T-DM1. 88

Figure 5.5 PBPK model results and experimental biodistribution data. 89

Figure 5.6 T-DM1 Plasma clearance. 90

Figure 5.7 Quantitative Krogh cylinder simulation results and immunofluorescence imaging results. 91

Figure 5.8 T-DM1 distribution at 0:1 dosing ratio (only 3.6 mg/kg T-DM1). 92

Figure 5.9 T-DM1 distribution at 3:1 dosing ratio (3.6 mg/kg T-DM1 + 10.8 mg/kg unlabeled trastuzumab). 93

Figure 5.10 T-DM1 distribution at 8:1 dosing ratio (3.6 mg/kg T-DM1 + 28.8 mg/kg unlabeled trastuzumab). 94

Figure 5.11 Prediction of T-DM1 distribution versus trastuzumab carrier dose. 97

Figure 5.12 Prediction of T-DM1 distribution versus trastuzumab carrier dose. 97
Figure 5.13 Antibody tumor penetration over time. 98
Figure 5.14 Literature review of efficacy with constant small molecule dose but differing DAR and antibody doses. 102
Figure 5.15 Distribution and efficacy of non-bystander payloads. 103
Figure 5.16 Distribution and efficacy of bystander ADCs given at constant payload dose with different DAR/antibody doses. 103
Figure 5.17 Distribution and efficacy of a constant dose of antibody with increasing DAR for both bystander and non-bystander payloads. 104
Figure 5.18 Predicted and experimental impact of carrier dose on total tumor uptake. 105
Figure 5.19 Impact of carrier dose/DAR on healthy tissue targeting. 106
Figure 6.1 Improving T-DM1 tumor distribution through co-administration of trastuzumab. ... 124
Figure 6.2 Improving T-DM1 tumor distribution through co-administration of trastuzumab. ... 125
Figure 6.3 Immunofluorescence histology of T-DM1-800 (green) dosed at 14.4 mg/kg (same total antibody dose as 3:1 trastuzumab:T-DM1 ratio). 126
Figure 6.4 Immunofluorescence histology of HER2 antigen. 127
Figure 6.5 T-DM1 dye conjugate binding affinity. 127
Figure 6.6 In vitro toxicity of trastuzumab alone. 129
Figure 6.7 *In Vitro* Cytotoxicity. 130
Figure 6.8 Dye conjugation to T-DM1 does not affect in vitro cytotoxicity. 131
Figure 6.9 NCI-N87 cell viability data fit with a competitive binding model. 131
Figure 6.10 NCI-N87 cell uptake and viability. 132

Figure 6.11 KEY FIGURE: Co-administration of trastuzumab with T-DM1 results in a significant reduction in tumor growth compared to T-DM1 alone. 134
Figure 6.12 Individual Kaplan-Meier curves with 95% confidence interval generated using PRISM software. 135
Figure 6.13 Individual tumor growth curves for all animals. 135
Figure 6.14 Percent weight change during treatment. 136
Figure 6.15 *In vitro* T-DM1 metabolism and pharmacodynamics. 139
Figure 6.16 *In vivo* T-DM1 metabolism in tumor. 140
Figure 6.17 Immunofluorescence histology after treatment. 142

List of Tables

Table 2.1 Physicochemical and optical properties of NIR dyes.....13

Table 3.1 Plasma clearance fitted biexponential parameters from PRISM.....31

Table 3.2 Normalized AUC for antibody-dye conjugates.....36

Table 5.1 Fitted PBPK model parameters.....89

Table 5.2 Krogh cylinder simulation parameters from literature.....95

Table B.1 Table of PBPK-Krogh Cylinder Model Parameters.....178

List of Appendices

Appendix A – Dual Label NIR Fluorescence Ratio Imaging Protocol 166

Appendix B – Table of PBPK-Krogh Cylinder Model Parameters..... 178

Appendix C – PBPK-Krogh Cylinder Model Equations 181

Abstract

Antibody-drug conjugates (ADCs) are a targeted cancer therapy combining the tumor cell specificity of antibodies with small-molecule chemotherapy. Despite the widespread use of ADC therapeutics, they exhibit a heterogeneous, perivascular distribution in tumors, often leaving significant portions of the tumor untargeted. Furthermore, the relationship between the heterogeneous distribution of ADCs in tumors and their overall efficacy is poorly understood and therefore can be underappreciated. In this thesis, I develop experimental techniques to quantify ADC distribution in tumors using near-infrared (NIR) fluorophores, construct a computational model to simulate antibody distribution at several length scales, and show, for the first time, that the antibody distribution in the tumor plays an important role in the efficacy of ADCs. To better characterize the multiscale distribution of ADCs, I first measure the residualization properties of common NIR dyes, identifying both non-residualizing and residualizing dyes. Next, I show that fluorescent dye structure and dye-to-protein ratio can be optimized for labeling antibodies with NIR fluorophores to prevent the dye from impacting antibody pharmacokinetics. I then develop a novel dual label, ratio-imaging technique to quantify antibody distribution and metabolism *in vivo* with unprecedented single cell resolution. Using this technique, I show the clinical dose of 3.6 mg/kg the distribution of T-DM1 is heterogeneous in high HER2 expressing tumors, only targeting 10% of tumor cells. Examining the absolute uptake of ADC in targeted cells shows that they actually receive more ADC than necessary to kill the cell, despite most of the tumor not receiving any ADC. In the second part of my thesis, I develop a multiscale modeling framework combining a physiologically-based pharmacokinetic (PBPK) and Krogh Cylinder tissue model to

predict both the systemic and tumoral distribution of antibodies. Using this model, I predict, and verify experimentally, that coadministration of trastuzumab with T-DM1 at 3:1 and 8:1 ratios drives a constant dose of T-DM1 deeper into the tumor. Using this dosing strategy, the total number of cells targeted increases albeit with a lower average number of ADC molecules per cell. These results are consistent across a number of antibodies, targets, and payloads, indicating the model can be used to predict ADC distribution in other tumor models. Finally, I test the efficacy of coadministration of trastuzumab with T-DM1 in a trastuzumab resistant xenograft mouse model. T-DM1 therapy alone showed a significant improvement in efficacy and survival, as expected, while trastuzumab alone had no impact. Counterintuitively, coadministration of trastuzumab, which has no efficacy *in vivo* and is antagonistic to T-DM1 *in vitro*, actually acts synergistically with T-DM1 *in vivo*. Coadministration of trastuzumab at 3:1 and 8:1 trastuzumab to T-DM1 dosing levels show a statistically significant improvement in survival over T-DM1 alone. These results are the first to show that the tumoral distribution of ADCs plays a major role in their overall efficacy. Overall, this dissertation provides unique tools to study antibody and ADC distribution and metabolism, quantitative computational tools to simulate *in vivo* distribution, and concrete guidance on how to improve efficacy of ADC therapeutics. Although I show the importance of the antibody distribution in the tumor for efficacy, additional imaging with other ADC systems, lower and more heterogeneous antigen expressing tumors, and the antibody distribution in clinical samples will further improve our understanding of the relationship between distribution and efficacy.

Chapter 1

Introduction

1.1 Antibody Therapy

Antibody-based therapeutics have achieved remarkable success in the clinic over the past several decades and remain an important treatment strategy for both hematological malignancies and solid tumors (*1*). Since their introduction in 1986, the number of approved antibody-based therapeutics has grown at a rate of approximately four per year, and there are now over 60 FDA approved therapeutics (*2*). In fact, in 2017 there was a record number of ten FDA approvals of antibody therapeutics (*3*). Additionally, it is expected that marketing applications will be submitted for least 12 antibody therapeutics in 2018, and there are 19 others in late-stage clinical trials with endpoints in 2018 (*3*). The worldwide sales of antibodies have followed this rapid growth trend, rising from around $75 billion in 2013 to a projected $125 billion in 2020 (*2*). Improving antibody therapy is imperative since antibody-based therapeutics will continue to be a critical part of cancer therapy for the foreseeable future.

Antibodies are large proteins produced by the immune system to specifically bind and neutralize foreign pathogens (*4*). The most common antibody in the blood is the immunoglobulin G or IgG. These 150 kDa, "Y-shaped" IgG proteins have two binding arms, known as the fragment antigen binding region or Fab, which allows them to recognize an antigen with high specificity, and a constant region, known as the Fc region (crystallizable fragment), which allows

them to interact with immune cells. The Fab regions contain areas called complementarity determining regions (CDRs) that make up the antibody paratope, which binds the epitope on the target antigen, similar to the induced fit model of an enzyme binding a substrate (*4*).

Antibodies are versatile therapeutics that can combine several mechanisms of action (*1*). They are engineered to strongly and specifically bind to a tumor-associated antigen. After engaging the target antigen some antibodies, such as cetuximab and trastuzumab, can block receptor dimerization, resulting in a loss of downstream signaling and/or kinase activation, and ultimately leading to a loss of proliferation and apoptosis (*1*). Furthermore, receptor binding by the antibody can lead to internalization, degradation, and downregulation of the receptor (*5*). The Fc portion of antibodies can also direct the immune system to target and kill tumor cells through several mechanisms of action (*1*,*6*). Macrophages can phagocytose tumor cells by binding the antibody Fc region through the FcγR receptors (*6*,*7*). Antibodies coating a tumor cell can also bind with complement protein C1q, ultimately leading to complement cascade and complement-dependent cytotoxicity (CDC) (*1*,*6*). Additionally, NK cells binding the antibody with the FcγRIIIa leads to antibody-dependent cell-mediated cytotoxicity (ADCC) through perforin/granzyme release and lysis of the targeted tumor cell (*1*,*6*). A more recent strategy of antibody therapy involves blocking immunosuppressive interactions, such as CTLA4-CD80/86 or PD1-PDL1, to prevent the inactivation of T cells and other immune cells in the tumor (*8*). Finally, antibody-drug conjugates (ADCs) combine the tumor cell specificity of antibodies with toxic small molecule drugs to improve discrimination between target and healthy tissue (*9*).

1.2 Antibody Drug Conjugates (ADCs)

Antibody-drug conjugates (ADCs) are an antibody-based therapeutic where a linker connects the antibody backbone and a cytotoxic, small molecule payload (also known as a warhead). In contrast to conventional chemotherapy with a small molecule, which does not discriminate between tumor and healthy cells, ADCs are a targeted therapy aimed at reaching only tumor cells to improve the therapeutic window (Figure 1.1). The antibody binds a tumor-specific or tumor-associated antigen with high affinity, thereby preferentially delivering the toxic payload to the tumor tissue instead of healthy tissue. Once the ADC engages the target antigen, the receptor-ADC complex is internalized into lysosomes for degradation. Some ADCs use enzymatically cleavable linkers, which will release the payload once in the lysosomes (*10*–*12*), while other ADCs use non-cleavable linkers, where the payload is released as a lysine-payload adduct after the antibody is fully degraded (*11*,*13*). Once the payload is released into the cell it is able to bind its target, which is commonly microtubules or DNA.

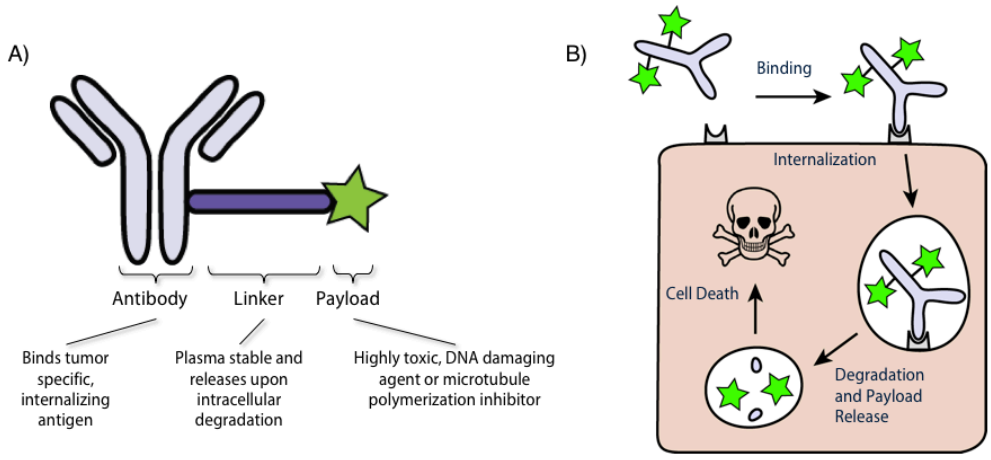

Figure 1.1 Antibody-drug conjugate structure and mechanism of action.
(A) ADCs are comprised of a small molecule payload, linker, and antibody backbone. (B) ADC mechanism of action consists of binding their target antigen, internalization, degradation, and payload release. Once the payload is released it can exert its cytotoxic effect on the tumor cell.

Although ADCs have found some success in the clinic, they have not fully lived up to their potential. Two of the four FDA approved ADCs, brentuximab vedotin (Adcetris), and trastuzumab emtansine (Kadcyla, T-DM1), have achieved remarkable success in the treatment of relapsed Hodgkin lymphoma/systemic anaplastic large cell lymphoma and breast cancer, respectively. For brentuximab vedotin, 34% of patients with relapsed/refractory Hodgkin lymphoma achieved in complete remission in one clinical trial (*14*). In the EMILIA clinical trial, T-DM1 improved survival by nearly 6 months compared to standard therapy in heavily pretreated patients that were resistant to trastuzumab and taxane chemotherapy (*15*). Inotuzumab ozogamicin (Besponsa) was recently approved in 2017 and after the INO-VATE ALL clinical trial showed 80% complete remissions with ADC therapy compared to 29% for standard care for relapsed or refractory B-cell precursor acute lymphoblastic lymphoma (ALL) (*16*). The fourth FDA approved ADC, Mylotarg, was originally approved in year 2001. However, after 9 years it was removed from the market after subsequent trials failed to confirm a clinical benefit (*17*). Mylotarg was reapproved in 2017 after it was shown an alternative dosing schedule improved the therapeutic index (*18*). Currently, there are several other promising ADCs in late-stage clinical trials that may soon be approved, including mirvetuximab sorvastine, glembatumumab vedotin, and oportuzumab monatox (*3*). While there are several promising ADCs on the horizon, there is a need to improve our understanding of why ADCs fail in the clinic to improve the development of future ADC therapeutics.

Significant efforts have been made to engineer each part of the ADC, including site-specific linker conjugation sites on the antibody (*19*,*20*), antibody affinity, antibody glycosylation (*21*), more stable linker conjugation chemistries (*22*), linker stability (*11*,*23*),

linker hydrophobicity (*24*), more potent payloads (*25–27*), varying drug-to-antibody ratios (DARs) (*28*,*29*), etc. Because there is not a "one size fits all" approach for the development of ADCs, each unique ADC therapeutic requires a multifactorial optimization of each component. Despite the significant investments into ADC therapy, the tumor distribution is often overlooked and rarely mentioned in the literature when considering the efficacy of these therapeutics.

1.3 Antibody Heterogeneity in the Tumor

A major problem with antibody therapy in cancer is the heterogeneous, perivascular distribution of antibodies in solid tumors. These distribution limitations of antibody therapy in human patients has been known for several decades. Before the introduction of antibody humanization technology, antibodies used for therapy were derived from mouse hybridomas. The distribution of mouse antibodies in human clinical samples could easily be detected through anti-mouse Fc staining and immunohistochemical or immunofluorescence microscopy (*30*). For example, an anti-melanoma mouse antibody given at doses of 3 and 7 mg/kg localized to highly vascular areas, leaving large areas of the tumor untargeted (*30*,*31*). At the highest dose of 500 mg (~7 mg/kg) there was significant interpatient variability, and the total tumor antigen saturation ranged from 20% to 90%, while lower doses, around 100 mg, were undetectable in some patients (*32*). Autoradiographic images confirmed that the antibody localized around the vasculature and tumor periphery, leaving the poorly vascularized center of some tumors untargeted (*33*). These results are consistent among other mouse (*34*) and humanized (*35*) antibodies in clinical samples, as well as clinical antibodies in mouse xenografts (*36*).

The lack of antibody penetration into the tumor is due to both the physicochemical properties of the antibody and the physiology of the tumor microenvironment. The large size of antibodies (150 kDa) limits the rate of extravasation from blood vessels into the tumor tissue (*37*). The elevated interstitial pressure in tumors prevents convective flow from tumor blood vessels into the interstitium, thereby limiting the transport of antibody to passive diffusion across the endothelium (*38*). Once in the tumor interstitium, the fast binding rate of the antibody relative to its rate of diffusion through the tissue combined with high target expression in the tumor results in targeting of cells immediately outside of the vessel. As the antibody-receptor complex is internalized and new antigen is trafficked to the cell surface it results in a dynamic saturation front, commonly referred to as the "binding site barrier" (*39*,*40*). Antibody penetration into the tumor is dependent on dose (*41*), binding affinity (*37*,*42*), and target expression (*43*), and several antibody therapies in the clinic still exhibit highly heterogeneous distributions (*36*), often leaving significant portions of the tumor untargeted (*44*). Additionally, the total amount of antibody entering the tumor is low, barely reaching 0.01% of the injected dose per gram of tissue in humans (*45*). Antibody therapy is often given around 5-10 milligrams per kilogram bodyweight; however, doses as high as multiple grams per kilogram bodyweight may be needed to achieve full tumor saturation. Tumor cells untargeted by antibody therapy may lead to the selection of resistant cancer cells (*44*) or lead to tumor regrowth in between treatments (*46*).

In ADC therapy the payload is the major driver of toxicity (*47*), and, because the payloads are often highly toxic, ADCs have much lower maximum tolerated doses (MTD) than many unconjugated antibody therapeutics. For example, the MTD of the FDA approved ADC Kadcyla (trastuzumab emtansine, T-DM1) is 3.6 mg/kg (*48*), while the unconjugated antibody

trastuzumab is well tolerated even at doses as high as 18 mg/kg over three weeks (*49*). Since ADCs are given at lower doses, they traverse only a few cell layers from the vasculature in tumors with high antigen expression (*36*,*37*,*46*). However, it is not well understood how this perivascular tissue distribution of ADCs impacts their overall efficacy. In fact, during development of ADC therapeutics it is rare to see any mention of the ADC tumor distribution, and many reviews of ADC therapeutics in the clinic fail to mention their heterogeneous distribution (*8*,*50*,*51*). Despite these distribution limitations of antibodies/ADCs and lack of data showing ADC distribution, ADC therapy is still effective in the clinic for many patients. This dissertation will outline computational and experimental techniques to quantify ADC distribution in tumors and develop strategies to improve the tumor penetrance of ADCs.

1.4 Near-infrared (NIR) Fluorescence Imaging

Currently there is a wide array of tools to understand protein distribution at several length scales (*52*). For example, basic measurements of plasma clearance can be determined using radiolabels, fluorescent labels, ELISA, and mass spectrometry to give blood concentration over time. Using radioactive labels and/or nuclear imaging, the organ uptake and whole animal distribution can be measured in the form of percent-injected dose per gram measurements as well as real time imaging with PET/SPECT. Histology can be performed using autoradiography, immunohistochemistry, and immunofluorescence to understand the tissue scale distribution. Flow cytometry and *in vitro* measurements are used to quantify fluorescence at the single cell scale. However, these conventional methods have several disadvantages and limitations. Biophysical techniques, such as ELISA and mass spectrometry, have limited spatial resolution (ELISA) and/or difficulty in measuring low concentration proteins in complex samples (e.g.

mass spectrometry imaging). Radiolabels cannot achieve cellular and subcellular resolution and are more cumbersome to use than fluorescent labels due to radioactive half-life time constraints and safety/licensing issues. Immunohistochemistry is not an accurate measure of organ distribution with limited ability to measure cellular kinetics. None of these methods are capable of measuring cellular kinetics *in vivo*, and a combination of different techniques with several animals is needed to obtain data on all the relevant length scales. NIR wavelengths have low tissue autofluorescence and can penetrate to a depth of 1-2 cm for live *in vivo* imaging. NIR fluorescence combines the whole animal and biodistribution capabilities of radiolabels (*53*) with the tissue and cellular kinetic measurements of fluorescence (*54*). NIR also has higher sensitivity than mass spectrometry imaging and visible light fluorescence and is capable of tracking metabolic degradation products while reducing the safety concerns, time/half-life constraints, and expense of radioactivity.

With the increased interest in novel biologics and in particular antibody-drug conjugates (*55*), there is a need to understand the effect of ADCs from the subcellular scale (e.g. number of ADCs each cell receives) to the tissue level (e.g. number of targeted cells in the tumor) to whole organ biodistribution. This dissertation outlines techniques using NIR fluorescence to investigate the distribution and metabolism of therapeutic proteins at the subcellular and cellular scale *in vitro*, and, importantly, at multiple scales *in vivo*.

Chapter 2

Residualization Rates of Near Infrared Dyes for the Rational Design of Molecular Imaging Agents

2.1 Publication Information

Cilliers, C., J. Liao, L. Atangcho, and G.M. Thurber**.** *Residualization rates of near infrared dyes for the rational design of molecular imaging agents*. Molecular Imaging and Biology. 2015; 17(6): 757-62.

Modifications have been made to the published document to adapt the content to this text. The goal of this chapter is to characterize the residualization rates of several near-infrared (NIR) fluorophores. These properties are used to select the wavelength and residualizing nature of NIR dyes for molecular imaging agent design.

2.2 Abstract

Near infrared (NIR) fluorescence imaging is widely used for tracking biological molecules *in vivo*. Clinical and preclinical applications include intraoperative imaging, tracking therapeutics, and fluorescent labeling as a surrogate for subsequent radioactive tags. Despite their extensive use, one of the fundamental properties of NIR dyes, the residualization rate within cells following internalization, has not been systematically studied. This rate is required for the rational design of probes and proper interpretation of *in vivo* results. In this brief report, we measure the cellular residualization rate of eight commonly used dyes encompassing three core structures (cyanine, BODIPY, and oxazine/thiazine/carbopyronin). We identify residualizing

(half-life > 24 hrs) and non-residualizing dyes (half-life < 24 hrs) in both the far red (~650-680 nm) and near infrared (~740-800 nm) regions. This data will allow researchers to independently and rationally select the wavelength and residualizing nature of dyes for molecular imaging agent design.

2.3 Background

Near infrared (NIR) imaging is increasingly being used during the development of novel imaging agents either in dual-labeling approaches or interchanging the labeling moiety during development (*56–58*). One of the biggest factors in determining the *in vivo* distribution of the label is the fate of the metabolic product after internalization. Despite the importance of this parameter and the well-characterized literature on radioactive tags (*59–62*), data on the residualization of NIR tags is quite limited. Understanding the behavior of the NIR tag following local metabolism is critical in selecting fluorophores that will be representative of the radiolabeled compounds in preclinical development and designing effective fluorescent imaging agents for intraoperative applications. This information is also necessary in predictive mechanistic models used in drug and imaging agent design (*63*,*64*). In this report, we compare the cellular loss of signal following internalization and degradation of labeled antibodies.

The increased use of NIR dyes during the development of molecular imaging agents stems from the high spatial and temporal resolution of fluorescence imaging. NIR labeled probes can be followed in real-time *in vitro* and *in vivo* (*65*), and imaging techniques exist to monitor distribution from the whole animal and organ level down to cellular and subcellular resolution (*66–68*). This allows the researcher to quickly and inexpensively optimize molecular properties

of the probe, determine clearance rates and optimal imaging windows, measure uptake in different cell types for heterogeneous tissues, and validate the agent *in vivo* prior to undertaking more expensive PET, SPECT, MRI, and CT validation studies. The fluorophore can then be replaced by a radioactive tag with similar physiochemical properties, or the dual labeled targeting agent can be loaded with a radioactive isotope. NIR probes have significant advantages over visible light dyes due to their drastically lower autofluorescence and high tissue penetration of light. The low background enables the detection of very low (nM) concentrations of dyes, and the high tissue penetration allows longitudinal whole animal imaging to follow the probe kinetics. Commercially available instrumentation has increased the use of these techniques in preclinical development.

Many different options are available for near-infrared labeling of molecules including organic dyes, quantum dots (*69*), and fluorescent proteins (*70*). For imaging agent conjugation, the organic dyes are the smallest labeling options and therefore least likely to dominate the pharmacokinetics and/or disrupt binding. While there has been extensive research into organic dye NIR fluorophore development, three of the most common (and commercially available) structures are cyanine dyes, red-shifted BODIPY fluorophores, and smaller polycyclic dyes (e.g. oxazine (*71*), thiazine (*72*), or carbopyronine (*73*) structures). A diverse set of cyanine dyes are available with multiple conjugation chemistries and varying charge, and these dyes are commonly used due to their high absorption coefficient and reasonable quantum yield (resulting in excellent brightness). Given the diversity in physiochemical properties of these fluorophores including a wide range in molecular weight, charge, and pKa, we sought to determine the cellular retention rate of fluorescently labeled antibodies for a direct comparison between dyes.

Radiolabels and fluorescent dyes are often grouped as 'residualizing' or 'non-residualizing,' although this classification is somewhat arbitrary since the half-life of signal decay is a continuous spectrum. Often, half-lives less than 24 hours such as iodine are referred to as 'non-residualizing,' while half-lives greater than 24 hours (e.g. ^{111}In) are considered residualizing.

Labels that are trapped within cells for long periods of time (strongly residualizing labels) tend to provide higher target to background contrast by remaining within the tissue following degradation of the targeting agent. However, these labels often have significant uptake in off-target tissues that could be problematic either due to high background in clearance organs (liver and kidney) or large radiation doses (*74*). Non-residualizing probes can lower these signal and are more representative of intact protein therapeutics for tracking pharmacokinetics. They are also better surrogates for non-residualizing radioisotopes in molecular imaging. The cellular half-life following internalization is a major determinant of whether the label stays within the tissue or is cleared following local metabolism. The NIR fluorophores tested in this work include both residualizing and non-residualizing dyes.

2.4 Results

Eight commercially available NIR dyes available as NHS esters were chosen for this study. They represent three different classes of molecules with varying optical and physiochemical properties (Table 2.1). The structures include several cyanine dyes with varying

numbers and positions of sulfate groups (Figure 2.1). The structures for AF750 and Atto740 are proprietary and are not included in Figure 2.1.

Table 2.1 Physicochemical and optical properties of NIR dyes

Dye	Ex/Em (nm)	Extinction Coefficient (cm^{-1} M^{-1})	MW (kDa)	Net Charge	LogD (pH 7.4)	$t_{1/2}$ (day)
DDAO	648/656	42,000	408	-1 (pKa = 5.0)	2.04	0.99 (±0.4)
BODIPY-650	651/660	100,000	546	0	0.85	2.43 (±0.3)
Cy5.5	675/694	250,000	900	-3	-4.72	3.92 (±0.5)
AF680	684/707	183,000	857	-2	-6.39	2.43 (±0.1)
Atto740	740/764	120,000	451	+1	NR	0.85 (±0.1)
SulfoCy7	740/773	240,600	708	-1	0.13	2.92 (±0.3)
AF750	753/782	290,000	~1200	NR	NR	2.55 (±0.2)
IRDye 800CW	774/789	240,000	1000	-3	-4.71	2.33 (±0.1)

All the dyes were conjugated to cetuximab successfully, although the lipophilic BODIPY-650 dye could not be completely purified of free dye after the reaction (data not shown). The fluorescent cetuximab molecules specifically labeled the surface of A431 cells following 30 minutes at 40 nM (Figure 2.2). The labeled cetuximab molecules were internalized and trapped in punctate vesicles throughout the cell with varying degrees of unquenching inside the cell. The cyanine dyes retained signal at 24 and 48 hours. DDAO and Atto740 signals were lower at 24 hours and not visible at 48 hours. A small amount of unquenching of Atto740 after internalization results in the higher microscopy signal at 24 hours but faster half life of cell clearance.

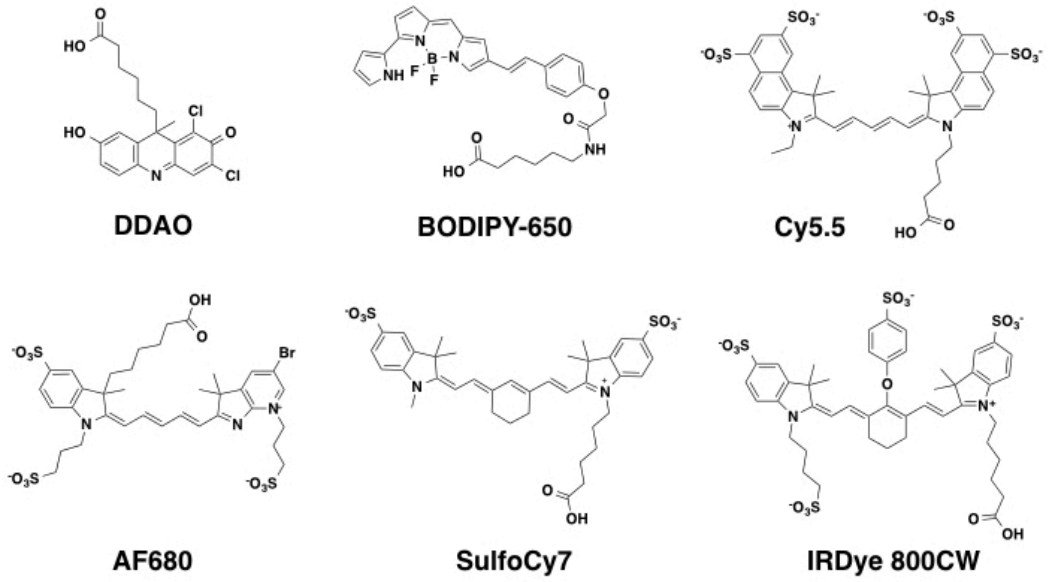

Figure 2.1 Selected NIR Dye structures.
Published dye structures used in this study including cyanine-based structures, boron-dipyrromethene (BODIPY), and the acridine-based (7-hydroxy-9H-(1,3-dichloro-9,9-dimethylacridin-2-one)) dye DDAO. These structures represent the hydrolyzed NHS ester form of the dyes.

To quantify the overall retention over long times, a plate assay was used to measure the bulk fluorescence over 168 hours (Figure 2.3). To eliminate the effects of internalization, degradation, and un-quenching, the half-life was measured from the time of peak signal onward. Half-lives for each of the dyes was calculated using PRISM and are reported in Table 2.1 Physicochemical and optical properties of NIR dyes. DDAO and Atto740 cleared from the cells with a half-life < 24 hours (non-residualizing) while the cyanine based probes all had half-lives greater than 48 hours. To check if passive diffusion through membranes could explain the more rapid loss of signal from internalized and degraded probe, a PAMPA assay was used to measure the membrane permeability of the free dye. The values were low (< 10^{-6} cm/s) for all the dyes, but only DDAO, Atto740, and BODIPY-650 gave measurable signal in the acceptor well. These

data point to a passive mechanism of signal loss by diffusion through membranes after degradation.

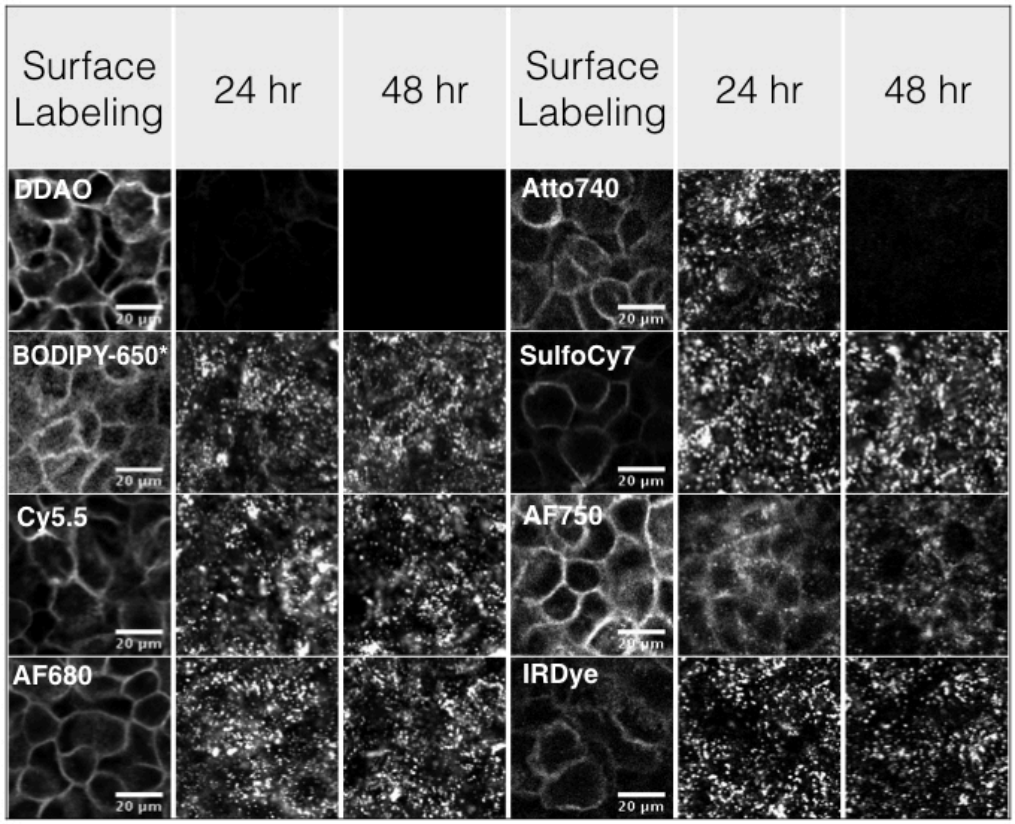

Figure 2.2 Confocal microscopy of A431 cells following surface labeling with antibody-dye conjugates.
Confocal microscopy of cells immediately after surface labeling or after 24- and 48-h incubation. Punctate spots after incubation show the substantial internalization, while the non-residualizing dyes DDAO and Atto740 have little signal at later times.

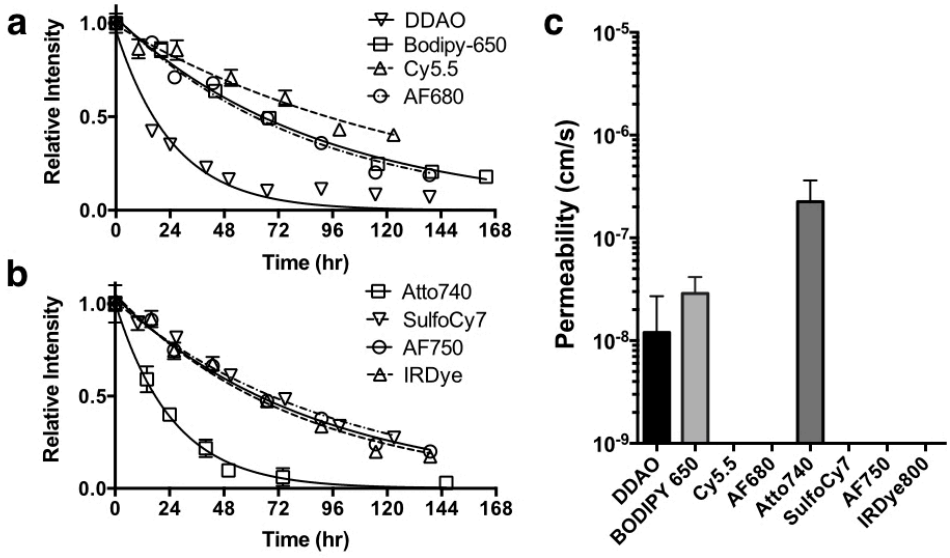

Figure 2.3 Dye residualization quantification and PAMPA Assay.
The signal intensity for each labeled antibody is plotted from the time of peak signal. To avoid fluorophore unquenching effects on the half-life, only the later time points during signal decay were used (a, b). To determine if passive diffusion through membranes could explain the loss in signal, all the free dyes (carboxylic acid derivatives) were tested in a PAMPA assay to quantify their membrane permeability (c).

2.5 Discussion

Understanding the cellular kinetics of NIR dyes is critical for designing imaging agents and predicting in vivo behavior. Whether used in direct applications for intraoperative imaging (*65*), in multi-modality imaging (*56*), or during preclinical development of radiolabeled probes, the rate at which the degraded probe diffuses out of cells is a major determinant of the time course and concentration of signal within the tissue. In this work, a wide range in the cellular residualization rate of NIR dyes was found following uptake by a monoclonal antibody (cetuximab) based on the dye properties.

To quantify the cellular half-life, we selected the clinical anti-EGFR antibody cetuximab as the model targeting agent. This is a well-studied internalizing antibody (*75*), and our imaging

results showed virtually complete internalization within 24 hours. A431 cells were selected for two reasons. First, they express high numbers of EGFR, resulting in a strong signal that can be tracked over many days. Second, the cell line exhibits contact inhibition, so they could be cultured as a confluent monolayer. This reduced the impact of cell growth during the assay so the signal did not drop during repeated cell division. The degree of labeling (DOL) was kept below 1 for most dyes to minimize the presence of multiple dyes on a single antibody. For future in vivo work, this can have a strong impact on distribution (*76*). Assuming a Poisson distribution, given that cetuximab contains greater than 80 lysines, an average DOL of 1 results in a surprisingly high 63% of the fluorescence signal originating from antibodies with multiple dyes. Only labeled antibodies are detected, and the problem is compounded by antibodies with multiple labels giving a higher signal. Since lysine conjugation is not site-specific, the easiest way to ensure a large fraction of single labeling is to have a low average DOL.

At early times (within 24 to 48 hours of cell surface labeling), the fluorescence signal is a combination of internalization, degradation, pH effects, and subcellular compartmentalization. Several dyes showed significant increases in signal as the covalently labeled antibody was degraded, resulting in an unquenching effect of the dye. At later times, however, the decrease in signal followed a single exponential decay that could be accurately and reproducibly quantified.

The clearance rates of several of the probes can be anticipated from the physiochemical properties of the core dye structure. The larger molecular weight cyanine dyes with permanent negative charges from sulfonic acid groups do not readily cross endosomal or plasma membranes and are retained with a > 2-day half-life. Positively charged dyes can localize to mitochondria

(*77*), while weak bases are trapped within lysosomes. Highly lipophilic dyes can more readily cross membranes, but protein binding and partitioning into the membrane may slow cell clearance (*78*). The weak acid, DDAO, has a pKa of 5.0 (*79*) where most of the dye remains charged within the cell. Although the exact mechanism is debated, this allows a portion of the uncharged neutral form to cross the lipophilic bilayer while the charged form prevents significant partitioning into the membranes. Fluorescein, a visible light fluorescent weak acid (pKa ~ 6.4), also washes out of cells quickly (*80*). The low molecular weight Atto740 also diffused out of cells quickly.

BODIPY-650 diffused out of cells at a similar rate as the charged cyanine dyes, but the lipophilic neutral dye also brings up additional considerations. BODIPY-650 conjugates show strong membrane partitioning and protein binding (*68*), which likely contributed to the slow loss in signal despite measurable membrane permeability (Figure 2.3). Protein binding can also impede extravasation into the tissue (*81*,*82*). If this mimics the radiolabel of interest or increased plasma protein binding is desired to reduce renal filtration, this can be an asset. However, good separation between labeled cetuximab and unreacted dye could not be obtained. SDS-PAGE analysis of the labeled antibody always showed a significant free dye band indicating that unreacted dye could not be removed in aqueous solution.

To test our hypothesis that passive diffusion from the cell dictates the residualization rate, the permeability of the dyes was measured using a parallel artificial membrane permeability assay (PAMPA). This eliminates any effect from drug transporters such as p-glycoprotein or organic anion transporters which can shuttle dyes across membranes (*83*,*84*). While the

permeability of all the dyes was low, only measurable permeation through the membranes was detectable for DDAO, Atto740, and BODIPY-650, providing evidence that these dyes can exit the cells by passive diffusion after degradation of the antibody.

While the dye residualization rate has a major impact on imaging properties, several other factors need to be considered in the context of imaging agent design. First, the dye properties alone are not solely responsible for the rate of washout after cell labeling. The linker region, conjugation chemistry, and/or targeting molecule can have a major impact on the residualizing behavior of a dye (*85*), and properly designed linkers can increase cellular retention if desired. In this work, the intrinsic rate of several commercially available dyes containing a common NHS ester lysine linkage was quantified. Second, plasma protein binding, particularly to albumin, affects the extravasation rate of the molecule, especially for smaller probes (*82*). The number and spacing of charges on the dye will impact the extent of protein bound fluorophore (*86*,*87*). Third, the labeled product may have significantly different distribution depending on the size and properties of the targeting moiety (*65*). Finally, the optical properties impact the background signal and light penetration. Dyes in the 630-680 nm range will have significantly lower target to background ratios due to a higher contribution of autofluorescence to both the target and background signal (*88*,*89*). In this work, residualizing and non-residualizing dyes in both the 630-680 nm and the 700-800 nm range were identified, allowing the researcher flexibility in designing probes with the desired wavelength and residualizing properties.

There are several other steps to washout from the tissue in vivo. After exiting the cell, the fluorescent degradation product must diffuse through the tissue to a capillary or lymph vessel

and intravasate before exiting the tissue. These steps can occur within minutes (*90*), so the hours required for exiting the cell are often the rate-limiting step. The in vitro assay here does not capture all the complexity in vivo, however, so care must be taken when extrapolating to animal data.

2.6 Conclusion

Commonly used and commercially available NIR dyes exhibit varying rates of cellular retention after internalization. DDAO and Atto740 diffuse out of cells quickly following internalization and degradation, while the cyanine-based probes had significant retention in cells over several days. Residualizing dyes are useful for studying protein metabolism, signal amplification of internalizing targets, and fluorescent surrogates for residualizing radioisotopes. For monitoring the distribution of intact protein therapeutics, reducing signal in clearance organs, and fluorescent surrogates for non-residualizing radioisotopes such as iodine, the non-residualizing fluorophores are ideal. Fortunately, this study has identified both residualizing behaviors in far-red and near-infrared wavelength dyes, allowing investigators to select the wavelength and residualizing properties appropriate for their application. These rates should prove useful in experimental design, in vivo data interpretation, and molecular probe development.

2.7 Experimental Methods

Materials

A-431 cells were obtained from ATCC (Manassas, Virginia). Cetuximab (Bristol-Myers Squibb, Princeton, New Jersey) was conjugated according to the manufacturer's instructions

with each of the following dyes: CellTraceTM Far Red DDAO-SE (DDAO) (Life Technologies, Eugene, Oregon), IRDye® 800CW NHS Ester (IRDye)(LI-COR, Lincoln, Nebraska), Alexa Fluor® 680 NHS Ester (AF680) (Life Technologies, Eugene, Oregon), Alexa Fluor® 750 NHS Ester (AF750) (Life Technologies, Eugene, Oregon), Sulfo-Cyanine7 (SulfoCy7) (Lumiprobe Corporation, Hallandale Beach, Florida), Cy5.5 (GE Healthcare Bio-Sciences, Pittsburgh, Pennslyvania), Bodipy® 650/660-X (BODIPY-650) (Life Technologies, Eugene, Oregon), Atto 740 NHS Ester (Atto 740) (Sigma-Aldrich Corp., St. Louis, Missouri). Dyes were reacted in 10% sodium bicarbonate and antibody solution (2 mg/mL) for 2 hours at room temperature. A molar ratio of 1.0 was used for all dyes. The antibody-dye conjugates were purified using 800uL of 5g/50mL water of Biogel P-6, Fine (Bio-Rad, Hercules, California) in Spin-X centrifuge filter tubes (Corning, Corning, New York). The final degree of labeling was determined by the absorption at 280 nm corrected for the fluorophore and the max absorption wavelength of each dye using a NanoDrop 1000 spectrophotometer. A western blot was performed to ensure that there was no free dye remaining.

Residualizing Dye Plate Assay

The rates of dye cellular dye loss were measured over a period of eight days with the Odyssey Imaging System (LI-COR). Cells were plated in 96-well plates overnight at between 90-100% confluency. The cells were labeled with cetuximab-dye conjugates at 40 nM for 30 minutes at 37°C, then subsequently washed three times to remove excess probe. The cells were washed daily with media (DMEM supplemented with 10% fetal bovine serum, 2% sodium bicarbonate, and 1% penicillin/streptomycin) and then scanned with the Odyssey Imaging

System to obtain the bulk fluorescence signal for each well. The fluorescent intensities for each dye were normalized to the maximum signal achieved after internalization and unquenching.

Confocal Microscopy

Falcon™ Culture Slides (Fisher Scientific, Pittsburgh, Pennsylvania) were imaged with an upright Olympus FV1200 confocal microscope using 405, 633, and 750 nm lasers and a 60x objective. Cells were plated overnight at 90-100% confluency. Cells were labeled with each antibody-dye conjugates at 0, 24, and 48 hours under the same conditions described above and subsequently were washed twice with media. After 48 hours cells were incubated with Hoechst 33342 for 5 min at room temperature, washed with media, and then imaged.

PAMPA Assay

Membrane permeability was measured using the BD Gentest™ Pre-coated PAMPA Plate System. Briefly, NHS ester derivatives of all dyes were mixed into aqueous solution overnight at room temperature to allow dyes to hydrolyze into the unreactive carboxylic acid form. 1 μM hydrolyzed dye was used in the donor wells and was incubated for 5 hours at room temperature. Donor and acceptor concentrations were obtained using the Odyssey Imaging System and the permeability was then calculated according to manufacturer's instructions.

Chapter 3

Tracking Antibody Distribution with Near-Infrared Fluorescent Dyes: Impact of Dye Structure and Degree of Labeling on Plasma Clearance

3.1 Publication Information

Cilliers, C., I. Nessler, N. Christodolu, and G. M. Thurber. *Tracking Antibody Distribution with Near-Infrared Fluorescent Dyes: Impact of Dye Structure and Degree of Labeling on Plasma Clearance*. Molecular Pharmaceutics. 2017; 14(5): 1623-33.

Modifications have been made to the published document to adapt the content to this text. The previous chapter identified several residualizing NIR fluorophores for molecular imaging. This chapter builds on this previous *in vitro* work by outlining conditions to label the antibodies with NIR fluorophores without impacting the pharmacokinetics of the antibody *in vivo*.

3.2 Abstract

Monoclonal antibodies labeled with near infrared (NIR) fluorophores have potential use in disease detection, intraoperative imaging, and pharmacokinetic characterization of therapeutic antibodies in both the preclinical and clinical setting. Recent work has shown conjugation of NIR fluorophores to antibodies can potentially alter antibody disposition at a sufficiently high degree of labeling (DoL); however, other reports show minimal impact after labeling with NIR fluorophores. In this work, we label two clinically approved antibodies Herceptin (trastuzumab) and Avastin (bevacizumab) with NIR dyes IRDye 800CW (800CW) or Alexa Fluor 680 (AF680), at a 1.2 and 0.3 dyes/antibody and examine the impact of fluorophore conjugation on

antibody plasma clearance and tissue distribution. At 0.3 DoL, AF680 conjugates exhibited similar clearance to unlabeled antibody over 17 days while 800CW conjugates diverged after 4 days, suggesting AF680 is a more suitable choice for long-term pharmacokinetic studies. At the 1.2 DoL, 800CW conjugates cleared faster than unlabeled antibodies after several hours, in agreement with other published reports. The tissue biodistribution for bevacizumab-800CW and -AF680 conjugates agreed well with literature reported biodistributions using radiolabels. However, the greater tissue autofluorescence at 680 nm resulted in limited detection above background at low (~2 mg/kg) doses and 0.3 DoL for AF680, indicating that 800CW is more appropriate for short-term biodistribution measurements and intraoperative imaging. Overall, our work shows a DoL of 0.3 or less for non-site specifically labeled antibodies (with a Poisson distribution) is ideal for limiting the impact of NIR fluorophores on antibody pharmacokinetics.

3.3 Background

Monoclonal antibodies are the largest class of biologics and they continue to grow due to multiple applications in cancer treatment, autoimmune disorders, and other diseases. Currently there are over 50 FDA approved therapeutics, and, as of mid-November 2015, there were 53 in phase 3 clinical trials and over 470 in various stages of the clinical pipeline (*91*). Antibodies exhibit complex pharmacokinetics because of their large size, long circulating half-life (including FcRn recycling), target mediated drug disposition (TMDD), limited tumor penetration, and immunogenic responses, making *a priori* predictions of monoclonal antibody distribution exceedingly difficult. Therefore, robustly characterizing the pharmacokinetics of novel next-generation antibodies, antibody-drug conjugates, bispecific antibodies, and other

protein scaffolds in the preclinical and clinical setting can aid in development and help produce lead therapeutic candidates with a higher likelihood of clinical success.

Bioanalytical methods remain the industry standard for measuring plasma clearance of biologics, since any modification (radiolabel, fluorophore, etc.) can potentially modify the distribution of an agent (*92*,*93*). Conventional techniques for determining antibody disposition include plasma clearance measurements using ELISA or LC-MS, and tissue distribution using immunohistochemistry and immunofluorescence. However, these bioanalytical techniques do not have the high spatial and temporal resolution, the ease of measuring drug metabolism, or the direct detection of radiolabeling or fluorescence techniques. Radiolabeling methods made significant improvements during early studies with monoclonal antibodies (e.g. (*94*)) in the stability of the conjugation chemistry and without disrupting binding (*95*). Several results have shown negligible changes in plasma clearance relative to unlabeled antibodies (*76*,*96*). Therefore, radiolabels remain the gold standard for quantifying bulk organ and tissue distributions using scintillation counting and *in vivo* imaging, such as positron emission tomography (PET) (*97*). Although experimental methods are approaching the cellular scale (*98*), their resolution is intrinsically limited by the path length of the positron and imaging equipment. Additionally, the time/half-life constraints, safety concerns, and expense of radioactivity limit its broad applicability for high-resolution imaging and single-cell measurements.

There is growing interest in using near infrared (NIR) fluorescent dyes as molecular imaging agents for pharmacokinetic tracking, disease characterization/detection (*99*), and intraoperative imaging (*65*,*100*) due to the high spatial and temporal resolution of fluorescence

imaging, low tissue autofluorescence, and deep tissue penetration of light (*101–105*). For example, in a recent publication, we used the high spatial resolution of fluorescence to demonstrate the importance of tumor penetration on antibody drug conjugate (ADC) efficacy, highlighting one application where tissue-level distribution in addition to organ-level biodistribution is important for describing drug effects (*106*). NIR dyes provide a convenient and safe method to quantify pharmacokinetics at the subcellular to tissue level while retaining the possibility for quantifying macroscopic organ biodistribution (e.g. (*53*), although more tissue processing is required compared to radiolabeling). Radiolabeling techniques remain the gold standard for whole animal imaging and organ biodistribution, but NIR fluorescent dyes can complement these results with high resolution tissue distribution (fluorescence microscopy) and single-cell data (flow cytometry) while providing biodistribution data for validation between the methods (i.e. comparing fluorescence %ID/g (*107*) with radiolabeled results). Additionally, conventional visible light dyes can easily be used with NIR dyes for multichannel flow cytometry or immunofluorescence (*81*).

Despite these advantages for high resolution and single cell imaging, NIR fluorescence labeling techniques have room for improvement to lower the impact of labeling on distribution and clearance (just as radiolabeling techniques did decades ago (*76*,*108–110*)). In particular, there is no consensus on the optimum degree of labeling (DoL), or average number of dyes per antibody that should be used to prevent the dye from altering antibody pharmacokinetics. Some recent work with the NIR fluorophore IRDye800CW (800CW, LI-COR) demonstrates that antibody clearance can be altered upon fluorophore conjugation (*76*,*107*,*111*,*112*), and higher degrees of labeling result in increased liver uptake. While this may not be an issue for imaging

and detection applications, it would limit the use for pharmacokinetic characterization of antibodies. These groups also showed that lower degrees of labeling result in a reduced impact on distribution; however, some of these studies were performed with dual radiolabeled and fluorophore labeled antibodies, thereby preventing independent comparisons between unlabeled and labeled antibodies.

In this work, we examined the effects of conjugation of 800CW and another commonly used fluorophore, Alexa Fluor 680 (AF680), on the pharmacokinetics of two clinically approved antibodies, Herceptin (trastuzumab) and Avastin (bevacizumab). We selected 800CW because of its clinical relevance for NIR intraoperative imaging and literature precedent and compared it to AF680 (excited in far-red and emitting in near infrared) because of the similar cyanine based structures and residualization properties (*113*). Our previous work with NIR labeled peptidomimetics also showed that AF680 has one of the lowest plasma protein binding rates of all the NIR dyes tested (*114*). We used a 1.2 and 0.3 DoL of each dye, measured plasma clearance by fluorescence and ELISA, and performed tissue biodistribution experiments to see if fluorophore conjugation altered antibody distribution. Additionally, we labeled the clinically approved antibody-drug conjugate (ADC) Kadcyla (trastuzumab emtansine) with AF680 and tracked its tumor distribution out to seven days as an example application studying tissue pharmacokinetics.

3.4 Results

A space-filling model of a full IgG1 antibody (PDB code: 1igy) (*96*,*115*) (gray) conjugated to a single molecule of AF680 (blue) and 800CW (red) shows the relative size

difference between a typical antibody and dye (Figure 3.1). Both dyes are shown non-specifically conjugated to lysines on the heavy chain of the antibody. Lysines, which are a common site for non-specific conjugation of small molecules or fluorescent dyes using ester chemistry, are shown in green. (The number and placement of lysine residues will vary between antibodies.) For bevacizumab and trastuzumab there are 86 and 90 lysines, respectively, with a majority appearing on the heavy chain (62 and 64, respectively) (*116*). Figure 3.1 shows the chemical structure of AF680 and 800CW conjugated to the amine of a lysine on the antibody (*117*). Both cyanine dyes share a similar structure and have similar hydrophilicity; however, AF680 has one less sulfate group, giving it a net -2 charge compared to 800CW's net -3 charge. Also, the optical properties for AF680 and 800CW make them ideal for use with the 700 and 800 channels of the Odyssey CLx, respectively.

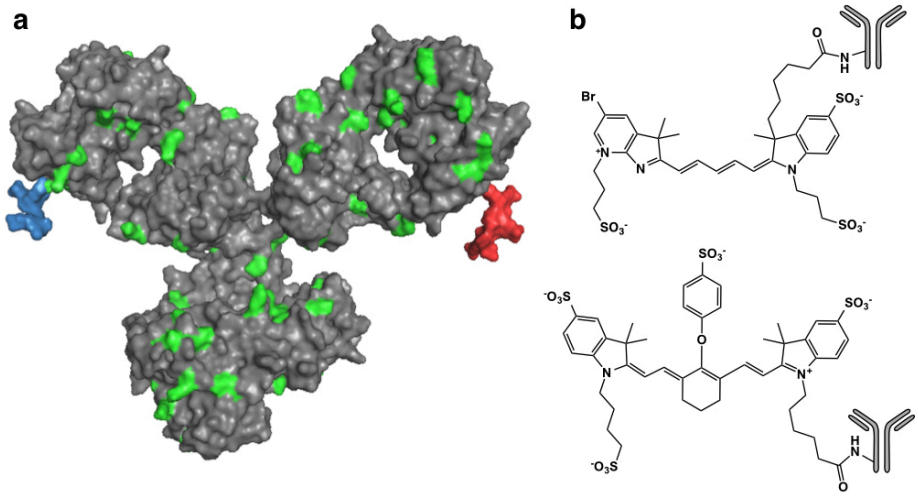

Figure 3.1 Dye structures and relative size of dyes to antibody.
Space filling model of an IgG (PDB ID: 1igy) (*115*) with both AF680 (blue) and 800CW (red) attached to lysines (green) on the heavy chain (A). Dye structures were exported from MarvinSketch as a pdb file and merged with the IgG in Pymol. (B) Chemical structure of AF680 (top) and 800CW (bottom).

After conjugation and purification, all antibody-dye conjugates were run on SDS-PAGE and the gel was scanned on the Odyssey CLx to ensure free dye was removed (Figure 3.2). This

indicates less than 3% free dye remaining (*118*). Differences in relative labeling of the heavy or light chain could cause differences in antibody pharmacokinetics between the dyes; however, the relative intensities of heavy to light chain are similar, indicating any observed differences are likely due to the dye and not differences in labeling location. Absorbance spectra used for DoL characterization is shown in Figure 3.3.

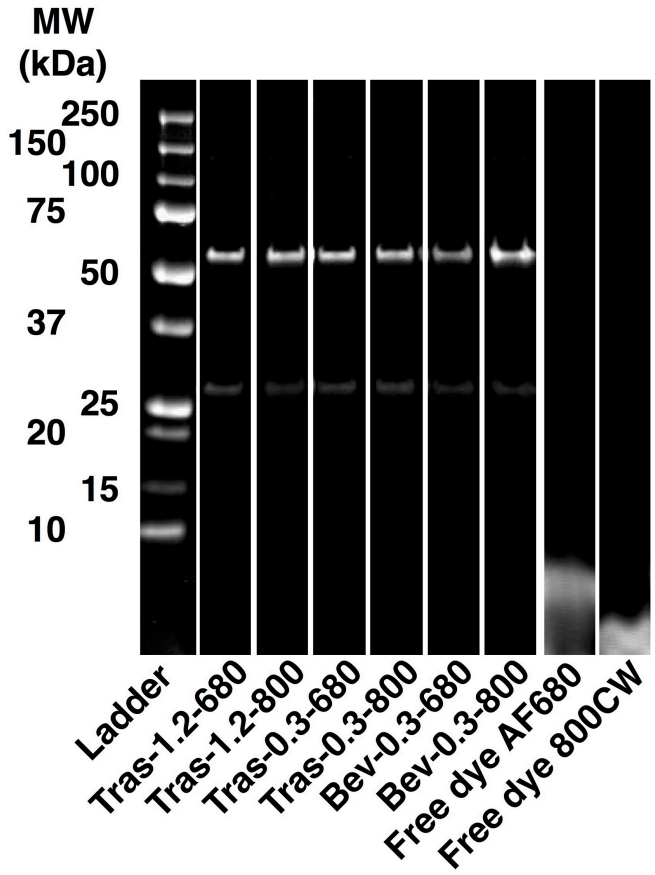

Figure 3.2 SDS-PAGE of antibody-dye conjugates and free dye.
After reaction and purification all conjugates were run on SDS-PAGE and scanned on the Odyssey CLx NIR scanner to ensure free dye was removed. Window leveling adjusted for similar brightness from heavy chain. Tras, trastuzumab; Bev, bevacizumab.

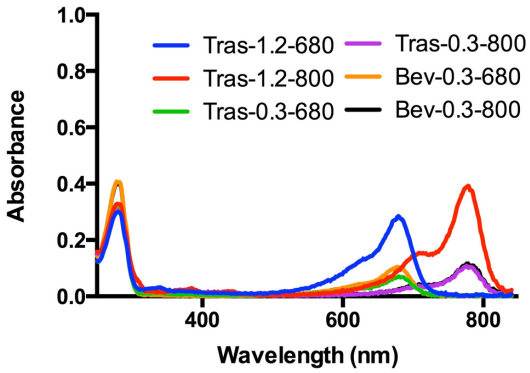

Antibody-Dye Conjugate	280nm Absorbance	Dye Max Absorbance	Protein Conc. (μM)	Dye Conc. (μM)	DoL
Bev-0.3-800	0.399	0.115	17.5	4.8	0.3
Tras-0.3-800	0.314	0.108	13.7	4.5	0.3
Tras-1.2-800	0.326	0.392	13.6	16.3	1.2
Bev-0.3-680	0.405	0.103	17.8	5.7	0.3
Tras-0.3-680	0.323	0.070	14.2	3.9	0.3
Tras-1.2-680	0.300	0.283	12.7	15.7	1.2

Figure 3.3 Antibody-dye absorbance spectra.
After reaction and purification, the absorbance spectrum for each antibody-dye conjugate was used to determine the DoL as described in the methods section. DoL was determined by dividing bulk fluorophore concentration by antibody concentration. Tras, trastuzumab; Bev, bevacizumab.

Plasma clearance for each antibody-dye conjugate was determined by fluorescence and the total antibody clearance by ELISA. The plasma concentration as measured by fluorescence and ELISA was normalized to the initial concentration and fit to a biexponential decay using PRISM. Table 3.1 shows the fitted parameter values. Figure 3.4 and Figure 3.5 show the biexponential decay of the normalized plasma clearance over 4 days (top) and 17 days (bottom). The absolute plasma concentration time profiles are shown in Figure 3.6. At a 1.2 DoL, the fluorescent Tras-800CW exhibited faster clearance than the total trastuzumab, even 8 hours post-injection (which have non-overlapping error bars) (Figure 3.4). At longer times, the beta phase clearance diverges significantly indicating 800CW altered the pharmacokinetics of the antibody.

These data agree with Conner et al. where the clearance of a different antibody-800CW conjugate showed faster clearance at a similar DoL of 1.5 (*76*). At a 0.3 DoL, however, both Tras-800CW and Bev-800CW showed similar clearance over the first several days, and only after 4 days does the clearance diverge significantly. The AUC for the normalized plasma clearance (Table 3.2) shows the fluorescence AUC is significantly different from the total antibody AUC for all 800CW conjugates at 17 days. The serum stability of Tras-AF680 and Tras-800CW was also measured over 17 days (Figure 3.7, Figure 3.8). Tras-AF680 and Tras-800CW maintain 95% and 85% of their initial signal at day 4 and >80% and >60% by day 17, respectively; indicating serum stability/dye quenching is not the cause of faster clearance. The lack of free dye formation in plasma (Figure 3.9) and serum stability samples indicates that dye deconjugation is likely not causing the faster clearance of fluorescent antibody.

Table 3.1 Plasma clearance fitted biexponential parameters from PRISM.

Conjugate	% alpha	alpha (day^{-1})	beta (day^{-1})	AUC
Bev-0.3-680-F	61.6	4.410	0.054	7.27
Bev-0.3-680-E	55.3	7.741	0.065	6.94
Bev-0.3-800-F	60.5	4.123	0.166	2.53
Bev-0.3-800-E	58.9	5.817	0.056	7.41
Tras-1.2-680-F*	60.6	3.316	0.083	4.92
Tras-1.2-680-E*	58.4	3.063	0.038	11.10
Tras-1.2-800-F	70.8	3.917	0.181	1.79
Tras-1.2-800-E	55.3	3.505	0.054	8.38
Tras-0.3-680-F	61.6	3.403	0.080	5.01
Tras-0.3-680-E	80.9	1.083	0.011	18.01
Tras-0.3-800-F	66.6	2.383	0.174	2.20
Tras-0.3-800-E	78.5	1.234	0.011	21.05

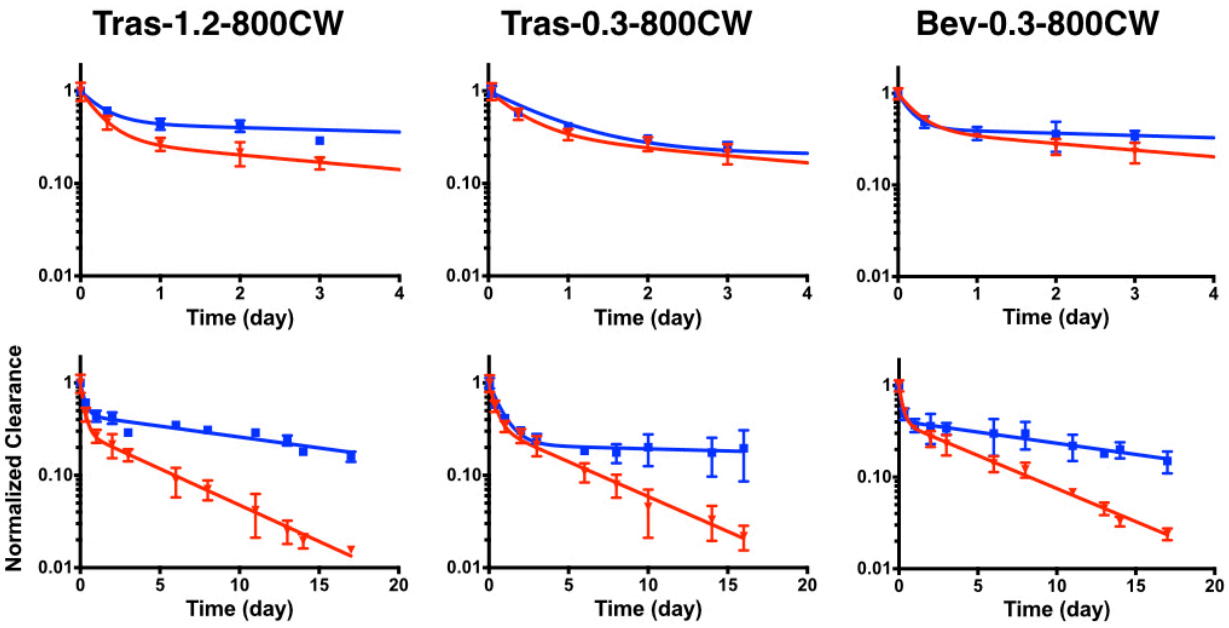

Figure 3.4 Antibody-800CW conjugate plasma clearance.
Normalized clearance as measured by fluorescence (red) and ELISA (blue) for trastuzumab with a DOL of 1.2 and 0.3 (left and middle, respectively), and bevacizumab with a 0.3 DOL (right) for 800CW conjugates. Clearance over the first 4 days is shown on top. Trast, trastuzumab; Bev, bevacizumab.

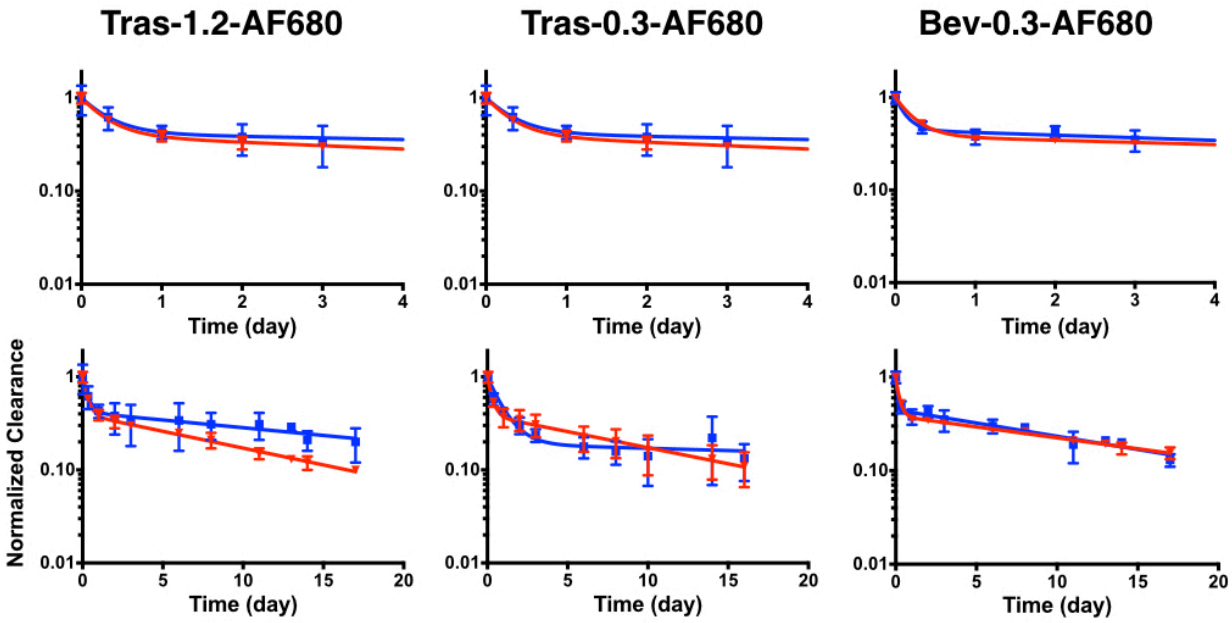

Figure 3.5 Antibody-AF680 conjugate plasma clearance.
Normalized clearance as measured by fluorescence (red) and ELISA (blue) for trastuzumab with a DoL of 1.2 and 0.3 (left and middle, respectively), and bevacizumab with a 0.3 DoL (right) for AF680 conjugates. Clearance over the first 4 days is shown on top. Trast, trastuzumab; Bev, bevacizumab.

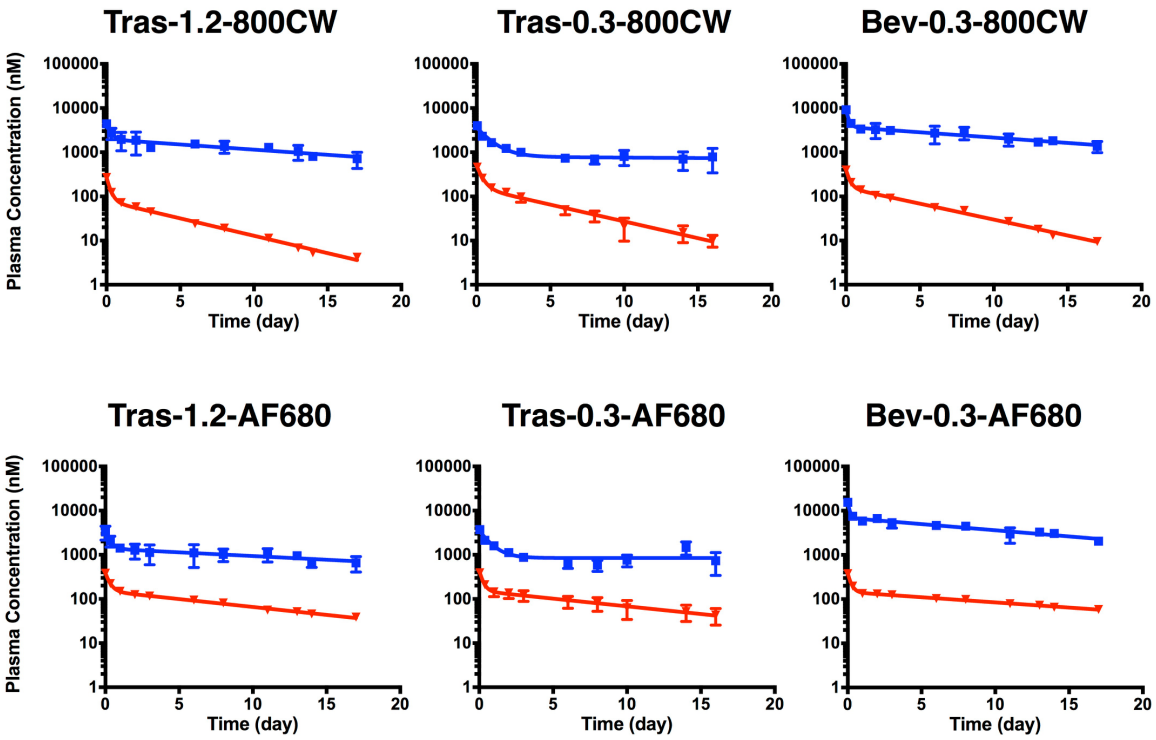

Figure 3.6 Absolute concentrations of antibody-dye conjugate plasma clearance.
The plasma concentration as measured by fluorescence (red) and ELISA (blue) for trastuzumab-dye conjugates with a low (1.2) and tracer (0.3) DOL (left and middle, respectively), and bevacizumab-dye conjugates with a tracer DOL (right). ELISA concentrations are higher due to the 550µg of total antibody versus 50µg of labeled antibody. Figure 3.4 and Figure 3.5 was generated by normalizing each data set to the initial concentration. Tras, trastuzumab; Bev, bevacizumab.

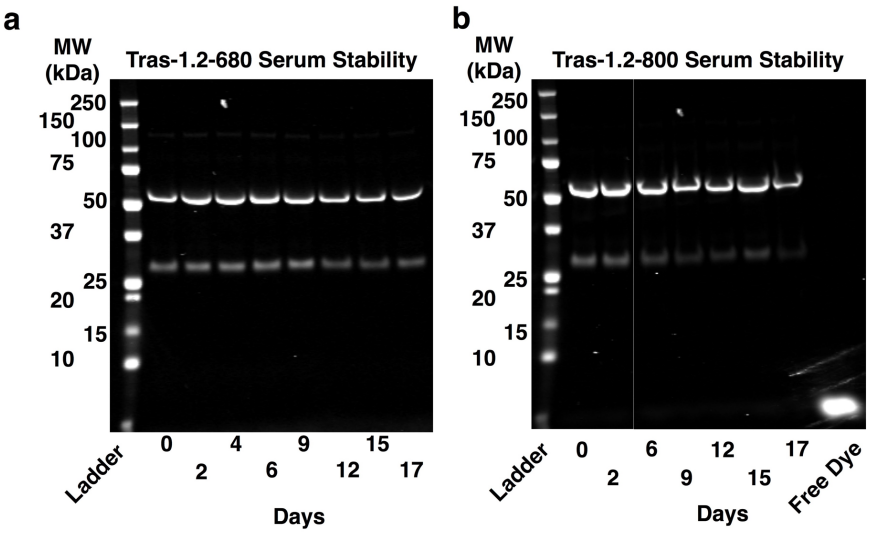

Figure 3.7 SDS-PAGE of serum stability samples.
Serum stability samples show intact antibody out to 17 days and no detectable formation of free dye.

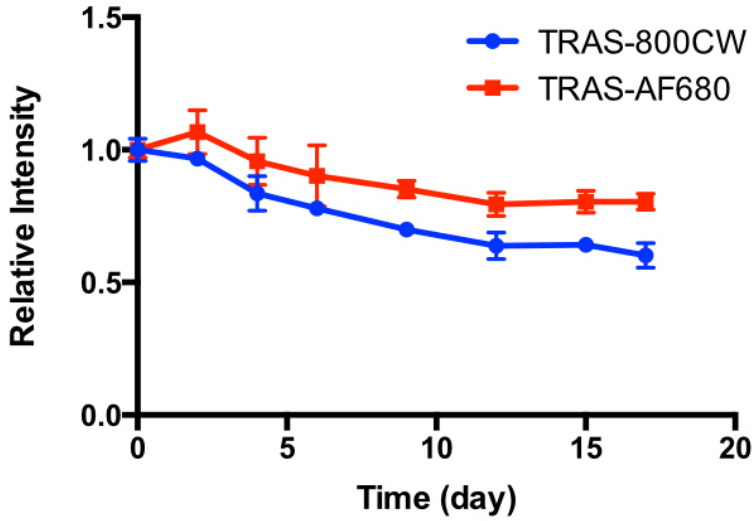

Figure 3.8 Antibody-dye conjugate serum stability.
Both Tras-AF680 and Tras-800CW show slight loss in fluorescence over 17 days (80% and 60% of initial, respectively); however, the loss in fluorescence does not account for the rapid drop in fluorescent signal seen with 800CW in Figure 3.4. Therefore, the loss of fluorescent signal in Figure 3.4 is due to clearance of the antibody-dye conjugate, not loss of fluorescence from the dye being in serum. Tras-AF680 and Tras-800CW, both with a DoL of 1.2, were mixed with fetal bovine serum (FBS) at 30nM. The serum/antibody-dye aliquots were thawed rapidly in a 37°C water bath and incubated at 37°C for the number of days shown. The samples were thawed and placed at 37°C in reverse order (17 day time point first) so the samples could all be measured on the same day. 15 µL of each sample was scanned in a 384 well plate on the Odyssey CLx, and the experiment was performed in triplicate.

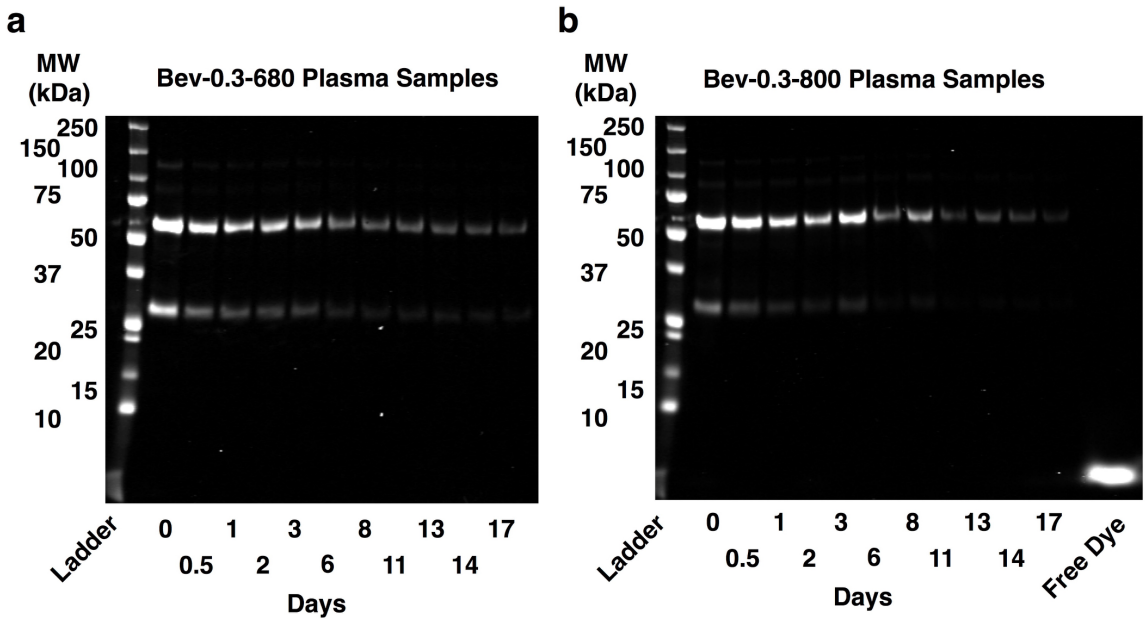

Figure 3.9 Fluorescence SDS-PAGE of bevacizumab-dye conjugate blood samples.
SDS-PAGE of bevacizumab-AF680 (A) and bevacizumab-800CW (B) plasma clearance samples. Over the course of the experiment bevacizumab-dye conjugates remain intact and there is no detectable formation of free dye.

In comparison, AF680 exhibits less impact on the pharmacokinetics of the antibodies (Figure 3.5). Even at a 1.2 DoL, Tras-AF680 shows similar clearance to total antibody out to 9 days. At a 0.3 DoL both trastuzumab and bevacizumab exhibited similar clearance over 17 days. Although the biexponential fit for Tras-AF680 appears to have a faster beta phase decay, the data points are overlapping at each point. For Bev-AF680, the clearance is nearly identical. Furthermore, the fluorescence AUC does not differ significantly from total antibody for any AF680 conjugates (Table 3.2), even at the higher DoL. These results indicate a 0.3 DoL of AF680 does not significantly affect antibody disposition for these antibody-dye conjugates.

Table 3.2 Normalized AUC for antibody-dye conjugates.

Conjugate	$AUC_{day\ 0\text{-}3}$ (day)	$AUC_{day\ 0\text{-}17}$ (day)
Tras-1.2-800-F	**0.92 ± 0.03***	**1.77 ± 0.07***
Tras-1.2-800-E	**1.41 ± 0.39**	**4.92 ± 1.16**
Tras-1.2-680-F	1.26 ± 0.15	3.81 ± 0.41
Tras-1.2-680-E	1.39 ± 0.38	5.45 ± 1.82
Tras-0.3-680-F	1.27 ± 0.25	3.69 ± 1.10
Tras-0.3-680-E	1.26 ± 0.06	3.59 ± 0.92
Tras-0.3-800-F	1.13 ± 0.18	**2.14 ± 0.48***
Tras-0.3-800-E	1.26 ± 0.03	**3.77 ± 0.53**
Bev-0.3-680-F	1.24 ± 0.06	4.48 ± 0.25
Bev-0.3-680-E	1.33 ± 0.15	4.70 ± 0.59
Bev-0.3-800-F	1.11 ± 0.06	**2.45 ± 0.16***
Bev-0.3-800-E	1.24 ± 0.20	**4.70 ± 1.08**

For non-site specific labeling techniques, such as conjugation to surface lysine residues using N-hydroxysuccinimide (NHS) chemistry, the number of possible labeling sites is relatively large. Therefore, the number of dyes per antibody is anticipated to result in a Poisson distribution (*119–121*). Assuming the non-specific lysine conjugation of fluorophores follows this distribution, Figure 3.10 shows the expected fractions of the number of dyes per antibody in samples with a DoL of 0.3 and 1.2. For the 0.3 DoL, the distribution of antibody labeling is approximately 75% unlabeled, 22% singly labeled, and <5% with 2 or more dyes per antibody. At the higher DoL of 1.2, the fraction of unlabeled antibody decreases (30%) and the percentage of singly labeled increases (36%); however, the fraction of antibody with 2 or more labels also dramatically increases to 44%. When using fluorescence detection, the unlabeled antibodies do

not contribute to overall signal, and antibodies with 2 dyes would contribute twice as much signal (assuming no quenching effects). Accounting for these two phenomena, Figure 3.10 shows the expected theoretical contributions to the overall fluorescent signal from a DoL of 0.3 and 1.2 (assuming no self-quenching). For a DoL of 0.3, 74% of the measured fluorescence signal is expected to be from antibodies with a single dye, while only 30% of the signal is expected to be from singly labeled antibodies at a DoL of 1.2. Importantly, the percentage of signal from antibodies with 3 or more dyes is less than 4% of the total signal for a DoL of 0.3. Conversely, over a third of the signal for DoL 1.2 comes from 3 or more dyes per antibody. The 1.2 DoL also caused a slight increase in the K_d compared to no difference with 0.3 DoL (Figure 3.10).

Reduced autofluorescence in the NIR region of the electromagnetic spectrum has prompted the use of NIR fluorescent dyes in tissue biodistribution studies with the Odyssey CLx scanner (*53*,*76*,*106*,*122*). Whole organ fluorescence scans suffer from depth of imaging artifacts and provide arbitrary values (requiring the digest and dilution) but agree qualitatively with the organ digest results (Figure 3.11). Previous studies have compared 800CW to radiolabels and have found antibody disposition is not significantly altered at sufficiently low DoL (*107*,*111*). Because tissue autofluorescence is higher in the 680 nm region of the spectrum (relevant for AF680) compared to the 800 nm region, we chose to compare the biodistribution of AF680 and IRDye labeled antibodies. To limit variability between animals, we compared the distribution in the same mice using both the 700 and 800 channels on the Odyssey CLx (since there is negligible cross talk between the dyes in the different channels). The biodistribution of Bev-AF680 and Bev-800CW, both with a 0.3 DoL, 48 hours after IV administration is shown in

Figure 3.12. For comparison, the biodistribution 48 hours after tail-vein injection of radiolabeled bevacizumab was plotted from Paudyal et al. (*123*). This data set was chosen because of the matching times, use of a residualizing label (as are IRDye800CW and AF680 (*113*)) and lack of flushing the organs (which will remove blood signal but could also alter tissue values). Paudyal and colleagues quantified the distribution of a 20 μg dose of ^{64}Cu-DOTA-bevacizumab after blocking any specific interactions (*123*). The biodistribution of Bev-800CW agrees well with the radiolabeled data, with no significant differences between any of the organs. Although 800CW appears to impact antibody clearance over longer times, at 48 hours the similar plasma clearance (Figure 3.4, Figure 3.5) and systemic distribution (Figure 3.12) does not appear to significantly alter the distribution at a 0.3 DoL. Bev-AF680 distribution also agrees well with the radiolabeled data for the liver, kidney, and spleen; however, the signal to noise ratio (SNR) is less than or equal to one (Figure 3.12) for several organs because of the higher autofluorescence in the 700 channel, the 0.3 DoL and moderate dose (~2.0 mg/kg). In particular, the heart and lungs show much lower uptake for Bev-AF680 likely because the detectable signal is still in the range of background autofluorescence for this dosing level, resulting in a significant difference from Bev-800CW and ^{64}Cu-DOTA-bevacizumab (*123*). For the liver and kidney, the SNR is higher and specific signal can be detected over background. The lower autofluorescence and correspondingly high SNR for all of the organs make 800CW more suitable for whole organ distribution studies. AF680 at a 0.3 DoL may also be used in organ biodistribution studies, but to improve the SNR ratio in some organs may require higher doses than the 50 μg/mouse dose used in this study.

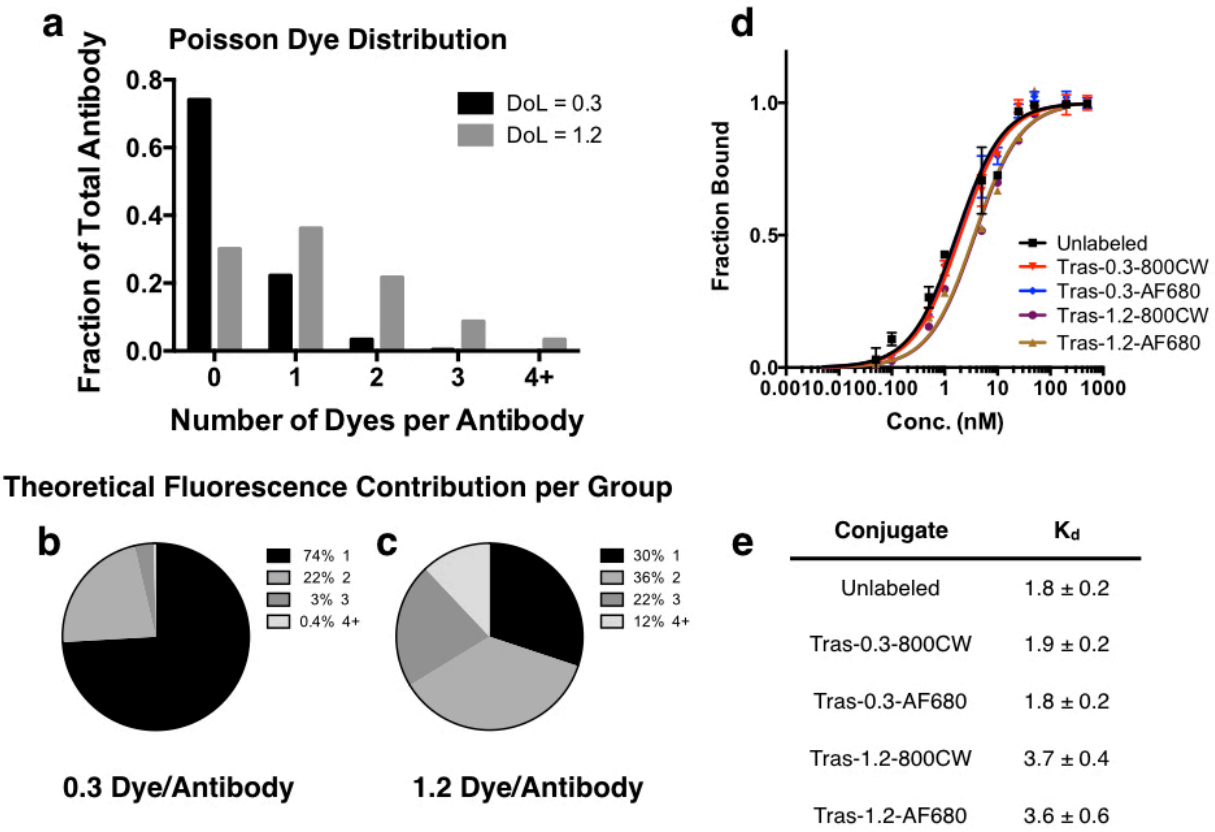

e

Conjugate	K_d
Unlabeled	1.8 ± 0.2
Tras-0.3-800CW	1.9 ± 0.2
Tras-0.3-AF680	1.8 ± 0.2
Tras-1.2-800CW	3.7 ± 0.4
Tras-1.2-AF680	3.6 ± 0.6

Figure 3.10 Theoretical dye per antibody distribution and fluorescence contribution.
(A) Expected number of dyes per antibody for DoL 1.2 and 0.3, assuming Poisson distribution. Theoretical fluorescence contribution for antibodies with 1, 2, 3, or 4+ dyes per antibody at a 0.3 (B) and 1.2 (C) DoL. (D, E) Binding curves and affinities of unlabeled trastuzumab and trastuzumab-dye conjugates. Tras, trastuzumab.

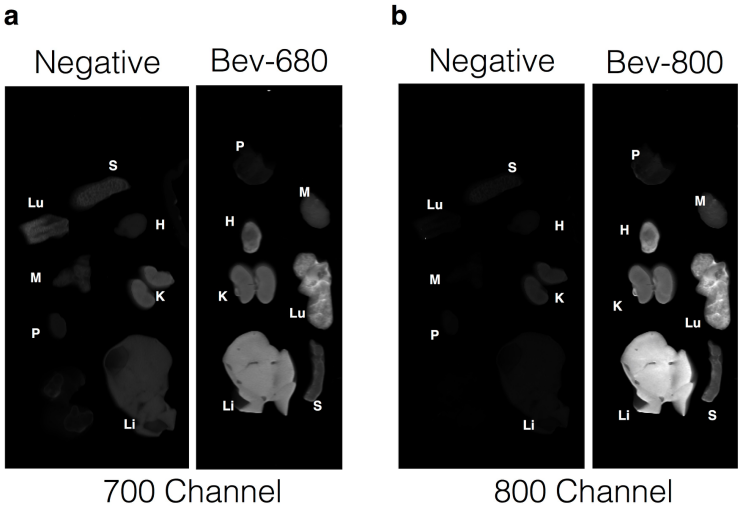

Figure 3.11 Fluorescence scan of whole organs.
(A) 700-channel scan of negative (uninjected) organs and bevacizumab-AF680 48 hours after injection. (B) 800-channel scan of negative (uninjected) organs and bevacizumab-AF680 48 hours after injection. Before further processing for biodistribution, whole organs were scanned on the Odyssey Clx. Qualitatively the signal intensity from organ scans matches the quantitative uptake from biodistributions Figure 3.12. Window leveling is the same for each channel. Li, liver; Lu, lung; K, kidneys; S, spleen; H, heart; M, muscle; P, pancreas.

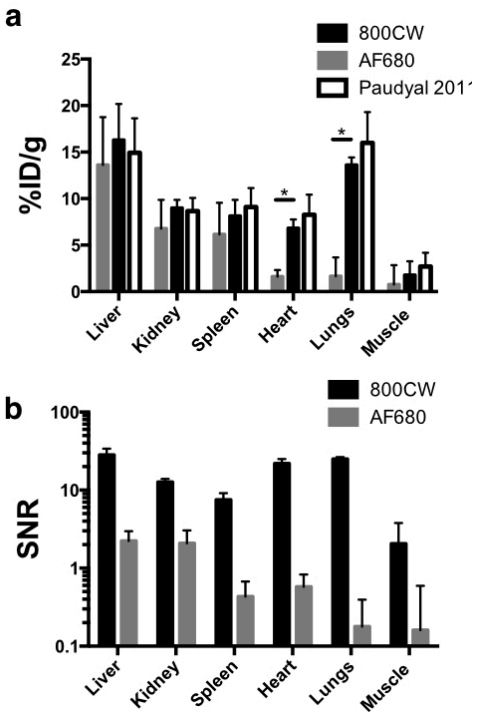

Figure 3.12 Bevacizumab biodistribution at 0.3 DoL.
(A) Biodistribution of Bev-800CW and Bev-AF680 48 hours post tail-vein injection. (B) Signal to noise ratio (SNR) in each organ for 800CW and AF680.

Despite the higher autofluorescence in whole organ biodistribution experiments, AF680 signal is high enough to detect the distribution of antibodies in NCI-N87 tumors by histology following clinical doses (e.g. 3.6 mg/kg for ado-trastuzumab emtansine/Kadcyla). The NCI-N87 tumor cell line is a human gastric carcinoma cell line that highly expresses HER2 (~1 x 10^6 receptors per cell). As an application of the direct detection provided by NIR fluorophores, we conjugated AF680 to the clinically approved antibody-drug conjugate (ADC) T-DM1 and tracked the tumor distribution over 1 week. Administration of T-DM1-AF680 at the clinical dose of 3.6 mg/kg resulted in a heterogeneous distribution in NCI-N87 tumor xenografts (Figure 3.13). Injection of Hoechst 33342 and immunofluorescence staining with anti-mouse CD31 further show that antibody disposition is limited to cells adjacent to tumor vasculature. The heterogeneous and perivascular distribution of the intact and internalized antibody (AF680 is a residualizing dye (*113*)) is maintained over 7 days, while anti-Fc staining shows a loss of intact antibody (Figure 3.14). This is consistent with the continuous internalization and degradation of HER2 (*124*), which results in antibody targeting cells close to the vessels and a majority of the tumor never receiving the therapeutic (*37*).

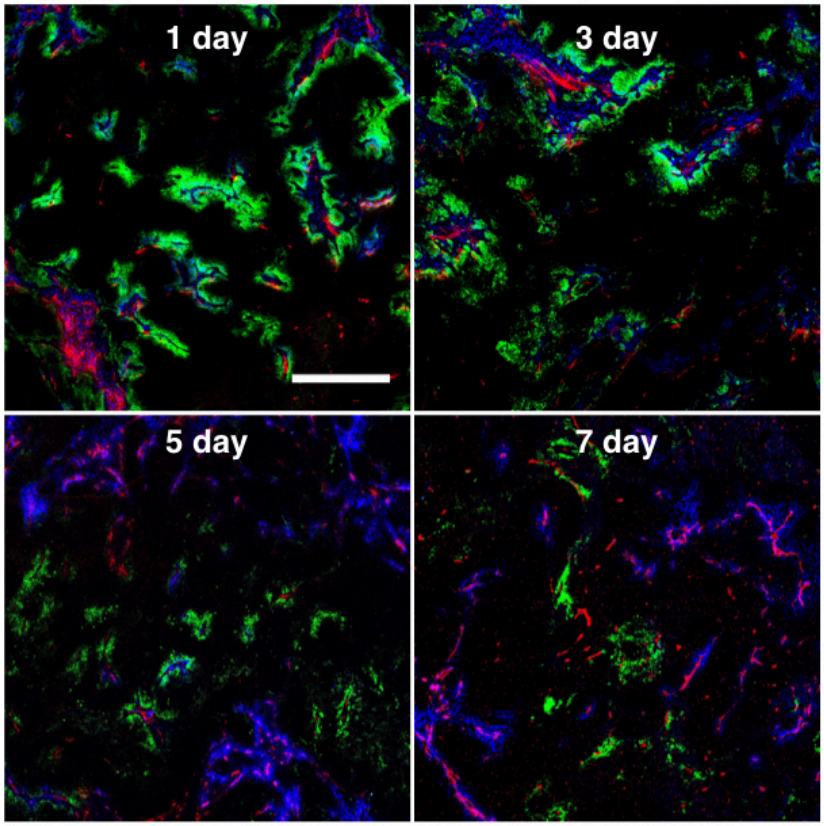

Figure 3.13 Fluorescence histology following injection of T-DM1-AF680.
Fluorescent tumor histology following injection of clinical dose (3.6 mg/kg) of T-DM1-AF680 (green) imaged at 1, 3, 5, and 7 days post-injection. 30 minutes prior to sacrifice Hoechst 33342 (blue) was injected at 15 mg/kg to highlight functional vasculature. *Ex vivo* staining was done with anti-mouse CD31-AF555 (red) to show all (functional and non-functional) tumor vasculature. Scale bar is 500μm. Window leveling is different for each image.

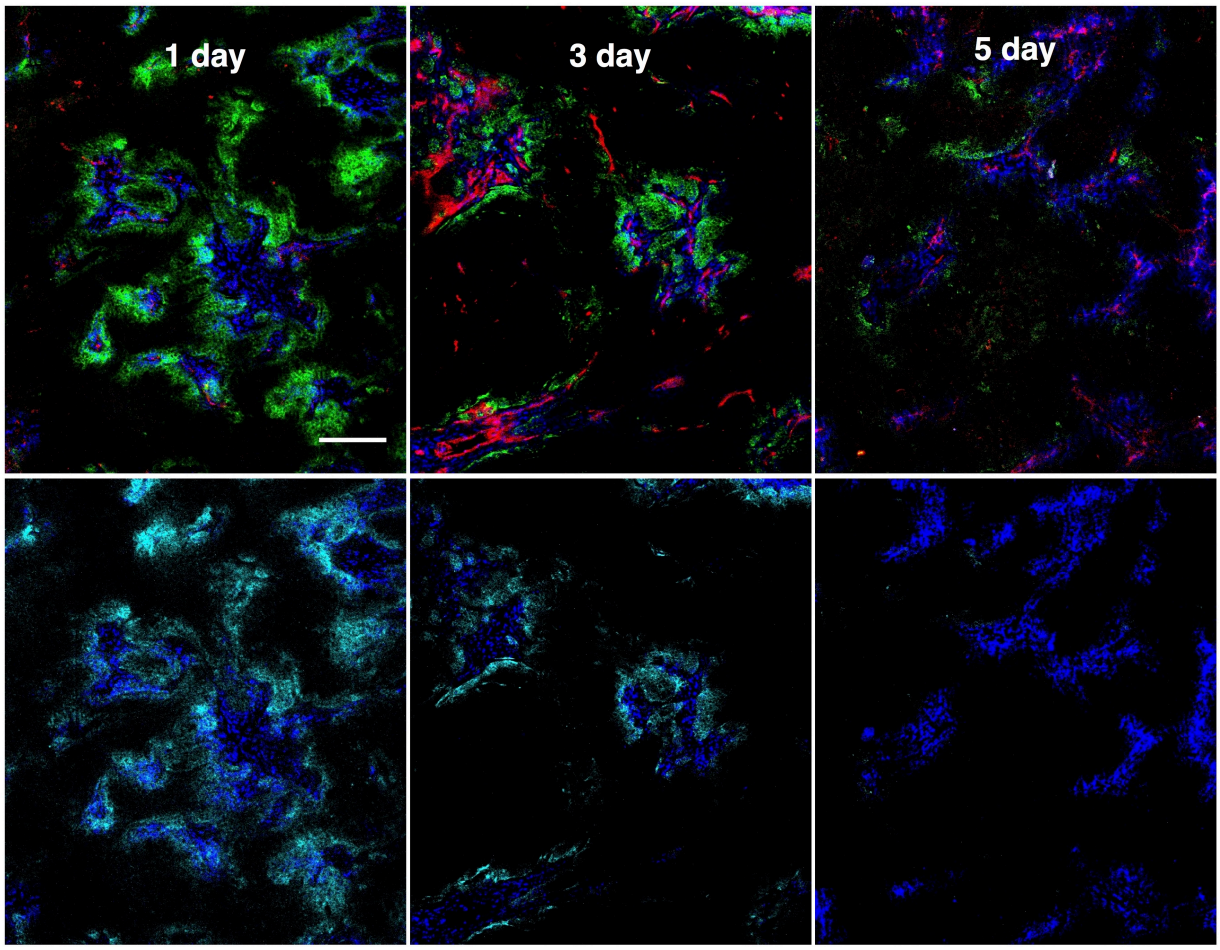

Figure 3.14 Immunofluorescence histology of T-DM1-AF680 with antihuman Fc staining. Comparison of fluorescence detection of directly labeled antibody with a residualizing probe versus immunofluorescence detection of intact antibody over 5 days following administration of 3.6 mg/kg T-DM1-AF680 (green). Hoechst 33342 (blue) was administered 30min prior to sacrifice. Anti-mouse CD31-AF555 (red) and anti-human IgG Fc–AF488(cyan) were labeled *ex vivo*. Scale bar is 200µm.

3.5 Discussion

Here we present a study of two commonly used NIR fluorophores (Figure 3.1) and their effects on the pharmacokinetics of two clinically approved antibodies. The goal of the investigation was to identify labeling conditions with a minimal impact on antibody distribution for use in pharmacokinetic studies. Our results agree with other literature reports of 800CW causing increased antibody clearance and altered tissue distribution (compared to unlabeled or radiolabeled antibodies) at DoLs greater than 1.0 (Figure 3.4) but lower impact at early times (<

4 days) at tracer levels (DoL = 0.3 or less). Building on these results, we tested an additional NIR fluorophore, AF680, which has reduced plasma protein binding compared to 800CW (*114*). AF680 antibody-dye conjugates showed nearly identical plasma clearance compared to unlabeled antibodies at 0.3 DoL, and even at 1.2 DoL did not have a significantly different normalized AUC (Figure 3.5, Table 3.2). These results should help clarify conflicting reports in the literature, delineate the impact of NIR labeling on plasma clearance, biodistribution, and tissue penetration studies, and aid in the selection of labeling conditions for different applications. In particular, the ability of fluorescence to provide cellular and subcellular resolution images (e.g. histology) and quantitative single cell data (e.g. flow cytometry) make fluorescence an attractive technique for providing high resolution pharmacokinetic data that cannot be obtained by other current methods.

Both dyes have relative strengths and weaknesses highlighted by these results. IRDye800CW is currently being tested in the clinic with antibodies (e.g. Trial: NCT01508572) making it an attractive option for antibody labeling. (The only FDA approved cyanine dye, indocyanine green (ICG), does not have a functional group for labeling. After NHS ester functionalization, fluorescence is significantly quenched after antibody conjugation (*125*).) The maximum uptake of antibodies in tumors often occurs after only a couple days, so for imaging and diagnostic applications the negligible impact of 800CW at short times (less than 4 days) would have a low impact during this time. In fact, a higher DoL will likely maximize tumor signal, which is important for depth of detection (*65*,*88*). The increase in signal from the larger number of dyes per antibody outweighs the reduction in signal from lower tumor uptake (%ID/g) due to faster clearance. However, 800CW's impact on antibody disposition at longer times may

limit its broad applicability in studying pharmacokinetic distribution of antibodies. Conversely, AF680 may be a more suitable choice for antibody clearance studies (provided the DoL is low) and tissue distribution studies at longer time periods (e.g. greater than 4 days) despite having greater autofluorescence than 800CW. The higher 680 nm tissue autofluorescence, however, makes AF680 less appropriate for biodistribution studies at low doses and low degrees of labeling.

When labeling an antibody with any fluorophore for *in vivo* delivery, these results highlight the importance of keeping the DoL low to maximize the signal from singly labeled proteins (Figure 3.10). The ease of labeling proteins non-site specifically with NHS-ester/lysine chemistry make this convenient for studying antibody distribution in preclinical models. The large number of surface accessible lysines, however, results in a Poisson distribution. Because any unlabeled antibodies are not fluorescently detected, and antibodies labeled with 2 or more dyes have approximately twice (or more) the fluorescence as a singly labeled antibody, the total signal is skewed towards antibodies with several dyes, which are more likely to have altered distribution. Figure 3.10 shows that although the 1.2 DoL has an average of ~1 dye per antibody, the Poisson distribution results in a surprising 70% of the fluorescence signal coming from antibodies with 2 or more dyes. While the Poisson distribution is well-known, once the unlabeled antibodies and weighting of the fluorescence signal is taken into account it is somewhat striking that an average DoL of 1 is too high for measuring singly labeled antibodies. Over-labeling antibodies with radiolabels, small molecules, or fluorescent dyes has been shown to cause rapid clearance (*24*,*28*,*95*,*96*,*109*); therefore, maximizing the signal from singly labeled antibodies by using a DoL of 0.3 or less is critical for applications requiring negligible impact on clearance.

For both 800CW and AF680, these results indicate a DoL of 0.3 or less has the least impact due to less than 5% of total signal coming from antibodies with 3 or more dyes. Although using a lower DoL results in less overall signal, the negligible background in the NIR, and the exceptional brightness and photostability of these dyes make both practical options for protein distribution studies. Alternatively, site-specific labeling, such as maleimide-cysteine chemistry, may give improved pharmacological behavior (*19*,*23*) and signal, but these techniques typically require modification of the antibody amino acid sequence, which could also alter stability, distribution, and clearance.

Several other groups have examined 800CW as a tool for tracking antibody disposition. Cohen et al. studied the effects of fluorophore labeling on an ^{89}Zr labeled antibody and showed antibodies with 0.5 dyes per antibody did not show significantly different biodistribution than cetuximab or bevacizumab with only the radiolabel (*107*,*111*). As they increased the DoL for 800CW, the biodistribution started to diverge from the lower DoL and radiolabeled-only antibodies. In particular, liver uptake increased and other organ uptake decreased with higher 800CW DoL for both bevacizumab and cetuximab (*107*,*111*). These results suggest a sufficiently high DoL of 800CW causes increased liver uptake, consistent with other reports showing increased hepatic uptake of radiolabels with high DoL's (*108*). However, as Conner et al. mentioned, even at lower DoL the effects of 800CW may be masked by the radiolabel/desferal moiety (*76*). These authors studied differences in plasma clearance and biodistribution against unlabeled and ^{125}I antibodies and found the dye altered the pharmacokinetics. In this study they used 800CW with a DOL of 1.2 - 1.4 and showed high liver uptake and faster plasma clearance than radiolabeled or ELISA measurements. Our results are consistent with these findings, where

labeling with 800CW can increase plasma clearance at times longer than 4 days. Mouse liver has been shown to take up proteins with a high negative charge density (*95*,*126*), therefore it is paramount to keep a low DoL (for both fluorophores and radiolabels) to minimize possible alteration of protein pharmacokinetics. Additionally, disruption of FcRn or FcRγ binding could result in faster clearance or altered antibody distribution. Although the exact mechanism of altered distribution is unclear, our work suggests a 0.3 DoL results in an undetectable difference in antibody pharmacokinetics. Importantly, we examined the pharmacokinetics and biodistribution in healthy animals, while these antibodies will likely be used in animals with tumors, where TMDD may play a role. However, the similar clearance (Figure 3.4, Figure 3.5), biodistribution (Figure 3.12), and microscopic tumor distribution (Figure 3.13, Figure 3.14) (*106*), suggests the labeled antibodies accurately capture the pharmacokinetics of unlabeled antibody.

The published studies on the biodistribution of various antibodies and other proteins with 800CW and encouraging plasma clearance results with AF680 warranted a comparison of the dye effects on measured biodistribution. For both Bev-800CW and Bev-AF680 at a 0.3 DoL the plasma clearance was not significantly different at 48 hours from unlabeled antibodies (measured with ELISA), prompting us to compare the systemic biodistribution. The biodistribution measured with both dyes (Figure 3.12) agreed well for organs where there was sufficient signal intensity relative to autofluorescence variability (liver and kidney); however, the SNR was too low in several other organs to distinguish signal from the higher background for AF680. The Bev-800CW 48 hour biodistribution agreed well with another published biodistribution study using the residualizing ^{64}Cu-labeled bevacizumab at 48 hours, supporting the aforementioned

studies showing similar antibody disposition at low DoL (*123*). These data also qualitatively agree with other published biodistribution data of bevacizumab (*111*,*127*), although in some of these studies the mice were exsanguinated (resulting in less measured organ uptake) or the biodistribution measurements were performed at different times post injection, making direct comparisons difficult. For imaging agents, 800CW provides a superior SNR and contrast to noise ratio (CNR) compared to AF680, making it a more suitable choice for live *in vivo* imaging.

Despite the higher autofluorescence in the 680 nm range, the signal from AF680 is sufficient to detect in targeted tumors for several days at clinical doses (Figure 3.13). Both AF680 and 800CW can be detected in tumors using fresh-frozen tissue sectioning. Here we used thicker (16 μm) slices versus a more typical 5 μm slice thickness to improve signal detection. Both dyes can be excited with a 635 nm and 750 nm laser, respectively (~40% of the maximum absorption for AF680 and 55-60% of the maximum absorption for 800CW) and detected with PMTs. Since both dyes are residualizing, the signal results from the total targeted antibody in comparison to Fc labeling (Figure 3.14), for example (*36*), which only labels intact protein. This can be useful for applications such as studying ADC's, where the degraded antibody correlates with the released payload (e.g. non-cleavable, impermeable small molecules), so NIR detection can be used as a surrogate for small-molecule delivery (*13*).

We examined two dyes in detail for this study based on their current use in clinical trials (800CW) and the low plasma protein binding (and associated low non-specific dye interactions) of AF680 (*114*). There are a variety of other NIR dyes with different physicochemical properties that are commercially available, although not all of them have disclosed structures. For example,

our lab has examined the residualization rates, permeability, and plasma protein binding of several NIR dyes (*113*,*114*). Although some of these fluorophores may have similar properties *in vitro*, their *in vivo* behavior may differ significantly. We have shown that the zwitterionic dye ZW800 has similar plasma protein binding as AF680 (*114*) and beneficial rapid clearance when conjugated to small molecule imaging agents, consistent with literature reports (*87*). Additionally, its fluorescence is in the optimal 800 nm range. However, in contrast to labeling small molecules, after conjugation to an antibody there was a gradual change in the absorbance spectra upon incubation in plasma and a rapid loss of fluorescent signal after injecting *in vivo* (data not shown). In our hands, therefore, this dye is more suitable for rapidly cleared imaging agents than monoclonal antibodies. This result emphasizes that although the structures of other cyanine-based dyes (Cy5.5, SulfoCy7, etc.) may be similar to AF680 and 800CW, they each affect antibody disposition differently (e.g. (*104*,*112*)). Similar to radiolabeling techniques, the modification of any protein, however slight, can affect different proteins in unique ways, particularly if the modified residue (e.g. lysine, cysteine, tyrosine, etc.) is located in an important binding region for that molecule. The slow clearance of antibodies and complex interactions with the immune system and FcRn receptor make them sensitive even to small interactions from fluorophores or surface residues/charges (*128–130*). The conjugation of fluorophores to smaller proteins or agents may not have much of an impact on the distribution if they are rapidly cleared by the kidneys[6], but similar methods of validation for distribution should be employed. This work can be used to help guide the selection of fluorophores depending on the particular application in a manner analogous to the selection of chelators and radioisotopes for radiolabeling techniques.

3.6 Conclusion

In conclusion, to limit the impact of non-site-specific fluorophore labeling on antibody pharmacokinetics, these results show that the DoL should be kept at or below 0.3 dyes/antibody. At this tracer DoL, AF680 showed negligible impact on plasma clearance out to 17 days compared to unlabeled antibody, while 800CW showed similar clearance out to 4 days but faster clearance at later times. Both dyes can be used with tissue distribution studies; however, the greater autofluorescence for AF680 requires higher doses to achieve a sufficient SNR while the signal from 800CW is well above the autofluorescence background in the 800 nm range. For short-term *in vivo* studies (less than 4 days), the reduced autofluorescence, greater SNR and CNR, and increased tissue penetration of light for 800CW makes it suitable for tissue biodistribution studies or live *in vivo* imaging. Although both dyes have distinct advantages and limitations, the efficient optical properties, stability, ease of use, and low autofluorescence for both fluorophores provide broad utility in studying protein pharmacokinetics in the preclinical setting.

3.7 Experimental Methods

Antibodies and Imaging Agents

Trastuzumab (Herceptin, Roche), bevacizumab (Avastin, Roche), and trastuzumab emtansine (T-DM1, Kadcyla, Roche) were obtained from the University of Michigan pharmacy. Alexa Fluor 680 NHS Ester (AF680, ThermoFisher Scientific) and IRDye800CW (800CW, LI-COR) were conjugated to each antibody following the manufacturers' instructions as previously described (*106*,*113*). Briefly, dyes were reacted at an antibody concentration of 2 mg/mL in PBS

with 10% sodium bicarbonate (v/v) for 2 hours at 25°C and then purified using Biogel P-6, Fine (Bio-Rad) in Spin-X centrifuge filter tubes (Corning) (*113*). Dye to antibody molar ratios of 3.0 and 0.5 were used for the 1.2 and 0.3 degrees of labeling, respectively. The degree of labeling was determined by using a NanoDrop 2000c Spectrophotometer (ThermoFisher Scientific) to measure fluorophore absorption and the protein absorbance at 280nm, corrected for the fluorophore. The degree of labeling is defined as the average dye to protein concentration ratio. Sample absorption spectra are shown in Figure 3.3. After purification, conjugates were run on SDS-PAGE and scanned on an Odyssey CLx to ensure all free dye was removed (Figure 3.2). Binding affinities were performed as previously described (*103*) using HCC1954 cells. Briefly, titrations of unlabeled antibody and antibody-dye conjugates were incubated with 50,000 HCC1954 cells on ice for 3 hours and washed. After the primary incubation, cells were further incubated with antihuman IgG Fc-AlexaFluor488 at 40nM for 30min on ice, washed, and subsequently run on an Attune Focusing Cytometer (Applied Biosystems). K_d was estimated using PRISM and is reported as $K_d \pm$ standard error.

Plasma Clearance

All animal studies were approved and conducted in compliance with the Institutional Animal Care and Use Committee (IACUC) of the University of Michigan. Animal studies were conducted in C57BL/6J or Foxn1 nude (Jackson Laboratories) mice. Plasma clearance was measured after tail-vein injection of 500 µg unlabeled stock antibody with 50 µg labeled antibody at the different DoL's described above (N=3 for each DoL). Plasma concentration was determined by fluorescence and ELISA for each sample. Plasma samples were obtained through retroorbital sampling 10 µL of whole blood, mixing with 15 µL PBS-EDTA (10mM),

centrifugation at 3000x*g* for 1 minute, and freezing 18 μL of the resulting plasma. The concentration of fluorescent probe was determined by scanning 15 μL of plasma on the NIR Odyssey CLx Scanner (LI-COR) and comparing the signal intensity to a calibration curve of known concentration to signal intensity at the same scan settings. Plasma concentration as measured by fluorescence and ELISA was normalized to the initial value and then the clearance was fit to a biexponential decay using PRISM (GraphPad). Absolute plasma concentrations at 1 min were compared with theoretical initial concentrations based on the dose and estimated plasma volume of the mouse. The area under the curve (AUC) for normalized clearance for ELISA and fluorescence was determined for each conjugate at 3 and 17 days using the trapezoidal rule. The normalized fluorescence AUC was compared to normalized ELISA AUC by a one tailed, paired Student's t-test, and a significance level of $p < 0.05$ was considered significant.

Total Antibody ELISA

Immulon IV 96 well plates (Fisher Scientific, 14-245-153) were coated with mouse anti-human IgG Fc antibody (BioLegend, 409302) overnight at 4°C and 1 μg/mL in PBS. Wells were then washed 3 times (PBS with 0.05% Tween-20), blocked with 2% PBS-BSA, 0.05% Tween-20 for 2 hour at room temperature, and washed 3 more times. Samples were diluted at least 1:100 in diluent (PBS, 1% BSA, 0.05% Tween-20) and incubated for 1 hour at room temperature. After sample incubation, plates were washed 3 times, and the detection antibody, mouse anti-human IgG Fc HRP (Southern Biotech, 9040-05), was diluted 1:10000 in diluent, added to each well, and incubated for 1 hour at room temperature. Plates were then washed 4 times and developed

using TMB substrate (Fisher Scientific, ENN301). Assay ranges for both trastuzumab and bevacizumab were between 6 ng/mL and 1.2 μg/mL.

Biodistribution

The biodistribution of bevacizumab conjugates was determined as previously described (*53*,*106*,*122*). Briefly, 48 hours after tail-vein injection of 50 μg of bevacizumab-dye conjugate (assumed to be in a linear clearance range due to no target binding and negligible Fc receptor saturation), animals were euthanized and organs were resected. Organs were then homogenized by mechanical disruption, incubated with RIPA buffer (Fisher Scientific, NC9517624)/PBS solution supplemented with 6 mg/mL collagenase IV (Fisher Scientific, NC9919937) for 1.5 hours, disruption using a FB-120 Sonic Dismembrator, and incubated in RIPA buffer/0.025% trypsin-EDTA solution for 1.5 hours. After homogenization, organs were serially diluted and scanned on the Odyssey CLx scanner to ensure fluorescence detection was in the linear range. The signal intensity was compared to a calibration curve and normalized to organ weight and homogenate volume in order to compute the percent injected-dose per gram (%ID/g). Calibration standards were made in mouse plasma and subjected to the same incubations above. The signal to noise ratio (SNR) was also calculated for each organ. The SNR is defined as the organ fluorescence minus the autofluorescence signal from control (uninjected) mice divided by the standard deviation of autofluorescence from the control mice. The %ID/g for each organ for Bev-AF680 and Bev-800CW was compared by a two-tailed, paired Student's t-test. Each organ for Bev-AF680 and Bev-800CW were compared to Paudyal et al. (*123*) by a two-tailed, unpaired Student's t- test. A significance level of $p < 0.05$ was considered significant.

Fluorescence Histology of Antibody Distribution

As previously described (*81*,*106*), the tumor distribution of T-DM1-AF680 was analyzed using fluorescence microscopy at 1, 3, 5, and 7 days. Briefly, nude mice were inoculated with $5x10^6$ NCI-N87 cells in the rear flanks and the clinical dose (3.6 mg/kg) of T-DM1-AF680 was administered via tail-vein injection once the longest axis of the tumor was approximately 10-12mm. Before euthanizing mice at the aforementioned times, Hoechst 33342 (ThermoFisher Scientific, H3570) was administered via tail-vein at 15 mg/kg to label functional vasculature in the tumor[31]. After euthanizing the mice, tumors were resected, flash frozen in OCT using isopentane chilled on dry ice and cut for histology on a cryostat (16 μm slices). Before imaging, slices were stained with anti-mouse CD31 (BioLegend, 102402) conjugated with Alexa Fluor 555, and mouse anti-human IgG Fc antibody (BioLegend, 409302) conjugated with Alexa Fluor 488. Microscopy was performed using an upright Olympus FV1200 confocal microscope equipped with a 20x objective and 405, 488, 543, and 635 lasers. Tumor images were obtained by stitching smaller images with the Olympus software. Images were exported and analyzed using ImageJ image analysis software as described previously (*81*,*106*).

Chapter 4

Absolute Quantification of Protein Metabolism with Single Cell Resolution In Vivo Using Near-Infrared Ratio Imaging

4.1 Abstract

Current tools for studying the pharmacokinetics of biologics, such as radiolabeling or mass spectrometry, lack single-cell resolution to quantify specific cell binding, heterogeneous tissue distribution, and cellular metabolism *in vivo*. This protocol describes a robust dual-labeling technique using two near-infrared dyes with widely differing residualization rates to efficiently measure therapeutic protein distribution and metabolism *in vivo* at the single cell level. Example applications are shown for four biologics with varying rates of cellular metabolism. Organ level biodistribution, tissue level confocal microscopy, and cellular level flow cytometry were used to image the multi-scale distribution of these agents in tumor xenograft mouse models. The technique reveals highly heterogeneous delivery of these proteins to tumors. The single-cell metabolism results show the delay between peak tumor uptake and maximum protein metabolism. This method should have broad applicability in tracking the tissue and cellular distribution of novel protein therapeutics for drug development.

4.2 Background

Therapeutic proteins remain one of the fastest growing areas of pharmaceutical development in the treatment of many diseases, including cancer and autoimmune disorders

(*1*,*131*). The widely varying physicochemical properties of these novel proteins, including molecular weight, molecular radius, avidity, charge, etc., can result in unexpected pharmacokinetics, making it difficult to predict their distribution (*52*). Although these agents act at the molecular scale, it is necessary to quantify both the microscopic (sub-cellular and cellular) and macroscopic (tissue and organ) distribution in order to bridge the understanding between pharmacokinetics (PK) and pharmacodynamics (PD) and design effective therapeutics (*132*). For example, in the case of antibody-drug conjugates (ADCs), there is a need to understand the metabolism and payload release at the subcellular scale, the average number and variability of payload molecules required to achieve cell death *in vivo* at the cellular scale (*46*), the number of cells in the tumor receiving a therapeutic dose at the tissue scale, and the healthy tissue exposure and resulting toxicity at the whole organ level (*133*).

The approach outlined in this chapter is based on the different residualization properties of two NIR fluorescent dyes, which are used to distinguish intact versus degraded protein (*63*,*85*,*113*). The residualization properties of different imaging agents including radiolabels and other visible light fluorophores have been known for many years (*80*,*85*). For example, ^{125}I is a non-residualizing label and ^{111}In, ^{68}Ga, ^{98}Zr are residualizing agents (*134*). In an elegant approach, Ferl et al. dually labeled different engineered protein variants with residualizing ^{111}In and non-residualizing ^{125}I radioisotopes to measure *in vivo* metabolism (*60*). Motivated by this approach, the residualization properties of NIR fluorophores were measured (*113*), and both residualizing and non-residualizing dyes were identified. Using a dual non-residualizing and residualizing label, the local intact and metabolized protein can be detected (*63*). With radiolabels, the non-residualizing ^{125}I approximates the intact protein, while the ^{111}In

approximates the cumulative uptake (*59*). To model the degradation within each organ, a known quantity of each isotope was injected and the relative amount of ^{125}I to ^{111}In was measured over time. The current approach is similar in concept but uses NIR fluorescence to increase the resolution. This allows measurement of the distribution across multiple length scales using the higher spatial resolution of fluorescence and ability to quantify kinetic rates such as extravasation (at the tissue level) and internalization (at the cellular level). NIR wavelengths have low tissue autofluorescence and can theoretically penetrate to a depth of 1-2 cm for live *in vivo* imaging (*99*,*135*). NIR fluorescence combines the whole animal and biodistribution capabilities of radiolabels (*53*,*107*) with the tissue and cellular kinetic measurements of fluorescence (*54*). The method also takes advantage of the sensitivity of NIR imaging (higher than current mass spectrometry imaging and visible light fluorescence) and metabolic tracking of degradation products while reducing safety concerns, time/half-life constraints, and expense of radioactivity. It allows for the investigation of both distribution and metabolism of therapeutic proteins at the subcellular and cellular scale *in vitro*, and, importantly, at multiple scales *in vivo* in the *same* animal, providing insight into heterogeneity and inter-animal variability.

We apply the dual label technique to four well-characterized proteins, EGF, cetuximab, T-DM1, and anti-A33 antibody, both *in vitro* and *in vivo* to demonstrate the wide applicability of the technique for the measurement of cellular metabolism and tissue distribution of other novel protein therapeutics. The ability to track the delivery of therapeutic proteins from whole animal to subcellular resolution enables investigation of the multi-scale distribution of lead compounds *in vitro* and *in vivo* and facilitates the development of predictive models for lead compound selection.

4.3 Results

Two NIR fluorescent dyes were chosen that have widely differing residualization rates (*113*) and do not overlap spectrally. Figure 4.1 shows a graphic depiction of the technique. As the labeled protein binds to the surface, gets internalized, and subsequently degraded, low molecular weight degradation products labeled with DDAO and IRDye are released (red and green stars in Figure 4.1, respectively). The low molecular weight, lipophilicity, and moderate pKa allow DDAO to passively diffuse out of the cell upon protein degradation, while the larger, highly charged, hydrophilic IRDye remains trapped in lysosomes (*113*). DDAO therefore approximates the intact protein, since it is cleared upon degradation, while IRDye approximates the cumulative uptake in the cell, since it is 'trapped' within the cell (*63*). This method was chosen over alternative mechanisms, such as pH effects (*136*) or quenching/FRET, because it is irreversible (unlike pH effects) and does not require a high degree of labeling or larger dye-quencher conjugate. The plasma clearance of the dually labeled antibody was measured as described in Chapter 3 and it showed similar clearance to antibody only labeled with IRDye (Figure 4.1). This indicates that the addition of the DDAO does not impact clearance of the antibody. Figure 4.2 shows a sample absorbance spectrum for the dually labeled antibody.

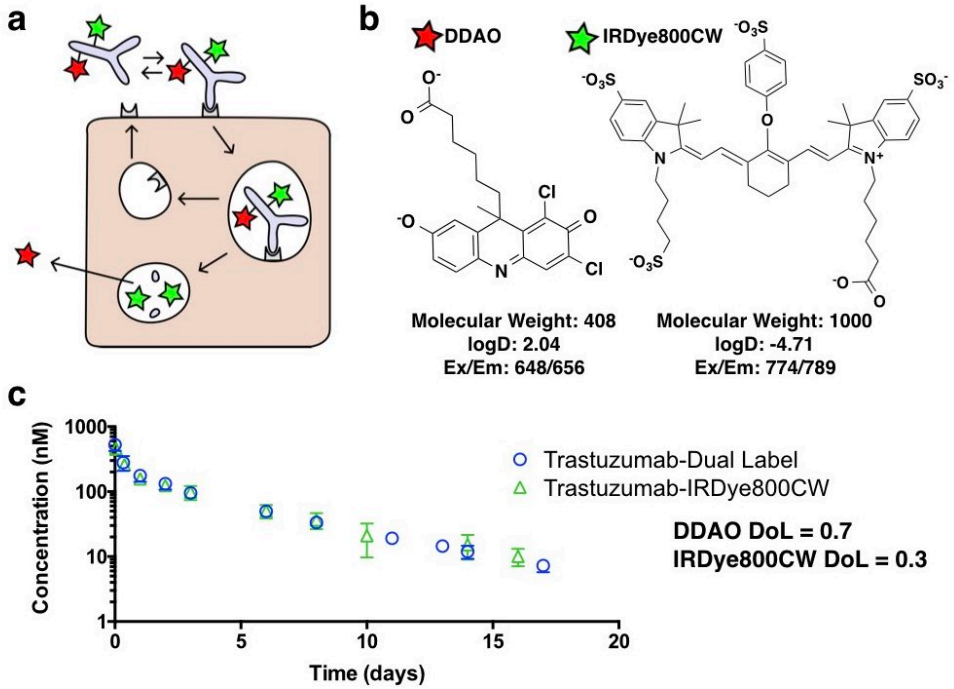

Figure 4.1 Dual label NIR fluorescence imaging technique concept.
(a) Graphic depiction of dually labeled antibody binding the cell, internalizing, and degrading. The non-residualizing DDAO (red star) leaks out of the cell, while the residualizing IRDye (green star) is trapped. (b) DDAO and IRDye dye chemical structures, molecular weights, maximum excitation/emission, and logD (pH 7.4) calculated by MarvinSketch. (c) The plasma concentration over time of IRDye or dually labeled (IRDye and DDAO) trastuzumab is cleared at the same rate (which is equal to unlabeled trastuzumab over 3-4 days) (*137*). DoL, degree of labeling.

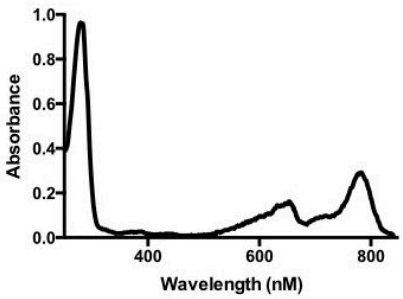

	Wavelength	Absorbance	CF	ε	Conc. (μM)	DoL
Antibody	280	0.963	-	225,000 cm^{-1} M^{-1}	41.0	-
DDAO	650	0.158	0.2 (280 nm)	42,000 cm^{-1} M^{-1}	30.7	0.74
IRDye	778	0.29	0.03 (280 nm) 0.1 (650 nm)	240,000 cm^{-1} M^{-1}	12.1	0.29

Figure 4.2 Example absorbance spectra of dually labeled T-DM1.
CF, correction factor at specified wavelength; ε, molar extinction coefficient; DoL, degree of labeling.

Three model compounds were selected for *in vitro* and *in vivo* validation based on their rate of internalization (Figure 4.3). EGF is internalized and degraded quickly with a 17 min half-life (*138*), cetuximab is slower at an approximately 2 hour half-life (*138*), and the tight-junction associated A33 target and antibody is the slowest with a 56 hour half-life (*139*) representing a wide range of internalization rates for validation. A431 cells were used for EGF and cetuximab, and LS-174T cell lines were used with A33 due to high expression of their respective targets (*140*,*141*). Plasma clearance for each agent over 24 hours was fit using a biexponential decay in PRISM and the values are reported in Figure 4.4.

To test the system *in vitro*, cetuximab and A33 were dually labeled with DDAO and IRDye800CW, while a 1:1 ratio of EGF-DDAO to EGF-IRDye was used. The clinical ADC Kadcyla (T-DM1) that targets HER2 was also tested *in vitro* on NCI-N87 cells. Figure 4.3 shows the representative flow cytometry plots and the final flow cytometry results for the normalized ratio of signal of DDAO to IRDye for each probe over 48 hours. To measure the normalized ratio, the cells were analyzed on flow cytometry and the median fluorescent intensity for each channel (DDAO and IRDye) was measured at different times. Then each channel was normalized to the initial time point, and the DDAO to IRDye ratio was calculated. This value yields the approximate ratio of intact protein to cumulative uptake. As protein is degraded, the DDAO/IRDye ratio decreases as the intact signal approaches zero. EGF showed a rapid drop in the ratio while A33 maintained strong signal over several days, validating the approach *in vitro*. Cetuximab and T-DM1 decreased at a moderate rate as expected *in vitro* (*124*,*138*). Imaging the

cell lysate with fluorescence SDS-PAGE shows the formation of low molecular weight IRDye products, while the non-residualizing DDAO does not (Figure 4.6).

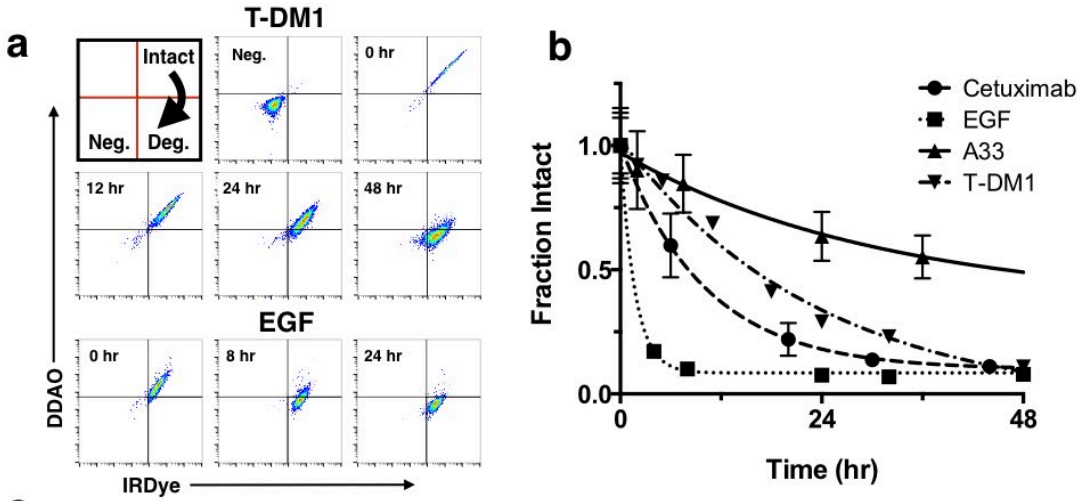

c

Agent	MW (kDa)	Cell Line	Receptors/ Cell	Internalization Half-life
EGF	6.4	A431	4×10^6	17 min
cetuximab	152	A431	4×10^6	1.7 hr
T-DM1	149	NCI-N87	1×10^6	5.8 hr
anti-A33	150	LS174T	5×10^5	56 hr

Figure 4.3 *In vitro* flow cellular metabolism.
(a) Representative flow cytometry plots of dually labeled T-DM1 and EGF gated on cells. Intact protein appears in the DDAO(+)/IRDye(+) quadrant. Over time as the biologic is degraded, there is a gradual shift towards DDAO(-)/IRDye(+). (b) Fraction of intact protein for four agents over time. EGF shows rapid internalization and degradation, while A33 maintains signal over several days. Cetuximab and T-DM1 decrease at a moderate rate as expected. (c) Model system for validation of dual channel technique. For each model protein the molecular weight and plasma clearance is listed. The associated cell line used for xenografts, receptor density, and internalization half-life are also listed.

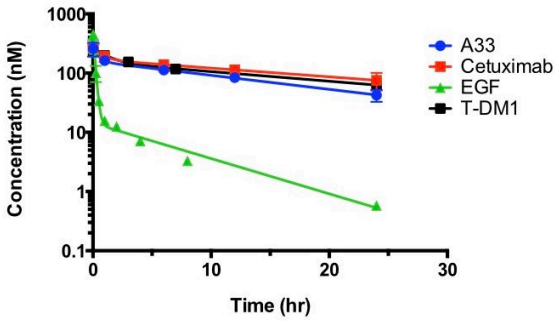

Probe	alpha (hr^{-1})	beta (hr^{-1})	fraction alpha (%)
EGF	6.141	0.14	96.8
cetuximab	1.29	0.03	36.7
A33 MAb	2.08	0.05	39.8
Kadcyla	0.76	0.04	43.1

Figure 4.4 Plasma clearance for each agent over 24 hours.
Biexponential fits were performed using PRISM and the fitted alpha, beta, and fraction alpha parameters are listed.

To visualize the change in ratio, cells were imaged using a confocal microscope at similar time points. Figure 4.5 shows separate DDAO (red) and IRDye (green) channels for each agent. All four agents showed similar behavior but on different time scales. IRDye800CW initially labels the surface receptors but is internalized, degraded, and trapped in punctate endosomes and lysosomes. DDAO predominately labels the surface. As it is degraded, the dye leaks out of the cells as seen by a drop in signal. Although the DDAO does lose some fluorescence due to pH effects (pKa = 5)(23), lysed cells show very low levels of DDAO indicating that loss of signal dominates over pH effects (*113*).

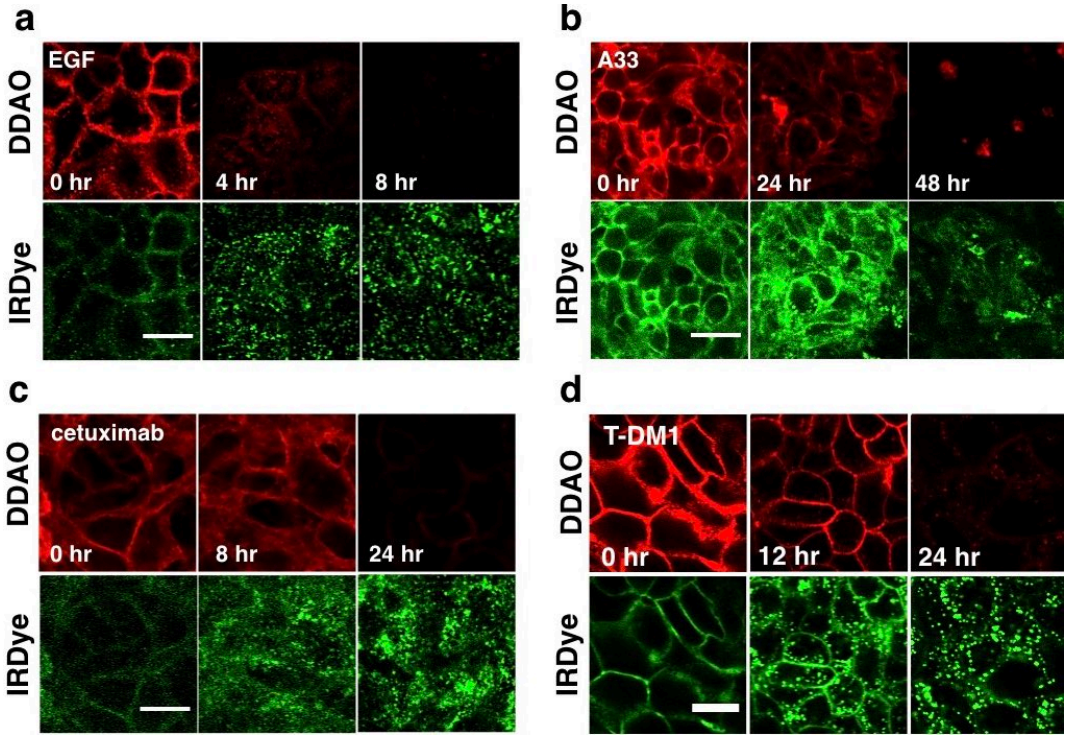

Figure 4.5 *In vitro* confocal microscopy of dually labeled proteins.
(a), A33 (b), cetuximab (c), and T-DM1 (d). For each agent DDAO (red) shows cellular labeling and loss of signal over time, while IRDye (green) also shows cellular labeling initially and then the formation of punctate spots as it is trapped in endosomes and lysosomes. The degradation kinetics of each agent is consistent with flow cytometry. Scale bar = 10 μm.

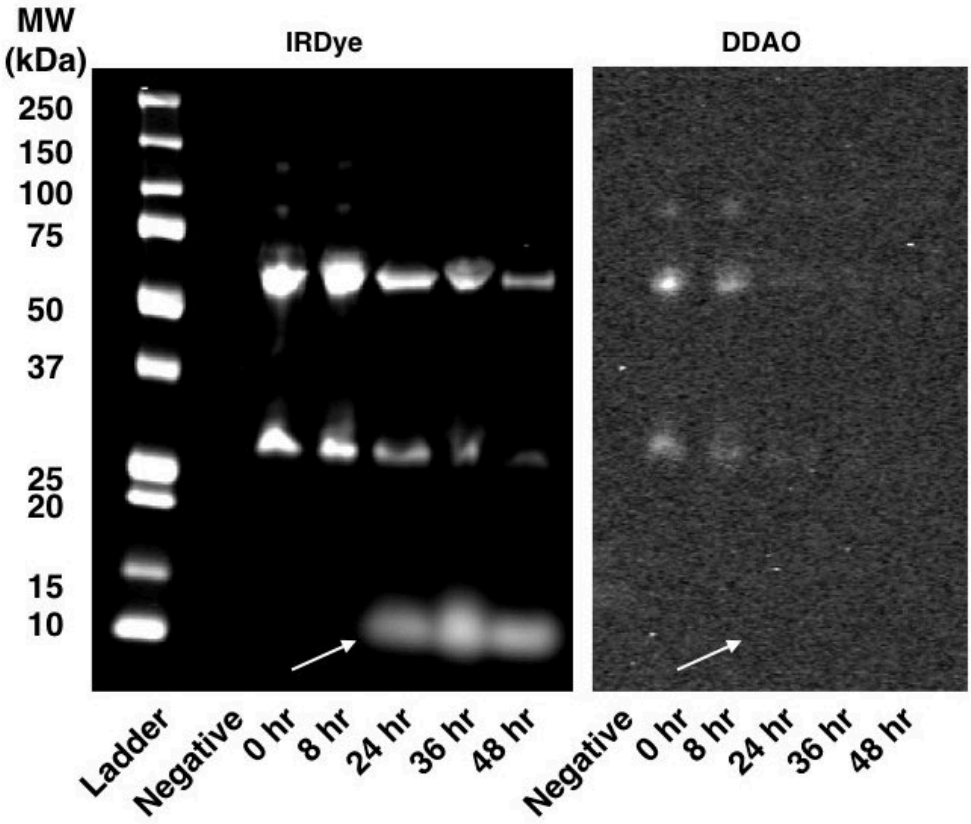

Figure 4.6 NIR Fluorescence SDS-PAGE of dual labeled T-DM1.
Similar to Figure 4.3 and Figure 4.5, NCI-N87 cells were pulsed for 30 minutes with dual labeled T-DM1 at the corresponding time points. Cell lysate was run on a reducing SDS-PAGE gel and scanned using the NIR Odyssey CLx Scanner. At later times the residualizing IRDye shows formation of lysine-dye adducts (left arrow), while the non-residualizing DDAO does not (right arrow).

The promising *in vitro* results needed to be verified *in vivo*, since many imaging techniques behave well in cell culture but do not provide robust results in the heterogeneous *in vivo* environment. In particular, the DDAO fluorophore has lower brightness relative to many cyanine-based dyes, so the detection above autofluorescence in tissue needed to be verified. Figure 4.7 shows stitched whole organ histology images of an A431 tumor and kidney for cetuximab and EGF doses, respectively. Figure 4.7 shows fresh frozen section following a subsaturating (~4 mg/kg) dose of cetuximab 24 hours post injection. Further *ex vivo* staining of the vasculature using CD31-AF555 is shown in cyan. The subsaturating dose results in a

characteristic perivascular staining (shown in the high resolution inset) where the antibody signal is concentrated around blood vessels but does not diffuse homogeneously throughout the tumor (*41*,*43*,*54*). CD31 staining shows the degree of vascularization of the tumor and can be used to quantify the penetration distance (*41*). Figure 4.7 also shows stitched whole kidney images for EGF 24 hours post injection. EGF is below the molecular weight cut off for renal filtration; it is filtered by the glomerulus, degraded in the proximal tubule, and the peptide/amino acids are taken up by cells in the renal cortex (*142*,*143*). High-resolution images shown in the inset give further detail at the cellular scale, where the NIR dyes are seen in individual tubules.

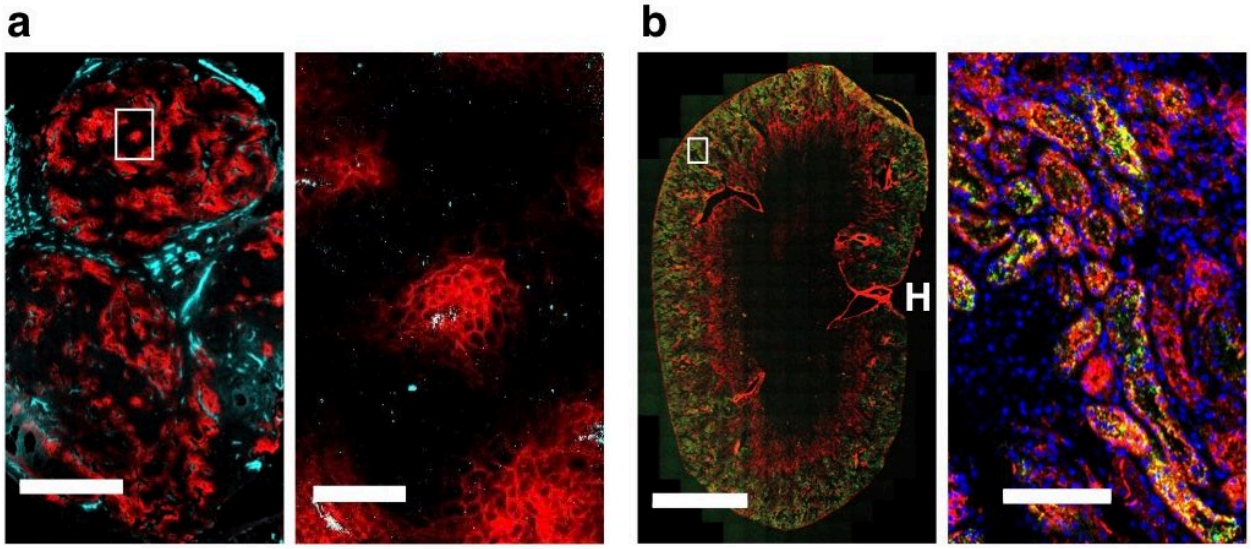

Figure 4.7 Whole organ immunofluorescence histology.
(a) High resolution images of A431 xenograft frozen sections 24 hours post injection of 100 µg (~4 mg/kg) of dual labeled cetuximab (DDAO, *red*). Sections were stained with anti-CD31-AF488 (*cyan*) *ex vivo*. Left scale bar is 1 mm and right is 100 µm. (b) High resolution images of kidney frozen sections 24 hours post injection of EGF-DDAO (*red*) and EGF-IRDye (*green*). Sections were stained with Hoechst 33342 (*blue*) *ex vivo*. Left scale bar is 2 mm and right is 100 µm.

Applying the dual NIR labeling technique to EGF, T-DM1, and cetuximab *in vivo* yielded insight into the single-cell and tissue distribution of these proteins *in vivo* (Figure 4.8).

For example, the clinical dose of T-DM1 (3.6 mg/kg) does not fully penetrate the tumor tissue (*46*,*106*,*137*) and only targets approximately 10% of cells by flow cytometry (Figure 4.8). This penetration depth did not change after 7 days (*137*) indicating that the therapeutic drug likely never reaches all the tumor cells. However, T-DM1 is clinically approved and effective in breast cancer, indicating that despite this heterogeneity, it still shows a clinical response. Examining the DDAO/IRDye ratio *in vivo* through flow cytometry shows how the systemic delivery of the protein plays an important role in the intact versus aggregate degraded probe. EGF, which is cleared rapidly from the blood (Figure 4.4) and internalized rapidly *in vitro*, shows little intact protein at 24 hours post-injection (Figure 4.8). However, the slowly clearing antibodies cetuximab and T-DM1 show mostly intact protein (a ratio of ~1) at 24 hours post-injection from having a constant intact supply from the blood and an initial time to accumulate in the tumor, even though *in vitro* the fraction intact decreased significantly after 24 hours (Figure 4.3). Only at 3 days, once the plasma concentration is lower and after maximum tumor uptake, is the majority of the ADC degraded and the payload released (Figure 4.8). Understanding degradation kinetics is crucial for many ADCs since they only release their toxic payload after degradation, and cell trafficking is a potential mechanism of resistance (*144*). In addition to organ biodistributions, the lower autofluorescence in the NIR region of light allows for direct whole animal imaging to see protein localization. In Figure 4.9, the three antibodies showed primarily tumor localization while the smaller EGF showed some tumor targeting with high kidney uptake.

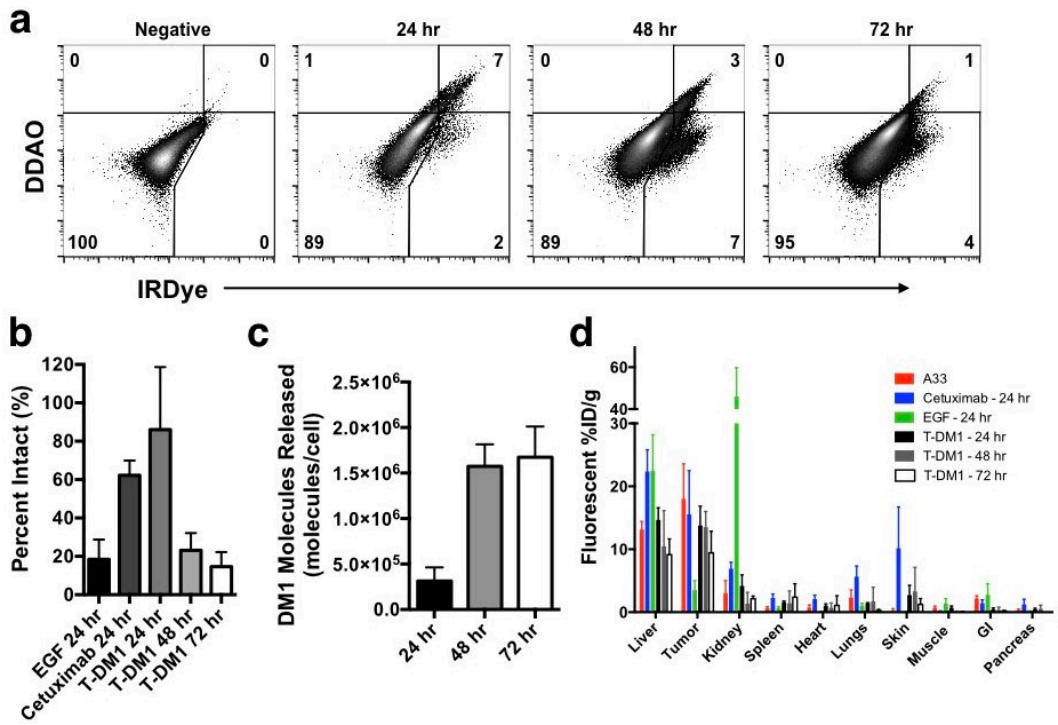

Figure 4.8 *In vivo* cellular metabolism and distribution.
(a) Representative flow cytometry plots of single cell suspension from NCI-N87 tumors at 24, 48, and 72 hours post-injection of 3.6 mg/kg of dually labeled T-DM1. Intact dually labeled T-DM1 appears in DDAO(+)/IRDye(+) quadrant. Over time as ADC is degraded there is a gradual shift towards DDAO(-)/IRDye(+). (b) T-DM1, EGF, and cetuximab degradation in tumor cells. At 24 hours EGF (a rapidly clearing protein), is mostly degraded in the tumor. However, the slowly clearing cetuximab and T-DM1 show mostly intact protein. Over 48-72 hours, after maximum uptake is reached, T-DM1 is increasingly degraded. Data plotted as mean ± standard deviation. (c) Molecules of DM1 payload released per target cell *in vivo* for the targeted cells calculated using the total cell uptake and fraction intact. Data plotted as mean ± standard deviation. (d) Fluorescence biodistribution of EGF, cetuximab, and A33 at 24 hours and T-DM1 at 24, 48, and 72 hours. Some data is duplicated in Figure 6.16 for ease of viewing.

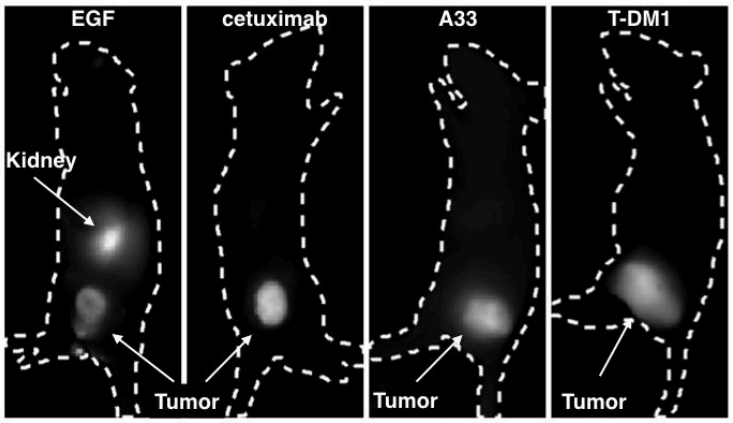

Figure 4.9 Whole animal imaging 24 hours post injection for each agent using the PerkinElmer In Vivo Imaging System (IVIS).
The low autofluorescence in the near-infrared and residualizing properties of IRDye make it suitable for whole animal imaging. In agreement with the organ biodistribution from Figure 4.8, the three antibodies show high tumor uptake, while the EGF shows high renal uptake and limited tumor uptake.

4.4 Discussion

In this study, a novel dual channel near-infrared fluorescence ratio technique to quantify the metabolism and distribution of therapeutic proteins from subcellular to whole animal scales is presented and validated for several biologics. We apply this technique to three well-characterized proteins, EGF, cetuximab, and A33, as a proof-of-concept (Figure 4.3) and then show how this technique can give important pharmacokinetic data for a clinically relevant ADC, T-DM1. Using NIR fluorescence provides much higher spatial resolution than conventional techniques, such as nuclear imaging, particularly in the preclinical setting. NIR fluorescence also provides a safe and facile method for tracking biologics that is more widely available and less expensive than radiolabeling. It can provide multiplexed information from the subcellular (Figure 4.5) to tissue and whole organ (Figure 4.7) distribution. In comparison to previous visible light approaches (*85*), using the NIR region of light provides less background autofluorescence and better tissue penetration, up to 1-2 cm, allowing for live imaging *in vivo*

and absolute biodistribution (%ID/g, Figure 4.8). Importantly, this technique provides distribution information across multiple length scales down to the single cell level using flow cytometry to measure millions of cells and subcellular distribution using confocal microscopy; both techniques can easily be integrated with visible light fluorescence approaches to examine pharmacodynamics, the impact of the tumor microenvironment, and single cell variability.

For proof of concept we chose three well-characterized proteins, EGF, cetuximab, and A33, with varying internalization rates to show how this technique can be used to gather both metabolism and distribution data at several length scales. *In vitro* metabolism studies compared the DDAO to IRDye normalized ratio over time using flow cytometry and confocal microscopy. These results were as expected where the rate of decrease in the DDAO/IRDye ratio was proportional to internalization time (Figure 4.3).

Examining the DDAO/IRDye ratio *in vivo* through flow cytometry (Figure 4.8) shows how the systemic delivery of the protein plays an important role in the intact versus aggregate degraded probe. EGF, which is cleared rapidly from the blood (Figure 4.4) and internalized rapidly *in vitro*, shows little intact protein at 24 hours post-injection. However, the slowly clearing antibodies cetuximab and T-DM1 show mostly intact protein (a ratio of ~1) at 24 hours post-injection from having a constant intact supply from the blood, even though *in vitro* the ratio decreased significantly after 24 hours. Only after 3 days, once the tumor has reached post-maximal uptake and plasma concentrations are lower, does it appear that most of the antibody has been degraded. Understanding this kinetics is crucial for many ADCs since they only release

their toxic payload after degradation, and cell trafficking is a potential mechanism of resistance (*144*).

Another major advantage of this technique over conventional nuclear imaging is the ability to easily quantify cellular uptake for millions of cells *in vivo* with flow cytometry. Although techniques with radiolabeled probes are approaching the single cell level (*98*), the resolution is intrinsically limited by the path length of the positron and/or imaging equipment. Because the fluorescent residualizing dye gets trapped in the lysosomes, it approximates the cumulative uptake in each cell. For ADCs this provides the aggregate number of small-molecule drugs internalized per cell, and the method can be used to quantify the single cell variability in the number of antibody molecules required to achieve a therapeutic outcome *in vivo* in preclinical models. Also, with therapeutic proteins and antibodies, the *in vivo* rate of internalization is a critical design characteristic (*145*). Although this method does not directly measure the internalization rate, it measures the rate at which the protein is degraded *in vitro* and *in vivo*. This is a more relevant rate for many drugs because it determines either how long the active intact protein can achieve its therapeutic effect on the cell surface and in endosomes (*146*), or, in the case of ADCs, how long until the small molecule is released.

This technique also allows for a multi-scale understanding of distribution in the *same* mouse. Antibodies are known to distribute heterogeneously throughout the tumor (*147*). Combined with tumor microenvironment heterogeneity (e.g. differences in vascularization, macrophage infiltration, and necrosis) and animal-to-animal variability, this makes comparisons between animals especially difficult. In tumors that have differing vascular density, the overall

delivery of the antibody will change and could significantly influence the clinical outcome. Using this technique, *in vivo* metabolism at the cellular scale and distribution at the cellular, tissue, organ, and whole animal scales is done in the same animal, allowing for a more direct analysis of impact at the site of action with macroscopic response. Immunofluorescence staining shows how the specific tissue microenvironment for each animal affects delivery. The combination of flow cytometry data for single cell metabolism and uptake with the tissue distribution better informs how novel protein therapeutics acting at the microscopic scale affect the tissue distribution (normalization or vascular collapse) and ultimate response.

We chose to study the distribution and metabolism of T-DM1 given the dose limitations from small molecule toxicity, which could result in heterogeneous distribution, and the importance of protein metabolism to release the small molecule payload. Applying this dual NIR labeling technique to T-DM1 yielded several important results. First, the clinical dose of T-DM1 (3.6mg/kg) does not fully penetrate the tumor tissue and only reaches several cell layers. This penetration depth did not change after 3 or more days (*137*) indicating that the therapeutic drug likely never reaches all the tumor cells. However, T-DM1 is clinically approved and effective in breast cancer, indicating that despite this heterogeneity, it still shows a clinical response. Although the mechanism of cell death from the small molecule DM1 is well understood (*148*), understanding how T-DM1 is therapeutically effective in the tumor is more complicated. It could act by killing cells layer after layer with each successive treatment until it reaches farther into the tumor. Alternatively, killing the cells immediately surrounding a blood vessel could cause collapse of the vessel resulting in poor delivery of oxygen and indirect cell death. Also, trastuzumab has been shown to exhibit vasculature normalization properties, meaning that

consecutive therapy with T-DM1 may increase the overall delivery to the tumor (*149*) if the increase in vessel density outweighs a reduction in macromolecular permeability. However, others have reported that vascular normalization decreases uptake of trastuzumab (*150*). Understanding the complex interplay of pharmacokinetics and pharmacodynamics (PK/PD) of both the antibody and small molecule requires understanding distribution from subcellular to the entire tumor and facile integration with pharmacodynamic measurements across these same size ranges (tumor growth curves, tissue level vascular effects, and single cell efficacy). The method presented here provides the tools to make these measurements in a cost-effective manner with unprecedented cellular resolution. As T-DM1 remains the only FDA approved drug for treating solid tumors, understanding the tissue and cellular effects is important for developing new ADCs directed against other targets and cancers (*55*), particularly in light of recent failed clinical trials of ADCs.

While this method has several advantages over alternate technologies (radiolabeling, mass spectrometry, ELISA, conventional fluorescence, etc.), it is important to understand the limitations. First, similar to radiolabeling, it is important to note that the NIR fluorescence measures the distribution of the dye and not the protein itself (*92*). Second, decorating the surface with fluorophores can change the physicochemical properties of the protein, thereby changing the plasma clearance and/or distribution (*76*,*104*). Although significant differences in plasma clearance do not occur at early times (Figure 4.1, Figure 4.4, (*151*)), following the antibodies over days to weeks can result in faster clearance rates. Therefore, this technique is better suited for shorter studies. The same phenomenon can be observed with some negatively charged and/or radiolabeled antibodies (*95*,*126*), and care must be taken to not over-label the

protein. In this study, the degree of labeling was kept very low, around 0.3 for IRDye and 0.7-1 for DDAO to minimize the impact of the dyes and better approximate the true protein distribution (*137*). Assuming a Poisson distribution, an average degree of labeling of 0.2 may be ideal to limit signal to antibodies labeled with 1 dye per protein. In the preclinical development of ADCs this is especially important because the degree of small molecule drug loading can also affect clearance (*152*). Similar to radiolabeled antibodies, basic quality control measures must be performed to ensure the labeling efficiency, lack of free dye, and no loss in binding affinity. Finally, the fluorescence intensity of DDAO was not large enough to measure the bulk organ digest signal accurately. DDAO was selected based on its rapid washout rate from cells following degradation (*113*). However, its optical properties are lower than the cyanine-based dyes. The IRDye800CW signal is much higher than the background at this wavelength, but for DDAO, the higher 650 nm autofluorescence and lower dye brightness results in a similar signal. Specifically, the trends behaved as expected (e.g. the ratio of DDAO to IRDye was very low in the kidney of mice injected with dual labeled EGF), but the error bars were too large for useful measurements (low contrast to noise ratio). Fortunately, the signal is bright enough for both confocal microscopy and flow cytometry measurements, thereby only limiting the type of technique and not the dual label method.

4.5 Conclusions

In conclusion, here we present a facile method for investigating the tissue and cellular distribution of therapeutic proteins using dual label NIR fluorescence imaging. Tracking protein distribution from the subcellular and cellular scales to organ and whole animal level was demonstrated using four different biologics along with measurements of protein metabolism at

the cellular scale both *in vitro* and *in vivo*. Using this technique we can investigate the complex interactions of heterogeneous delivery to the tumor and cellular metabolism of therapeutics, and begin to relate the tissue and cellular distribution to therapeutic efficacy. In particular, we show that the FDA approved drug Kadcyla only reaches a small fraction of tumor cells in mice over several days. Applying this technology to novel biologics in the preclinical setting will allow for quick and effective characterization of the microscale pharmacokinetics using a limited numbers of animals.

4.6 Experimental Methods

A detailed protocol of the dual label technique can be found in Appendix A. The methods outlined in this protocol are listed in brief below.

Imaging agents and Cell lines

Cetuximab (Bristol-Myers Squibb, Princeton, New Jersey), A33 (R&D systems, Minneapolis, Minnesota), and Kadcyla® (T-DM1)(Genentech USA, San Francisco, California) were conjugated with CellTrace™ Far Red DDAO-SE (DDAO)(Life Technologies, Eugene, Oregon) and IRDye® 800CW NHS Ester (IRDye)(LI-COR, Lincoln, Nebraska) according to manufacturer's instructions as previously described (*113*). The final degree of labeling was determined to be between 0.7-1.0 and 0.2-0.4 for DDAO and IRDye, respectively. The DOL for IRDye was chosen to be below 0.5 to minimize any physicochemical effects (size and -3 net charge) of the dye on the antibody (SI). All conjugates were run on SDS-PAGE and scanned on an Odyssey CLx Scanner (LI-COR, Lincoln, Nebraska) to ensure all free dye was removed.

IRDye 800CW EGF Optical Probe (EGF-IRDye) was purchased from LI-COR. EGF-DDAO was synthesized by reacting DDAO-SE with EGF (R&D Systems) at a molar ratio of 6, concentrating/purifying with a 3kDa cutoff Amicon filter, and polishing using reverse phase HPLC. MALDI-TOF was performed on the product to ensure the desired product was at a DOL of 1.0 or below.

A431, LS-174T, NCI-N87 cells were obtained from ATCC (Manassas, Virginia). A431 and LS-174T lines were grown in DMEM containing 10 % (v/v) FBS, 50 U/ml penicillin, 50 μg/ml streptomycin, and 1.5 g/l sodium bicarbonate (A-431 only). NCI-N87 lines were grown in RPMI-1640 containing 10 % (v/v) FBS, 50 U/ml penicillin, and 50 μg/ml streptomycin.

Animal Models

All animal studies were approved and conducted in compliance with the University of Michigan University Committee on Use and Care of Animals (UCUCA). Tumor xenograft studies were done using A-431, LS-174T, and NCI-N87 cell lines. $2x10^6$ cells (A-431 and LS-174T) or $5x10^6$ cells (NCI-N87) were inoculated into the rear flanks of nude mice. Tail vein injections were done when the longest axis of the tumor was approximately 10 mm, approximately 2 (A-431 and LS-174T) or 4 (NCI-N87) weeks after inoculation. Unless otherwise specified, tail-vein injections consisted of 100 μg (~4 mg/kg) for A33, cetuximab, and T-DM1, and 3 nmol EGF-DDAO and 1 nmol EGF-IRDye for EGF. All experimental conditions were repeated in at least three mice.

In Vitro Cellular Clearance and Confocal Imaging

The rates of cellular dye loss were measured over a period of 72 hours similar to previous reports (*113*). Briefly, cells were plated in 96-well plates overnight at 80-90% confluency. Then cells were labeled with cetuximab, EGF, A33, or T-DM1, washed, and incubated at 37°C at different times up to 72 hours. Cells were washed twice daily to remove any dye from solution, and the signal was quantified on a per cell basis using an Attune Acoustic Focusing Cytometer (Life Technologies, Eugene, Oregon).

Confocal Imaging

Slides were imaged with an upright Olympus FV1200 confocal microscope using 405, 542, 635, and 750 nm lasers. In vitro experiments were done using Falcon™ Culture Slides (Fisher Scientific, Pittsburgh, Pennsylvania). Incubation conditions and times are the same as described above for the three probes. After 72 hours, cells were incubated with Hoechst 33342 for 5 min at room temperature, washed twice with 400μL of cell media, and imaged using a 60x objective. Histology slices of tissue were imaged using a 20x objective and high-resolution images of organs were obtained using a series of stitched smaller images and the Olympus software. Immunofluorescence staining was done using MAC3 (BD Biosciences, San Jose, CA) and CD31 (Biolegend, San Diego, CA) conjugated with Alexa Fluor 555 (Life Technologies, Eugene, Oregon). The conjugation and characterization protocol follows the one listed above. All confocal images were exported and analyzed using ImageJ image analysis software.

Biodistribution protocol for %ID/g

Biodistribution was measured using a previously published protocol (*53*,*122*). Briefly, after the animals were euthanized, organs were resected, weighed, and homogenized. Homogenization consisted of incubating with a RIPA buffer/PBS mixture supplemented with 6mg/mL collagenase IV solution, cell disruption using FB-120 Sonic Dismembrator, and further incubation with a RIPA buffer/0.05% trypsin-EDTA solution, as previously described (*122*). After homogenization, each sample was serially diluted in a 96 well plate and scanned using the Odyssey CLx scanner. The percent injected dose per gram (%ID/g) was determined by comparing signal from the Odyssey CLx scanner to a calibration curve and then normalizing by organ weight and homogenate volume. A density of 1 g/mL was assumed for each tissue.

Plasma clearance

Each agent was administered to the tumor xenograft nude mice via tail-vein injection. Blood samples were obtained via retroorbital sampling, mixed with 15 μL of 10mM EDTA in PBS per 10 μL of whole blood, centrifuged (1 min, 3000xg), and scanned in a 384 well plate with the Odyssey CLx. Signal intensity was converted to absolute concentration using calibration curves of known concentrations of each agent in plasma and fit using a biexponential decay in PRISM.

Whole animal imaging

Whole animal images were obtained 24 hours post injection for each agent after sacrificing and before biodistribution using IVIS® Series Pre-Clinical In Vivo Imaging System

(PerkinElmer). Animals were scanned using 750/800nm excitation/emission filters and images were processed using ImageJ image analysis software.

In Vivo Tumor Protein Metabolism

To study the ratio of DDAO to IRDye, tumor xenografts were resected, digested, and analyzed on flow cytometry (similar to the in vitro assay). For EGF, 3 nmol EGF-DDAO and 1 nmol EGF-IRDye was injected vial the tail-vein and animals were sacrificed 24 hours post injection. For cetuximab and T-DM1, 100µg of dually labeled antibody was injected via tail-vein and animals were sacrificed at 24 and 72 (T-DM1 only) hours. After sacrifice, tumors were resected and sliced before being placed in a collagenase IV solution (5mg/mL). The tissue was digested for 25 min before centrifugation (5 min, 300xg). The cell pellet was resuspended in media and filtered through an 80µm filter. The cell suspension was then stained with a non-competitive anti-EGFR-AF488 (EGF and cetuximab) or cetuximab-488 (T-DM1) for 30 min at room temperature, followed by two washes. Cells were then analyzed on flow cytometry and gated by size and AF488 signal to determine intact tumor cells. The ratio of DDAO and IRDye was examined in these cells by taking the ratio of the background subtracted signals and normalizing to the initial ratio. The initial ratio was determined by labeling tumor cells from an un-injected mouse ex vivo and in vitro cells on ice. Flow cytometer settings were kept constant for tumor types and imaging agents.

Chapter 5

Multiscale Modeling of Antibody-Drug Conjugates: Connecting Tissue and Cellular Distribution to Whole Animal Pharmacokinetics and Potential Implications for Efficacy

5.1 Publication Information

Cilliers, C., H. Guo, J. Liao, N. Christodolu, and G. M. Thurber. *Multiscale Modeling of Antibody-Drug Conjugates: Connecting Tissue and Cellular Distribution to Whole Animal Pharmacokinetics and Potential Implications for Efficacy*. The AAPS Journal. 2016; 18(5): 1117-30.

Khera, E., **C. Cilliers**, S. Bhatnagar, and G. M. Thurber. *Computational transport analysis of antibody-drug conjugate bystander effects and payload tumoral distribution: implications for therapy*. Mol Syst Des Eng. 2018; 3(1): 73-88.

Modifications have been made to the published documents to adapt the content to this text. Previous chapters demonstrate experimental techniques to quantify the distribution of antibodies in tumors. This chapter complements the experimental approaches by providing a modeling framework to simulate the multiscale distribution of antibodies and antibody-drug conjugates from the cellular scale in the tumor to the whole animal.

5.2 Abstract

Antibody drug conjugates exhibit complex pharmacokinetics due to their combination of macromolecular and small molecule properties. These issues range from systemic concerns, such as deconjugation of the small molecule drug during the long antibody circulation time or rapid clearance from non-specific interactions, to local tumor tissue heterogeneity, cell bystander

effects, and endosomal escape. Mathematical models can be used to study the impact of these processes on overall distribution in an efficient manner, and several types of models have been used to analyze varying aspects of antibody distribution including physiologically based pharmacokinetic (PBPK) models and tissue-level simulations. However, these processes are quantitative in nature and cannot be handled qualitatively in isolation. For example, free antibody from deconjugation of the small molecule will impact the distribution of conjugated antibodies within the tumor. To incorporate these effects into a unified framework, we have coupled the systemic and organ-level distribution of a PBPK model with the tissue-level detail of a distributed parameter tumor model. We used this mathematical model to analyze new experimental results on the distribution of the clinical antibody drug conjugate Kadcyla in HER2 positive mouse xenografts. This model is able to capture the impact of the drug antibody ratio (DAR) on tumor penetration, the net result of drug deconjugation, and the effect of using unconjugated antibody to drive ADC penetration deeper into the tumor tissue. This modeling approach will provide quantitative and mechanistic support to experimental studies trying to parse the impact of multiple mechanisms of action for these complex drugs.

5.3 Background

Antibody-drug conjugates (ADCs) provide a powerful method to selectively deliver toxic small molecules to cancer cells while reducing non-specific uptake in healthy tissue. Significant effort has gone into designing the multiple aspects of these complex prodrugs, including the target selection, antibody structure and conjugation site, small molecule drug, linker design, and ratio of small molecule to antibody (drug antibody ratio, DAR) (*9*,*13*,*20*,*23*,*153*). Currently there are two FDA approved ADCs, with Kadcyla (ado-trastuzumab emtansine, T-DM1) being the

only ADC approved for solid tumors, and there are over 30 ADCs in various stages of the clinical pipeline (*17*,*154*). Although the mechanism of individual cell death by the cytotoxic small molecule is well documented, the multiple and complex steps in delivery involving both tumor uptake of the macromolecule, local metabolism, and distribution of the small molecule effector make it challenging to design an optimal drug. Mathematical simulations provide an efficient method for exploring the vast parameter space and selecting agents with an increased likelihood of success, reducing the thousands of possible combinations of these complex drugs to a few testable approaches.

Physiologically based pharmacokinetic (PBPK) models have become ubiquitous in translational research for evaluating the behavior of lead compounds in dosing regimens and providing valuable information into reaction kinetics and transport phenomena *in vivo*. PBPK models have been used extensively to data fit dosing curves for more accurate interspecies dose scaling (*155–161*) and in predictive methods for first in animal studies (*42*,*162–165*). Because these models are arranged anatomically they often provide better dosing estimations than simple one- or two-compartment models or allometric scaling. Also, these models provide a framework to estimate unknown parameters or rates that might be difficult to measure accurately *in vivo*. However, there is strong motivation within this framework to develop more predictive models (versus data fitting) so that the pharmacokinetic behavior of lead compounds can be simulated and used to streamline preclinical and clinical studies.

Current PBPK models for antibodies vary in how the organ compartments are structured. For example, a model by Baxter uses two-pore formalism to estimate the extravasation of the

antibody into the surrounding tissues (*156*). Models by Ferl and Davda also used two-pore formalism but added FcRn recycling into select organ compartments to capture this important antibody metabolism pathway (*157*,*166*). Another model from Garg et al. incorporated FcRn recycling into all tissues and used one-pore formalism to model antibody extravasation (*158*). Recently, Shah et al. developed a platform PBPK model that incorporates up to 18 compartments, each with detailed mechanistic behavior that subdivides each organ into plasma, blood cell, endothelial, interstitial, and cellular sub-compartments and uses FcRn interactions (*161*). While all these models share a similar framework, there is not a general consensus on the optimal way to describe the organ compartments (*167*). This likely results from the trade-offs of more detailed models being able to capture more complex behavior at the cost of additional parameters that could result in an underspecified system or one where it is difficult to independently measure values for predictions.

Although organ-level PBPK models can simulate systemic and individual organ concentrations over time, they lack detailed tissue level distribution and do not provide a framework for predicting the heterogeneous tumor distribution associated with antibodies. The most common method for capturing these tissue scale dynamics is through a Krogh cylinder or tumor cord geometry (*168–172*). Using this geometry along with mixed boundary conditions to capture permeability limitations, explicit blood flow and axial gradients to measure blood flow limitations, and diffusion with non-linear binding kinetics to quantify diffusion limitations, tissue level models are useful for determining the uptake and distribution of a diverse range of drugs, including small molecules, therapeutic proteins, and antibodies (*43*,*90*,*173–175*). For antibodies, the tumor cord geometry has been validated by multiple groups and has been used to estimate

whole organ distribution and uptake (*81*,*90*,*176–179*). The lack of functional lymphatics in tumors (*180*) also lends itself to this geometry focused on transcapillary exchange and distribution. However, the Krogh geometry requires the systemic (plasma) concentration as an input, therefore limiting its ability for purely predictive studies. Combining the Krogh cylinder to describe the tumor compartment with a general PBPK model for systemic distribution would give an accurate, multi-scale depiction of antibody distribution. Additionally, since self-consistent therapeutic parameters are available for a wide range of molecules including antibodies and small molecule drugs (*42*,*81*,*181*), the Krogh cylinder simulations are able to simultaneously capture multiple different species within the tumor.

Here we present a multi-scale model integrating two previously published and validated models: a PBPK model for organ and whole body distribution and a tumor tissue Krogh cylinder to simulate the distribution of the clinically used ADC T-DM1. This model combines the strength of PBPK models by simulating the systemic distribution while accurately capturing the heterogeneous antibody distribution in the tumor. To highlight the importance of systemic and tumor concentrations, we use two clinically relevant therapeutics: the monoclonal antibody Herceptin (trastuzumab) and the ADC T-DM1. Through simulation and experiment we show that at the clinical dose of T-DM1 (3.6 mg/kg) the tumor distribution is highly heterogeneous, resulting in a typical perivascular tumor distribution. Additionally we show that co-administration of trastuzumab with a constant T-DM1 dose results in a significantly more homogeneous tumor distribution, thereby targeting more tumor cells with the potent cytotoxic small molecule drug. Importantly, the total tumor uptake of the ADC does not change significantly, but *in vivo* experimental data shows a drastically different tumor distribution. The

combined PBPK-Krogh cylinder model accurately captures the systemic organ concentrations and the considerably different tumor distribution, something that neither model can do alone. The interplay between systemic level pharmacokinetics and tumor distribution is important for ADCs, and several literature examples are shown in the context of tissue penetration. The impact of dose, DAR, deconjugation, receptor expression, and trafficking all strongly impact the distribution. This model is therefore useful in accurately capturing the complex distribution resulting from varying the DAR, linker stability, and antibody distribution on tumor efficacy.

5.4 Results

A graphic depiction of the combined PBPK and Krogh cylinder model is shown in Figure 5.1. This multi-scale model captures the systemic and organ level concentrations (PBPK model, Figure 5.1) along with the heterogeneous tissue distribution in the tumor and cellular metabolism of the ADC (Krogh cylinder model, Figure 5.1). Currently, the endosomal processing and escape of the metabolite are not included but could be added to the modeling framework as others have done (*177*,*182*). The higher vascular density in healthy tissue (resulting in shorter diffusion distances between vessels) and lack of specific binding in most tissue results in a homogeneous antibody distribution (*37*). Therefore, only the tumor compartment is represented explicitly with a Krogh cylinder model. The small molecule metabolite for T-DM1 is relatively hydrophilic, resulting in little bystander effect within the tissue (*13*), so the diffusion of the metabolite was not simulated. The metabolite is represented by the green arrows.

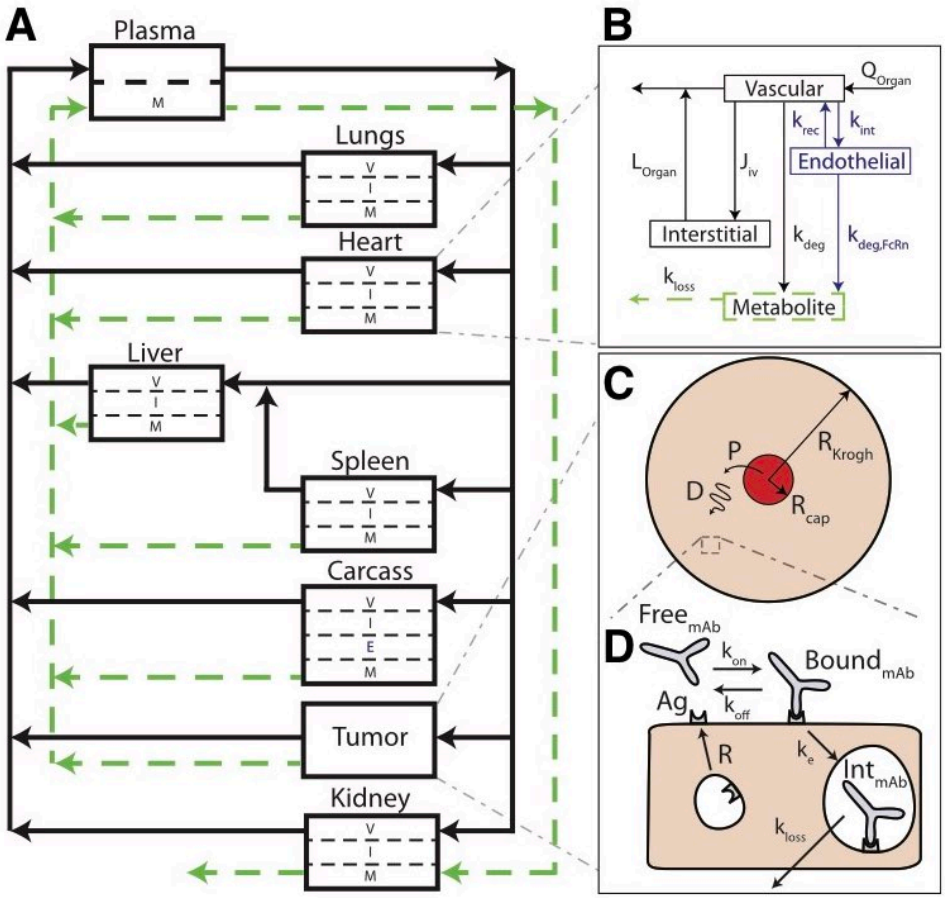

Figure 5.1 Multi-scale PBPK-Krogh cylinder model diagram.
A, PBPK model tracks systemic distribution of both antibody and ADC. Solid black lines correspond to antibody/ADC flow and green dotted lines correspond to metabolite flow. B, representative organ compartment model. All organs except the tumor and carcass are divided into vascular, interstitial, and metabolite compartments. The endothelial compartment is added in the carcass to account for FcRn recycling. C, the tumor compartment is modeled by a 1-D Krogh cylinder tissue model with permeability (P) across the endothelium (extravasation) and diffusion (D) through the surrounding tissue. D, cellular-scale model showing binding, internalization, and degradation rates of both antibody and ADC.

The tumor distribution of antibody and small molecule drug is a function of the dose, DAR, systemic clearance, and *in vivo* kinetics (such as deconjugation depending on the linker(*183*,*184*)). To capture the impact of the antibody dose relative to small molecule delivery, a constant dose of T-DM1-AF680 was given with increasing doses of trastuzumab. This could represent a constant small molecule dose while decreasing the DAR (assuming both free antibody and ADC behave similarly as seen with T-DM1 (*184*)), the impact of deconjugation

and free antibody accumulation in the plasma, or an intentional effort to increase antibody tissue penetration by competing for available antigen. Figure 5.2 shows that the clinical dose of T-DM1-AF680 (3.6 mg/kg) is highly heterogeneous in NCI-N87 tumor xenografts. Figure 5.3 and Figure 5.4 show that the plasma clearance and tumor distribution of unlabeled T-DM1 and T-DM1-AF680 are similar. Co-administration of trastuzumab at a 3:1 or 8:1 ratio dramatically increases penetration of T-DM1 by competing for receptor sites within the tissue. These results also agree with literature reports where increasing the antibody dose results in more homogeneous distribution throughout the tumor (*36*,*41*,*178*).

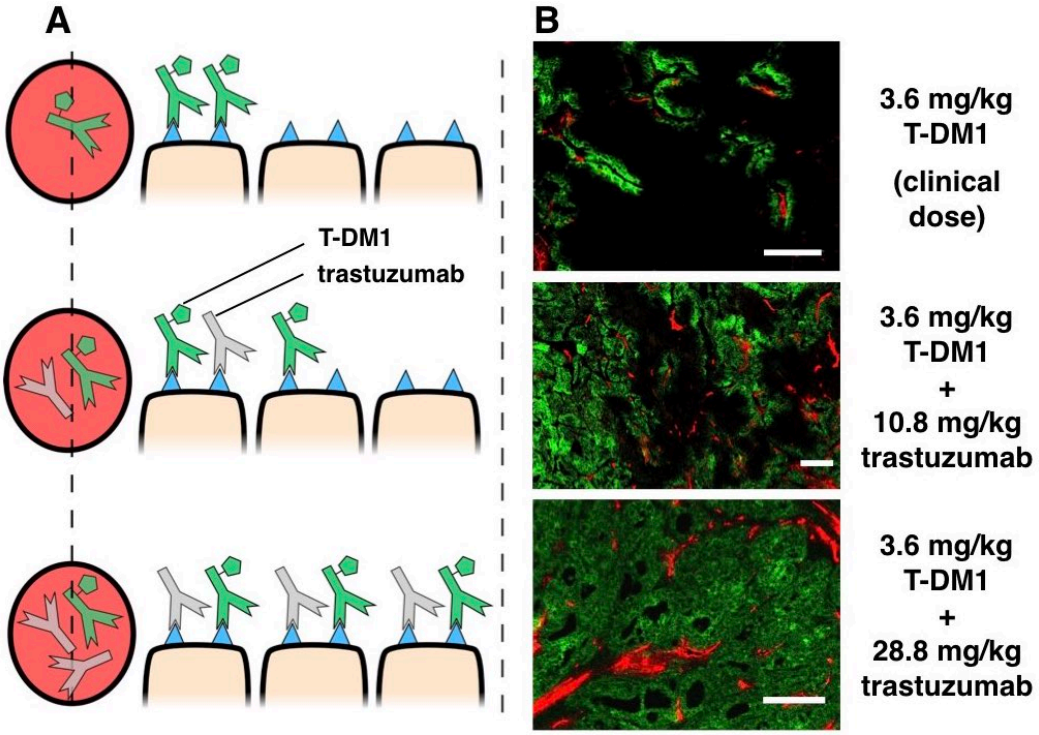

Figure 5.2 Heterogeneous ADC distribution.
A, graphic depiction of T-DM1 tumor distribution with co-administration of trastuzumab. Without a carrier dose of trastuzumab, tumor distribution of T-DM1 is perivascular. Co-administration of T-DM1 with 'carrier' doses of trastuzumab (at constant T-DM1 doses) results in significantly more T-DM1 tumor penetration. B, immunofluorescence imaging following co-administration of 3.6 mg/kg of AlexaFluor 680 tagged T-DM1 (green) with trastuzumab at 0:1, 3:1, and 8:1 ratios (0 mg/kg, 10.8 mg/kg, and 28.8 mg/kg unlabeled trastuzumab, respectively). Immunofluorescence staining with CD31-AF555 (red) shows tumor vasculature. Window leveling of images is different. Scale bar = 200 μm.

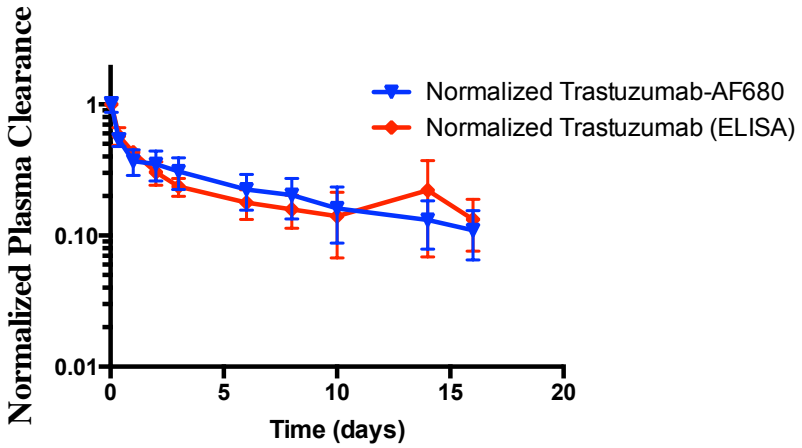

Dose	alpha (hr^{-1})	alpha 95% CI	beta (hr^{-1})	beta 95% CI	fraction alpha (%)	fraction alpha 95% CI
Trastuzumab	1.43	0.64-2.22	0.03	0.0-0.07	76.87	64.92-88.81
Trastuzumab-AF680	3.35	2.19-4.51	0.08	0.06-0.09	61.31	56.47-66.14

Figure 5.3 Normalized plasma clearance of trastuzumab and trastuzumab-AF680. Conjugation of AF680 to trastuzumab at a low degree of labeling (0.3 dyes per antibody) does not significantly alter the plasma clearance of trastuzumab over 16 days. 500 µg of unlabeled trastuzumab and 50µg of trastuzumab-AF680 were administered via tail-vein injection to N=3 mice. Blood samples were processed as described in Materials and Methods section. Samples were first scanned on the Odyssey NIR Imaging System and then used with a Human IgG1 ELISA kit (eBioscience, Cat. No. 88-50560-22).

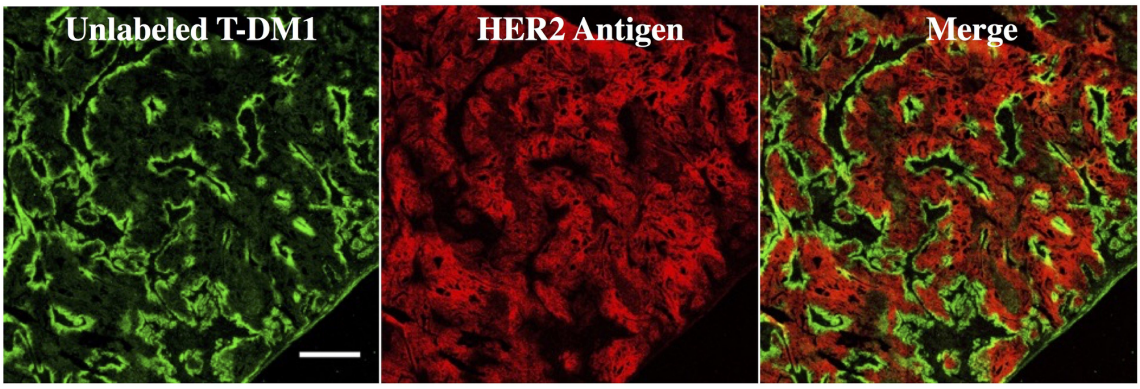

Figure 5.4 Distribution of unlabeled T-DM1.
Immunofluorescence imaging 24 hour post injection of unlabeled T-DM1 (green) shows perivascular distribution, similar to Figure 5.2, Figure 5.7, and Figure 5.8. *Ex vivo* staining was first done with anti-human-Fc-AF680 (green), washed, then stained with trastuzumab-AF488 (red) to show free HER2 receptor. Scale bar 500 μm.

A PBPK model using a compartmental model for the tumor can accurately capture the average tissue concentration (*64*), but does not describe the tumoral distribution. The increasing doses of trastuzumab do not significantly impact the *average concentration* of T-DM1 in the tumor or other organs prior to saturation (Figure 5.5), but it dramatically changes the ADC tissue *distribution* (Figure 5.2). The increased penetration lowered the concentration of T-DM1 on each cell (resulting in lower fluorescence intensity per cell) but did not lower the total tumor uptake. The lack of significant binding in other organs results in a minor difference in non-specific distribution (Figure 5.5). The molecules co-exist in these tissues but do not interact/compete for binding sites. Because the PBPK portion of the simulation was adapted from a previously published model, the organ concentrations were fit to biodistribution data and plasma clearance (Figure 5.5 and Figure 5.6) using a minimal number of fitted agent-specific parameters for n = 3 mice per dose level, and the fitted parameters are shown in Table 5.1. For parameter estimates, the 24-hour time point was used for biodistribution studies because this is the approximate time for maximum uptake of trastuzumab and other antibodies (*36*,*60*,*64*) along with plasma clearance data out to 72 hours.

Table 5.1 Fitted PBPK model parameters.

Parameter	Value	Units	%CV	95% C.I.	Description
$k_{deg,liver}$	7.4×10^{-6}	mL/s	34.5	3.1×10^{-6} to 1.2×10^{-5}	Liver degradation rate
$k_{deg,organ}$	3.2×10^{-7}	mL/s	72.1	0* to 7.0×10^{-7}	Organ degradation rate
U	6.9×10^{-4}	s^{-1}	65.8	0* to 1.5×10^{-3}	Metabolite urinary excretion rate
k_{loss}	5.2×10^{-5}	s^{-1}	20.9	3.4×10^{-5} to 7.1×10^{-5}	Metabolite loss rate

*Confidence interval was constrained to zero because lower bound was negative.

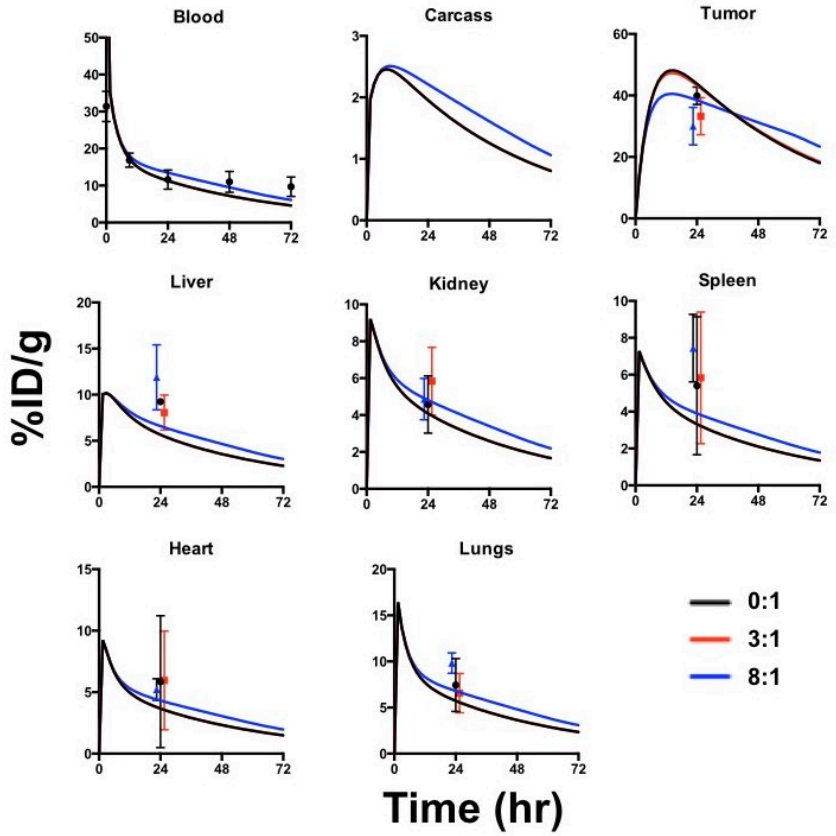

Figure 5.5 PBPK model results and experimental biodistribution data.
PBPK model shows systemic distribution of 3.6 mg/kg T-DM1 with trastuzumab at 0:1 (black), 3:1 (red), and 8:1 (blue) ratios (trastuzumab:T-DM1, N=3 mice for each). 0:1 and 3:1 distributions overlap since the tumor is below saturation at these dosing levels. At 8:1 ratio, the dose is slightly above tumor saturation resulting in lower tumor %ID/g and slower clearance. Experimental data shows T-DM1 distribution at 24 hours for the respective ratios; data points were shifted slightly for visibility. The PBPK results are similar despite widely differing distribution seen within the tumors in Figure 5.2.

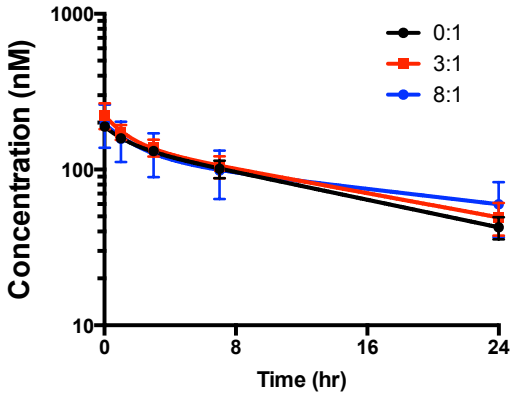

Figure 5.6 T-DM1 Plasma clearance.
Plasma clearance of 3.6 mg/kg T-DM1 with co-administration of trastuzumab at 0:1, 3:1, and 8:1 ratios (0 mg/kg, 10.8 mg/kg, and 28.8 mg/kg unlabeled trastuzumab, respectively). The addition of a carrier dose had a negligible impact on clearance.

The Krogh cylinder portion of the model was used to predict the tumor tissue distribution following co-administration of trastuzumab and T-DM1 at 0:1, 3:1, and 8:1 ratios (0 mg/kg, 10.8 mg/kg, and 28.8 mg/kg unlabeled trastuzumab, and 3.6 mg/kg T-DM1, respectively)(Figure 5.7). It should be noted that none of the parameters used in this portion of the model were fit to new experimental data but were all taken from literature. The penetration distance increases from strongly perivascular distribution with the 0:1 ratio to homogeneous distribution with the 8:1 ratio while the T-DM1 concentration per cell is reduced. These results agree favorably with all tumors tested (Figure 5.8, Figure 5.9, Figure 5.10). Macroscopic images of a larger tumor region are shown (Figure 5.7) along with a higher magnification of the boxed region. The Krogh cylinder parameters used for all simulations are shown in Table 5.2.

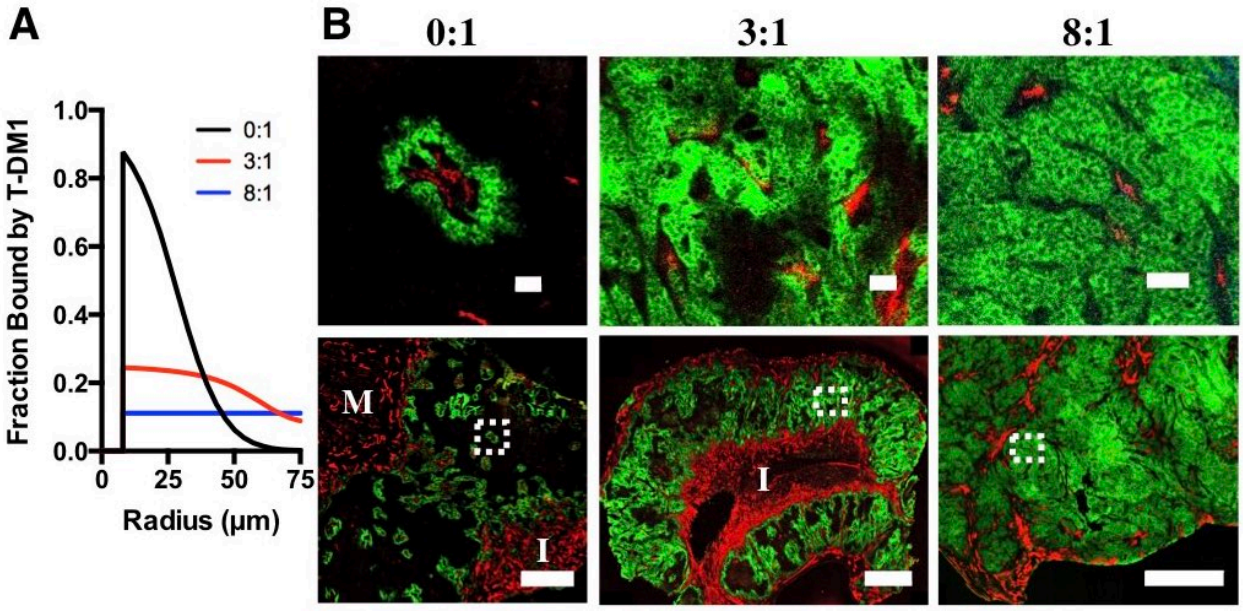

Figure 5.7 Quantitative Krogh cylinder simulation results and immunofluorescence imaging results.

A, model predictions of bound T-DM1 with co-administration of trastuzumab at 0:1, 3:1, and 8:1 ratios 24 hours post injection. B, experimental validation of model predictions. Whole tumor (bottom) and inset (top) T-DM1 (green) distribution following injection of 3.6mg/kg T-DM1 with trastuzumab at 0:1, 3:1, and 8:1 ratios. Immunofluorescence staining with CD31-AF555 (red) shows tumor vasculature. I and M show regions of inflammatory cells and muscle, respectively. Window leveling between different carrier dose images is different. Scale bar = 50 μm (top) and 1 mm (bottom).

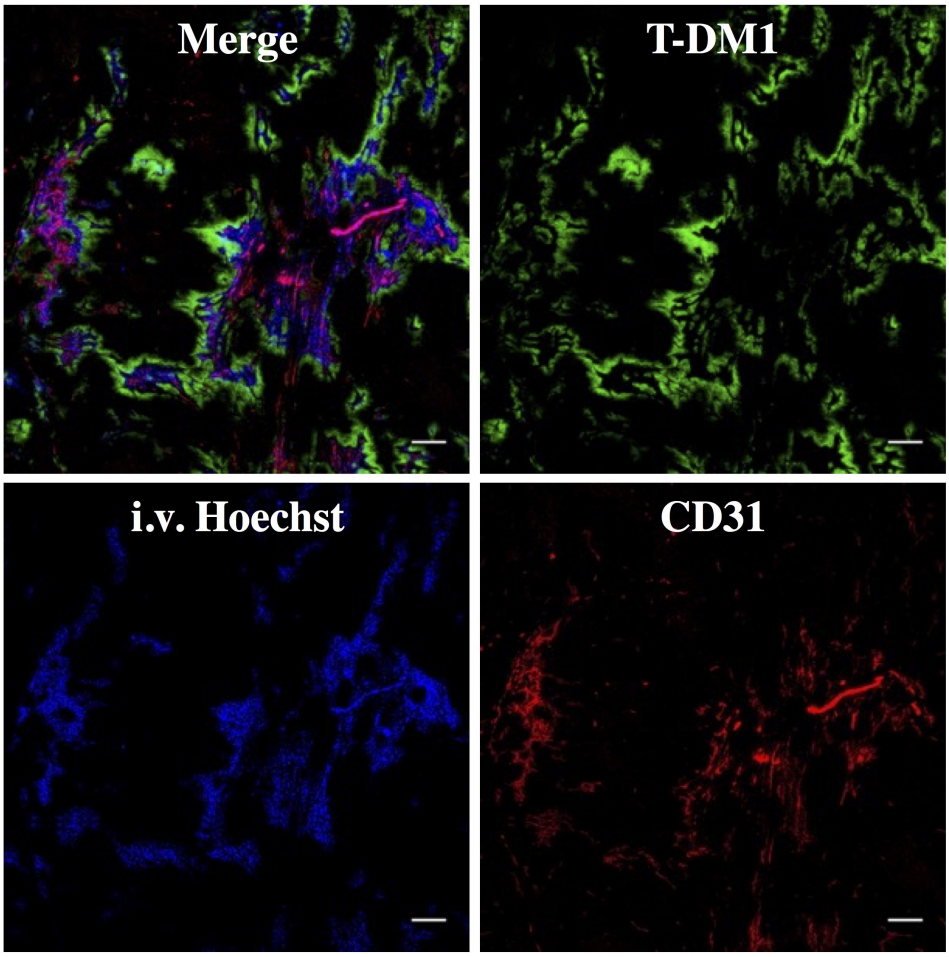

Figure 5.8 T-DM1 distribution at 0:1 dosing ratio (only 3.6 mg/kg T-DM1).
Immunofluorescence imaging 24 hour post injection of T-DM1 (green) shows perivascular distribution. 30 min prior to sacrifice Hoechst 33342 (blue) was injected at 15 mg/kg to highlight functional vasculature. *Ex vivo* staining was done with CD31 (red) to further show tumor vasculature. Window leveling different than Figure 5.9 and Figure 5.10. Scale bar 200 μm.

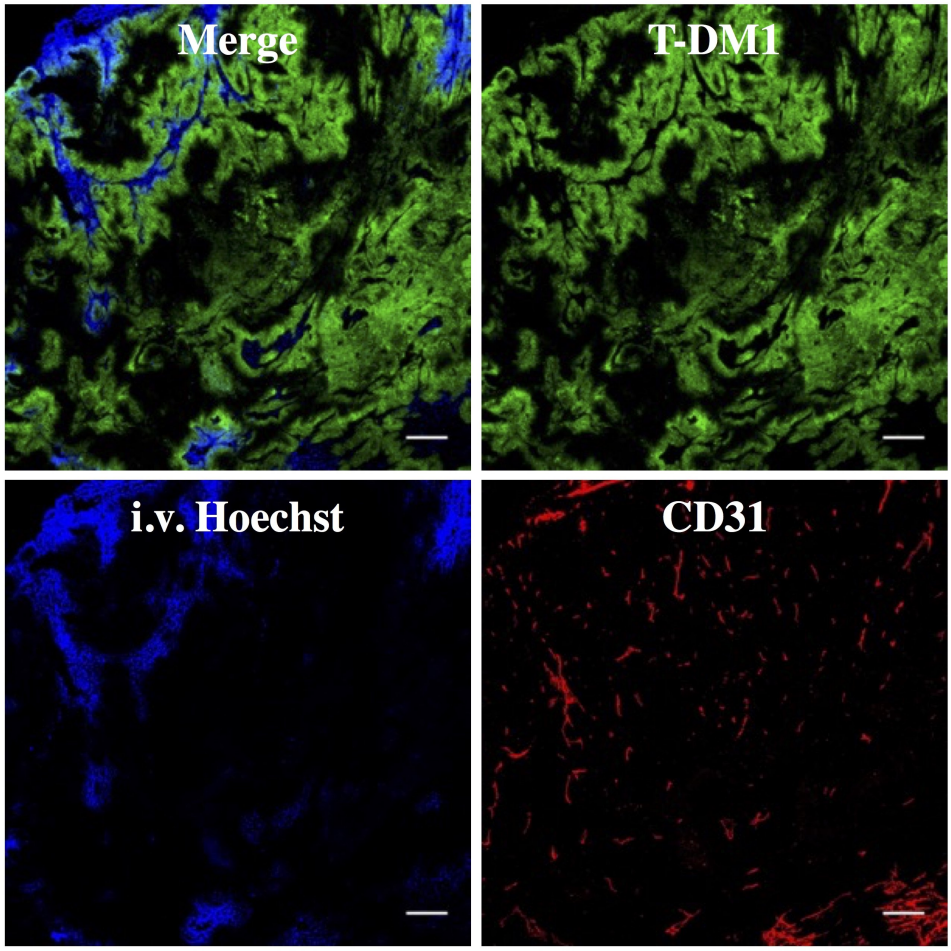

Figure 5.9 T-DM1 distribution at 3:1 dosing ratio (3.6 mg/kg T-DM1 + 10.8 mg/kg unlabeled trastuzumab).
Immunofluorescence imaging 24 hour post injection of T-DM1 (green) shows further penetration into tumor. 30 min prior to sacrifice Hoechst 33342 (blue) was injected at 15 mg/kg to highlight functional vasculature. *Ex vivo* staining was done with CD31 (red) to further show tumor vasculature. Window leveling different than Figure 5.8 and Figure 5.10. Scale bar 200 μm.

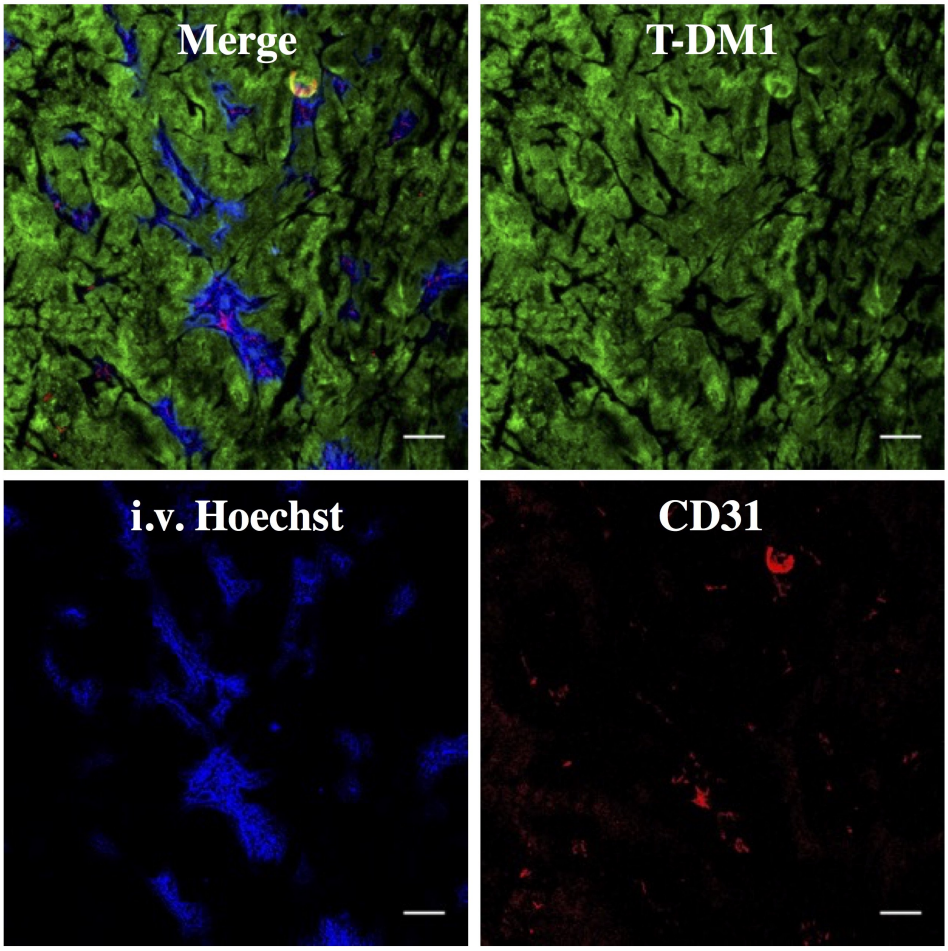

Figure 5.10 T-DM1 distribution at 8:1 dosing ratio (3.6 mg/kg T-DM1 + 28.8 mg/kg unlabeled trastuzumab).

Immunofluorescence imaging 24 hour post injection of T-DM1 (green) shows homogeneous distribution throughout tumor. 30 min prior to sacrifice Hoechst 33342 (blue) was injected at 15 mg/kg to highlight functional vasculature. *Ex vivo* staining was done with CD31 (red) to further show tumor vasculature. Window leveling different than Figure 5.8 and Figure 5.9. Scale bar 200 μm.

Table 5.2 Krogh cylinder simulation parameters from literature.

Parameter	Value	Units	Reference	Description
D	10	$\mu m^2/s$	(*90*)	Antibody diffusivity
P	3×10^{-9}	m/s	(*185*)	Antibody permeability
k_{on}	7.1×10^5	$M^{-1}\ s^{-1}$	(*186*)	Trastuzumab binding rate
K_d	0.5	nM	(*186*)	Trastuzumab dissociation constant
k_{off}	3.5×10^{-4}	s^{-1}	(*186*)	Trastuzumab dissociation rate
R_{Krogh}	75	μm	(*36*,*187*)	Krogh cylinder radius
$R_{capillary}$	8	μm	(*188*)	Capillary radius
$[Ag]_0$	0.83	μM	(*43*,*189*,*190*)	Initial Antigen concentration (10^6 HER2/cell, 5×10^8 cells/mL)
ε	0.24	Dimensionless	(*42*)	void fraction
H	0.45	Dimensionless	(90)	Hematocrit
k_e	3.3×10^{-5}	s^{-1}	(*124*)	Trastuzumab internalization rate
Q	0.0015	mL/g/s	(*60*)	Blood flow rate to tumor
Rs	3.3×10^{-5}	s^{-1}	(*124*)	Antigen recycle rate

The penetration depth of antibodies is a complex function of dose, receptor expression and trafficking, and tumor physiology (permeability, vascular density, etc.). Figure 5.11 shows the predicted T-DM1 radial distribution as the competitor trastuzumab "carrier" dose is increased. When no carrier dose is added (only T-DM1 from 0 to 3.6 mg/kg total ADC dose), T-DM1 exhibits a perivascular distribution where cells immediately outside the blood vessel are

saturated and cells farther away receive almost no ADC. As carrier trastuzumab is added, however, it competes for receptors, allowing T-DM1 to penetrate farther into the tumor, albeit with lower T-DM1 concentration per cell. (Note that higher doses of T-DM1 would also achieve additional penetration, but TDM-1 is limited by toxicity at 4.8 mg/kg (*48*).) As more carrier dose is added, the carrier dose continues to spread out the ADC distribution until all the binding sites are occupied by trastuzumab or TDM-1. At the theoretical receptor saturating concentration for total antibody, T-DM1 (and trastuzumab) penetrates evenly throughout the tumor. Above this total antibody saturating concentration, the T-DM1 concentration remains homogeneous throughout the tumor. However, the average intra-tumoral T-DM1 concentration starts to drop because the increasing amount of trastuzumab competes for receptors, and there are no additional binding sites deeper in the tissue once saturation is achieved. Importantly, receptor expression (and therefore the saturation dose) can vary significantly between patients and within tumors/metastases. To highlight the relationship between receptor expression, penetration depth, and total antibody dose (ADC plus free antibody), three-dimensional plots of radial concentration versus total dose with different receptor expression are shown in Figure 5.11. These simulations were done using a high ($1x10^6$ receptors per cell) and moderate ($3x10^5$ receptors per cell) HER2 expression level (Figure 5.11 and Figure 5.12), which roughly corresponds to 3+ and 2+ IHC staining (*191*).

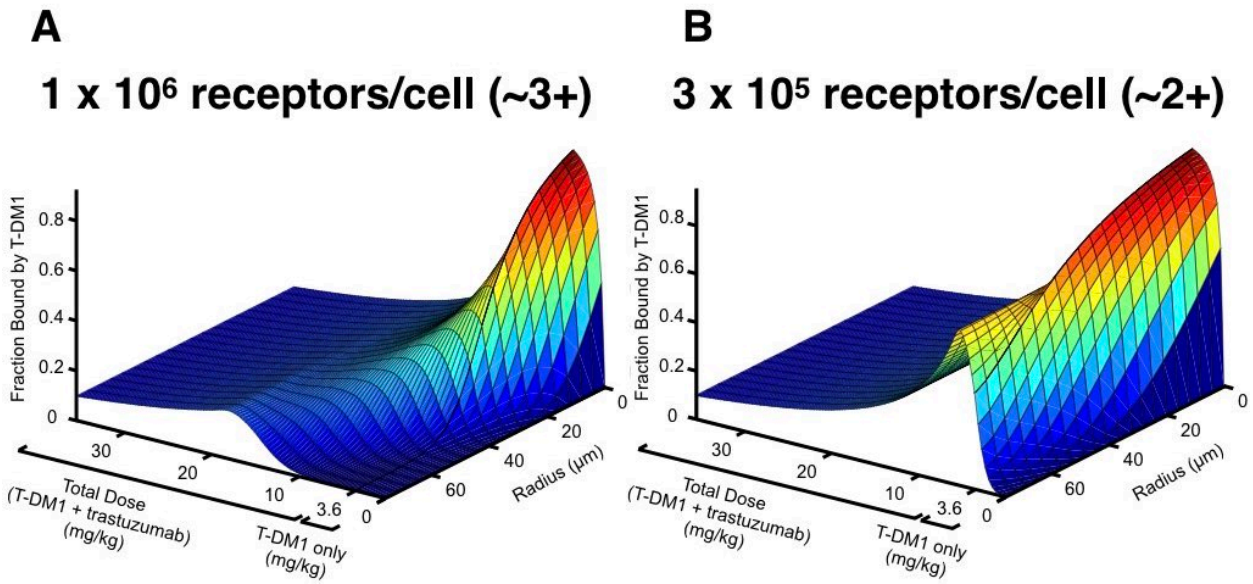

Figure 5.11 Prediction of T-DM1 distribution versus trastuzumab carrier dose.
Predicted perivascular tumor distribution following dosage with T-DM1 and trastuzumab for tumor cells expressing 1 x 10^6 receptors per cell, A, and 3 x 10^5 receptors per cell, B, corresponding to ~3+ and ~2+ IHC staining, respectively. From 0 to 3.6 mg/kg total dose only T-DM1 is dosed. After 3.6 mg/kg the T-DM1 dose is kept constant (3.6 mg/kg) and trastuzumab carrier dose is increased.

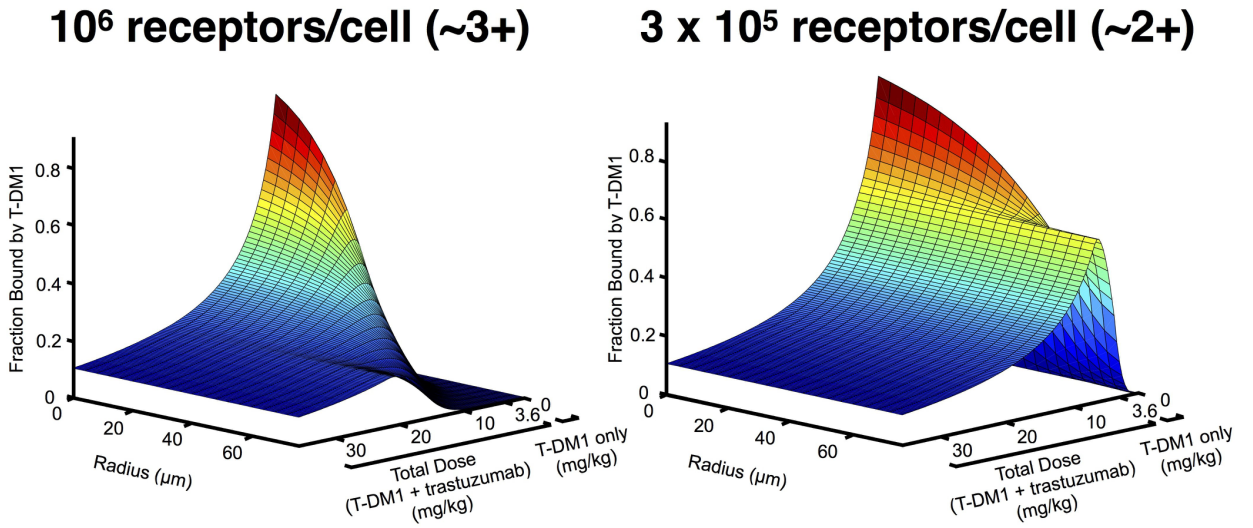

Figure 5.12 Prediction of T-DM1 distribution versus trastuzumab carrier dose.
Predicted tumor distribution following dosage with T-DM1 and trastuzumab for tumor cells expressing 1 x 10^6 receptors per cell and 3 x 10^5 receptors per cell, corresponding to 3+ and 2+ IHC staining, respectively. From 0 to 3.6 mg/kg total dose only T-DM1 is dosed. After 3.6 mg/kg the T-DM1 dose is kept constant (3.6 mg/kg) and trastuzumab carrier dose is increased. Axis corresponds to total dose (T-DM1 + trastuzumab). Graph is identical to Figure 5.11 but at alternate viewing angle.

The antibody penetration depth is also a function of time. Figure 5.13 shows the radial profile of 3.6 mg/kg T-DM1 along with a 3:1 and 8:1 trastuzumab co-administration. The penetration depth quickly reaches the maximum distance at 24 hours and then stalls. This is caused by continuous internalization preventing further penetration even as the antibodies continue to extravasate. The longer circulation time of antibodies does not increase the penetration depth due to this constant internalization, making C_{max} a critical factor in determining tissue penetration depth (*37*,*43*).

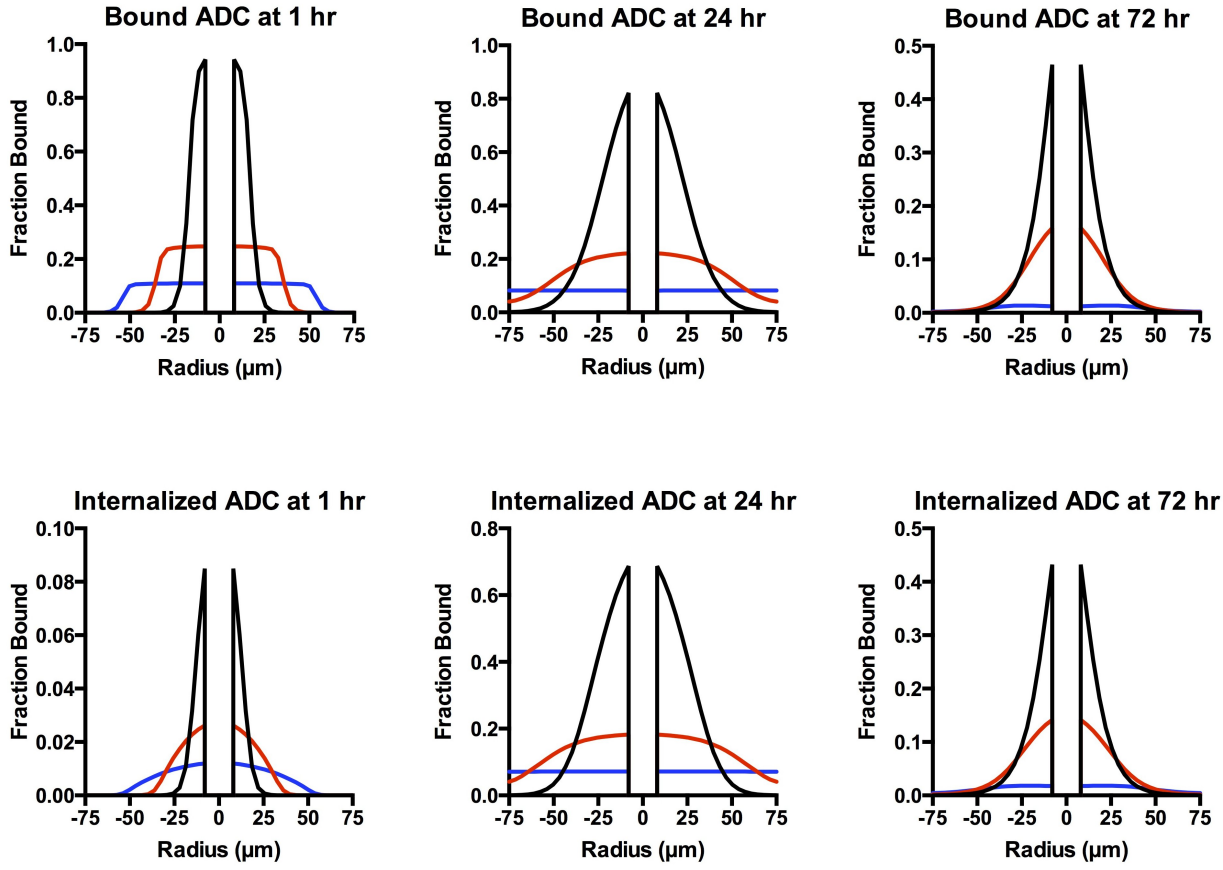

Figure 5.13 Antibody tumor penetration over time.
Penetration depth reaches a maximum at approximately 24 hours, and continuous internalization prevents further penetration as additional antibody continues to extravasate.

Co-administration of trastuzumab with T-DM1 lowers the average effective DAR since the same amount of small molecule payload is administered with more antibodies. Multiple groups have examined the impact of DAR on plasma clearance and efficacy. Figure 5.14 highlights the results of several groups (using different ADCs against different targets) where the overall small molecule dose was similar but the DAR and ADC dose was varied. For clarity, only tumor growth curves where there is an equivalent small molecule dose spread over a different ADC dose (and different DAR) are shown. Previous work by several groups has demonstrated the importance of DAR on systemic clearance (*24*). Two important mechanisms include DAR-dependent clearance and DAR-dependent deconjugation. In DAR-dependent clearance, a high number of small molecule drugs per antibody can increase systemic clearance of the entire antibody-drug conjugate. With DAR-dependent deconjugation, a larger number of small molecule drugs can result in faster loss of the small molecule while the antibody (with a lower DAR or without a payload, i.e. DAR0) remains in circulation. Only a few informative studies have measured the dynamic change of individual DAR species *in vivo*. Using these studies, we modeled the effective difference in small molecule AUC and divided the results into cases where the antibody exposure, and therefore penetration distance into the tumor, was much higher than the difference in payload exposure (Figure 5.14), and cases where DAR-dependent clearance and/or deconjugation dominated over differences in antibody AUC. Vertical red lines and boxes show the approximate percentage difference between the small molecule payload AUC, typically chosen at a time point when the tumor growth curves begin to diverge. The results in Figure 5.14 highlight the fact that at a similar small molecule exposure,/AUC a higher antibody concentration (corresponding to increased tumor penetration) generally has higher efficacy. Individual cells receive less small molecule drug, but the IC_{50} is lower than the K_d for

these agents, so cells within the saturated perivascular region still receive a toxic dose. The lone exception is a paper using a less toxic small molecule, and this is also the only paper where the IC_{50} is greater than the K_d. These studies provide preliminary (but indirect) evidence that a more homogeneous distribution may result in better ADC efficacy. The studies shown in Figure 5.14 highlight the importance of DAR-dependent clearance. In Lyon et al. the linker was varied, and significant differences in the clearance were seen with the DAR8 conjugates. The faster clearance ultimately resulted in worse efficacy. Similarly, in Hamblett et al. the higher small molecule exposure resulted in better efficacy; however, the higher antibody dose at the time of maximum uptake in the tumor (predicted to occur approximately 1 day after the ADC was dosed) would result in higher tumor penetration, thereby complicating the interpretation.

To examine the role of the bystander effect, the tumor growth studies were grouped by payloads that are not capable of diffusing into neighboring cells (non-bystander payloads) in Figure 5.15, and payloads that are (bystander payloads) in Figure 5.16 (*192*). Several of the tumor growth studies in Figure 5.15, Figure 5.16, and Figure 5.17, are taken from Figure 5.14, but are arranged by payload properties for clarity. Expectedly, for non-bystander payloads at constant payload dose, the high ADC dose/low DAR strategy consistently resulted in greater tumor shrinkage and better efficacy (Figure 5.15). Bystander payloads like MMAE are able to efflux from the cell and diffuse into and target adjacent cells to exert their cytotoxic effects. While an important role for these payloads is killing antigen negative cells, they also have the ability to penetrate farther into the tumor beyond ADC-saturated perivascular cells, and potentially improve ADC efficacy. In contrast to non-bystander payloads, bystander payloads that are delivered at a higher dose than needed for cell killing (‘overkill’) can diffuse deeper into

the tissue, thus improving the penetration distance of the payload and killing additional cells. Literature review of cases using a constant payload dose with different ADC doses/DAR revealed that improved tissue penetration still improves efficacy (Figure 5.16). Importantly, this shows that direct targeting by the ADC is more efficient at delivering the payload to the tumor cell than the bystander effect. Finally, we examined the effect of keep the antibody dose constant and increasing the payload dose for both bystander payloads and non-bystander payloads (Figure 5.17). Literature review of cases using a constant bystander ADC dose with increasing DAR revealed that for an equivalent dose of bystander ADC, higher DAR consistently improves efficacy. However, increasing the DAR for non-bystander payloads (at a constant ADC dose) may only further concentrate payload in perivascular tumor cells, exacerbating the 'overkill' of these cells but not necessarily altering the overall efficacy. Despite delivering twice the payload dose, Junutula et al. showed comparable efficacy and Jackson et al. showed less efficacy with the higher DAR ADCs. However, Pillow et al. showed improved efficacy with the higher DAR, indicating tissue distribution is one factor of many properties impacting ADC efficacy. We hypothesize that additional factors (DAR-dependent clearance and/or tissue-level effects in vascularization) may be responsible for these deviations when similar efficacy is predicted due to equivalent tissue penetration.

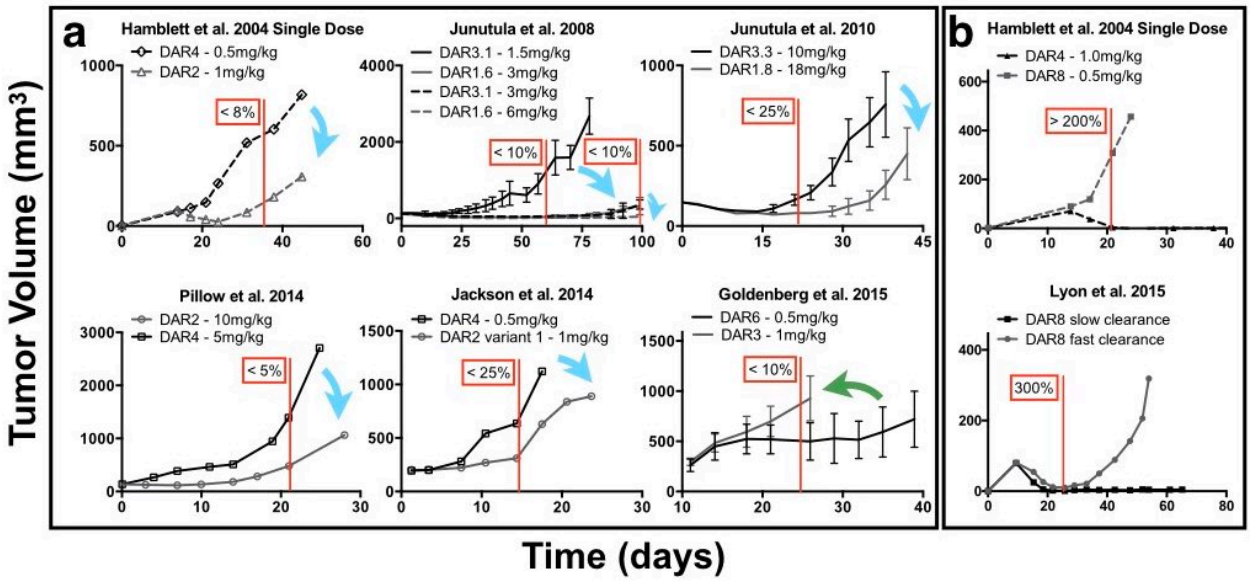

Figure 5.14 Literature review of efficacy with constant small molecule dose but differing DAR and antibody doses.
A, at a constant small molecule dose, ADCs with a higher DAR and lower antibody dose (black) are generally less efficacious than ADCs with a lower DAR and higher antibody dose (gray). Blue arrows correspond to six cases where a constant small molecule dose delivered with a higher antibody dose improved efficacy and is predicted to have increased tissue penetration. In one case the reverse was true (green arrow); however, here the small molecule had an IC_{50} reported to be greater than the K_D of the antibody due to a less toxic payload. This would require saturation of cells with a high DAR antibody for efficacy. Red lines and boxes correspond to the estimated difference in small molecule AUC between different DAR/antibody doses using literature reports of DAR-dependent deconjugation and clearance rates in a pharmacokinetic model. B, DAR-dependent clearance can significantly affect the efficacy, making it difficult to parse tumor penetration effects from small molecule AUC.

The increasing trastuzumab doses do not appreciably lower the tumor uptake of T-DM1 (Figure 5.18). Because extravasation is the rate-limiting step in antibody uptake (*37*), T-DM1 molecules that extravasate but are blocked from binding perivascular cells will continue to diffuse deeper in the tissue rather than intravasate and wash out. Eventually they bind to a cell with free receptor. Similar to radiolabeled antibodies (*193*), only after the tumor is saturated will the %ID/g start to decrease (Figure 5.18).

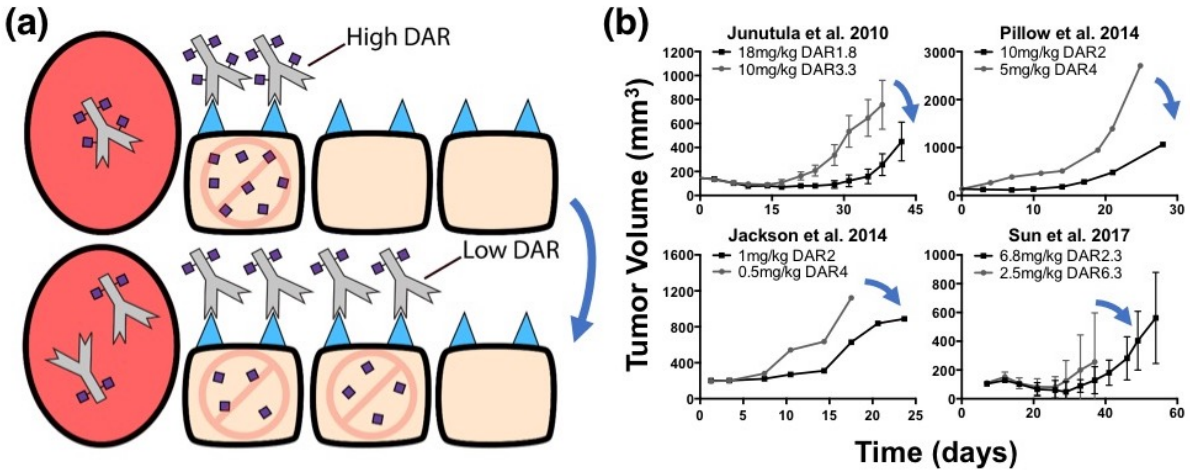

Figure 5.15 Distribution and efficacy of non-bystander payloads.
(a) Graphic depiction of the same payload dose for non-bystander ADCs with a high and low DAR (*top* and *bottom*, respectively). Higher antibody doses result in better tumor penetration (*bottom*) but the lower DAR results in a lower average number of payloads per cell. This is still sufficient for cell death with high potency payloads. (b) Literature review of cases using a non-bystander ADC at the same payload dose but with different DARs/ADC doses. In all these cases the higher antibody dose (lower DAR) improved efficacy despite the same payload dose. Blue arrows indicate cases where the lower DAR improved efficacy at a constant payload dose.

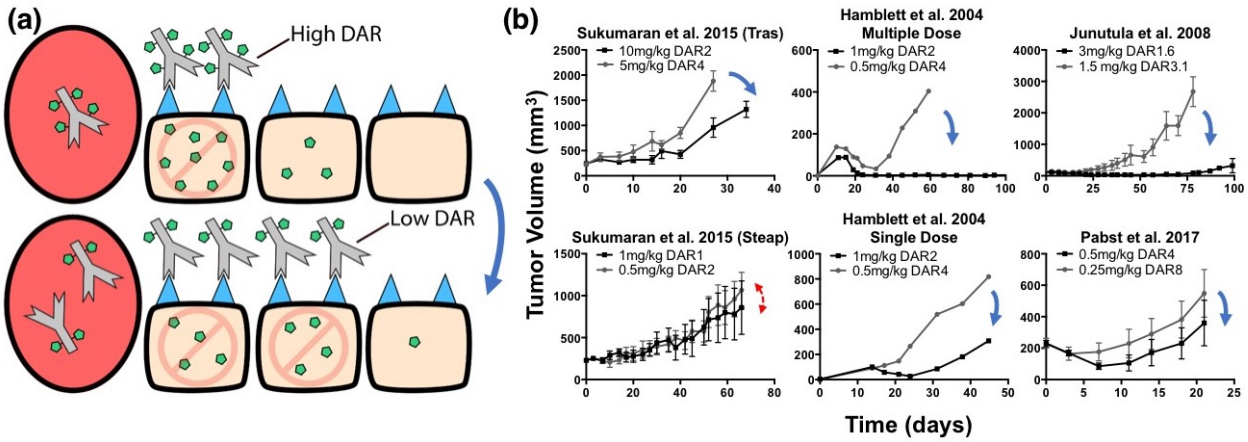

Figure 5.16 Distribution and efficacy of bystander ADCs given at constant payload dose with different DAR/antibody doses.
(a) Graphic depiction of the same payload dose for ADCs with a high and low DAR (top and bottom, respectively). Higher ADC doses target more cells, but the lower DAR results in a lower average number of payloads per cell.. (b) Literature review of cases using a bystander payload at the same payload dose. Although bystander payloads are able to diffuse farther into the tumor, in almost all cases the lower DAR ADC had improved efficacy, indicating direct cell targeting by the ADC may improve payload distribution more than bystander effects. Blue arrows indicate cases where the lower DAR (or higher ADC dose) improved efficacy despite a constant payload dose. Red double-sided arrows indicate similar efficacy. Tumor growth data taken from references8, 9, 44, 82. Tras, trastuzumab; Steap, anti-Steap.

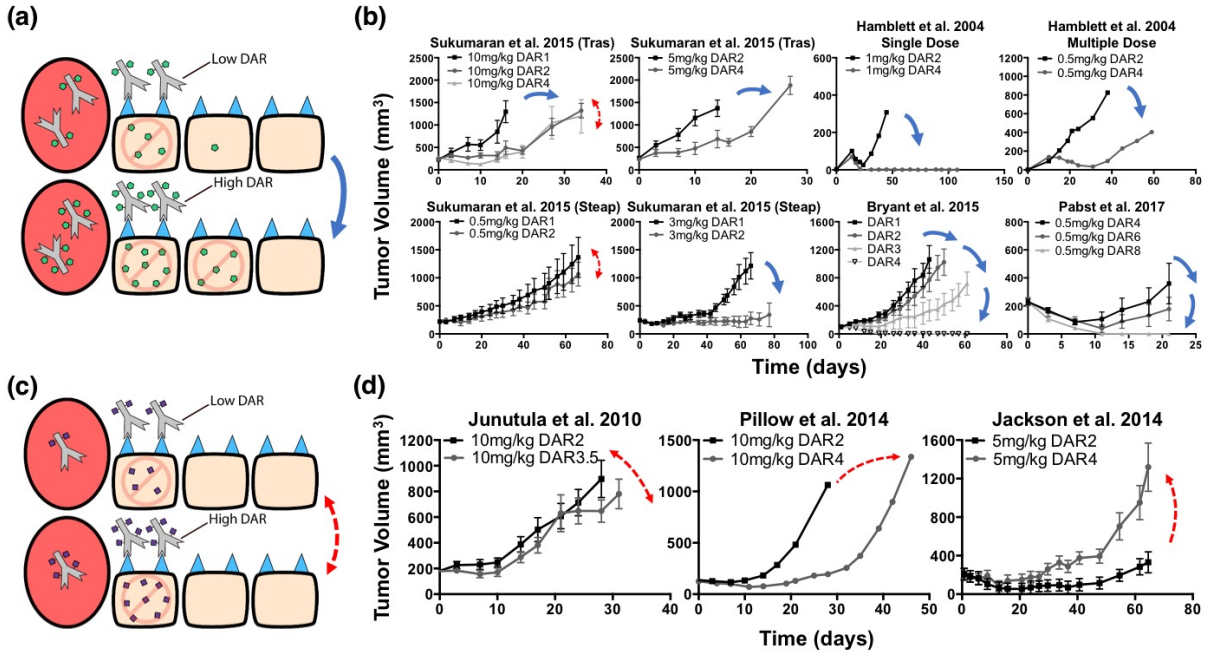

Figure 5.17 Distribution and efficacy of a constant dose of antibody with increasing DAR for both bystander and non-bystander payloads.

(a) Graphic depiction of the same ADC dose given with increasing DAR. The same ADC dose targets the same number of cells; however, bystander payloads are able to diffuse farther into the tumor, reaching more cells than initially targeted. (b) Literature review of cases using a constant bystander ADC dose with increasing DAR. Higher DAR bystander ADCs at the same ADC dose gave improved efficacy in ten cases (blue arrows). Two cases showed similar efficacy (red double-sided arrows). (c) Graphic depiction of the same ADC dose given with increasing DAR. Non-bystander payloads are unable to diffuse farther into the tumor and an equivalent ADC dose targets the same number of cells resulting in similar efficacy between high and low DAR non-bystander ADCs. (d) Literature review of cases using a constant non-bystander ADC dose with increasing DAR. Red double-sided arrows indicate negligible change in efficacy. Single-sided arrows indicate opposing differences in efficacy.

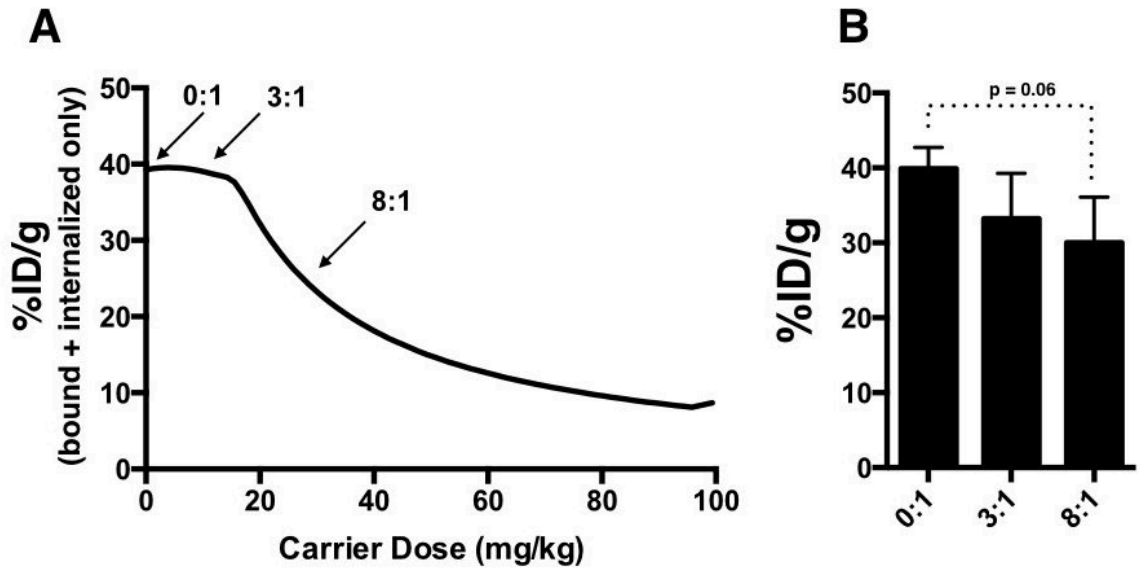

Figure 5.18 Predicted and experimental impact of carrier dose on total tumor uptake.
A, bound and internalized uptake of T-DM1 in tumor with increasing trastuzumab carrier dose. Prior to saturation, the addition of a carrier dose (or equivalently, delivering a constant small molecule dose while lowering the DAR) does not lower total tumor uptake of a constant T-DM1 dose (3.6 mg/kg). It only changes the distribution. B, experimentally measured %ID/g of T-DM1 at respective ratios. Differences of %ID/g were not statistically significant between the 0:1 to 8:1.

In addition to the tumor site, some antigens are expressed in healthy tissue, and this is an important aspect of target-mediated toxicity. The higher vascular density results in homogeneous ADC distribution that can be accurately represented with a compartmental model. If the healthy tissue is saturated with ADC (which is likely given higher vascularization and often lower receptor expression), the co-administration of free antibody will lower the ADC uptake in this healthy tissue (Figure 5.19) while having insignificant ($p = 0.06$) impact on tumor uptake (Figure 5.18). This could potentially increase the therapeutic window provided the carrier dose has a neutral or positive impact on tumor efficacy due to increased drug penetration.

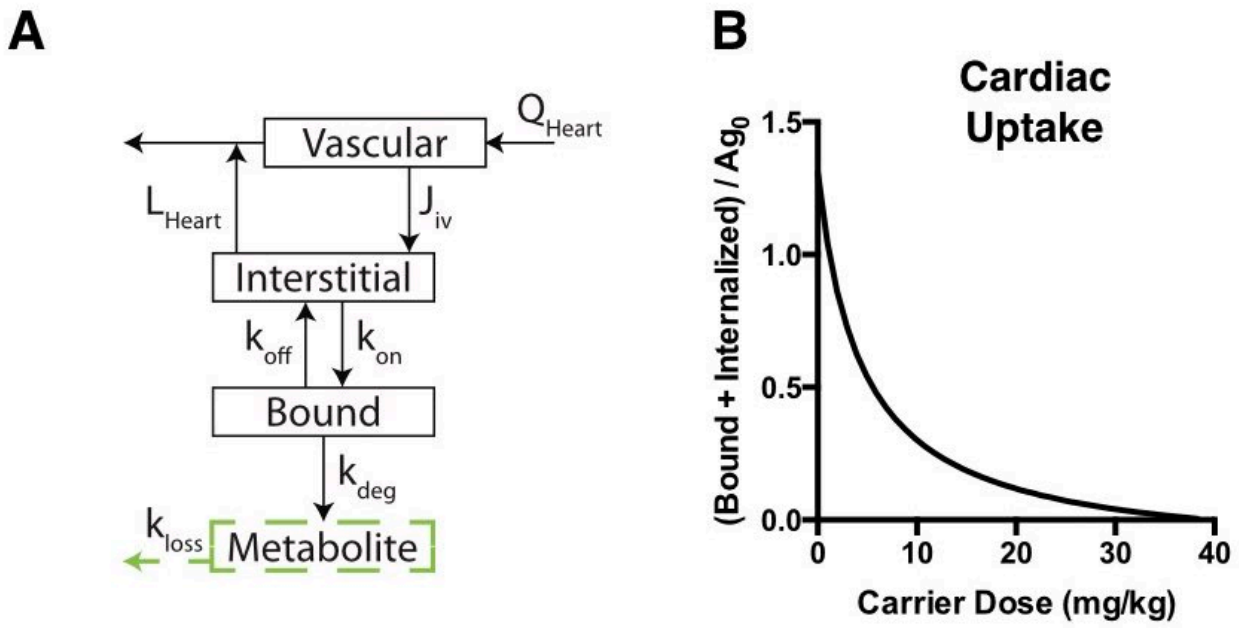

Figure 5.19 Impact of carrier dose/DAR on healthy tissue targeting.
A, graphic depiction of specific binding added to the heart organ compartment. A bound compartment was added to represent the low levels of HER2 antigen expressed in the heart. B, Bound and internalized T-DM1 (constant 3.6 mg/kg dose) in heart compartment with increasing trastuzumab carrier dose shows lower healthy tissue uptake with a carrier dose or lower DAR. The y-axis is normalized to initial unbound antigen in heart.

5.5 Discussion

Antibody drug conjugates display complex pharmacokinetics at multiple scales: systemic clearance as a function of DAR and deconjugation, organ heterogeneity from specific and non-specific processes, tumor tissue heterogeneity due to target binding, and cellular/subcellular kinetics of endosomal escape and bystander effects. Here we present a novel pharmacokinetic model for antibody biodistribution where a mechanistic Krogh cylinder geometry tissue based model is integrated into a PBPK framework (Figure 5.1). We show theoretically and experimentally that the tumor distribution of T-DM1 in NCI-N87 xenografts at clinical doses is highly heterogeneous, and that co-administration of trastuzumab effectively spreads out T-DM1 homogeneously throughout the tumor (Figure 5.2, Figure 5.7). Importantly, a compartmental

treatment of the tumor would show similar average uptake of the ADC with and without the co-administration of trastuzumab but would not be able to discern any impact on distribution. The combined model accurately captures the similar average organ uptake but drastic differences in tumor heterogeneity (Figure 5.2, Figure 5.5, Figure 5.7).

To highlight the importance of the integrated tissue distribution model, we showed how co-administration of T-DM1 with trastuzumab results in a significantly different tumor distribution with a similar systemic distribution. At the clinical dosage level of T-DM1 (3.6 mg/kg), the tumor distribution was perivascular with limited penetration, similar to trastuzumab (*36*). Adding a carrier dose of trastuzumab at a 3:1 ratio considerably increased the tumor penetration with limited changes in the overall uptake. The total ADC per cell is lower, but more tumor cells are receiving the therapeutic. Similarly with the 8:1 ratio, although the overall concentration received by the cells is less than the 3:1 ratio, the distribution in the tumor is even more homogeneous. Since the 8:1 dose is close to the theoretical receptor-saturating dose, this resulted in a slight (but not statistically significant, $p = 0.06$) reduction in total uptake.

Compartmental PBPK models do not take into account the tissue-scale distribution of antibodies or ADCs. The integrated tissue model based on the Krogh cylinder, however, uses a systems approach based on the physicochemical properties of the ADC to predict tissue distribution. Although the combined model presented here is not purely predictive because several agent-specific PBPK parameters were fit to experimental data, the Krogh cylinder portion of the model only requires the systemic concentration as input since published parameter correlations are available for the other values (*42*,*81*,*90*). Importantly, the mechanistic tissue

model gives the ability to easily change simulation parameters based on the specific therapeutic or target (Figure 5.11). These simulations were based on literature parameters for trastuzumab/T-DM1 binding affinity, antibody diffusivity/permeability, NCI-N87 receptor expression, and HER2 receptor kinetics. However, these parameters are often measured for other therapeutics and targets, giving the model broad applicability.

It has been known for some time that antibody distribution in tumors is heterogeneous (*194*), saturating doses are required to obtain even distribution (*178*), and very high doses are required to saturate tumors in the clinic (*195*,*196*). Many monoclonal antibodies for solid tumors are given frequently (often weekly) at relatively high doses (2-15 mg/kg), making it possible to approach tumor saturation. However, the potency of the small molecule payload often limits the dose and frequency of administration with ADCs. This limitation on dose and frequency, combined with current ADCs that often use high affinity antibodies, potent payloads, and highly expressed targets, can result in subsaturating (and therefore heterogeneous) distribution as we have shown when dosing T-DM1 at the clinical dosage (Figure 5.2, Figure 5.7, Figure 5.8). The importance of heterogeneity on therapeutic efficacy of antibodies and ADCs is still debated. The choice of model could implicitly bias the data interpretation (popularly phrased by Maslov's hammer). Examining the systemic clearance or deconjugation will focus on the impact these mechanisms have on efficacy. Likewise, measuring the tissue level heterogeneity will center the discussion on the impact of tumor distribution. By including both systemic and tissue level effects, the relative contribution of each can be quantified with this model and corresponding experiments.

We conducted an extensive literature search to determine if there is potential evidence of heterogeneity impacting ADC efficacy. Importantly, it depends on the toxicity of the payload. If receptor saturation with an ADC is required for cell death, then spreading out the ADC using a carrier dose may lower efficacy due to a subsaturating number of ADCs delivered per cell (a potency limitation). Conversely, if the ADC is toxic to cells at subsaturating concentrations, then heterogeneous delivery results in more drug being delivered to perivascular cells ("overkill") while other cells receive no treatment (a delivery limitation). In this case, a more uniform distribution would benefit efficacy by using the 'excess' ADC to reach and kill more cells. This is counter-intuitive, where the most potent drug is often pursued during development, but considering the tumor heterogeneity and high toxicity of the payloads, is possible. Looking at *in vitro* cell killing curves, the toxic payloads, high expression levels, and efficient internalization often result in IC_{50} values well below the antibody K_d, indicating they are toxic at subsaturating concentrations (*148*,*190*). To demonstrate that heterogeneity is having an impact on efficacy, the same payload must be delivered with varying heterogeneity to isolate and quantify the influence of heterogeneity on efficacy. One set of data available for this analysis are studies manipulating the DAR and dose. For example, an antibody with half the DAR but twice the antibody dose will deliver approximately the same small molecule payload to the tumor but spread out over twice the number of cells (assuming the plasma clearance and/or deconjugation of different DAR ADCs are similar). Several studies were identified that fit these criteria.

In the study by Hamblett et al. the effects of differing DAR and ADC dose to tumor killing was examined (*28*). When keeping the overall small molecule dosage the same (e.g. antibodies with a DAR of 2, and 4 dosed at 1, and 0.5 mg/kg, respectively), they found the best

clinical response with the highest antibody dose, or the dosage that would penetrate into the tumor the farthest. Similarly, Junutula et al. examined the efficacy of ADCs with DARs of 1.6 and 3.1 (*19*) and found the same pattern. They also showed that for the same antibody dose (but different DAR) the outcome was not significantly different, despite having different small molecule exposure. (Simulations show that this would deliver more small molecule to cells that are already receiving a toxic dose.) In another study with a different ADC and target Junutula and colleagues again showed that when keeping the small molecule dose the same, a significantly better outcome was seen with higher antibody doses (*197*). Jackson et al. did not find a difference in efficacy between DAR2 and DAR3.8 when the antibody dose was the same (which would reach the same number of cells) but observed much higher efficacy when the same small molecule dose was delivered with a higher antibody dose (*190*). A recent study by Pillow et al. (*198*) examined the efficacy of different DARs of THIOMAB conjugates, and they found that DAR2 conjugates dosed at 10 mg/kg were more efficacious than DAR4 conjugates dosed at 5mg/kg. In other words, having higher drug loading per antibody did not improve efficacy, and correspondingly, when injecting the same dose of small molecule, the drug spread out over more antibodies is more efficacious. In contrast to these other 6 examples (blue arrows, Figure 5.14), Goldenberg et al. found that with a low potency payload, a high DAR was needed.

To summarize the above results, we identified 6 publications with data suitable for analysis (*19*,*28*,*190*,*197–199*). Intriguingly, 5 of the 6 results showed higher efficacy with a lower DAR, where the same small molecule drug delivered with a larger antibody dose (due to lower DAR) resulted in reduced tumor growth (Figure 5.14). Most of the cell lines used in these studies were also resistant to the free antibody therapy, indicating the higher antibody dose alone

is not responsible for the effect. Upon closer inspection, the sole exception (Goldenberg et al. (*199*)) used a lower potency drug (SN-38 versus maytansinoids) with moderately lower expression (~10^5 receptors/cell versus ~10^6). Notably, the IC_{50} values for this ADC (range 1-33 nM, median 2 nM) were higher than the K_d of the antibody (0.564 nM). This is also consistent with the "overkill" hypothesis, where agents that require saturation for cell killing would not significantly benefit from a more even distribution, as this lowers the efficacy of all targeted cells. From a tissue penetration standpoint, matching the IC_{50} to the K_d of the ADC by lowering the DAR would be ideal. If the small molecule drug is dose-limiting, this maximizes the antibody dose to achieve maximum penetration while maintaining a toxic dose for the targeted cells. This also maximizes other mechanisms of action, such as cell-signaling disruption (*200*) and Fc-effector functions (*201*) compared to other strategies for increased penetration (such as lower affinity (*54*,*202*,*203*)). The model described here can help design experiments to determine if this strategy is effective in preclinical models.

DAR-dependent clearance and/or DAR-dependent deconjugation that significantly lowered the payload AUC/delivery could potentially explain the higher efficacy of lower DAR molecules. To quantify any impact of DAR-dependent clearance or DAR-dependent deconjugation, we modeled the small molecule exposure for each case. Pharmacokinetic measurements from each study were used to estimate the small molecule exposure (small molecule AUC). Since a detailed study of deconjugation or DAR-dependent clearance was not performed in all cases, we combined data from related studies to model the impact on small molecule AUC from deconjugation (unless data were presented showing deconjugation was negligible) or DAR-dependent clearance. The studies in Figure 5.14 had a small difference in

small molecule AUC (<25% and in most cases, <10%) relative to the large difference in antibody exposure (~100% or greater). On the contrary, the results in 6B showed a much larger difference in small molecule AUC (200-300%) relative to antibody exposure. Compared to the Lyon et al. paper, the studies in Figure 5.14 showed a larger difference in tumor efficacy despite drastically lower differences in payload AUC, indicating systemic clearance is unlikely to explain the differences in efficacy in Figure 5.14. It is also worth noting that the Goldenberg et al. paper shows the exact opposite trend that one would expect if DAR-dependent clearance or deconjugation were playing a role but is consistent with a potency-limited (versus a distribution-limited) ADC.

This analysis is not proof that antibody penetration is the only element (or even a dominant factor) in determining efficacy. For example, the relative contribution between more efficient small molecule distribution versus higher tumor antibody levels is unknown, although most cell lines were resistant to unconjugated antibody. However, the lack of quantitative models in the literature between DAR-dependent clearance/deconjugation versus tumor tissue heterogeneity makes it difficult to draw strong conclusions about the relative contributions of these phenomena. Clearly, DAR-dependent clearance and deconjugation are important, both for tumor exposure and potential toxicity. Lyon et al. showed ADCs having the same DAR but different clearance rates have proven the importance of plasma clearance on efficacy (*24*). While not proof, these 6 papers are consistent with heterogeneity impacting efficacy. The effect of individual tumor cell death on the eradication of the tumor is complex (*149*,*150*,*204*). The model developed here, by accounting for both systemic factors (like plasma clearance and linker

stability) and tumor tissue heterogeneity, will be able to quantitatively examine the impact of both to design more efficient clinical agents.

Besides ADC distribution, the PBPK model can help track secondary tissue toxicity. Because ADCs have higher toxicity caused by the small molecule drug, it is important to track their accumulation in healthy tissue. For example, trastuzumab and T-DM1 are both known to exhibit some cardiac toxicity because of low HER2 expression in the heart (*205*). By increasing the trastuzumab carrier dose in these simulations the overall cardiac uptake of the ADC is lowered. In this case both the antibody and ADC show toxicity but for other possible targets, co-dosing with the unconjugated antibody could result in less overall toxicity to healthy tissue. Similarly, Boswell et al. showed that the intestines were acting as an antigen sink when dosing the ADC anti-TENB2-MMAE; however, co-administration of an anti-TENB2 antibody with the anti-TENB2-MMAE ADC significantly reduced ADC uptake in the intestines (*206*). These approaches are analogous to 'cold' dosing prior to radiolabeled antibody distribution (*207*). Although some unconjugated antibodies in the clinic are given at high doses, such as bevacizumab (15 mg/kg) or IVIG (multiple grams per kg), it is important to consider that co-administration of the naked antibody at 3 to 8 times the ADC dose could reach dose-limiting toxicities in the clinic. However, antibodies such as trastuzumab are well-tolerated even when delivering 18 mg/kg over a 3 week period (*49*).

There are a couple important model limitations. First, the pharmacodynamics of the therapeutic can affect the pharmacokinetics of delivery in the tumor. This coupling of PK and PD makes simulations of efficacy very challenging. For example, it has been reported that

trastuzumab may result in vascular normalization (*149*), which can increase the functional vascular density in the tumor and lower the permeability of the vessels by making them less 'leaky.' Increasing the vascular density would result in a smaller Krogh cylinder radius in the model resulting in less carrier antibody needed for saturation. Since antibodies are extravasation/permeability limited, a decrease in the membrane permeability would result in less antibody extravasating out of the vessel (*150*). Additionally, vascular collapse and/or revascularization of areas (particularly during the 3 weeks between clinical treatment with T-DM1, for example) are difficult to predict. The second limitation is the impact of bystander effects. For T-DM1, the more hydrophilic nature of the metabolite results in few bystander effects (relative to more lipophilic conjugates that can diffuse out of the original targeted cell (*25*) or from the interstitium (*208*) and into a local cell (*13*)). Cytosolic access of hydrophilic metabolites may even require transporters within the target cell for toxicity (*209*). Bystander effects from more lipophilic payloads such as MMAE may explain why higher DAR can improve efficacy with the same antibody dose (e.g. (*210*)), while in the examples above with a hydrophilic payload, it had little benefit. The diffusion of the metabolite in the tissue could be incorporated into this model to predict the additional penetration of the metabolite into tumor tissue as a function of lipophilicity (*81*) and whether this reaches therapeutic concentrations far from the original site of antibody degradation. Finally, a recent study by Müller et al. showed that effector functions of T-DM1 (and not trastuzumab) could activate the immune system, where T-DM1 increased tumor vulnerability to immune attack (*211*). Modeling these complex immune interactions is difficult, but the simulations can help design experiments to test the overall impact on efficacy.

5.6 Conclusion

In conclusion, the multi-scale PBPK-Krogh cylinder model is able to track both the systemic and tissue scale distributions of antibodies and ADCs. We show that at clinical doses T-DM1 exhibits a heterogeneous perivascular distribution and through co-administration of trastuzumab the effective DAR is lowered and a homogeneous distribution is achieved. Modeling both the systemic and tissue level distribution can provide a facile method to facilitate ADC development by quantitatively combining complex factors such as target, linker stability, DAR, small molecule, and antibody backbone and their impact on efficacy.

5.7 Experimental Methods

In Vivo Experimental Work

T-DM1 and trastuzumab were obtained through the University of Michigan Pharmacy. Alexa Fluor 680 (AF680) was conjugated to T-DM1 following the manufacturer's instructions and as previously described (*113*). For reactions, a molar ratio of 0.7 was used that resulted in an overall degree of labeling of 0.3 to mitigate any potential physicochemical effects from the dye on the antibody. Conjugates were run on SDS-PAGE and scanned on an Odyssey CLx NIR scanner to ensure free dye was removed.

Animal studies were approved and conducted in accordance with University of Michigan University Committee on Use and Care of Animals (UCUCA). NCI-N87 cells were obtained from ATCC and were grown in RPMI-1640 containing 10 % (v/v) FBS, 50 U/ml penicillin, and 50 μg/ml streptomycin. Tumor xenograft studies consisted of $5x10^6$ NCI-N87 cells inoculated in the rear flanks of nude mice. Tail vein injections were done approximately 4 weeks after

inoculation when the longest axis of the tumor was approximately 10-12mm. Tail vein injections consisted of 3.6 mg/kg of T-DM1-AF680 and either 0, 10.8, or 28.8 mg/kg of unlabeled trastuzumab.

Plasma clearance was measured via retroorbital sampling, mixed with 15 μL of 10mM EDTA in PBS per 10 μL of whole blood, centrifuged (1 min, 3000xg), and scanned in a 384 well plate with the Odyssey CLx. Signal intensity was converted to absolute concentration using calibration curves of known concentrations of each agent in plasma and fit using a biexponential decay in PRISM. Animals were euthanized after 24 hours (the time of maximum tumor uptake, data not shown and (*36*)) for biodistribution and histology measurements.

The biodistribution protocol was adapted from previously published protocols (*53*,*122*). Briefly, after the animals were euthanized, organs were resected, weighed, and homogenized. Homogenization consisted of incubating with a RIPA buffer/PBS mixture supplemented with 6mg/mL collagenase IV solution, cell disruption using FB-120 Sonic Dismembrator, and further incubation with a RIPA buffer/0.05% trypsin-EDTA solution. After homogenization, each organ was serially diluted in a 96 well plate and scanned using the Odyssey CLx scanner. The percent-injected dose per gram (%ID/g) was determined by comparing signal from the Odyssey CLx scanner to a calibration curve and then normalizing by organ weight and homogenate volume. A density of 1g/mL was assumed for each tissue.

To quantify the tumor distribution of the antibodies, nude mice bearing NCI-N87 xenografts were euthanized 24 hours after tail vein injection of antibody, and the tumors were

resected and flash frozen in OCT using isopentane chilled on dry ice. Histology slices (16 micron) were imaged with an upright Olympus FV1200 confocal microscope using 405, 542, and 635 lasers, and a 20x objective. Sixteen micron sections were used relative to the more typical 5 micron slices to improve signal-to-noise from the NIR fluorescence imaging. High-resolution images of organs were obtained using a series of stitched smaller images and the Olympus software. Immunofluorescence staining was done using CD31 conjugated with Alexa Fluor 555. All confocal images were exported and analyzed using ImageJ image analysis software.

PBPK Model

For this study, the PBPK model was adapted from Ferl et al. (*60*). A graphical depiction of the model is shown in Figure 5.1. Changes from this previously published and validated model were as follows. Heart and lung compartments were added and follow the general structure of the other organ compartments. Physiologic parameters for the heart and lung were taken from Baxter et al. (*155*). The PBPK tumor compartment was removed and instead represented using a distributed parameter model with Krogh cylinder geometry (described below). Each organ compartment was divided into vascular, interstitial, and metabolite subcompartments, and the carcass contained an endothelial subcompartment for FcRn kinetics (Figure 5.1). All parameter values can be found in Appendix B and model equations can found in Appendix C. Other changes from the original PBPK model include changing the permeability surface area product for large and small pores to values for intact IgG. The model was constructed for both unconjugated antibodies and ADCs to simulate the distribution of each individually.

Robust predictions of the whole animal distribution of biologics are not yet possible, so several agent specific parameters not found in the literature were fit to experimental data using Matlab as shown in Table 1. These parameters are the degradation rates for the liver ($k_{deg,liver}$), degradation rate in all other organs ($k_{deg,organ}$), the metabolite urinary excretion rate (U) and metabolite loss rate (k_{loss}). Percent coefficient of variation (%CV) values and 95% confidence intervals (95% C.I.) for these fitted parameters are listed in Table 5.1.

Tissue Disposition Model

A tissue distribution model based on previously published work (*43*,*81*,*90*) was incorporated into the PBPK model (Figure 5.1). This modeling approach has been validated for the tissue distribution of antibodies and ADCs by our group and others (*43*,*90*,*176*,*177*,*179*). Briefly, this model is based on the Krogh cylinder geometry of tumor blood vessels. Because antibodies are permeability limited, a one-dimensional model with only radial gradients was used. The model consisted of free antibody, free ADC, free target, bound antibody, bound ADC, internalized antibody, and internalized ADC. Detailed equations and parameter values can be found Appendix B and C, and Table 5.2, but briefly, trastuzumab and T-DM1 extravasate from a blood vessel and are free to diffuse and bind to HER2 receptor in the tissue, upon which they are internalized and degraded. These molecules compete for the same pool of HER2, and after internalization, HER2 recycles back to the cell surface, consistent with experimental studies (*124*). The tissue disposition model is connected to the PBPK model by the entering and exiting plasma concentrations adjusted by the efflux into the tumor to capture any target-mediated drug disposition effects (*212–214*). Importantly, all parameters in the Krogh cylinder were taken from the literature and were not changed or fit to data.

Chapter 6

Improved Tumor Penetration and Single-Cell Targeting of Antibody Drug Conjugates Increases Anticancer Efficacy and Host Survival

6.1 Publication Information

Cilliers, C., B. Menezes, I. Nessler, J. Linderman, and G. M. Thurber. *Improved Tumor Penetration and Single-Cell Targeting of Antibody Drug Conjugates Increases Anticancer Efficacy and Host Survival*. Cancer Research. 2018; 78(3): 758-68.

Modifications have been made to the published document to adapt the content to this text. The previous chapter outlined a dosing strategy of coadministering trastuzumab with a constant dose of T-DM1 to improve T-DM1 tumor penetration. In this chapter, the dosing strategy is tested *in vivo* and, for the first time, is shown to result in significantly improved efficacy in a trastuzumab resistant mouse model.

6.2 Abstract

Current antibody-drug conjugates (ADC) have made advances in engineering the antibody, linker, conjugation site, small molecule payload and drug-to-antibody ratio (DAR). However, the relationship between heterogeneous intratumoral distribution and efficacy of ADC is poorly understood. Here we compared trastuzumab and ado-trastuzumab emtansine (T-DM1) to study the impact of ADC tumor distribution on efficacy. In a mouse xenograft model insensitive to trastuzumab, co-administration of trastuzumab with a fixed dose of T-DM1 at 3:1 and 8:1 ratios dramatically improved ADC tumor penetration and resulted in twice the improvement in median survival compared to T-DM1 alone. In this setting, the effective DAR

was lowered, decreasing the amount of payload delivered to each targeted cell but increasing the number of cells that received payload. This result is counterintuitive because trastuzumab acts as an antagonist in vitro and has no single-agent efficacy in vivo, yet improves the effectiveness of T-DM1 in vivo. Novel dual-channel fluorescence ratios quantified single-cell ADC uptake and metabolism and confirmed that the in vivo cellular dose of T-DM1 alone exceeded the minimum required for efficacy in this model. Additionally, this technique characterized cellular pharmacokinetics with heterogeneous delivery after one day, degradation and payload release by two days, and in vitro cell killing and in vivo tumor shrinkage 2-3 days later. This work demonstrates that the intratumoral distribution of ADC - independent of payload dose or plasma clearance - plays a major role in ADC efficacy.

6.3 Background

Antibodies and antibody-drug conjugates (ADCs) make up the largest portion of the growing biologics market. Currently, there are over 50 FDA approved antibodies, and nearly 500 in the various stages of the clinical pipeline (*91*). Although there are currently over 70 ADCs in the clinical pipeline (*50*,*215*) only four, Adcetris, Besponsa, Mylotarg, and Kadcyla (T-DM1), are currently approved by the FDA. While these ADCs have had clinical success, the factorial optimization of the antibody, linker, conjugation site, small molecule payload, drug loading, and target selection make development of each ADC a unique challenge. Although there have been advances in engineering the biophysical characteristics to improve safety, stability, and develop more homogeneous products, ADCs continue to be limited by toxicity, which is typically driven by the toxicity of the small molecule payload (*19*,*47*). In particular, several of the recent ADC failures may have been prevented by marginal gains in tolerability (*215*).

It is widely known that antibodies/ADCs exhibit heterogeneous distribution in solid tumors (*36*,*37*,*41*,*54*,*81*,*178*); however, it is not well understood how the heterogeneous tissue distribution of ADCs impacts their overall efficacy. ADC efficacy requires a multi-step process, which includes the distribution of intact ADC in the tumor, cellular uptake and degradation of the antibody, release of the small molecule payload, induction of apoptosis by the cytotoxin, and potentially bystander effects on neighboring cells (*25*,*216*,*217*). Therefore, there is a need to understand the ADC's effects from the subcellular scale (e.g. how many ADCs are required to achieve cell death *in vivo*) to the tissue level (e.g. how many cells in the tumor are receiving a therapeutic dose) to whole organ biodistribution (e.g. what is the healthy tissue exposure and resulting toxicity) in order to develop effective therapeutics.

Previously we developed a combined tissue and physiologically-based pharmacokinetic (PBPK) model to describe both the tumor and systemic distribution of T-DM1 (*106*). We found that co-administration of trastuzumab with T-DM1 (trastuzumab linked to the payload DM1, which therefore competes for the same binding epitope of HER2) dramatically improved tumor penetration, but total tumor uptake of ADC was unchanged. Co-administration of trastuzumab with T-DM1 lowers the effective drug to antibody ratio (DAR) while competing with T-DM1 for HER2 receptors and driving penetration deeper into the tissue. The higher the trastuzumab dose, the farther the ADC will penetrate into the tumor; however, the average DM1 payload concentration in each targeted cell will be lower. Several studies in the literature demonstrate that cohorts of mice treated with ADCs having different DAR but the same overall payload dose (i.e. DAR2 given at 2 mg/kg vs. DAR4 given at 1 mg/kg) had better outcomes with the lower

DAR (and therefore higher antibody dose which correlates with better tumor penetration) (*106*). These results are consistent with tumor penetration playing a major role in efficacy independent of the target antigen, antibody, linker, payload, or bystander effects. However, these were not prospective studies, and although certain mechanisms, such as DAR-dependent clearance, did not appear to play a role in the analysis, they could have affected the data interpretation. Therefore, we wanted to design an experimental study to isolate the impact of distribution on efficacy.

Here, we demonstrate that co-administration of trastuzumab with T-DM1 improves efficacy (tumor growth reduction and overall survival as measured by tumor volume endpoint) in a trastuzumab-insensitive mouse xenograft model. Against trastuzumab-insensitive cell lines the addition of trastuzumab was antagonistic *in vitro* (i.e. lowered efficacy by blocking T-DM1 uptake), as expected. Counterintuitively, co-administration of trastuzumab (which acts as an antagonist *in vitro* and has no single-agent efficacy in this animal model *in vivo*) with T-DM1 showed a significant improvement in efficacy in a mouse xenograft model despite the same small molecule dose and tumor uptake as T-DM1 alone. In fact, the combination of trastuzumab, which had no single agent efficacy, and T-DM1 was synergistic, meaning the net improvement was greater than additive (since trastuzumab alone had no impact on efficacy in the absence of T-DM1). Histological imaging showed a significant increase in T-DM1 tumor penetration with the co-administered trastuzumab. Additionally, we present a novel near-infrared (NIR) fluorescence ratio technique with dually labeled ADCs to track the metabolism and distribution of ADCs at the single-cell level. Applying this technique to single agent T-DM1 therapy showed the delivery of ADC to cells within the targeted population *in vivo* was higher than the threshold

required for cell death, while the majority of tumor cells did not receive any ADC. These results demonstrate that the intratumoral distribution of ADCs in tumor tissue plays a major role in determining their efficacy independent of the amount of total tumor payload delivered. To our knowledge, this is the first time that the distribution itself, independent of the other parameters that affect efficacy and tumor penetration such as dose, plasma clearance, and molecular weight, significantly impacted survival.

6.4 Results

Co-Administration of Trastuzumab with T-DM1 Improves T-DM1 Tumor Penetration

ADC tumor distribution is dependent on many parameters including dose, DAR, systemic clearance, antigen expression and internalization rate in tumor (and healthy tissue), and the surface to volume (S/V) ratio of the vasculature. The clinical dose of T-DM1-AF680 (3.6 mg/kg) shows a heterogeneous, perivascular distribution in NCI-N87 tumor xenografts (Figure 6.1, Figure 6.2) consistent with high affinity antibodies that target highly expressed receptors and are dosed at subsaturating levels (*41*,*202*,*218*). Co-administration of unlabeled trastuzumab at 10.8 or 28.8 mg/kg (3:1 or 8:1, respectively) dramatically increases tumor penetration of a constant T-DM1 dose (Figure 6.1), allowing more cells to receive the cytotoxic payload. However, adding trastuzumab lowers the effective DAR, increasing the number of targeted cells while reducing the average number of payload molecules delivered per cell. Immunofluorescence staining with antihuman IgG Fc-488 shows antibody distribution is more homogeneous with increasing doses of trastuzumab (Figure 6.1). Similarly, increasing the dose of T-DM1 alone also improved tumor penetration (Figure 6.3), but this exceeds the maximum tolerated dose in humans. HER2 was stained ex vivo with trastuzumab-AF750 to ensure the heterogeneous distribution is not from

lack of available antigen (Figure 6.4). T-DM1 binding affinity was unchanged by fluorophore conjugation (Figure 6.5).

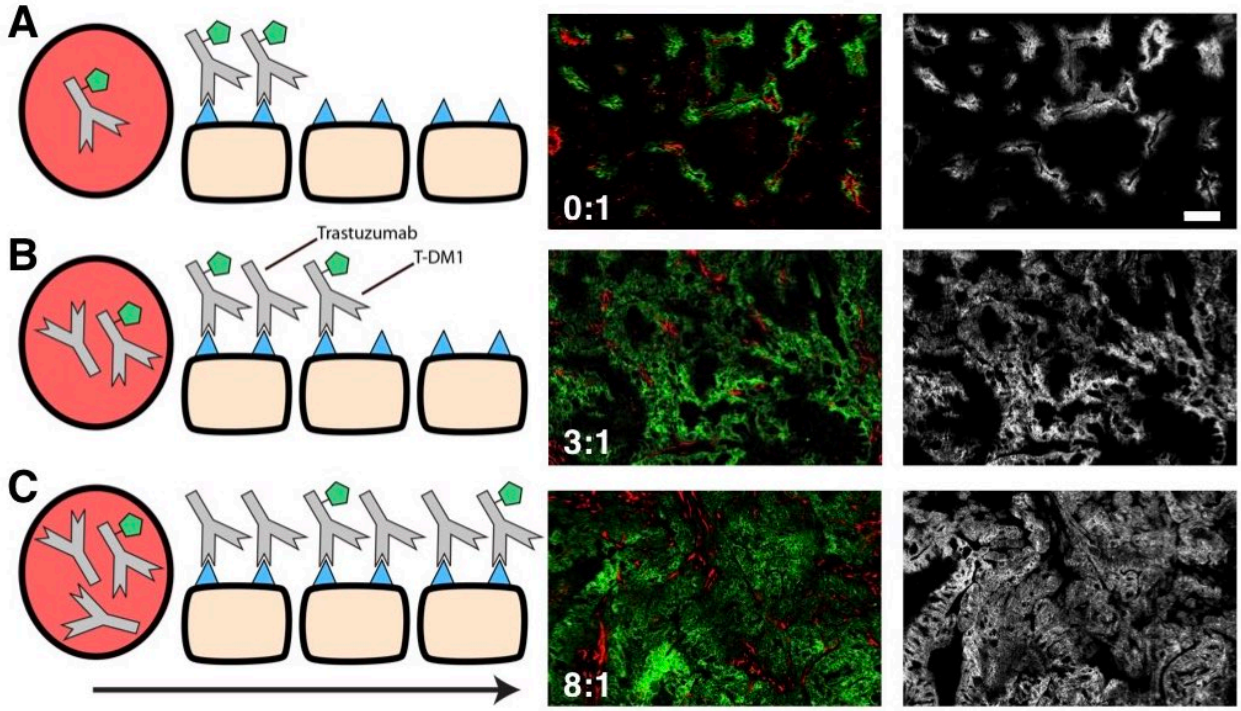

Figure 6.1 Improving T-DM1 tumor distribution through co-administration of trastuzumab.
Administration of T-DM1 at 3.6 mg/kg (single agent) results in a heterogeneous, perivascular distribution due to rapid binding relative to transport in the tissue (A). The tumor penetration of a constant dose of T-DM1 is improved when co-administered with a subsaturating (B) or saturating (C) dose of trastuzumab. Trastuzumab competes for binding sites, increasing T-DM1 penetration. The middle column shows distribution of AF680-labeled T-DM1 (*green*) at 3.6 mg/kg with unlabeled trastuzumab at 0:1, 3:1, and 8:1 trastuzumab:T-DM1 ratios (0, 10.8, and 28.8 mg/kg, respectively). Immunofluorescence staining with CD31-AF488 (*red*) shows the tumor vasculature. The right column shows immunofluorescence staining with antihuman IgG Fc-AF555 (*gray*). The window leveling between images is different since the intensity of the T-DM1 decreases with an increasing ratio while the anti-Fc staining labels both trastuzumab and T-DM1 thereby maintaining a constant intensity while the penetration increases (see Figure 6.2). Scale bar is 200 μm.

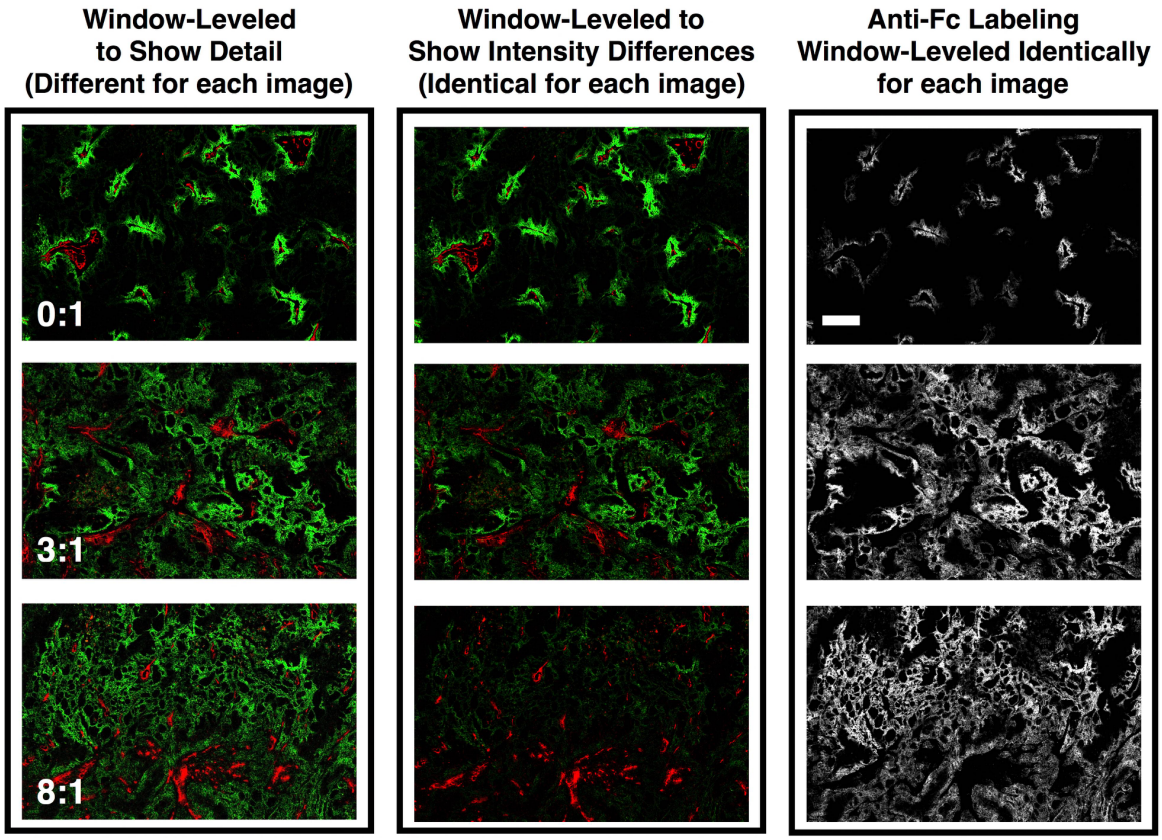

Figure 6.2 Improving T-DM1 tumor distribution through co-administration of trastuzumab.

Similar to Figure 6.1, administration of T-DM1 at 3.6 mg/kg (single agent) results in a heterogeneous, perivascular distribution due to rapid binding relative to transport in the tissue (top row). T-DM1 distribution is improved when co-administered with a subsaturating (middle row) or saturating (bottom row) dose of trastuzumab. The left and middle column shows distribution of AF680 labeled T-DM1 (green) at 3.6 mg/kg with unlabeled trastuzumab at 0:1, 3:1, and 8:1 trastuzumab:T-DM1 ratios (0, 10.8, and 28.8 mg/kg, respectively). Microscope settings and window leveling are identical for the top row, middle row, and bottom row images in the middle column to show differences in intensity (less ADC per targeted cell), while the images of the top, middle, and bottom rows of the left column are window leveled to highlight the better tumor penetration of ADC. Immunofluorescence staining with CD31-AF488 (red) shows the tumor vasculature. The right column shows immunofluorescence staining with antihuman IgG Fc-AF555 (gray). All tumors were resected 24 hours after injection. Scale bar is 200 μm.

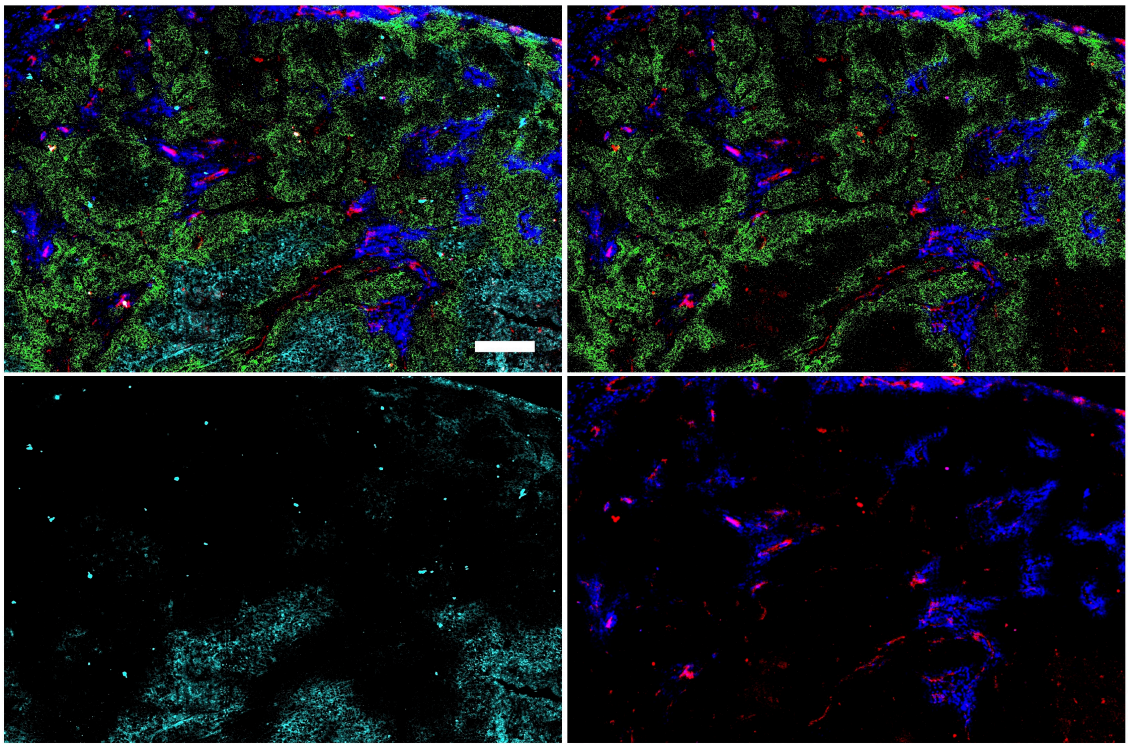

Figure 6.3 Immunofluorescence histology of T-DM1-800 (green) dosed at 14.4 mg/kg (same total antibody dose as 3:1 trastuzumab:T-DM1 ratio).
Hoechst 33342 (blue) was injected prior to sacrifice to stain functional vasculature as outlined in Materials and Methods. CD31-555 (red) and trastuzumab-AF488 (cyan) were stained ex vivo. Trastuzumab only binds free receptors in regions not targeted by T-DM1 at this time point. Similar to increasing the dose of trastuzumab, tumor penetration is improved with higher doses of single agent T-DM1. Although tumor penetration is improved with higher ADC doses, ADC toxicity limits the maximum tolerated dose. Top left, all stains; top right, T-DM1 (green), Hoecsht 33342 (blue), and CD31 (red); bottom left, free HER2 antigen (trastuzumab ex vivo, cyan); bottom right, Hoechst and CD31. Scale bar is 200 μm.

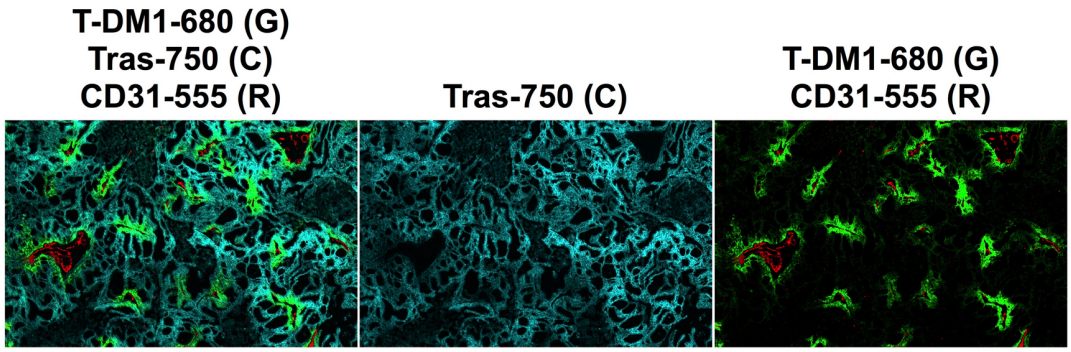

Figure 6.4 Immunofluorescence histology of HER2 antigen.
Slices were stained with trastuzumab-AF750 to ensure the perivascular distribution of T-DM1-AF680 was not from a lack of available antigen farther from the vessels. The left column shows a merge of T-DM1-680 (green), trastuzumab-750 (cyan), and CD31-555 (red). The middle and right columns show unmerged images of trastuzumab-750 and T-DM1-680 with CD31, respectively. Tras, trastuzumab; G, green; C, cyan; R, red.

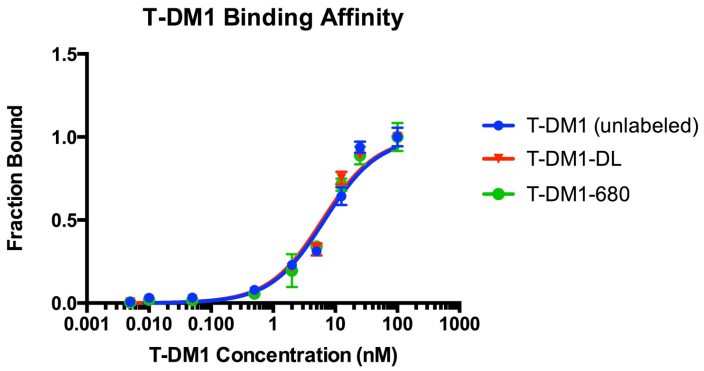

Agent	K_d (nM)
T-DM1 (unlabel)	6.7 ± 1.1
T-DM1-680	6.2 ± 1.0
T-DM1-DL	6.4 ± 0.9

Figure 6.5 T-DM1 dye conjugate binding affinity.
Conjugation of fluorophores to T-DM1 at a dye-to-protein ratio of 0.3 or less did not affect T-DM1 binding affinity. Binding affinity was performed as previously described (*93*,*137*). Briefly, concentrations of unlabeled antibody and antibody−dye conjugates were incubated with 50,000 HCC1954 cells on ice for 3 hours and washed with PBS. After the primary incubation, cells were further incubated with antihuman IgG Fc-AlexaFluor488 at 40 nM for 30 minutes on ice, then washed with PBS, and subsequently analyzed on an Attune Focusing Cytometer (Applied Biosystems). K_d was calculated using PRISM and is reported as K_d ± standard error. DL, dual-label (both IRDye and DDAO); 680, AlexaFluor680.

T-DM1 is Effective In Vitro When Occupying Only a Fraction of HER2 Receptors Even Under Saturating Antibody Conditions

The increasing doses of trastuzumab improve T-DM1 penetration into tumor tissue but lower the DM1 payload delivery by competing with HER2 receptors. To determine if the lower payload delivery was still sufficient to kill cells in vitro, we measured efficacy with T-DM1 alone or a saturating combination of total antibody (T-DM1 + trastuzumab) while varying the T-DM1 to trastuzumab ratio. Toxicity assays with trastuzumab alone showed only slight growth inhibition at the highest concentrations (Figure 6.6), consistent with literature reports that the NCI-N87 cell line is sensitive to T-DM1, while trastuzumab has a slight growth inhibitory effect in vitro (*219*). We measured the toxicity of T-DM1 in vitro with the NCI-N87 and HCC1954 cell lines and we found IC50 values of 82 and 33 pM for NCI-N87 and HCC1954 (Figure 6.7), respectively, consistent with other reports (*148*,*190*). Next, we performed toxicity assays with fluorescently tagged T-DM1-AF680 and examined cellular uptake of T-DM1 by flow cytometry. The IC50 for each cell line was much less than the concentration needed for half of the normalized uptake, indicating that complete surface receptor saturation is not needed for T-DM1 cytotoxicity in vitro. Additionally, we found that fluorophore conjugation had no impact on T-DM1 cytotoxicity in vitro (Figure 6.8). The maximum cellular uptake occurred at concentrations below the K_d (1.8 nM (*137*)), indicating treatment likely impacts uptake over this time scale. To mimic the effect of co-administering trastuzumab in vivo, we performed toxicity assays where the T-DM1 concentration was varied, but the total antibody concentration was kept constant at 10 nM (saturating) to see how competition for receptors would affect toxicity (Figure 6.7). T-DM1 still showed toxicity below the antibody K_d against both cells lines with the addition of trastuzumab, although the IC50 was higher likely due to competition from the trastuzumab.

Using a simple competitive inhibition binding model, we found that T-DM1 cytotoxicity was similar when adjusting for the fraction of receptors bound by T-DM1 (Figure 6.9). Additionally, a similar number of molecules of T-DM1 were required to achieve 50% cell death in both cases (Figure 6.10). Because trastuzumab increases the penetration (while lowering the single-cell delivery) of T-DM1 and T-DM1 remains toxic at sub-saturating conditions, we tested the efficacy of this combination in a trastuzumab-insensitive mouse xenograft model.

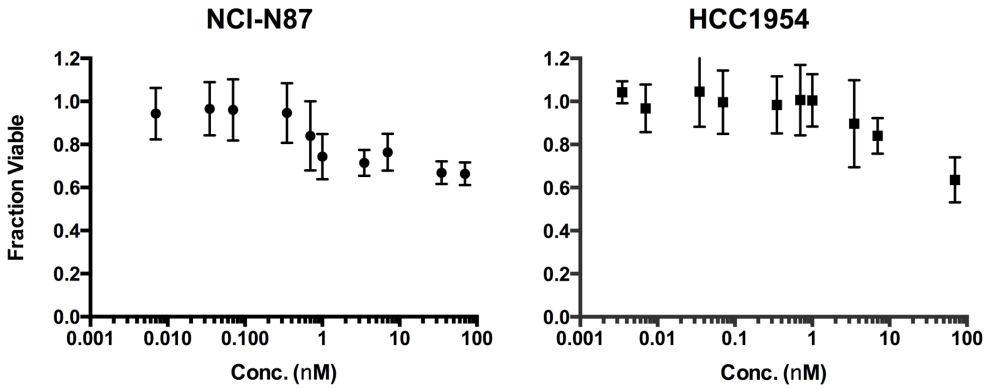

Figure 6.6 In vitro toxicity of trastuzumab alone.
NCI-N87 and HCC1954 cells were incubated with trastuzumab titrations over 6 days. Consistent with literature reports that these cell lines are resistant to trastuzumab, both cell lines showed only limited growth inhibition at the highest concentrations.

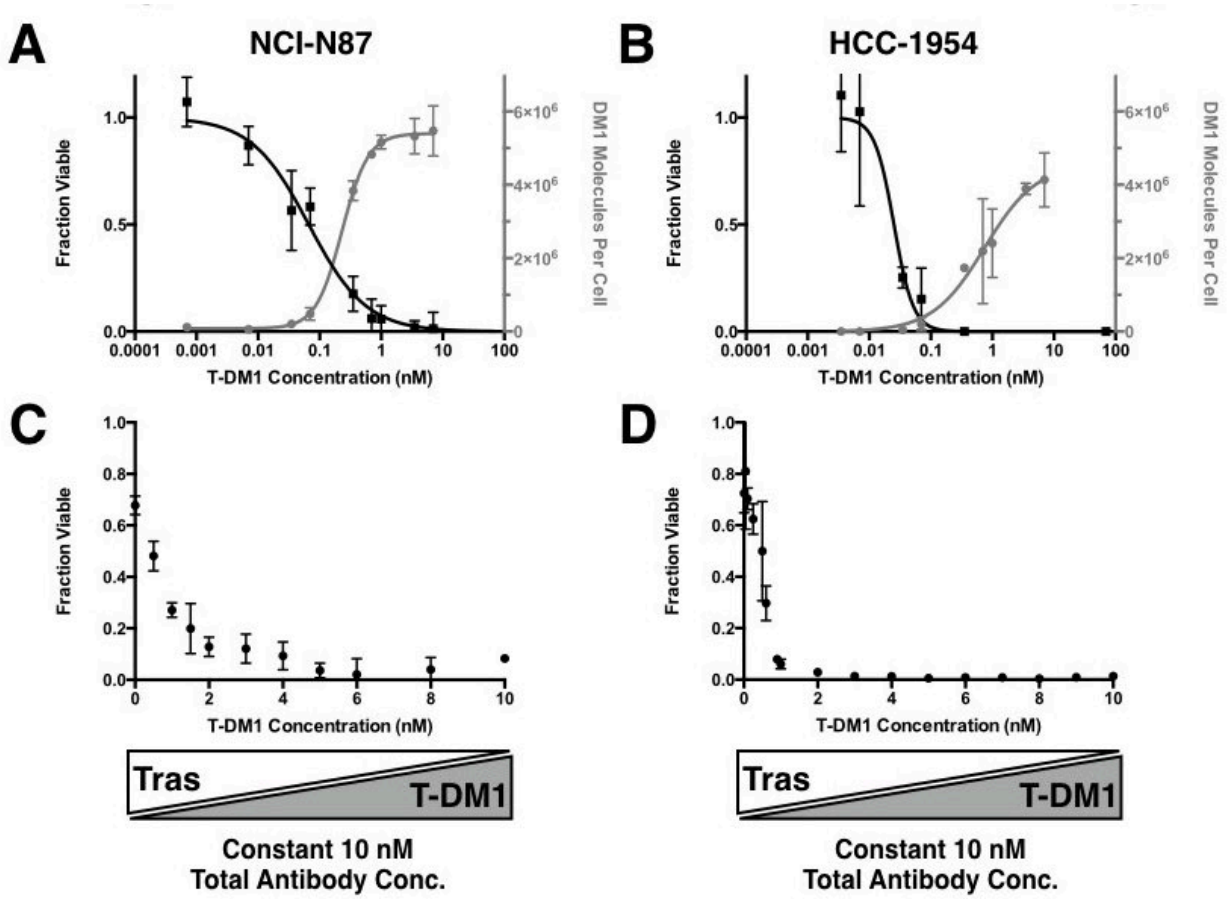

Figure 6.7 *In Vitro* Cytotoxicity.
(A, B) *in vitro* cytotoxicity of T-DM1 against NCI-N87 (A) and HCC1954 (B) cell lines. Assays were performed in triplicate and average IC50's were 82 ± 10 pM and 33 ± 20 pM for NCI-N87 and HCC1954 cell lines, respectively. The number of DM1 molecules per cell (*gray*) was estimated by measuring T-DM1-680 uptake with flow cytometry and quantitative beads. (C, D) *in vitro* cytotoxicity varying the T-DM1 concentration, while keeping total antibody concentration (T-DM1 + trastuzumab) constant at 10 nM. Cells were incubated with T-DM1 and/or trastuzumab in media for 6 days and media was replaced daily for all *in vitro* cytotoxicity assays. Data plotted as mean ± standard deviation.

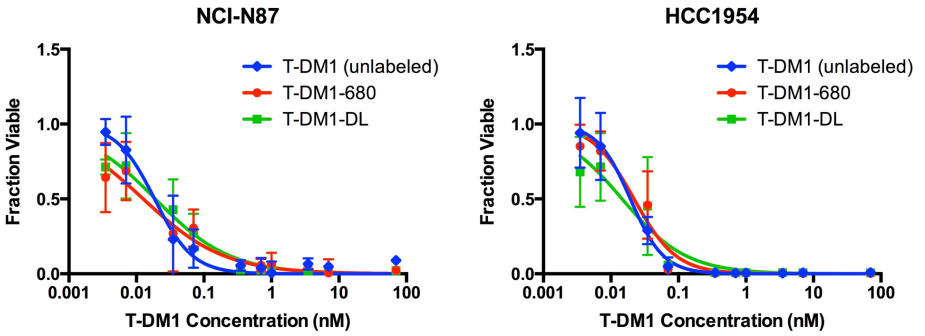

ADC Dye Conjugate	IC50 (pM)	95% Confidence Intervals (pM)
T-DM1 (unlabel)	19	14 to 25
T-DM1-680	13	8 to 21
T-DM1-DL	19	14 to 26

ADC Dye Conjugate	IC50 (pM)	95% Confidence Intervals (pM)
T-DM1 (unlabel)	19	17 to 22
T-DM1-680	22	15 to 32
T-DM1-DL	15	9 to 25

Figure 6.8 Dye conjugation to T-DM1 does not affect in vitro cytotoxicity.
Similar to Figure 6.7, NCI-N87 (left) and HCC1954 (right) cells were incubated with varying concentrations of T-DM1 or T-DM1 dye conjugates for six days, replacing the media daily. IC50 and 95% confidence interval was estimated using PRISM and is reported below each plot. DL, dual-label (both IRDye and DDAO); 680, AlexaFluor680.

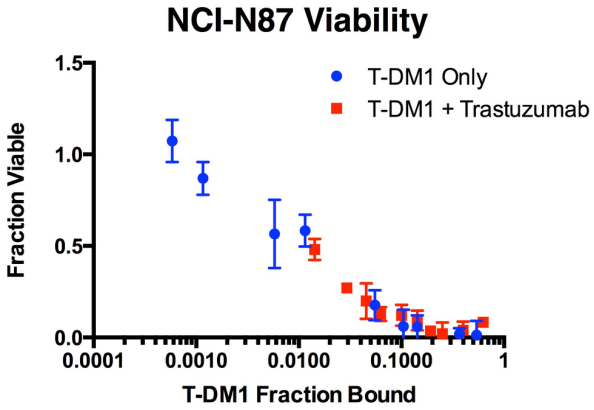

Figure 6.9 NCI-N87 cell viability data fit with a competitive binding model.
Using the affinity data from Figure 6.5 and our previous work with trastuzumab (*137*), we estimated the fraction bound of T-DM1 alone and T-DM1 with trastuzumab (Figure 6.7) using a simple competitive inhibition binding model. Although adding trastuzumab increased the IC50 in Figure 6.7, cell viability was similar when adjusting to the fraction of receptors bound by T-DM1.

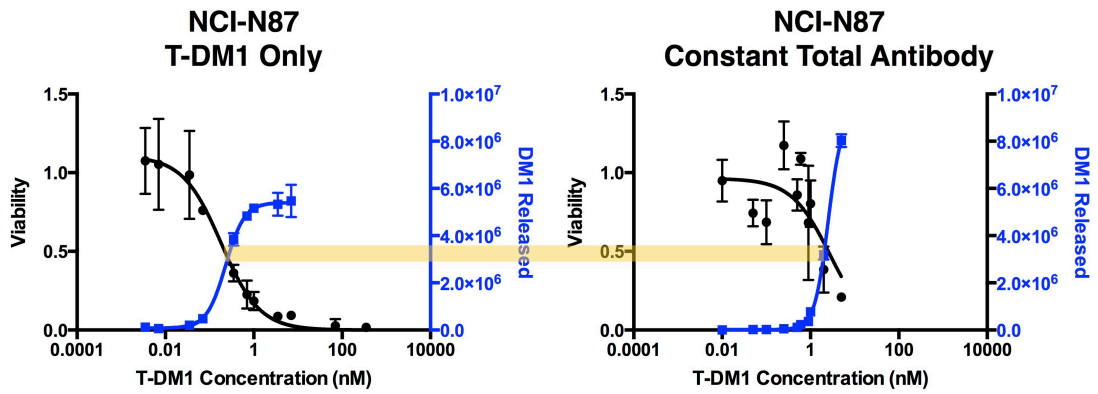

Figure 6.10 NCI-N87 cell uptake and viability.
Similar to other cytotoxicity assays, NCI-N87 cells were incubated with varying concentrations of T-DM1-680 for six days. Viability was measured using the PrestoBlue assay (Materials and Methods) and then cells were analyzed by flow cytometry to determine AF680 fluorescence signal. Quantitative beads were used to convert fluorescence signal to absolute number of molecules (and adjusting for the drug antibody ratio (DAR) and fluorophore degree of labeling (DoL). In both the T-DM1 alone and T-DM1 plus trastuzumab (constant 10 nM total antibody) cases, approximately 3.5 million molecules of DM1 are needed to achieve 50% cell killing. This agrees with Figure 6.9, where cell killing is determined by the amount of internalized T-DM1 and the amount of payload needed for cell death is not impacted by the presence or absence of trastuzumab.

Addition of Trastuzumab (an In Vitro Antagonist) to T-DM1 Therapy Improves In Vivo Efficacy in a Trastuzumab Resistant Xenograft Model

To examine the impact of ADC tumor distribution on efficacy, we administered a fixed dose (3.6 mg/kg) of T-DM1 with varying ratios of trastuzumab in an NCI-N87 tumor xenograft mouse model. Non-fluorescently labeled (clinical) T-DM1 and trastuzumab were used for in vivo efficacy studies. We selected the NCI-N87 cell line because a) it was less sensitive than the HCC1954 cell line to T-DM1 in vitro (Figure 6.7) and in vivo (*190*) providing more room to detect improvements in efficacy, and b) other groups have shown that at moderate doses, like the ones used in this study, trastuzumab treatment did not significantly alter tumor growth from control (*219*,*220*). Trastuzumab treatment results in modest (but statistically significant) growth inhibition at higher dosages (>60 mg/kg total dose) but does not result in tumor reduction even at highest doses of 280 mg/kg total dose over several weeks (*220–222*). Additionally, we chose to

use large established tumors that were 250 mm^3 or greater. Others have shown antibody-dependent cell-mediated cytotoxicity (ADCC) is reduced in larger established tumors, albeit with a different HER2 expressing cell line (*223*). Expectedly, the clinically approved T-DM1 therapy alone showed significant improvement over control (Figure 6.11). Although others have shown complete tumor regression using T-DM1 (*148*), the larger tumors and single administration prevented consistent cures. Addition of trastuzumab to T-DM1 resulted in slower tumor growth than T-DM1 alone for all dosage levels (Figure 6.11), with 3:1 and 8:1 (T:T-DM1) ratios having a statistically significant effect. The 3:1 and 8:1 dosing levels had several more partial responses and exhibited a statistically significant increase in survival with increasing trastuzumab doses (Figure 6.11). Kaplan-Meier survival plots with 95% confidence intervals calculated by PRISM and individual tumor growth curves are shown in Figure 6.12 and Figure 6.13, respectively. Animals receiving trastuzumab only were similar to saline control demonstrating that trastuzumab has no direct effect on efficacy at these doses. Additionally, mice receiving treatment were weighed over the course of the study and showed comparable tolerability (Figure 6.14), consistent with the payload and not the antibody dose driving toxicity. Since trastuzumab is tolerated at much higher doses than T-DM1 (*49*) and the same T-DM1 dose was given, all treatments were consistently well tolerated.

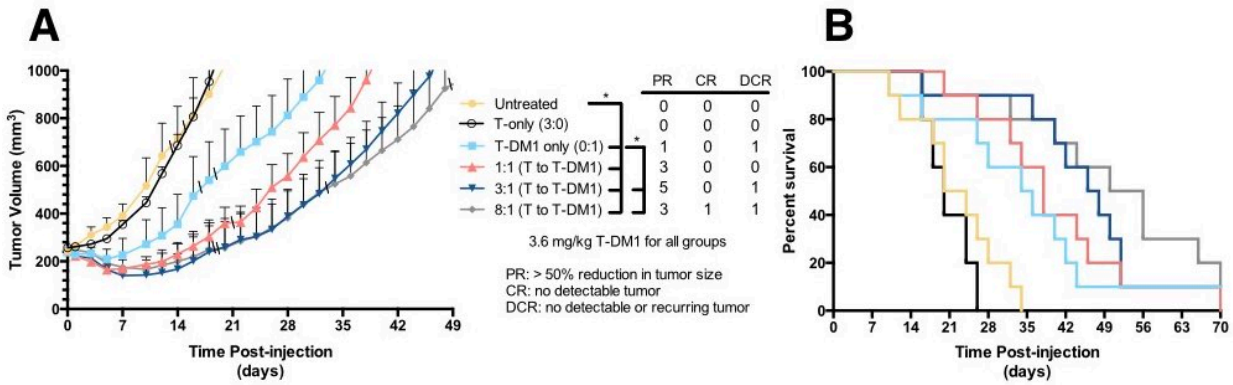

Figure 6.11 KEY FIGURE: Co-administration of trastuzumab with T-DM1 results in a significant reduction in tumor growth compared to T-DM1 alone.

(A) Tumor growth curves for mice bearing NCI-N87 tumor xenografts following treatment with a single administration of saline, single-agent trastuzumab (10.8 mg/kg), single-agent T-DM1 (3.6 mg/kg), or co-administration of trastuzumab and T-DM1 at 1:1, 3:1, and 8:1 dosage levels (T-DM1 constant at 3.6 mg/kg, trastuzumab varied at 3.6, 10.8, and 28.8 mg/kg). Non-fluorescently labeled T-DM1 and trastuzumab were used for tumor growth experiments. Data plotted as mean ± standard error. The number of partial responses, complete responses, and durable complete responses is tabulated. (B) Kaplan-Meier survival curves of time to progression to 1000 mm^3. Survival curves were analyzed by log-rank test (significance level of $p \leq 0.05$). All treatments except single-agent trastuzumab resulted in statistically significant improvements in survival ($p = 0.0442, 0.0021, 0.0006, 0.001$ for 0:1, 1:1, 3:1, 8:1, respectively). The 3:1 and 8:1 treatments significantly improved survival over the single-agent T-DM1 ($p = 0.0486, 0.0484$ for 3:1 and 8:1, respectively). N = 10 for each treatment. T, trastuzumab; PR, partial response; CR, complete response; DCR, durable complete response.

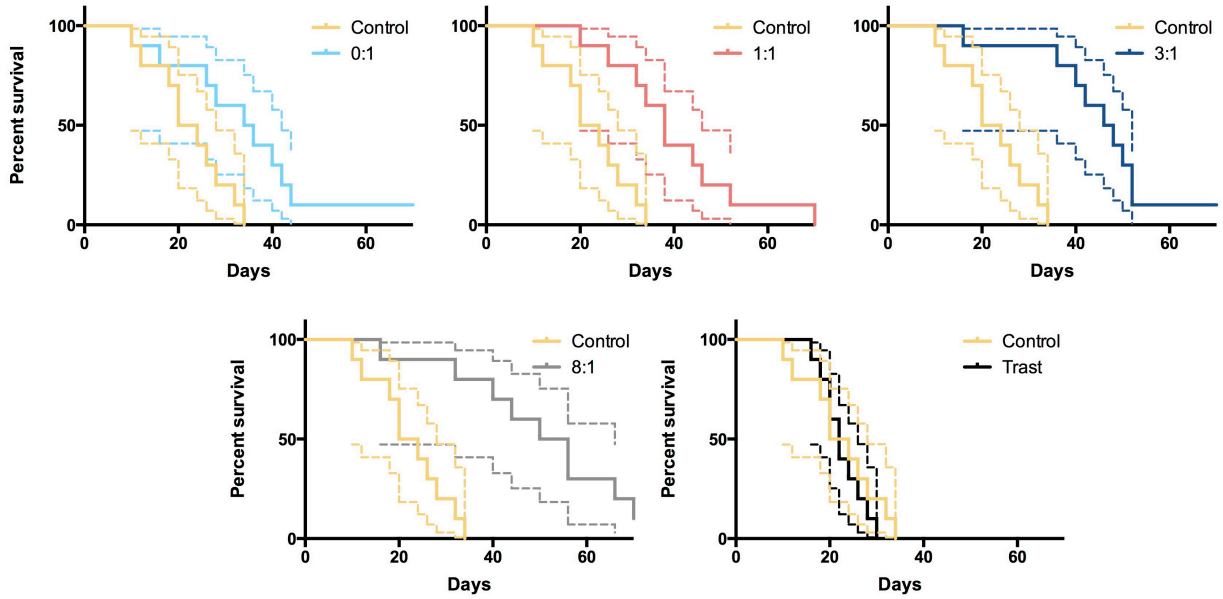

Figure 6.12 Individual Kaplan-Meier curves with 95% confidence interval generated using PRISM software.

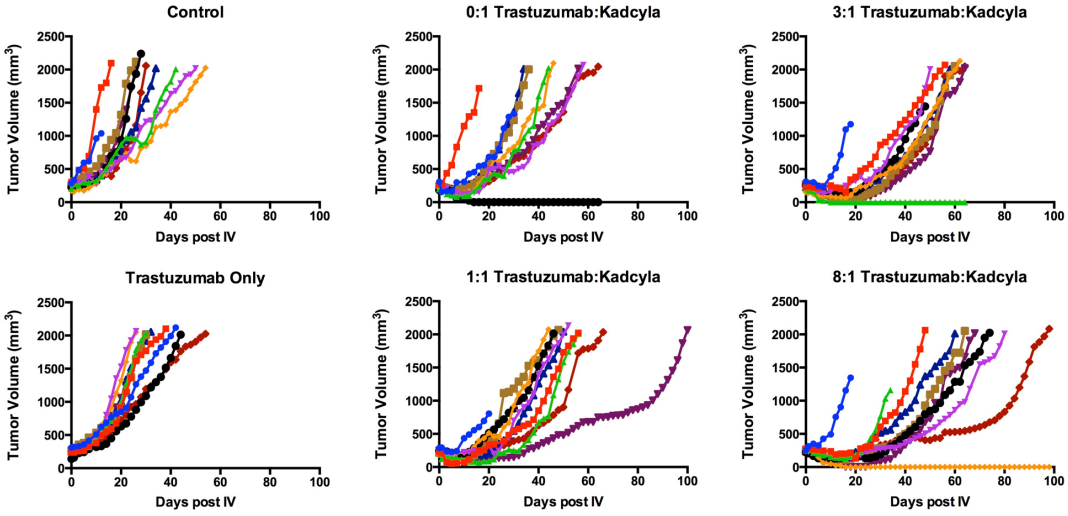

Figure 6.13 Individual tumor growth curves for all animals.

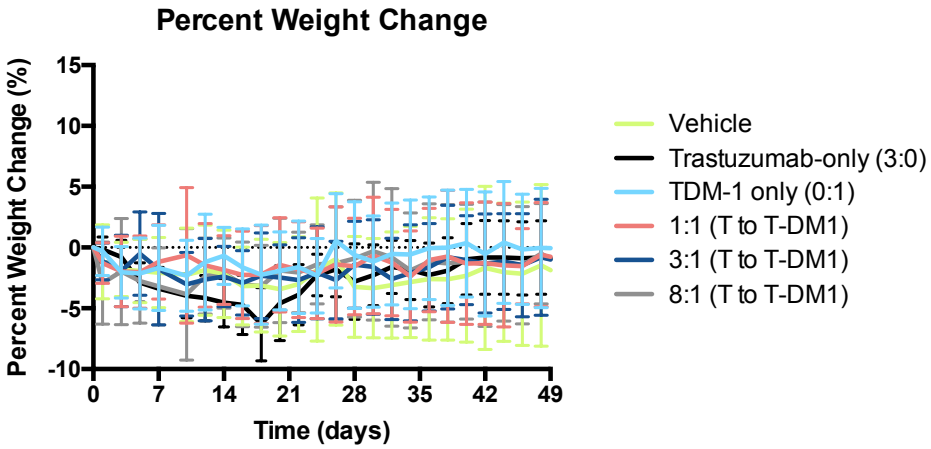

Figure 6.14 Percent weight change during treatment.
All treatments were well tolerated and no significant differences in mouse weight were encountered between treatments.

Single-Cell T-DM1 Uptake and Metabolism In Vivo Highlights a Fraction of Cells with Higher Delivery than Needed for Cell Killing While Other Cells Receive Negligible T-DM1

The fluorescence histology images (Figure 6.1) qualitatively show better penetration, but they cannot be used to quantify payload delivery. We utilized a novel NIR fluorescence ratio technique to determine the absolute uptake and payload delivery per cell in vivo. In particular, we applied the technique to single agent T-DM1 therapy to confirm that targeted tumor cells were receiving more payload than necessary to achieve cell death and the lack of tumor penetration was limiting efficacy in vivo. Figure 6.15 shows a graphic depiction of the technique. Two NIR fluorescent dyes, DDAO and IRDye, were chosen because of their widely differing residualization rates (*113*). The non-residualizing dye rapidly leaks out of the cell upon degradation, thereby approximating intact protein, while the residualizing dye is trapped in the cell, approximating cumulative ADC uptake. This approach is analogous to radiolabeling with ^{125}I as the non-residualizing probe and ^{111}In as the residualizing probe (*60*).

To visualize the change in fluorescence ratio and validate the method in vitro, cells were imaged using a confocal microscope after pulsing with labeled ADC for 30 minutes at different times over 48 hours. Figure 6.15 shows separate and merged channels for DDAO (red) and IRDye (green) for dually labeled T-DM1. Initially, DDAO and IRDye are only seen on the surface. As ADC is internalized and degraded, however, the DDAO signal gradually decreases, while IRDye forms punctate spots in lysosomes. Figure 6.15 shows the fraction intact of T-DM1 for HCC1954 (black) and NCI-N87 (grey) cell lines over time. Although both express the same antigen, the HCC1954 cell line degraded T-DM1 slightly faster than the NCI-N87 cell line. To quantify the kinetics of cell death following cell targeting, we measured the viability of both cell lines over six days (Figure 6.15). Consistent with the faster T-DM1 degradation of HCC1954 cells and published link between intracellular payload concentration and toxicity (*25*), their viability decreased more quickly than NCI-N87 cells. We used flow cytometry to quantitatively measure the cellular signal for DDAO and IRDye over time at the single-cell level (Figure 6.15). Initially the ADC is intact and the cell population is positive for DDAO and IRDye. Over time there is a gradual shift to DDAO(-)/IRDye(+), indicating that the ADC is degraded and DDAO has washed out.

After demonstrating the NIR fluorescence ratio technique in vitro, we applied the technique in vivo. Mice were injected via tail-vein with 100 μg (~4 mg/kg) of dually labeled T-DM1 and euthanized at 24, 48, and 72 hours. Then tumors were resected and digested into a single cell suspension and analyzed by flow cytometry (Figure 6.16). Representative flow cytometry plots of single cell tumor digests are shown in Figure 6.16. 24 hours post injection, targeted cells (IRDye(+)) show mostly intact protein (DDAO(+)/IRDye(+)) because there is a

constant supply of intact ADC from the blood. However, by 48 and 72 hours there is a shift from DDAO(+)/IRDye(+) to DDAO(-)/IRDye(+) for the targeted cells, indicating that much of the surface bound ADC was internalized and degraded. Additionally, consistent with the tumor histology (Figure 6.1), only a small fraction of cells in the tumor (around 10% according to flow cytometry and consistent with histology and a ~10-fold higher dose for saturation) are targeted with ADC, despite administering the clinical dose. Because IRDye is a residualizing dye and approximates the cumulative uptake of ADC (*113*), we used quantitative beads to convert the IRDye signal from targeted cells into the number of ADCs per cell. Combining the number of ADCs targeted per cell with the percent intact, we estimated the number of DM1 payload molecules released in targeted cells (Figure 6.16). Consequently, the amount of DM1 released increased dramatically between 24 and 48 hours and started to plateau by 72 hours.

In addition to single cell tumor metabolism from flow cytometry, the NIR fluorescence ratio technique was used to measure the biodistribution of ADC in the same animals (Figure 6.16) to verify the normal systemic distribution of the antibodies. The reduced autofluorescence in the near infrared window makes IRDye an appropriate dye for biodistribution studies (*53*,*107*,*137*). We have previously shown that at a dye to protein ratio of 0.3 or less there is no impact on protein pharmacokinetics over the first 3-4 days (*137*). The plasma clearance of dually labeled trastuzumab was similar to trastuzumab-IRDye, indicating the addition of the DDAO fluorophore did not impact clearance (Figure 4.1). The biodistribution of dually labeled T-DM1 shows primarily liver and tumor uptake and is similar to radiolabeling studies of trastuzumab, albeit with lower tumor uptake in this model (*224*). Consistent with the single cell flow

cytometry data, the maximum tumor uptake was reached 24 hours after injection and there was a gradual decrease at 48 and 72 hours (Figure 6.16).

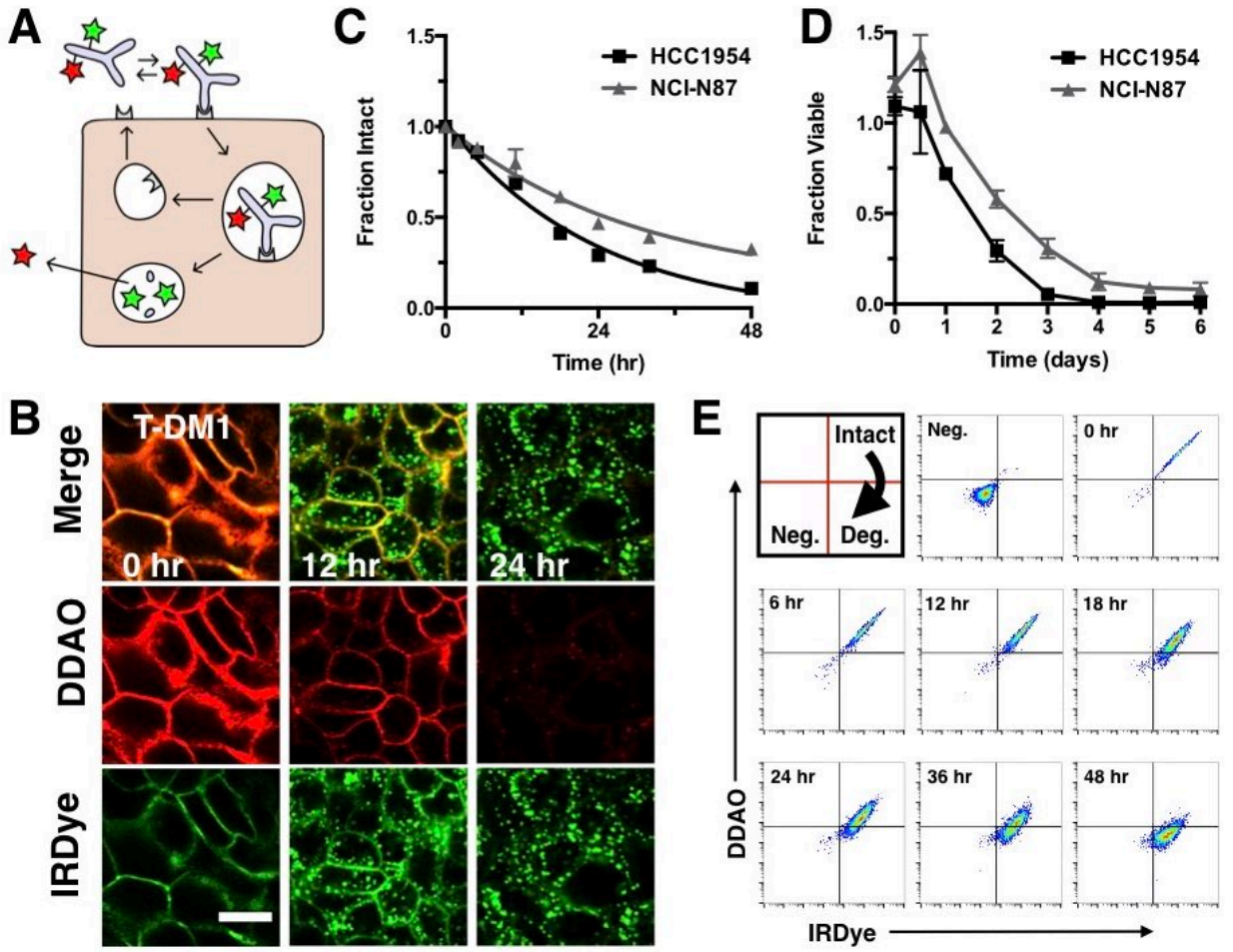

Figure 6.15 *In vitro* T-DM1 metabolism and pharmacodynamics.
(A) A graphic depiction of the NIR fluorescence ratio technique. The dually labeled antibody binds the target, is internalized, and degraded. The non-residualizing DDAO (red star) leaks out of the cell, while the residualizing IRDye800CW (green star) is trapped within in the cell. (B) Representative confocal images of dually labeled T-DM1. DDAO (red) shows cell surface labeling with a loss of signal over time. IRDye (green) shows initial cell surface labeling followed by the formation of punctate spots as it is trapped in the lysosomes. Scale bar is 10 μm. (C) T-DM1 metabolism. Fraction of intact ADC following pulse of dually labeled T-DM1 for HCC1954 (*black*) and NCI-N87 (*gray*) cells. Data plotted as mean ± standard deviation. (D) Timing of T-DM1 pharmacodynamics. The fraction of viable cells over time for HCC1954 (*black*) and NCI-N87 (*gray*) cells when treated with a constant 5 nM T-DM1. Non-fluorescently labeled (clinical) T-DM1 was used for this assay. Data plotted as mean ± standard deviation. (E) Representative flow cytometry plots of dually labeled T-DM1 gated on cells. Intact dually labeled T-DM1 appears in DDAO(+)/IRDye(+) quadrant. Over time as ADC is degraded there is a gradual shift towards DDAO(-)/IRDye(+).

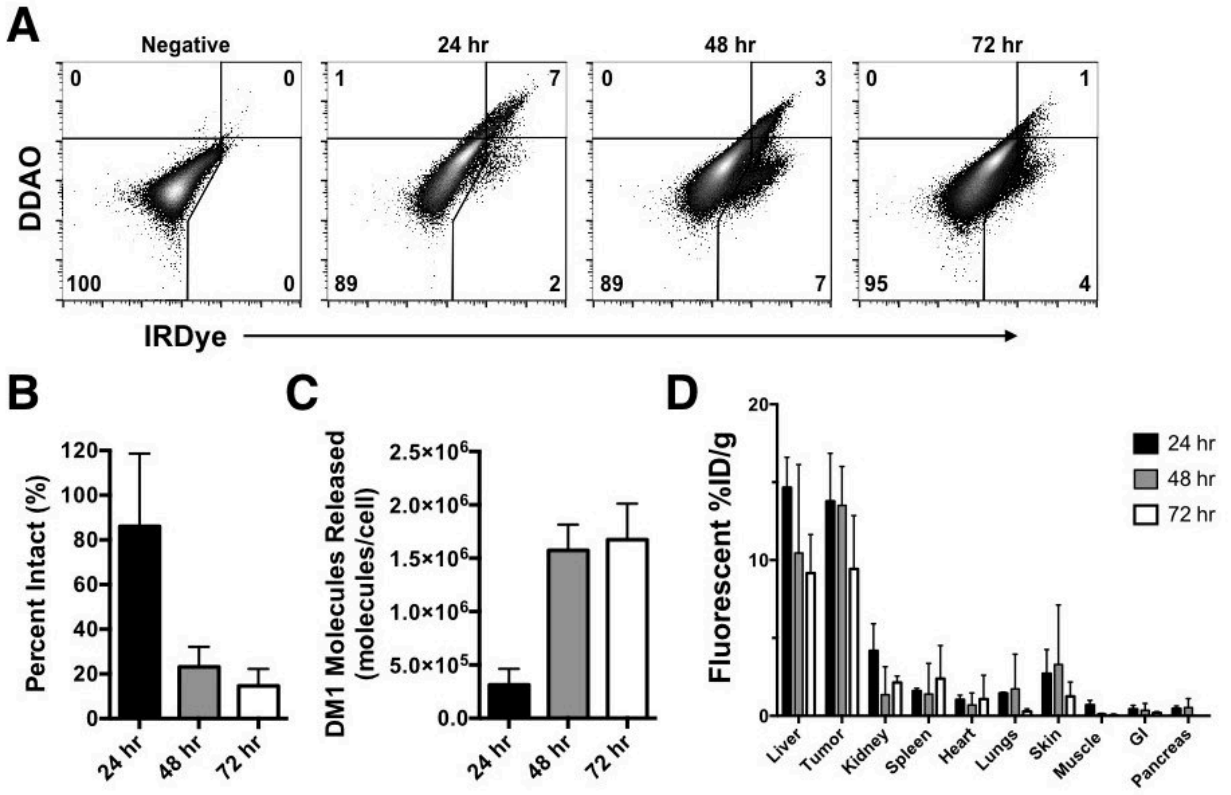

Figure 6.16 *In vivo* T-DM1 metabolism in tumor.
(A) Representative flow cytometry plots of single cell suspension from NCI-N87 tumors at 24, 48, and 72 hours post-injection of 3.6 mg/kg of dually labeled T-DM1. Intact dually labeled T-DM1 appears in DDAO(+)/IRDye(+) quadrant. Over time as ADC is degraded there is a gradual shift towards DDAO(-)/IRDye(+). Cells targeted with T-DM1 (IRDye+) were used to calculate percent intact as described in Materials and Methods. (B) T-DM1 degradation in tumor cells. The fraction of intact ADC (for the fraction of cells that are targeted by T-DM1 at this dose). Data plotted as mean ± standard deviation. (C) Molecules of DM1 payload released per target cell *in vivo* for the targeted cells calculated using the total cell uptake and fraction intact. Data plotted as mean ± standard deviation. (D) T-DM1 biodistribution. T-DM1 shows maximum uptake 24 hours post injection

Untargeted Tumor Cells Can Sustain Tumor Growth Through Newly Functional Tumor Vessels

To better understand the relationship between the heterogeneous T-DM1 distribution and efficacy, we imaged the distribution of T-DM1 and trastuzumab at maximum uptake and during treatment. The NIR fluorescence ratio technique showed that the maximum uptake was reached 24 hours post injection and payload release appeared to plateau around 3 days. From the tumor growth curves it appeared that the maximum shrinkage was occurring several days after payload

release, around 5 days after initial injection for T-DM1. Once tumor cells are killed, they are no longer able to internalize and degrade the drug, potentially allowing ADCs to penetrate deeper into the tissue. However, the tumor distribution of T-DM1-680 and trastuzumab-680 (3.6 mg/kg) at one and five days post-injection remained heterogeneous and perivascular with a significant fraction of the tumor untargeted (Figure 6.17). 15 minutes prior to sacrifice we injected Hoechst 33342 to stain functional tumor vasculature and then stained histology slices with antimouse CD31 ex vivo to show all (functional and nonfunctional) vasculature. Using an automated image analysis algorithm, we calculated the absolute vessel surface area to tumor volume ratio (S/V) along with the fraction of these vessels that had Hoechst and/or T-DM1 signal around them (Figure 6.17). 24 hours after injection, T-DM1 distribution was localized to functional vessels (Figure 6.17, arrows). By five days after injection there were several regions of the tumor that had functional vessels but no perivascular ADC (Figure 6.17, arrowheads), and the image analysis indicated a significant increase (Student's t test, $p < 0.0001$) in the fraction of functional vessels (Hoechst and CD31) lacking ADC, consistent with angiogenesis and/or opening of collapsed vessels. Collapsed vessels (CD31 vessels stained with ADC but not Hoechst, indicating they are no longer functional) were also present. These phenomena were present in both T-DM1 and trastuzumab treated tumors, indicating that they are not necessarily a result of T-DM1 efficacy. However, the formation of newly functional vessels in regions untargeted by T-DM1 could play a role in rescuing the tumor, further supporting the importance of ADC distribution on efficacy.

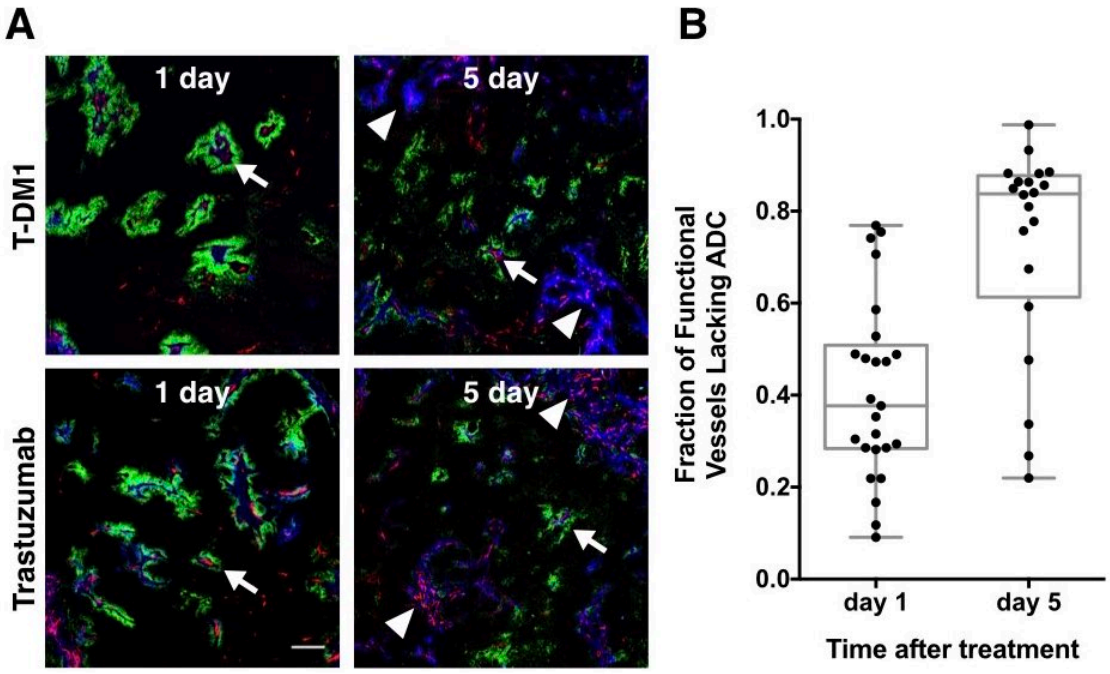

Figure 6.17 Immunofluorescence histology after treatment.
(A) Tumor distribution of 3.6 mg/kg of T-DM1-680 (*top, green*) or trastuzumab-680 (*bottom, green*) at 24 hours (*left*) or 5 days (*right*) after tail-vein injection. 15 minutes prior to sacrifice 15 mg/kg Hoechst 33342 (*blue*) was administered via tail-vein to label functional vasculature. CD31-555 (*red*) was stained *ex vivo* to label all vasculature (functional and nonfunctional). Arrows highlight examples of functional vessels that contain perivascular T-DM1 labeling, which dominate at early times after treatment. By 5 days, a significant fraction of functional vessels (CD31 and Hoechst labeled) lack perivascular T-DM1 (arrowheads). Since some vessels still contain perivascular T-DM1 at this time point, presumably these vessels are newly formed (or became functional) once a significant fraction of T-DM1 cleared. The window leveling is different for each image (qualitative distribution only). Scale bar is 200 μm. (B) Image analysis of histological samples. The fraction of functional vessels (Hoechst and CD31) containing perivascular T-DM1 at 5 days after treatment was significantly less than at 1 day ($p < 0.0001$), indicating angiogenesis and/or opening of collapsed vessels.

6.5 Discussion

The efficacy of ADCs is determined by a complex interplay between tumor uptake, distribution, cellular targeting, internalization, antibody degradation, and release of the small molecule payload. Here, we show that improving tumor penetration by co-administering trastuzumab enhances the efficacy of T-DM1 in a trastuzumab-insensitive mouse xenograft

model. These results have significant implications for the development of ADCs. Although substantial efforts have been made in optimizing the drug itself (high affinity antibodies, stable linkers, and highly potent small molecules), these data demonstrate the intratumoral distribution (independent of the payload dose) plays a major role in determining efficacy. Given that the ADC dose is often limited by the small molecule payload dose and not the amount of antibody, matching the potency of the ADC with delivery (rather than trying to maximize potency) may provide a way to improve the efficacy of ADCs while maintaining tolerability (*47*).

The rapid binding of antibodies relative to their tissue penetration results in receptor saturation of perivascular cells (*37*,*54*). To penetrate deeper into the tissue, additional antibody must enter the tissue, but the toxicity of ADCs generally prevents the administration of higher ADC doses. Although there are other strategies to improve tumor penetration, such as decreasing protein size (i.e. F(ab) or $F(ab')_2$ fragments) or lowering affinity, increasing the antibody dose has the potential to improve multiple mechanisms of action. The co-administration of unconjugated antibody improves penetration (Figure 6.1) and is generally well tolerated relative to the cytotoxic payload. For example, trastuzumab is well tolerated even at high doses, such as an intensive loading schedule totaling 18 mg/kg given over 15 days (*49*). This does not increase (or decrease) the amount of ADC uptake in the tumor; it only changes the distribution as long as the dose remains sub-saturating (*106*). (In the clinic, saturating doses can require multiple *grams* of antibody for highly expressed and/or rapidly internalized antigens (*225*), possibly higher with heavy tumor burdens due to target mediated binding (*226*).) More uniformly delivering the ADC could potentially lower efficacy on the perivascular cells that typically receive a high concentration of ADC. However, ADCs tend to have low IC50's, often over an order of

magnitude below the K_d (Figure 6.7) (*19*,*28*,*227*), indicating sub-saturating concentrations can result in cell death. Therefore, the heterogeneous delivery of ADC in the tumor can result in "overkill" of perivascular cells, where they receive more therapeutic than what is needed, while other cells receive none. When co-administering trastuzumab with T-DM1, the perivascular cells receive a smaller payload dose; however, more cells overall receive therapeutic levels of payload. At super-saturating doses (e.g. 60-120 mg/kg in this high expression model), it is anticipated efficacy would decrease since there would be no increase in penetration for a saturated tumor and payload uptake would decrease. Likewise, administering a saturating antibody dose a day before the ADC (e.g. (*228*)) can decrease efficacy.

These data show that the addition of an antagonist (trastuzumab, which antagonizes T-DM1 at high concentrations *in vitro*, Figure 6.7) with no single-agent efficacy (Figure 6.11) can improve *in vivo* efficacy and survival. The converse of this concept must also be considered. Newer and more potent payloads may be required for targets with low to moderate receptor expression and/or slow internalization rates (*229*). However, an ADC with higher *in vitro* potency may actually be less efficacious *in vivo* for some targets that are highly expressed. The increased potency (whether from higher DAR or a more toxic payload) could lower the maximum tolerated dose. This lower dose reduces the number of cells that can be targeted, thereby lowering the overall efficacy. When developing new ADCs, these results indicate that neither the maximum cellular potency nor the maximum antibody dose is optimal. Rather, this work emphasizes the need to match the single-cell potency with single-cell delivery to maximize efficacy.

In previous work (*106*), we identified studies that used a constant small molecule dose with different DAR/antibody doses and demonstrated the higher antibody dose (and correspondingly lower DAR) exhibited better efficacy. These studies included multiple targets, antibodies, linkers, and payloads (with and without bystander effects, e.g.(*25*,*197*)) indicating that the impact of tissue penetration is important across all ADCs studied to date. Since this publication (*106*) two other studies reported the same result – keeping the small molecule dose the same and increasing the antibody dose improved efficacy (*29*,*227*). However, a potentially confounding factor in these studies was that higher DAR ADCs tend to have faster clearance (DAR-dependent clearance), although the difference in payload AUC was less than 25% for these cases (*24*,*29*). The current work avoids potential DAR-dependent clearance by only using T-DM1. Another possible explanation could be that adding trastuzumab resulted in a dose dependent slower clearance of T-DM1 (*230*). However, the plasma clearance rates are similar with or without trastuzumab (*106*).

Using the NIR fluorescence ratio technique, the fraction of tumor cells targeted by ADC, the number of ADC molecules delivered per cell, and the fraction of intact ADC versus degraded were measured (Figure 6.16). The slowly clearing T-DM1 showed mostly intact protein (~85%) at 24 hours post-injection due to continuous delivery from the blood during this period with the highest plasma concentrations. Conversely, over half of the ADC was degraded by 24 hours *in vitro* when the ADC was pulsed (Figure 6.15). After 3 days, once the tumor had surpassed maximal uptake and plasma concentrations decreased, the majority of the ADC in the tumor was degraded (Figure 6.16). Consistent with the histology images, only ~10% of the tumor cells are targeted by a 3.6 mg/kg dose of T-DM1 at maximum uptake. This is also in agreement with the

9-fold higher antibody dose required for saturation of the tumor (Figure 6.1). The number of DM1 molecules delivered per targeted cell is estimated at 1.7 +/- 0.3 million. Given the 2-3 day residualization half-life of IRDye (*113*), this measurement at 3 days is likely lower than the actual payload delivery but significantly higher than the uptake at the IC50 *in vitro* (Figure 6.7). These results are consistent with a rapid targeting of ADC (~1 day) in perivascular cells at a higher concentration than needed for cell death. A large fraction of cells within the tumor (~90%) are not exposed to T-DM1 even after 48-72 hours when maximum payload delivery is achieved within the tumor. Therefore, a significant fraction of cells receives more drug than needed for cell killing, while a large fraction of cells completely escape therapy, lowering the overall tumor efficacy despite efficient targeting (15% ID/g in these 300-400 mm^3 tumors).

The fluorescently tagged ADC was used to image distribution during tumor response (the nadir in the tumor growth curves occurs around 5-7 days, Figure 6.11). The tumor distribution of both trastuzumab and T-DM1 5 days after injection shows both functional (CD31 vessels labeled with intravenous Hoechst) and nonfunctional vessels with signal. Additionally, there are functional vessels that do not have detectable ADC signal, indicating that after maximum uptake in the tumor is reached there may be new vessels that form, which won't receive significant payload until a high plasma concentration is achieved with the next dose (every 3 weeks in the case of T-DM1). The irregular, dynamic vasculature has important implications for ADC treatment when a significant fraction of cells are untargeted by ADC (Figure 6.17). New vessels deliver both oxygen/nutrients for survival and drugs for cell killing. However, the ADC requires approximately 1 day for uptake, 1 day for complete metabolism, and several days for cell killing, while oxygen and nutrients can rescue the cells more quickly. Therefore, the dynamic

vasculature within the tumor has the potential to repeatedly rescue untreated regions of the tumor even with continuous ADC in the plasma, which may stymie attempts to kill cells layer by layer with successive treatments.

Despite distribution limitations, ADCs and antibodies have had great success in the clinic and further insight into mechanisms of how a heterogeneous tissue distribution is able to result in complete tumor eradication is needed. The NIR fluorescence ratio technique provides a convenient way to monitor the multiple stages of ADC delivery with single-cell resolution and absolute quantification of delivery (molecules/cell). The heterogeneous tissue delivery can be imaged through microscopy, the fraction of targeted cells can be quantified through flow cytometry (Figure 6.1, Figure 6.16, Figure 6.17), and the kinetics of ADC degradation measured by ratio measurement on flow cytometry (Figure 6.16). Differences in target expression, antigen processing, possible target shedding, competition with endogenous ligands, accessibility (such as mucin blocking binding), and other mechanisms make the tumor distribution and development of each ADC uniquely challenging. Understanding these kinetics is crucial for developing ADCs since the majority release their toxic payload after degradation, and cell trafficking is a potential mechanism of resistance (*231*).

Similarly, the impact of payloads with bystander effects, which are not present in the T-DM1/trastuzumab model, is not completely defined. Intuitively, bystander effects would improve efficacy because therapeutic payload would reach cells beyond the penetration distance of the ADC (in addition to the benefit of targeting antigen negative cells). For example, tumor penetration issues may explain why similar antibody doses but higher DAR (and therefore a

higher toxic payload dose) did not improve efficacy in several animal models (*29*,*190*,*197*) using agents without bystander effects. The higher DAR delivers more payload to cells that are already receiving a toxic dose, resulting in "overkill" of these cells. However, this same scenario with a payload that exhibits bystander effects shows improved efficacy (*25*,*28*,*227*). Although the payload is delivered to the same cells, it has the ability to diffuse into adjacent cells to improve overall cell killing. Consistent with our results, several groups (*19*,*28*,*227*) have shown greater efficacy with increased antibody-driven penetration (greater total antibody dose but same payload dose) even with payloads that exhibit bystander effects. For these payloads, it appears that the dilution and washout of the free payload may prevent the same efficacy as antibody-driven penetration to reach cells far from vessels.

Although our results demonstrate that ADC tumor distribution has a significant role in efficacy, there remain several challenges to clinical implementation. First, matching the single-cell potency to single-cell delivery is challenging given that many targets are measured using immunohistochemistry rather than a more quantitative method capable of reporting receptors/cell. Second, selecting the optimum potency could be challenging given intra- and inter-patient variability where one could perfectly 'match' potency and delivery of an ADC to a primary tumor but not a metastasis with much higher or lower expression. It is unknown whether it is better to err on the side of higher potency (targeting fewer cells with a higher dose than necessary for cell killing which could help avoid mechanisms of drug resistance (*231*)) or higher delivery (increased tumor penetration at a sub-toxic dose). In this model system, higher penetration appears to be more beneficial. The use of higher antibody doses to increase ADC penetration has additional potential benefits, such as maximizing other mechanisms of action,

including receptor signaling blockade and/or immune cell interactions (*211*). Sacituzumab govitecan, an ADC that has received Breakthrough Therapy designation from the FDA, takes this approach using a lower potency payload with much higher antibody doses (8-10 mg/kg, Clinical Trial: NCT01631552) (*232*). Additionally, our modeling work shows that healthy tissue with low target expression would have less uptake when ADC and antibody are administered together compared to ADC alone (*106*). Finally, imaging may play a useful role in identifying optimal treatment regimens (*233*). The ZEPHIR trial looks to combine pretreatment and early metabolic response molecular imaging to select patients that respond best to T-DM1 therapy (*234*). Combining molecular imaging and pharmacokinetic models (*137*) to determine the optimum antibody/ADC dosage could provide an individualized treatment with potentially better outcome. Nonetheless, some patients that are HER2 positive may not have trastuzumab uptake (*234*), while other patients that have HER2 negative primary cancers may have metastases that are HER positive (*235*), making individualized treatment challenging.

6.6 Conclusion

In conclusion, we have shown that improving tumor penetration of a constant dose of T-DM1 by co-administration of trastuzumab (in a trastuzumab-insensitive xenograft model) results in significantly better efficacy than T-DM1 alone. Maximizing tumor penetration of ADCs in addition to optimizing the antibody, linker, and payload during development may help improve the efficacy of future ADCs in the clinic.

6.7 Experimental Methods

Antibodies and NIR Imaging Agents for Ratio Measurements

Herceptin (trastuzumab, Roche) and Kadcyla (T-DM1, Roche) were obtained from the University of Michigan Pharmacy. Alexa Fluor 680 NHS Ester (AF680, ThermoFisher Scientific, A37567), IRDye 800CW NHS Ester (IRDye, LI-COR, 929-70020), and CellTrace™ Far Red DDAO-SE (DDAO, ThermoFisher Scientific, C34553) were conjugated to the antibodies following the manufacturer's instructions as previously described (*106*,*113*). Antibody/ADC at 2 mg/mL supplemented with 10% sodium bicarbonate (v/v) was reacted with dye at molar ratios of 0.5 (AF680, IRDye) and 1.5 (DDAO) for 2 hours at room temperature and purified using P6 Biogel (1g gel/10mL PBS) resulting in dye to protein ratios of approximately 0.3 (AF680, IRDye) and 0.7 (DDAO). Our previous work has shown that the distribution of T-DM1 is unchanged after labeling with AF680 at dye to protein ratio of 0.3 or less (*137*). Antibody/ADC dye conjugates were run on SDS-PAGE and scanned on the Odyssey CLx Scanner (LI-COR) to ensure free dye was removed. For fluorescence histology, antimouse CD31 (BioLegend, 102402) was conjugated with Alexa Fluor 555 (ThermoFisher Scientific, A37571), mouse antihuman IgG Fc antibody (BioLegend, 409302) was conjugated with Alexa Fluor 488 (ThermoFisher Scientific, A20000), and trastuzumab was conjugated with Alexa Fluor 750 (ThermoFisher Scientific, A20011) at dye to protein ratios of 1.5.

Cell Lines and In Vitro Toxicity

NCI-N87 and HCC1954 cells were purchased from ATCC in May 2015 and June 2016, respectively. Cell line authentication was performed by ATCC. Cells were grown at 37°C with 5% CO_2 in RPMI 1640 growth medium supplemented with 10% (v/v) FBS, 50 U/ml penicillin,

and 50 μg/ml streptomycin. Mycoplasma testing was performed yearly using the Mycoalert testing kit (ThermoFisher Scientific, NC9719283). Cells were cultured 2-3 times per week up to passage number 50 (approximately 3-4 months). For cell viability assays, 5,000 cells were plated in 96 well plates. Titrations of T-DM1 or T-DM1 and trastuzumab were replaced daily for 6 days and viability was measured using the PrestoBlue Cell Viability Reagent (ThermoFisher Scientific, A13261). Briefly, cells were washed twice with media and a 1:10 dilution of PrestoBlue in media was incubated for 25 minutes at 37°C. After incubation, the fluorescence (560/590, Ex/Em) of each well was measured using a Biotek Synergy plate reader. Background signal from wells without cells was subtracted from all samples and then viability was normalized to untreated cells.

In Vitro NIR Fluorescence Ratio Measurements and Fluorescence Microscopy

ADC metabolism was studied by dually labeling T-DM1 with DDAO and IRDye as described above. As the labeled ADC binds to the cell surface receptor, gets internalized, and subsequently degraded, the low molecular weight and more lipophilic DDAO diffuses out of the cell while the IRDye remains trapped (*113*). DDAO therefore approximates the intact protein (since it is cleared upon degradation), while IRDye approximates the cumulative uptake in the cell (*63*). Unlike pH effects (*136*) or quenching/FRET, this provides an irreversible measurement of both intact protein and payload delivery without requiring a high degree of labeling (self-quenching approach) or larger dye-quencher conjugates. NCI-N87 and HCC1954 cells were plate in 96 well plates. Cells were labeled for 30 minutes at 37°C at different times over a 48 hour period. After each labeling cells were washed twice to remove excess media. After 48 hours cells were washed three times, then harvested using Cellstripper (Corning, 25-056-CI), a non-

enzymatic cell dissociation solution, and fluorescence intensity was quantified using an Attune Acoustic Focusing Cytometer (Life Technologies). The signal for each dye was normalized to the initial time point, and the normalized ratio of DDAO divided by IRDye was plotted to show the ratio of intact ADC to cumulative uptake. Alternatively, cells were imaged using fluorescence confocal microscopy (Olympus) with a 635 nm laser for DDAO and a 748 nm laser for IRDye.

Tumor Growth Studies

All animal studies were conducted in accordance with the University of Michigan Institutional Animal Care and Use Committee (IACUC). For all tumor xenografts studies, 5 x 10^6 NCI-N87 cells were inoculated in the rear flanks of mice (one flank for tumor growth studies, both flanks for all others). For tumor growth studies, tumor volume was measured using calipers every other day using the formula volume = 0.5*length*width^2. Trastuzumab, T-DM1, both trastuzumab and T-DM1 (all unlabeled), or saline were injected via tail vein once tumors reached 250 mm^3. For tumor growth studies 10 animals were used for all treated and untreated cohorts. Kaplan-Meier survival curves were generated in PRISM and were analyzed by log-rank test at significance level of $p \leq 0.05$.

In Vivo NIR Fluorescence Ratio Measurements and Fluorescence Histology

To study the cellular uptake and metabolism kinetics in vivo, tumor xenografts were treated with DDAO and IRDye labeled T-DM1, and the tumors were resected, digested into a single cell suspension, and analyzed on flow cytometry (similar to the in vitro assay). Once the longest axis of the tumor reached 9-10 mm, 100 μg of dually labeled T-DM1 was injected via

tail-vein and animals were sacrificed at 24, 48, and 72 hours. After sacrifice, tumors were resected and sliced before being placed in a collagenase IV solution (5 mg/mL). The tissue was digested for 25 minutes before centrifugation (5 min, 300 g). The cell pellet was resuspended in media, washed twice, and filtered through a 40 μm filter. Cells were then analyzed by flow cytometry. Uninjected negative control tumor digests were used to establish gates for DDAO and IRDye fluorescence. To determine the percent intact (from the DDAO/IRDye ratio) we examined cells that were targeted with T-DM1 (IRDye+). The background mean fluorescence intensity in RL1 and RL2 from negative control tumors was subtracted from the mean fluorescence intensity of DDAO (RL1) and IRDye (RL2) to get fluorescence per targeted cell. Then the DDAO signal was divided by IRDye to get the DDAO/IRDye ratio. To get the percent intact, this ratio was normalized to the initial intact ratio, which was determined by harvesting in vitro cells, labeling on ice for 25 minutes, washing twice, and analyzing by flow cytometry. In addition to running tumor cells on flow cytometry, part of the tumor was used for fluorescence biodistribution. The low autofluorescence in the near-IR makes IRDye a suitable fluorophore to determine organ uptake (*53*,*107*,*137*), and fluorescence biodistribution was performed as previously described (*106*,*122*,*137*). Fluorescence histology was performed as previously described (*106*,*137*).

Immunofluorescence Histology

Trastuzumab and Alexa Fluor 680 labeled T-DM1 (T-DM1-680) were administered via tail-vein at 0:1, 3:1, and 8:1 ratios (0, 10.8, and 28.8 mg/kg unlabeled trastuzumab with a constant 3.6 mg/kg T-DM1-680). Additionally, 15 minutes prior to sacrifice Hoechst 33342 (ThermoFisher Scientific, H3570) was injected via tail-vein at 15 mg/kg to labeled functional

vasculature (*236*). 24 hours post-injection animals were euthanized, tumors were resected, flash frozen in OCT, and cut into 16 μm slices for histology. Before imaging, slides were stained for 25 minutes with antimouse CD31-AF555 and antihuman IgG Fc-AF488, or trastuzumab-AF750. The CD31 stain was used to calculate the total vessel surface area, and an automated image analysis program identified which CD31 stained vessels were adjacent to Hoechst stained cells (functional vessels), ADC-stained cells, or both to calculate the fraction of functional vessels that delivered ADC.

Image Analysis

Imaging tumors following treatment can provide insight into tumor relapse and regrowth between therapies (once every 3 weeks for T-DM1). The residualizing nature of the IRDye 800CW and AF680 labels on T-DM1 provide a history of which cells received the payload. Co-injection of Hoechst 33342 labels the functional vessels at the time of tumor resection. To determine impacts of the tumor vasculature (which both supplies oxygen and nutrients for tumor growth but also drugs for cell killing), we imaged tumors 1 and 5 days after treatment with 3.6 mg/kg of T-DM1. Significant mismatch between the functional vessels (Hoechst labeled) and treated regions (perivascular T-DM1) appeared at 5 days. To quantify these results, we used an automated image analysis algorithm to calculate the absolute vessel surface area to tumor volume ratio (S/V) along with the fraction of these vessels that had Hoechst and/or T-DM1 signal around them.

In order to find the surface-volume ratio, standard stereology methods were used on tumor xenograft images (*237*). Briefly, random 'lines' were placed on histological images (5 images per tumor and 4 (day 5) or 5 (day 1) tumors per condition) and the number of 'cuts' of

the vessels was counted to yield the surface of the blood vessels- tumor volume ratio (S/V) as determined from the equation below (*188*,*238*).

$$\frac{S}{V} = \frac{2c}{Ln}$$

Where: c: cuts, L: length of lines (μm), n: number of lines.

A MATLAB code to automate this counting was created. Briefly, the three image channels representing the vessels, the intravenously delivered Hoechst signal (for functional vessels), and the antibodies were uploaded to the MATLAB script. A binary mask was generated to identify signal from background, and noise was removed. 10,000 lines were randomly placed on the image (to increase accuracy (*238*)), and the function checks for the number of 'cuts' from these lines across a vessel. The length of the line was also chosen to be small (71μm, equivalent to 50 pixels). The S/V for select images was calculated manually using 300 lines to ensure the code was accurate. Each cut is categorized as either cut from a vessel (total vascular density), a cut from a functional vessel (proximity to intravenously delivered Hoechst), a cut from a vessel that delivered ADC (proximity to intravenously delivered ADC), or cut from a functional vessel that delivered ADC (proximity to both intravenously delivered Hoechst and ADC). With all the cuts estimated, the respective S/V is calculated.

Chapter 7

Concluding Remarks and Future Directions

7.1 Summary of Work

In this dissertation, I developed computational and experimental techniques to study the distribution of antibody and ADC therapeutics in tumor at several length scales in order to design therapeutic agents with improved efficacy. In order to study the tumor distribution of antibodies with high sensitivity and subcellular resolution, I used near-infrared (NIR) fluorescently labeled antibodies. In Chapter 2, I characterized the residualization properties of NIR fluorophores to elucidate the relationship between fluorescence signal and intact vs. degraded protein. This also enabled fluorophore selection for optimal molecular imaging agent design. In Chapter 3, to ensure the pharmacokinetics (PK) and tumor distribution of NIR fluorescently labeled antibodies is indistinguishable from unlabeled antibodies, I determined the optimal degree of labeling (DOL) before further experimentation. I labeled two FDA approved antibodies with two commonly used NIR fluorophores, AlexaFluor680 (AF680) and IRDye800CW (800CW), measured the PK, biodistribution, and affinity and compared it to unlabeled. Unexpectedly, even an average degree of labeling of 1 dye per antibody was too high due to the Poisson distribution. I determined that AF680 labeled antibodies show nearly identical PK to unlabeled at a DOL of 0.3 or less, even out to nearly 3 weeks. IRDye showed similar PK over the first few days, and then gradual faster clearance at this DOL in agreement with other literature reports.

Building on the labeling guidelines, in Chapter 4, I developed a dual channel NIR labeling technique, which involves labeling an antibody with a non-residualizing dye (DDAO) and a residualizing dye (IRDye). As the dually labeled antibody binds the cells, internalized, and degraded, the non-residualizing dye permeates out of the cell, while the residualizing dye is trapped in the cell. In other words, the non-residualizing dye approximates the intact antibody, since it leaks out after antibody degradation, while the residualizing dye approximates the cumulative cellular uptake of antibody, since it is trapped in the cell and accumulates. I selected several model proteins and found that the dual label technique was able to capture their widely differing internalization half-lives, both in vitro and in vivo. I applied the dual label technique to T-DM1, and, using the single-cell resolution of flow cytometry, I found that the clinical dose of T-DM1 only targeted about 10% of cells in the tumor, and that targeted cells were receiving more ADC than necessary to achieve cell death. Importantly, this technique is the first to measure both protein metabolism and distribution in vivo with single-cell resolution.

In Chapter 5, I modeled both the systemic and tumor distribution of antibodies/ADCs using a novel, mechanistic, multi-scale model combining a PBPK model with the Krogh cylinder tumor model. Using this model, I predicted and experimentally verified the tumor distribution of a T-DM1 with and without the coadministration of the unconjugated antibody (trastuzumab). The unconjugated antibody binds and competes for the same receptor and drives T-DM1 further into the tumor, increasing the total number of cells targeted. Using the model as a theoretical framework, I imaged the tumor distribution of a constant 3.6 mg/kg T-DM1 as a single agent and with 10.8 mg/kg and 28.8 mg/kg trastuzumab (3:1 and 8:1 ratios, respectively) in a mouse tumor xenograft model. As a single agent, T-DM1 was highly heterogeneous, even at the dosage given

to patients in the clinic. Adding trastuzumab significantly improved the ADC tumor penetration, which resulted in a near homogeneous distribution at the 8:1 dosing level.

Encouraged by the modeling results in Chapter 5, I tested the efficacy of T-DM1 with and without trastuzumab in a trastuzumab resistant xenograft mouse model in Chapter 6. Expectedly, the administration of T-DM1 alone showed a significant improvement in efficacy and survival, while trastuzumab alone had no impact. However, despite trastuzumab having no efficacy by itself (and lowering the efficacy of T-DM1 in vitro), I demonstrated a clear trend where coadministration of trastuzumab at 1:1, 3:1, and 8:1 trastuzumab:T-DM1 ratios dramatically improved efficacy over T-DM1 alone. In fact, the 3:1 and 8:1 ratios showed a statistically significant improvement in survival over T-DM1 alone. These striking results are counterintuitive to the current dogma of the ADC field. Most pharmaceutical companies developing ADCs focus on engineering the ADC itself (making antibody bind better, making more stable linker, etc.) and do not consider the distribution of the molecule. Our results stand in contrast to this approach and clearly shows ADC distribution plays a major role in efficacy.

This dissertation provides unique tools to study antibody and ADC distribution and metabolism, quantitative computational tools to simulate in vivo distribution, and concrete guidance on how to improve efficacy of ADC therapeutics. Specifically, Chapters 2 and 3 offer guidelines for labeling antibodies with NIR fluorophores to study distribution with high spatial and temporal resolution. Chapter 4 presents a novel dual label technique that can quantify antibody distribution and metabolism in vivo with unprecedented single cell resolution. Chapter present a modeling framework to simulate both the systemic and tumoral distribution of

antibodies and ADCs. Finally, in Chapter 6 I present the first study to show antibody distribution itself plays a major role in efficacy and improve the efficacy of an FDA-approved ADC. Together, this dissertation will advance the growing field of ADCs and improve patient treatment.

7.2 Future Work and Directions

The work in this dissertation opens several new avenues of research, and, in this section, I briefly outline additional work to continue building our understanding of the relationship between ADC distribution and efficacy.

Applying the unconjugated antibody and ADC coadministration strategy in tumor models with low or heterogeneous antigen expression.

In Chapter 6, the efficacy study using a dosing strategy of ADC with unconjugated antibody was the first to show that ADC tumor distribution plays a major role in overall efficacy. Although testing ADC efficacy in mouse xenografts is the industry standard for ADC development, in the clinic there is significant intra- and interpatient tumor heterogeneity. Testing the coadministration dosing strategy in more realistic tumor models, such as patient-derived xenografts (PDX) or mosaic tumor models with mixed antigen positive and negative cells, may better mimic the clinical scenario where there is heterogeneous antigen expression. In these tumor models, we could apply several of the techniques outlined in this dissertation to, ideally, match the potency of the ADC to its distribution in the tumor. First, the tumor distribution of fluorescently labeled ADC at several doses can be imaged through fluorescence microscopy. Then, using flow cytometry, the fraction of cells targeted in the tumor and the absolute uptake of

ADC can be quantified. Using microscopy to visualize the tumor distribution and flow cytometry to quantitate ADC uptake will help enable the selection of dosing levels to optimize tumor distribution.

Testing the dosing strategy in a cell line with lower antigen expression may help determine if it is better to err on the side of higher potency (i.e. lower ratios of antibody to ADC) or better distribution (i.e. higher ratio of antibody to ADC). In our study, we used the NCI-N87 cell line because of its high HER2 expression (~one million receptors per cell) and selected a subsaturating (3:1) and saturating (8:1) dosing levels. In our case the saturating dose of 8:1 was the most effective treatment; however, there is likely an upper limit to the amount of antibody that can be coadministered with the ADC. In a tumor model with lower antigen expression, the tumor will reach saturation with much lower doses, and too high a ratio of antibody to ADC may decrease efficacy. To apply the coadministration strategy in the clinic, where antigen expression in the tumor is often highly variable, it will be critical to determine if there is an upper limit of the amount of antibody that can be coadministered with ADC to maximize efficacy.

Quantifying payload bystander effects through pharmacodynamic marker imaging

Payload cytotoxicity is one of the central drivers of ADC efficacy; however, relatively little imaging data are available of the payload distribution in tumors. In particular with bystander payloads, it is unclear how far they can diffuse from cells targeted with ADC. Although our group has modeled the bystander effect and predicted payload tumor distributions based on the physicochemical properties of the payload, more imaging data is required to confirm, or refute, these predictions. One potential method of quantify the bystander effect is

through imaging pharmacodynamic markers from the payload engaging its target. For example, in the case of PBD-based ADCs, after the PBD payload is released and it binds DNA, an anti-phospho-histone H2A.X antibody will bind the payload-DNA complex. The payload and antibody distribution can be compared by administering an antibody with a residualizing fluorophore in vivo, and then ex vivo staining of the pharmacodynamic marker with a different fluorophore. Theoretically, since PBD is a bystander payload capable of diffusing into neighboring cells, the payload would reach more cells than the antibody alone. Using image analysis tools similar to those in Chapter 6, the distance the payload traverses into the tumor can be quantified. Visualization of the payload distribution in tumors coupled with computational models will give further insight into the relationship between payload distribution and efficacy.

ADC therapy and the immune system.

When developing ADCs, it is common to test efficacy in immunodeficient mouse models, such as NOD/SCID or nude mice; however, several groups have shown that ADC therapy results in immune cell activation in immunocompetent mouse models. Since ADCs distribute heterogeneously in the tumor and may leave much of the tumor untargeted, it is possible that, in the clinic, ADCs activate immune cells, which are then able to kill tumor cells untargeted by the ADC. Müller et al. showed in a preclinical mouse model that T-DM1 does result in T cell activation; however, this study used very high doses of T-DM1 (15 mg/kg) (*211*). Studying immune cell activation in immunocompetent animal models following ADC therapy at more clinically tolerable doses would help determine the relative impact from immune cells versus the ADC payload on overall efficacy. Additionally, since most ADC research is conducted in immunodeficient mouse models, it is unclear how ADC therapy may synergize

with other immune-oncology agents, such as checkpoint inhibitors. For example, if ADC therapy is in fact stimulating the immune system, then combining ADC therapy with an anti-PD1 checkpoint inhibitor provides both tumor cell killing capabilities and immune stimulation from the ADC, while preventing immune cell suppression by disrupting the PD1-PDL1 immunosuppresive interaction.

7.3 Concluding Remarks

The current dogma for ADC development involves developing a humanized antibody against a tumor antigen of interest and attaching the most potent payload to it with a stable linker chemistry. Usually several variants are made and characterized before conducting *in vitro* testing. Then, the *in vitro* characterization of the ADC normally consists of cell viability assays against multiple cell lines, cell binding, and potentially fluorescence microscopy to visualize surface staining of the antigen. Often the most toxic agent *in vitro* is selected to move forward for *in vivo* testing, where it is used in tumor growth studies, biodistribution with radiolabels, and plasma clearance. Based on the work in this thesis, I believe that the assumption that the most toxic agent *in vitro* will be the best candidate *in vivo* oversimplifies the ADC as simply a vehicle for the payload to the tumor and neglects much of the dynamics of antibody therapy.

One of the critical findings in this thesis is that the distribution of ADCs plays an important role in the overall efficacy of these agents, and this is one of the major hurdles in developing ADCs against solid tumors. ADCs have shown great promise against blood cancers where there are fewer delivery limitations; however, they have struggled against solid tumors. The lack of available imaging data, from both preclinical and especially clinical samples, makes

it difficult to conclude with great certainty that distribution is the primary cause for failure of ADCs; however, the literature reviews and efficacy study outlined in this thesis make a compelling case that it has been significantly underappreciated. My hope is that this work will encourage those developing ADCs to make tumor imaging a staple of the ADC development process, and directly pair tumor imaging studies at the same doses as efficacy studies. Many pharmaceutical companies already use fluorescence imaging as part of the *in vitro* characterization process for ADCs, and it should be relatively facile to extend this imaging to histological sections. Although I have outlined labeling conditions and fluorophores for direct imaging of the ADC, at minimum, immunofluorescence or immunohistochemical staining should be used when the ADC consists of a humanized antibody in a mouse xenograft model because of the straightforward detection of the ADC using anti-human Fc secondary antibodies. Furthermore, I would encourage those developing ADCs to apply the methods described in this thesis to quantitate ADC delivery at the cellular level in the tumor with flow cytometry to allow for a direct comparison between *in vitro* and *in vivo* studies. I believe it is imperative to couple imaging studies examining the tissue and cellular scale distribution of ADCs with conventional tumor growth, biodistribution, and plasma clearance studies. This will improve our understanding of how ADCs acting at the cellular scale interact with the tumor microenvironment at the tissue scale and result in tumor regression at the organ scale.

I anticipate that making tumor imaging a staple of the ADC development will bring additional insights into the mechanisms of action of ADCs. Currently, most researchers in the ADC field view the payload as the *primary* driver of ADC efficacy *in vivo*. While, I believe that the payload is certainly one of the central mechanisms of action for ADCs, the fact that many

tumor cells remain untargeted by the ADC suggests that other mechanisms of action are playing a role in efficacy as well. Some of these may include direct effects, such as immune cell recruitment and/or activation, or indirect effects, such as vascular collapse. In Chapter 6, imaging the tumor during treatment revealed that additional vessels were forming in regions not targeted by the ADC as soon as five days after ADC administration; however, in the clinic, the ADC is administered every three weeks. It is possible that administering the ADC more frequently with lower doses may target newly formed vessels before the tumor is able regrow further. Rationally selecting and testing a more frequent dosing regimen such as this is not possible without directly visualizing the antibody distribution in the tumor microenvironment, and likely would not even come into consideration with the current dogma of ADC development. I hope that this dissertation brings a new perspective to those developing ADCs to continue improving these promising therapeutics.

Appendices

Appendix A – Dual Label NIR Fluorescence Ratio Imaging Protocol

MATERIALS

Reagents

Cell culture

- A431 cells (ATCC, cat. no. CRL-1555)
- LS174T cells (ATCC, cat. no CL-188)
- NCI-N87 cells (ATCC, cat. no. CRL-5822)
- RPMI with L-Glutamine (Thermo Fisher Scientific, cat. no. 11875-093)
- DMEM high glucose, pyruvate (Thermo Fisher Scientific, cat. no. 11995-065)
- Fetal bovine serum (FBS) (Thermo Fisher Scientific, cat. no. 10437-028)
- Phosphate buffered saline (PBS) (Thermo Fisher Scientific, cat. no. 10010-023)
- Penicillin-streptomycin (10,000 U/mL), 100 ml (Thermo Fischer Scientific, cat. no. 15140-122)
- Trypsin-EDTA (0.05%) (Gibco, cat. no. 25300054)
- CellStripper (Corning, cat. no. 25-056-CI)
- 96 well flat clear bottom black plates (Corning, cat. no. 3603)
- DMSO (Sigma-Aldrich, cat. no. D2438)
- Sodium bicarbonate (Thermo Fisher Scientific, cat. no. 25080-094)
- Quantum™ Simply Cellular® anti-Human IgG Quantitative Beads (Bangs Laboratories, cat. no. 816)

Gel Supplies

- MES Running Buffer (Thermo Fisher Scientific, cat. no. B0002-02)
- Loading Buffer
- Odyssey One-Color Protein Molecular Weight Marker (LI-COR, cat. no. 928-40000)

Imaging Agents

- DDAO-SE (Thermo Fisher Scientific, cat. no. C34553)
- IRDye 800CW NHS Ester (LI-COR, cat. no. 929-70020)
- Alexa Fluor 488 (Thermo Fisher Scientific, cat. no. A20000)
- Alexa Fluor 555 (Thermo Fisher Scientific, cat. no. A37571)

Antibody/Proteins

- IRDye 800CW EGF Optical Probe (LI-COR, cat. no. 926-08446)
- Human A33 Antibody (R&D Systems, cat. no. MAB3080)
- Erbitux (cetuximab), (Eli Lilly and Company)
- Herceptin (trastuzumab), (Genentech)
- Kadcyla (ado-trastuzumab emtansine), (Genentech)
- Antimouse CD31 (BioLegend, cat. no. 102402)
- Mouse antihuman IgG Fc antibody (BioLegend, cat. no. 409302)

Other

- NOD/SCID mice, female (Jackson Laboratories, 4–6 weeks) **! CAUTION** All animal experiments require approval by institutional review board and animal use and care committees and must be conducted in accordance with institutional and national regulations.

Equipment

General Equipment

- Pipet Tips (1000, 200, 10µL) (Thermo Fisher Scientific, cat. no. 94060716, 94060316, 94060116)
- Pipettors (Thermo Fisher Scientific, cat. no. 4700860N)
- T75 culture flasks (Fisher Scientific, cat. no. 12-556-010)
- CO2 incubator (Eppendorf, cat. no. CO17301001)
- Bright-Line Hemacytometer (Hausser Scientific, cat. no. 1483)
- Thermo Fisher Scientific Sorvall Legend X1R Centrifuge (Thermo Fisher Scientific, cat. no. 75004261)
- Labconco Purifier Logic+ Class II Type A2 Biological Safety Cabinet (Labconco, cat. no. 302310000)
- Razor blades (Fisher Scientific, cat. no. 12-640)
- MX35 Premier Disposable Low-Profile Microtome Blades (Thermo Fisher Scientific, cat. no. 3052835)
- 40 µm filters (Corning, cat. no. 352340)
- Bolt™4-12% Bis-Tris Plus Gels, 15 wells (Thermo Fisher Scientific, cat. no. NW04125BOX)
- Bio-Gel® P-6 Gel (Bio-Rad, cat. no. 150-4134)
- Costar Spin-X Centrifuge Tube Filter (Fisher Scientific, cat. no. 07-200-388)
- Nunc™ Lab-Tek™ II Chamber Slide™ System (Thermo Fisher Scientific, cat. no. 154534)

- Versa-Orb Digital Orbital Shakers (Chemglass Life Sciences, cat. no. CLS-4021-100)
- Fisher Scientific Model 120 Sonic Dismembrator (Fisher Scientific, cat. no. FB120110)

Imaging

- Olympus FV1200 (Olympus)
- 20× water immersion objective (Olympus, cat. no. UMPLFLN20XW)
- 60× water immersion objective (Olympus, cat. no. LUMFLN60XW)
- Odyssey® CLx Imaging System (LI-COR)
- Leica CM3050S Cryostat
- TissueTek O.C.T. Compound (VWR, cat. no. 25608-930)
- MX35 Premier Disposable Low-Profile Microtome Blades (Thermo Fisher Scientific, cat. no. 3051835)
- Attune Acoustic Focusing Flow Cytometer (Applied Biosystems)
- Nanodrop 2000c Spectrophotometer (Thermo Fisher Scientific, cat. no. ND-2000C)

Software

- FV10-ASW (Olympus)
- Image Studio (Odyssey CLx) (LI-COR)
- Fiji (https://fiji.sc)

Animal Work

- Fluriso (Isoflurane, USP) (VetOne, cat. no. 501017)
- AIN-93M Purified Diet (non-fluorescent rodent chow) (Teklad, cat. no. TD.94048)

REAGENT SETUP

Cell Culture Medium. Supplement RPMI 1640 medium and DMEM medium with 100 U/mL penicillin, 100 U/mL streptomycin solution and 10% (vol/vol) FBS. Filter-sterilize the medium and store the medium at 4 °C for up to 3 months. Use RPMI 1640 medium with the NCI-N87 cell line, and DMEM medium with A431 and LS174T cell lines.

P-6 Biogel. Dissolve gel in PBS at 10 mL/g of gel. Hydrate the gel by mixing for at least 2 hours on a stationary mixer. Store at room temperature for up to six months.

Collagenase digest solution #1. Weigh approximately 25 mg of collagenase IV. Dissolve in 5 mL PBS. Δ **CRITICAL STEP** Prepare digest solution immediately before use. Discard excess.

Collagenase digest solution #2. Weigh approximately 25 mg of collagenase IV. Dissolve in 2.5 mL of 1x RIPA buffer and 2.5 mL PBS. Δ **CRITICAL STEP** Prepare digest solution immediately before use. Discard excess.

Trypsin digest solution. Combine 2.5 mL of 1x RIPA buffer and 2.5 mL trypsin. Δ **CRITICAL STEP** Prepare digest solution immediately before use. Discard excess.

Hoechst 33342. Dilute stock to 0.5 mg/mL in deionized water. Store at 4ºC for 1 year. Before labeling cells for microscopy, dilute to 0.1 mg/mL in cell media. Discard immediately after use.

PBS-EDTA. Dissolve EDTA in PBS to a concentration of 5 mM. Store at room temperature for up to 1 year.

Antimouse CD31-AF488. Pipet at least 100 µg of antimouse CD31 into a microcentrifuge tube. Mix with 7.5% sodium bicarbonate solution at 10% (vol/vol). Dissolve AF488 NHS Ester in DMSO at 1 µg/µL. Add AF488 NHS Ester at a molar ratio of 4:1 to the antimouse CD31 solution. React for 2 hours at room temperature and protect from light. Follow

steps 4 and 5 for to purify the antibody-dye conjugate. Quantify antibody concentration and dye to protein ratio using a Nanodrop Spectrophotometer. The final concentration should be approximately 2-3 mg/mL of antibody and have a dye to protein ratio of approximately 2-3.

PROCEDURE

Protein Dual Labeling • TIMING 4-5 hours

1. For antibodies or ADCs adjust concentration to approximately 2 mg/mL in buffer free of amines. Mix with a 7.5% sodium bicarbonate solution at 10% (vol/vol). The pH should be approximately 8.5.
2. Dissolve IRDye and DDAO into DMSO at 1-4 µg/µL. Δ **CRITICAL STEP** Prevent repeated freeze thaw of fluorescent reagents. Store at -20ºC and protect from light.
3. Combine antibody/sodium bicarbonate solution with IRDye and DDAO at molar ratios of 0.5 and 1.0, respectively, for 2 hours at room temperature. Protect from light. ? Troubleshooting
4. Purify the antibody/ADC reaction using P-6 Biogel. Add 800µL of P-6 Biogel to spin tube. Centrifuge for 1 minute at 3500*g*. Remove supernatant.
5. Pipet up to 100 µL of reaction on top of column. Centrifuge for 1 minute at 3500*g*. Transfer antibody-dye conjugate to new microcentrifuge tube.
6. To ensure free-dye is removed, run the antibody-dye conjugate on SDS-PAGE, and scan the gel on the Odyssey CLx or similar NIR scanner. If free dye is still present in the solution repeat the purification with P-6 Biogel.
7. Determine absorbance using Nanodrop Spectrophotometer. Measure absorbance at 280nm, 650nm, and 778nm. Using the molar extinction coefficients and correction factors for the antibody, DDAO, and IRDye, calculate the protein and dye concentrations (Figure 4.2).
8. Calculate degree of labeling for both dyes using equations below. Δ **CRITICAL STEP** Ensure the degree of labeling is less than 0.3 for IRDye and 0.7 for DDAO. At a degree of labeling greater than 0.3, IRDye can impact protein pharmacokinetics. ■ Pause Point Antibody-dye conjugate should be used within 3 months. Store at 4ºC and protect from light. Aliquot labeled antibody into tubes and store at -80ºC for longer-term storage. (Avoid repeated freeze thaws.)

In Vitro Flow Cytometry • TIMING 3-5 days

9. Harvest cells by removing media, washing twice with PBS, then incubating with 0.05% trypsin for 5-10 minutes at 37ºC. Once cells are detached, add media (1:1), and transfer to a conical. Count cells with hemacytometer and plate approximately 100,000 cells per well in a 24 well plate. Allow cells to adhere to plate for at least 4 hours or overnight. Plate enough wells so each time point is run in triplicate.

10. Prepare stock of cell media with dually labeled antibody stock in a conical. Dilute dual-labeled antibody in media at 30 nM (>10 × K_d). Add media without antibody to another conical for a negative control. **! CAUTION** For steps 10-13 Use proper aseptic technique to avoid bacterial contamination.
11. For each time point, remove cell media and add 300 µL of the dual label antibody in media solution for 30 minutes at 37ºC.
12. After labeling cells for 30 minutes, aspirate dual label antibody media solution, wash twice with fresh media and replace media.
13. Repeat steps 11 and 12 for each time point.
14. After the final time point, wash all cells once with media and once with PBS to ensure any fluorophore that has leaked out of cells is washed away.
15. Detach the cells for flow cytometry by incubating with CellStripper at 37ºC for 10 minutes or until cells have detached.
16. Once cells are detached immediately place the plate on ice. Pipet the cells/CellStripper solution forcefully to dislodge cells from the plate and transfer to microcentrifuge tubes on ice. **! CAUTION** Do not scrape the cells off the plate as this may lyse them.
17. Wash the cells once by centrifuging cells at 300*g* for 5 minutes, removing CellStripper solution, adding 300µL media, centrifuging the cells at 300*g* for 5 minutes, and removing media. Place resulting cell pellets on ice for flow cytometry. **! CAUTION** Carefully remove cell media so that the cell pellet is not disturbed.
18. Immediately before running cells on the Attune Flow Cytometer, resuspend cells in PBS and filter through 40 µm filter tubes.
19. Run all samples on flow cytometer. Ensure the PMT settings for RL1 (DDAO) and RL2 (IRDye) are adjusted so the background signal is around 1000 to maximize the dynamic range for these fluorophores. Export data for analysis in FlowJo.
20. In FlowJo, gate around the cellular population and export the median intensity for both RL1 and RL2.
21. Background subtract RL1 and RL2 median fluorescence intensity for each channel. Divide the background subtracted intensity of each channel by the initial intensity from the zero time point. This gives the normalized intensity for RL1 and RL2. To estimate the percent intact antibody, divide the normalized intensity of RL1 (DDAO) by the normalized intensity of RL2 (IRDye). The ratio of the mean is a simple calculation for homogeneous cell populations. For heterogeneous populations, the mean of the ratio and full distribution is more descriptive.

In Vitro Microscopy • TIMING 3-5 days

22. Similar to step 9, harvest cells using trypsin and count cells. Plate approximately 75,000 cells in each well of a Chamber Slide.
23. Similar to step 10, prepare dually labeled antibody media solution at approximately 30 nM.
24. For each time point, remove cell media and add 300 µL of the dual label antibody media solution for 30 minutes at 37ºC. Ensure one well is available for a negative control. **! CAUTION** For Steps 24 and 25 Use proper aseptic technique to avoid bacterial contamination.

25. After pulsing cells, remove dual label antibody media solution, wash twice with fresh media and replace media.
26. Repeat steps 24 and 25 for each time point.
27. After the final time point, wash all cells twice with media to ensure any fluorophore that has leaked out of cells is washed away.
28. Prepare Hoechst/media solution. Add 300 µL to each well and incubate at room temperature for five minutes. Δ **CRITICAL STEP** The Hoechst/media solution should always be prepared fresh and excess should be properly discarded.
29. Remove Hoechst/media solution and wash twice with media.
30. Remove well divider using tools provided with Chamber Slide System. **! CAUTION** The glass culture slide can break if too much force is applied.
31. Place slide underneath microscope and image each well using a 60× microscope objective. Image using 405/635/750 laser lines for Hoechst, DDAO, and IRDye, respectively. Save each image as a '.oib' file.
32. Import images using Fiji. Assign colors to each channel (Hoechst, blue; DDAO, red; IRDye, green) and save as a '.tiff'.

Ex Vivo Flow Cytometry • TIMING 2-4 weeks

33. Establish xenograft tumors in both flanks of 4-6 week old female nude athymic mice (Jackson Laboratories Foxn1^{nu}). Ensure the appropriate protocol is in accordance with institutional review board and animal care and use regulations. Place animals on non-fluorescent rodent chow at least 4 days before conducting experiments to reduce background autofluorescence. Allow subcutaneous tumors to reach 10-12 mm along the longest axis (tumor volume should be approximately 300-500 mm^3).
34. Prepare injection of dual label antibody by combining desired amount of antibody with USP PBS. Δ **CRITICAL STEP** The background signal for flow cytometry, microscopy, and biodistribution should be measured using PBS injected negative control mice.
35. Anesthetize tumor-bearing mouse and perform tail-vein injection of prepared dual label antibody.
36. To obtain plasma clearance data, take blood samples through retroorbital or saphenous vein sampling. Mix 10 µL of blood sample with 15 µL PBS-EDTA. Centrifuge at 3000*g* for 1 minute. Remove 15 µL of plasma and place in 384 well plate to scan on Odyssey CLx. Repeat at desired time points and ensure that total blood withdrawn does not exceed the approved animal protocol limit (e.g. 200 µL).
37. (Optional) Prepare solution of Hoechst 33342 at 15 mg/kg in USP PBS. To label functional vasculature in the tumor, anesthetize tumor-bearing mouse and inject with Hoechst/PBS solution 15 minutes prior to euthanasia.
38. Euthanize mouse in accordance with relevant guidelines and regulations. For example, perform cervical dislocation under anesthesia and double pneumothorax to confirm death.
39. After euthanasia, immediately resect each tumor. Ensure that excess skin and muscle are removed from the tumors. Scan both tumors on the Odyssey CLx.
40. To measure the multi-scale distribution in the same animal, parts of the tumor will be used for flow cytometry, histology, and biodistribution. To divide the tumor, gently cut tumor along the longest axis with razor blade. Cut 3 mm thick section along the longest

axis and place in cryomold with OCT. This part of the tumor will be used for histological analysis (Skip to Step 55). Gently cut the rest of the tumor into 1-2 ×1-2 mm pieces. Half of the remaining pieces will be used for flow cytometry and the other half for biodistribution (Skip to Step 63).

41. Select the remaining slices of tumor that will be used for flow cytometry. Place tumor pieces in **collagenase digest solution #1** at 37ºC. Δ **CRITICAL STEP** **Collagenase digest solution #1** should be prepared fresh.
42. Incubate tumor in digest solution for 25 minutes. Δ **CRITICAL STEP** Incubating for longer than 25 minutes can damage tumor cells and result in cell lysis and excess cell debris.
43. After incubation, centrifuge tumor suspension/collagenase mixture for 5 minutes at 300*g*. Carefully aspirate the supernatant so as to not disturb the cell/tumor pellet.
44. Resuspend tumor cell mixture in 8-10 mL of media kept at 4ºC. Keep media on ice or at 4ºC. Repeatedly pipet to break apart any clumps. Pipet cell mixture through 40 µm filter into a 50 mL conical. Repeat this twice
45. Centrifuge cells at 300*g* for 5 minutes. Ensure the centrifuge temperature is at 4ºC
46. Carefully aspirate the supernatant and resuspend in cell medium. Place on ice or at 4ºC. Count cells using hemacytometer and divide the tumor cell solution into microcentrifuge tubes, transferring approximately 1 x 10^6 cells to each tube. Place each tube on ice.
47. (Optional) Since DDAO and IRDye occupy the red and near-IR wavelengths of the visible spectrum, the blue and green wavelengths are available for additional fluorophore-antibody staining. Other stains include, for example, pharmacodynamics markers for ADCs, cell lineage markers for immune cells, or other cell surface markers on tumors. As with all multicolor flow cytometry, proper controls and/or compensation should be used to mitigate any spectral overlap. ? Troubleshooting
48. Centrifuge the microcentrifuge tubes at 300*g* for five minutes and remove supernatant. Place resulting cell pellets on ice for flow cytometry.
49. Immediately before running cells on the Attune Flow Cytometer, resuspend cells in PBS and filter through 40 µm filter tubes.
50. Run all samples on Attune Flow Cytometer. Ensure the PMT settings for RL1 (DDAO) and RL2 (IRDye) are adjusted so the background signal is around 1000 to maximize the dynamic range for these fluorophores. Export experiment for analysis in FlowJo.
51. Label a positive control. Prepare a positive control by diluting dually labeled antibody to 30 nM in 1 mL of cell media and then placing the solution on ice. Harvest *in vitro* cells and count using the hemacytomer. Place 100,000 cells in a microcentrifuge tube. Wash cells by centrifuging for 5 minutes at 300*g*, removing supernatant, and resuspending in 400µL cell media. Centrifuge cells for 5 minutes at 300*g* and remove supernatant media. Resuspend cells with positive control solution and place on ice for 30 minutes. After labeling, wash cells twice with media and run on flow cytometer using same settings used for tumor digest. The positive control is used to normalize the ratio of cellular events in the tumor digest to the ratio of intact dually labeled antibody, similar to the initial time point in the *in vitro* flow cytometry (step 21). Δ **CRITICAL STEP** An *in vitro* positive control should be prepared for each tumor digest.
52. Data analysis in FlowJo. Gate around cell population and plot RL1-H versus RL2-H fluorescence signal. Using a negative control mouse set negative gates for positive and negative signal for RL1-H (DDAO) and RL2-H (IRDye). Gates should be adjusted so

that there are less than 1% of cellular events in the positive quadrants for a negative control tumor. Once gates are adjusted, tumor cells that were targeted with antibody (RL2+) can be analyzed.

53. In FlowJo, export the cellular events for targeted cells to a '.csv'. Open the .csv in Microsoft Excel or import the data into Matlab. For each cellular event, background subtract the mean autofluorescence signal (from a negative control mouse) for both the RL1-H and RL2-H channels and divide the RL1 signal by the RL2 signal. Repeat this for the *in vitro* positive control. Then normalize the tumor digest ratio by dividing the mean DDAO/IRDye ratio by the *in vitro* positive control ratio. Multiply the normalized ratio by 100 to get the percent intact antibody. ? Troubleshooting
54. Quantify absolute fluorescence signal with Quantum Simply Cellular anti-Human IgG Quantitative Beads using manufacturer instructions.

Ex Vivo Microscopy • TIMING 4-5 hours

55. Place the section of tumor set aside for histology in OCT in a cryomold. Allow the tumor to incubate in OCT for 15 minutes. While incubating, cool isopentane using dry ice.
56. Once isopentane is chilled (dry ice does not bubble when placed in it), add cryomold to isopentane and wait 3 minutes. Once the tumor block is completely frozen transfer to an -80ºC fridge for longer-term storage.
57. Process the frozen tumor samples by slicing the frozen tissue blocks with a microtome cryostat. When slicing the tumor or tissue blocks, set the slice thickness to 16 µm. Mount the frozen section on a glass slide and store slides at -80ºC. ■ Pause Point The frozen slides can be stored for 1 year at -80ºC. Δ **CRITICAL STEP** Using thicker 16 µm (instead of the conventional 4 µm) will increase the fluorescence signal for microscopy. If using a confocal microscope, fully open the pinhole aperture to ensure maximum fluorescence signal.
58. (Optional) Before imaging, use additional labels of interest to stain the tumor. We commonly stain with antimouse CD31-AF488 to show all (functional and non-functional) vasculature. For antibody staining, combine antimouse CD31-AF488 with PBS to a concentration of 30 nM. Allow section to air dry in opaque container (10-15 minutes). Add 100 µL of staining solution on top of frozen section. Protect from light and incubate for 30 minutes at room temperature.
59. Remove antibody and transfer to a clean container and perform two 25mL PBS washes (2-3 minutes each).
60. Dry the slides at room temperature. ■ Pause Point The stained slides can be stored for 2 weeks at -80ºC.
61. Image the stained tumor/organ sections using the Olympus FV1200. Secure the slide on the microscope stage, lower the objective, and pipet PBS between sample and objective. Bring the sample into focus. Once the sample is in focus, open the "Multi-area time lapse" function in the microscope software. Outline the tissue slice in the "Zoomed Stage Map" area using the "Mosaic Outline" tool. Once the entire sample is outlined and the desired settings are selected, apply the settings to the "Registered Point List," and click "Play." **! CAUTION** For extended scans ensure the sample and objective remain immersed in PBS. ? Troubleshooting

62. Once the scan is complete, use the "Stitch" function in the "Multi Area Time Lapse Viewer" to show the large tumor/organ scan. Save the image as a ".oib" file. Open the ".oib" file in Fijj to assign the desired colors and adjust the brightness/contrast, then save the file as a ".tiff".

Ex Vivo Biodistribution • TIMING 3-4 hours

63. Place the section of tumor set aside for biodistribution on a clean cutting surface (we use a glass plate).
64. Fill weight boats with PBS for washing. Resect other organs of interest. For antibodies or ADCs, we recommend resecting the liver, tumor, kidney, spleen, heart, lungs, muscle, pancreas, small intestine, and skin. Place each organ in a weigh boat with PBS to wash the organ for about 30 seconds to 1 minute. After washing, take organ out of PBS and dab dry on a kimwipe. Set each organ on the clean cutting surface. **Δ CRITICAL STEP** The fluorescence intensity will be normalized by the weight of the organ so ensure that excess fat or connective tissue is removed from the organ.
65. Manually disrupt organs using razor blade by repeatedly dicing them. Use a fresh razor blade for each organ to avoid cross contamination.
66. Place each organ into a microcentrifuge tube and record the weight. **! CAUTION** For large organs (large tumors or the liver) do not exceed 500 mg in the microcentrifuge tube.
67. Prepare **collagenase digest solution #2** and add to each organ. Record the volume of solution added to each organ. For organs weighing less than 150 mg, 150 µL should be added. For organs that weigh greater than 150 mg and less than 500 mg, approximately an equal amount of **collagenase digest solution #2** in microliters should be added for the organ weight in milligrams (e.g. add 250 µL of solution for an organ weighing 250 mg). **Δ CRITICAL STEP Collagenase digest solution #2** should be prepared fresh before use.
68. Gently centrifuge each microcentrifuge tube using a tabletop centrifuge (10-20 seconds) and vortex (setting 10) for 30 seconds to ensure the organ is suspended in the digest mixture. Incubate the organ digest mixture for 1 hour in a 37ºC water bath.
69. After the incubation, sonicate each sample for one minute using sonic dismembrator with amplitude 20% and pulsing every 10 seconds. The sample should appear nearly homogeneous. **! CAUTION** Sample sonication can result in formation of aerosols. Perform sonication in biological safety cabinet according to safety protocols.
70. Prepare **Trypsin digest solution** and add the same volume of **Trypsin digest solution** as **collagenase digest solution #2** in step 67. **Δ CRITICAL STEP Trypsin digest solution** should be prepared fresh before use.
71. Gently centrifuge each microcentrifuge tube using a tabletop centrifuge (10-20 seconds) and vortex (setting 10) for 30 seconds to ensure the organ is suspended in the digest mixture. Incubate the organ digest mixture for 1 hour in a 37ºC water bath.
72. After the incubation, sonicate each sample for one minute using sonic dismembrator with amplitude 20% and pulsing every 10 seconds. The sample should appear nearly homogeneous. **! CAUTION** Sample sonication can result in formation of aerosols. Perform sonication in biological safety cabinet according to safety protocols.

73. Add 200 µL of each homogenized organ to a 96 well plate and serially dilute in 100 µL of PBS.
74. Place the 96 well plate on the Odyssey CLx glass and scan at 3.5mm height, medium quality, and 169µm resolution.
75. To determine the autofluorescence background, perform the biodistribution on saline injected negative control mice. Quantify the fluorescence intensity from the same scan settings on the Odyssey to fluorescence signal per weight of tissue.
76. Prepare a calibration curve. Make a known concentration of dually labeled antibody in mouse plasma. Add **collagenase digest solution #2** and digest as outlined above (step 67). Add **trypsin digest solution** and digest as outlined above (step 70). Serially dilute in a 96 well plate with PBS and scan on the Odyssey CLx using the same scan settings as above (step 74). Make a calibration curve correlating the fluorescence intensity in each well to the concentration of dually labeled antibody.
77. Calculate the percent-injected dose per gram (%ID/g) for each organ. Calculate the fluorescence intensity per milligram of tissue. Assume a tissue density of 1 mg/µL for most tissues. Calculate the signal from autofluorescence by multiplying the autofluorescence signal per milligram by the amount of tissue in the well. Background subtract the autofluorescence signal. Using the calibration curve, correlate the fluorescence signal intensity to the concentration in the well. Multiply the fluorescence concentration in the well by the volume of solution in the well to receive the absolute amount of probe in the well. Divide the absolute amount in the well by the absolute amount injected and multiply by 100 to get the percent injected dose. Normalize by dividing by the organ weight in grams to receive the percent-injected dose per gram (%ID/g).

TROUBLESHOOTING

Step 3, determining optimal molar ratios for antibody labeling. Each protein, antibody, or ADC will require optimization of molar ratio for labeling. Increase or decrease the molar ratio accordingly; however, ensure the final dye to protein ratio does not exceed 0.3 for IRDye and 0.7 for DDAO.

Step 47, fixing/permeabilizing cells. Multicolor flow cytometry staining for intracellular targets may require permeabilization; however, permeabilization of cells will allow free dye (even residualizing dye) to permeate out of cell. Use an unpermeabilized control to calculate cumulative protein uptake.

Step 53, cell death in the in vitro microscopy or in vitro flow cytometry. Since the payload in ADCs may exert a cytotoxic effect on a cell, it can result in cell death before imaging or running on flow cytometry. If this occurs, shorten the time course to before the ADC can induce cell death.

Step 53, excessive debris on tumor digest. Digest for a shorter amount of time. Do not centrifuge at greater than 300*g*. Avoid selecting clearly necrotic tumor pieces for flow cytometry.

Step 53, variability in intact protein fraction from tumor digest. Perform the histogram analysis. 24-48 hours after injection, there may be two populations (intact and degraded). While the tumor takes up and degrades some antibody, there is still a constant supply of intact antibody from the blood, which can result in a bimodal distribution. The histogram analysis will show a more detailed cellular distribution of intact or degraded antibody while the mean shows the aggregate distribution.

Step 61, ex vivo fluorescence histology imaging. The radiant sensitivity and quantum efficiency of the Olympus FV1200 PMT decreases significantly at wavelengths above 825 nm. To maximize fluorescence signal the laser and PMT settings for the 800CW channel may have to increase to maximum. Additionally, increasing the pixel dwell time may improve signal; however, increasing the pixel dwell time for too long can result in photobleaching. Using Kalman filtering of 2-3 is highly recommended to reduce background noise.

Appendix B – Table of PBPK-Krogh Cylinder Model Parameters

Table B.1 Table of PBPK-Krogh Cylinder Model Parameters.

Parameters	Units	Value	Description	References
Q_kidney_sp	mL/s/g	0.0403	Flowrates on mass basis	(*60*)
Q_carcass_sp	mL/s/g	0.0017	Flowrates on mass basis	(*60*)
Q_liver_sp	mL/s/g	0.0120	Flowrates on mass basis	(*60*)
Q_spleen_sp	mL/s/g	0.0083	Flowrates on mass basis	(*60*)
Q_heart_sp	mL/s/g	0.0306	Flowrates on mass basis	(*156*)
Q_lung_sp	mL/s/g	0.3570	Flowrates on mass basis	(*156*)
L_kidney_sp	mL/s/g	8.05×10^{-05}	Lymph flowrate on mass basis	Blood flowrate divided by 500
L_carcass_sp	mL/s/g	3.40×10^{-06}	Lymph flowrate on mass basis	Blood flowrate divided by 500
L_liver_sp	mL/s/g	2.40×10^{-05}	Lymph flowrate on mass basis	Blood flowrate divided by 500
L_spleen_sp	mL/s/g	1.67×10^{-05}	Lymph flowrate on mass basis	Blood flowrate divided by 500
L_heart_sp	mL/s/g	6.12×10^{-05}	Lymph flowrate on mass basis	Blood flowrate divided by 500
L_lung_sp	mL/s/g	7.14×10^{-04}	Lymph flowrate on mass basis	Blood flowrate divided by 500
V_v_kidney_sp	mL/g	0.12	Vascular volume on per mass basis	(*60*)
V_i_kidney_sp	mL/g	0.339	Interstitial volume on per mass basis	(*60*)
V_v_carcass_sp	mL/g	0.02	Vascular volume on per mass basis	(*60*)
V_i_carcass_sp	mL/g	0.108	Interstitial volume on per mass basis	(*60*)
V_v_liver_sp	mL/g	0.1	Vascular volume on per mass basis	(*60*)
V_i_liver_sp	mL/g	0.2	Interstitial volume on per mass basis	(*60*)
V_v_spleen_sp	mL/g	0.1	Vascular volume on per mass basis	(*60*)
V_i_spleen_sp	mL/g	0.2	Interstitial volume on per mass basis	(*60*)
V_v_heart_sp	mL/g	0.046	Vascular volume on per mass basis	(*156*)
V_i_heart_sp	mL/g	0.125	Interstitial volume on per mass basis	(*156*)
V_v_lung_sp	mL/g	0.093	Vascular volume on per mass basis	(*156*)

Parameters	Units	Value	Description	References
V_i_lung_sp	mL/g	0.279	Interstitial volume on per mass basis	(*156*)
mass_kidney	g	0.304	mass of organ	(*60*)
mass_carcass	g	21.304	mass of organ	(*60*)
mass_liver	g	1.272	mass of organ	(*60*)
mass_spleen	g	0.127	mass of organ	(*60*)
mass_heart	g	0.152	mass of organ	(*161*)
mass_lung	g	0.204	mass of organ	(*161*)
Q_kidney	mL/s	0.0122	Flowrate to kidney	Calculated
Q_carcass	mL/s	0.0362	Flowrate to carcass	Calculated
Q_liver	mL/s	0.0153	Flowrate to liver	Calculated
Q_spleen	mL/s	0.0011	Flowrate to spleen	Calculated
Q_heart	mL/s	0.0047	Flowrate to heart	Calculated
Q_lung	mL/s	0.0728	Flowrate to lung	Calculated
L_kidney	mL/s	2.45×10^{-05}	Lymph flowrate in kidney	Calculated
L_carcass	mL/s	7.24×10^{-05}	Lymph flowrate in carcass	Calculated
L_liver	mL/s	3.06×10^{-05}	Lymph flowrate in liver	Calculated
L_spleen	mL/s	2.12×10^{-06}	Lymph flowrate in spleen	Calculated
L_heart	mL/s	9.30×10^{-06}	Lymph flowrate in heart	Calculated
L_lung	mL/s	1.46×10^{-04}	Lymph flowrate in lung	Calculated
V_plasma	mL	0.572	Volume of plasma	Calculated
V_v_kidney	mL	0.036	Vascular volume of kidney	Calculated
V_i_kidney	mL	0.103	Interstitial volume of kidney	Calculated
V_v_carcass	mL	0.426	Vascular volume of carcass	Calculated
V_i_carcass	mL	2.301	Interstitial volume of carcass	Calculated
V_v_liver	mL	0.127	Vascular volume of liver	Calculated
V_i_liver	mL	0.254	Interstitial volume of liver	Calculated
V_v_spleen	mL	0.013	Vascular volume of spleen	Calculated
V_i_spleen	mL	0.025	Interstitial volume of spleen	Calculated
V_v_heart	mL	0.007	Vascular volume of heart	Calculated
V_i_heart	mL	0.019	Interstitial volume of heart	Calculated
V_v_lung	mL	0.019	Vascular volume of lung	Calculated
V_i_lung	mL	0.057	Interstitial volume of lung	Calculated
k_deg_liver	mL/s	7.369×10^{-06}	Liver degradation rate in organ	Fit to experimental data
k_deg_FcRn	mL/s	5.220×10^{-03}	FcRn degradation rate	(*60*)
k_deg_organ	mL/s	3.176×10^{-07}	Organ degradation rate	Fit to experimental data
k_int	mL/s	2.450×10^{-05}	Internalization rate	(*166*)

Parameters	Units	Value	Description	References
k_rec	1/s	5.75×10^{-05}	FcRn recycle rate	(*166*)
U	1/s	6.963×10^{-04}	Urinary excretion rate	Fit to experimental data
k_loss	1/s	5.244×10^{-05}	Metabolite loss rate	Fit to experimental data
J_iso_kidney_sp	mL/s/g	4.18×10^{-06}	Fluid recirculation flowrate on mass basis	(*60*)
J_iso_carcass_sp	mL/s/g	2.42×10^{-06}	Fluid recirculation flowrate on mass basis	(*60*)
J_iso_liver_sp	mL/s/g	1.93×10^{-06}	Fluid recirculation flowrate on mass basis	(*60*)
J_iso_spleen_sp	mL/s/g	2.67×10^{-07}	Fluid recirculation flowrate on mass basis	(*60*)
J_iso_heart_sp	mL/s/g	5.60×10^{-05}	Fluid recirculation flowrate on mass basis	(*156*)
J_iso_lung_sp	mL/s/g	5.00×10^{-04}	Fluid recirculation flowrate on mass basis	(*156*)
PSL_sp	mL/s/g	4.44×10^{-08}	Permeability surface area product for large pores	(*156*)
PSS_sp	mL/s/g	1.30×10^{-07}	Permeability surface area product for small pores	(*156*)
sigma_L	dimension less	0.26	Reflection coefficient for large pores	(*166*)
sigma_S	dimension less	0.98	Reflection coefficient for small pores	(*166*)
alpha_L	dimension less	0.042	Fraction extravasation occurring via large pores	(*60*)
alpha_L_kidney	dimension less	0.002	Fraction extravasation occurring via large pores	(*60*)
B_max_heart	mol/mL	1.00×10^{-12}	Antigen concentration	Assumed

Appendix C – PBPK-Krogh Cylinder Model Equations

Krogh Cylinder Tissue Model Equations

Free mAb

$$\frac{\partial C_{mab}}{\partial t} = D_{eff}\left(\frac{1}{r}\frac{\partial}{\partial r}\left(r\frac{\partial C_{mab}}{\partial r}\right)\right) - k_{on}\frac{C_{mab}}{\varepsilon}T_{free} + k_{off}B_{mab}$$

Free ADC

$$\frac{\partial C_{ADC}}{\partial t} = D_{eff}\left(\frac{1}{r}\frac{\partial}{\partial r}\left(r\frac{\partial C_{ADC}}{\partial r}\right)\right) - k_{on}\frac{C_{ADC}}{\varepsilon}T_{free} + k_{off}B_{ADC}$$

Free Target

$$\frac{\partial T_{free}}{\partial t} = R_s - k_{on}\frac{C_{mab}}{\varepsilon}T_{free} - k_{on}\frac{C_{ADC}}{\varepsilon}T_{free} + k_{off}B_{mab} + k_{off}B_{ADC} - k_eT_{free}$$

Bound mAb

$$\frac{\partial B_{mab}}{\partial t} = k_{on}\frac{C_{mab}}{\varepsilon}T_{free} - k_{off}B_{mab} - k_{int}B_{mab}$$

Bound ADC

$$\frac{\partial B_{ADC}}{\partial t} = k_{on}\frac{C_{ADC}}{\varepsilon}T_{free} - k_{off}B_{ADC} - k_{int}B_{ADC}$$

Internalized mAb

$$\frac{\partial C_{int,mab}}{\partial t} = k_{int}B_{mab} - k_{loss}C_{int,mab}$$

Internalized ADC

$$\frac{\partial C_{int,ADC}}{\partial t} = k_{int}B_{ADC} - k_{loss}C_{int,ADC}$$

Boundary Conditions

1.

$$-D_{eff}\frac{dC_{free}}{dr}\Big|_{r=R_{capillary}} = P\left(C_{plasma} - \frac{C_{free}}{\varepsilon(1+R)}\right)$$

2.

$$D_{eff}\frac{dC_{free}}{dr}\Big|_{r=R_{Krogh}} = 0$$

3.

$$C_{plasma,in} = C_{plasma,PBPK}$$

Krogh cylinder exit concentration derivation

Although antibodies are permeability limited and do not possess significant axial gradients along the length of the blood vessel (*90*), the exchange with the tumor must be quantified to satisfy the mass balance. Here we assume pseudo-steady state, constant capillary length, capillary radius, Krogh cylinder radius, free fraction equals 1, and constant blood flow rate to the tumor.

$$\frac{dC_{plasma}}{dt} = -v * \frac{\partial C_{plasma}}{\partial L} - \frac{2P}{(1-H)R_{cap}}\left(f_{free}C_{plasma,in} - \frac{C_{free,mab}}{\varepsilon}\right)$$

$$v * \frac{C_{plasma,out} - C_{plasma,in}}{L} = -\frac{2P}{(1-H)R_{cap}}\left(C_{plasma,in} - \frac{C_{free,mab}}{\varepsilon}\right)$$

$$C_{plasma,out} = C_{plasma,in} - \frac{L}{v}\frac{2P}{(1-H)R_{cap}}\left(C_{plasma,in} - \frac{C_{free,mab}}{\varepsilon}\right)$$

$$v = \frac{Q * {R_{krogh}}^2 L}{{R_{cap}}^2}$$

$$C_{plasma,out} = C_{plasma,in} - \frac{2P}{(1-H)}\frac{R_{cap}}{{R_{krogh}}^2 Q}\left(C_{plasma} - \frac{C_{free,mab}}{\varepsilon}\right)$$

PBPK Model Equations

The general structure of this model was based on Ferl et al. 2006 (*60*). The equations describing the ADC portion of the model are identical to the free antibody PBPK model described below. The list of parameters used in the model can be found in Appendix B.

Kidney

$$\frac{dN_{K,v}}{dt} = \frac{Q_{kidney}}{V_{plasma}} N_{plasma} - \frac{Q_{kidney} - L_{kidney}}{V_{v,kidney}} N_{K,v} - J_{i,v} - k_{deg,kidney} N_{K,v}$$

$$\frac{dN_{K,i}}{dt} = J_{i,v} - \frac{L_{kidney}}{V_{i,kidney}} N_{T,i}$$

$$\frac{dN_{K,M}}{dt} = \frac{Q_{kidney}}{V_{plasma}} N_{M,plasma} + k_{deg,kidney} N_{K,v} - U N_{K,M}$$

Carcass

$$\frac{dN_{C,v}}{dt} = \frac{Q_{carcass}}{V_{plasma}} N_{plasma} + k_{rec} N_{C,E} - \frac{Q_{carcass} - L_{carcass}}{V_{v,carcass}} N_{C,v} - \frac{k_{int}}{V_{v,carcass}} N_{C,v} - J_{i,v}$$

$$\frac{dN_{C,i}}{dt} = J_{i,v} - \frac{L_{carcass}}{V_{i,carcass}} N_{C,i}$$

$$\frac{dN_{C,E}}{dt} = \frac{k_{int}}{V_{v,carcass}} N_{C,v} - k_{rec} N_{C,E} - k_{deg,FcRn} N_{C,E}$$

$$\frac{dN_{C,M}}{dt} = k_{deg,FcRn} N_{C,E} - k_{loss,C} N_{C,M}$$

Liver

$$\frac{dN_{L,v}}{dt} = \frac{Q_{liver}}{V_{plasma}} N_{plasma} + \frac{Q_{spleen} - L_{spleen}}{V_{v,spleen}} N_{S,v} - \frac{Q_{liver} - L_{liver} - (Q_{spleen} - L_{spleen})}{V_{v,liver}} N_{L,v}$$

$$- \frac{k_{deg,liver}}{V_{v,liver}} N_{L,v} - J_{i,v}$$

$$\frac{dN_{L,i}}{dt} = J_{i,v} - \frac{L_{liver}}{V_{i,liver}} N_{L,i}$$

$$\frac{dN_{L,M}}{dt} = \frac{k_{deg,liver}}{V_{v,liver}} N_{L,v} - k_{loss,L} N_{L,M}$$

Spleen

$$\frac{dN_{S,v}}{dt} = \frac{Q_{spleen}}{V_{plasma}} N_{plasma} - \frac{Q_{spleen} - L_{spleen}}{V_{v,spleen}} N_{S,v} - \frac{k_{deg,spleen}}{V_{v,liver}} N_{S,v} - J_{i,v}$$

$$\frac{dC_{S,i}}{dt} = J_{i,v} - \frac{L_{spleen}}{V_{i,spleen}} N_{S,i}$$

$$\frac{dC_{S,M}}{dt} = \frac{k_{deg,spleen}}{V_{v,spleen}} N_{S,v} - k_{loss,S} N_{S,M}$$

Plasma

$$\begin{aligned}\frac{dC_{plasma}}{dt} = {} & \frac{L_{kidney}}{V_{i,kidney}} N_{K,i} + \frac{L_{carcass}}{V_{i,carcass}} N_{C,i} + \frac{L_{heart}}{V_{i,heart}} N_{H,i} + \frac{L_{lung}}{V_{i,lung}} N_{L,i} + \frac{L_{spleen}}{V_{i,spleen}} N_{S,i} \\ & + \frac{L_{liver}}{V_{i,liver}} N_{L,i} + \frac{Q_{kidney} - L_{kidney}}{V_{v,kidney}} N_{K,v} + \frac{Q_{carcass} - L_{carcass}}{V_{v,carcass}} N_{C,v} \\ & + \frac{Q_{heart} - L_{heart}}{V_{v,heart}} N_{H,v} + \frac{Q_{lung} - L_{lung}}{V_{v,lung}} N_{L,v} \\ & + \frac{(Q_{liver} - L_{liver} - (Q_{spleen} - L_{spleen}))}{V_{v,liver}} N_{L,v} - \frac{Q_{liver}}{V_{plasma}} N_{plasma} \\ & - \frac{Q_{kidney}}{V_{plasma}} N_{plasma} - \frac{Q_{carcass}}{V_{plasma}} N_{plasma} - \frac{Q_{spleen}}{V_{plasma}} N_{plasma} - \frac{Q_{heart}}{V_{plasma}} N_{plasma} \\ & - \frac{Q_{lung}}{V_{plasma}} N_{plasma} + DOSE(t) - \frac{Q_{tumor}}{V_{plasma}} N_{plasma} + Q_{tumor} C_{plasma,Krogh\_exit}\end{aligned}$$

$$\frac{dN_{M,plasma}}{dt} = k_{loss,C}N_{C,M} + k_{loss,L}N_{L,M} + k_{loss,S}N_{S,M} + k_{loss,H}N_{H,M} + k_{loss,L}N_{L,M}$$

$$+ k_{loss,T}N_{T,M} - \frac{Q_{kidney}}{V_{plasma}}N_{M,plasma}$$

Heart

$$\frac{dN_{H,v}}{dt} = \frac{Q_{heart}}{V_{plasma}}N_{plasma} - \frac{Q_{heart} - L_{heart}}{V_{v,heart}}N_{H,v} - J_{i,v} - k_{deg,heart}N_{H,v}$$

$$\frac{dN_{H,i}}{dt} = J_{i,v} - \frac{L_{heart}}{V_{i,heart}}N_{H,i}$$

$$\frac{dN_{H,M}}{dt} = \frac{k_{deg,heart}}{V_{v,heart}}N_{H,v} - k_{loss,H}N_{H,M}$$

Lung

$$\frac{dN_{L,v}}{dt} = \frac{Q_{lung}}{V_{plasma}}N_{plasma} - \frac{Q_{lung} - L_{lung}}{V_{v,lung}}N_{L,v} - J_{i,v} - k_{deg,lung}N_{L,v}$$

$$\frac{dN_{L,i}}{dt} = J_{i,v} - \frac{L_{lung}}{V_{i,lung}}N_{L,i}$$

$$\frac{dN_{L,M}}{dt} = \frac{k_{deg,lung}}{V_{v,lung}}N_{L,v} - k_{loss,L}N_{L,M}$$

$$V_{plasma} = Total\ blood - V_{v,kidney} - V_{v,carcass} - V_{v,liver} - V_{v,spleen} - V_{v,heart} - V_{v,lung}$$

Two-pore

$$J_{i,v} = J_{L,organ}(1 - \sigma_L)\left(\frac{N_{organ,v}}{V_{v,organ}}\right) + PS_{L,organ}\left[\frac{N_{organ,v}}{V_{v,organ}} - \frac{N_{organ,i}}{V_{i,organ}}\right]\left[\frac{Pe_{L,organ}}{e^{Pe_{L,organ}} - 1}\right]$$

$$+ J_{S,organ}(1 - \sigma_S)\left(\frac{N_{organ,v}}{V_{v,organ}}\right)$$

$$+ PS_{S,organ}\left[\frac{N_{organ,v}}{V_{v,organ}} - \frac{N_{organ,i}}{V_{i,organ}}\right]\left[\frac{Pe_{S,organ}}{e^{Pe_{S,organ}} - 1}\right]$$

$$Pe_{L,organ} = \frac{J_{L,organ}(1 - \sigma_L)}{PS_{L,organ}}$$

$$Pe_{S,organ} = \frac{J_{S,organ}(1-\sigma_S)}{PS_{S,organ}}$$

$$PS_{L,organ} = PS_L Mass_{organ}$$

$$PS_{S,organ} = PS_S Mass_{organ}$$

$$J_{L,organ} = J_{iso,organ} + \alpha_{L,organ} L_{organ}$$

$$J_{S,organ} = J_{iso,organ} + \alpha_{S,organ} L_{organ}$$

$$J_{iso,organ} = J_{iso,organ,sp} Mass_{organ}$$

$$\alpha_S = 1 - \alpha_L$$

$$\alpha_{S,kidney} = 1 - \alpha_{L,kidney}$$

Heart with Bound Compartment

$$\frac{dN_{H,v}}{dt} = \frac{Q_{heart}}{V_{plasma}} N_{plasma} - \frac{Q_{heart} - L_{heart}}{V_{v,heart}} N_{H,v} - J_{i,v} - k_{deg,heart} N_{H,v}$$

$$\frac{dN_{H,i}}{dt} = J_{i,v} - \frac{L_{heart}}{V_{i,heart}} N_{H,i} + k_{off} N_{H,b} - k_{on} \left[B_{max} - \frac{N_{H,b}}{V_{i,heart}} \right] N_{H,i}$$

$$\frac{dN_{H,B}}{dt} = k_{on} \left[B_{max} - \frac{N_{H,b}}{V_{i,heart}} \right] N_{H,i} - k_{off} N_{H,b} - \frac{k_{deg,heart}}{V_{i,heart}} N_{H,v}$$

$$\frac{dN_{H,M}}{dt} = \frac{k_{deg,heart}}{V_{i,heart}} N_{H,v} - k_{loss,H} N_{H,M}$$

References

1. Scott AM, Wolchok JD, Old LJ. Antibody therapy of cancer. *Nat Rev Cancer*. 2012;12:278-287.
2. Ecker DM, Jones SD, Levine HL. The therapeutic monoclonal antibody market. *MAbs*. 2015;7:9-14.
3. Kaplon H, Reichert JM. Antibodies to watch in 2018. *MAbs*. 2018;10:183-203.
4. Murphy K, Travers P, Walport M, Janeway C. Janeway's immunobiology. New York: Garland Science; 2012.
5. Hudis CA. Trastuzumab — Mechanism of Action and Use in Clinical Practice. *N Engl J Med*. 2007;357:39-51.
6. Adams GP, Weiner LM. Monoclonal antibody therapy of cancer. *Nat Biotechnol*. 2005;23:1147-1157.
7. Li F, Ulrich M, Jonas M, et al. Tumor-Associated Macrophages Can Contribute to Antitumor Activity through FcγR-Mediated Processing of Antibody-Drug Conjugates. *Mol Cancer Ther*. 2017;16:1347-1354.
8. Beck A, Goetsch L, Dumontet C, Corvaïa N. Strategies and challenges for the next generation of antibody–drug conjugates. *Nat Rev Drug Discov*. 2017;16:315-337.
9. Wu AM, Senter PD. Arming antibodies: prospects and challenges for immunoconjugates. *Nat Biotechnol*. 2005;23:1137-1146.
10. Doronina SO, Mendelsohn BA, Bovee TD, et al. Enhanced activity of monomethylauristatin F through monoclonal antibody delivery: Effects of linker technology on efficacy and toxicity. *Bioconjug Chem*. 2006;17:114-124.
11. Erickson HK, Widdison WC, Mayo MF, et al. Tumor Delivery and In Vivo Processing of Disulfide-Linked and Thioether-Linked Antibody−Maytansinoid Conjugates. *Bioconjug Chem*. 2010;21:84-92.
12. Sun X, Widdison W, Mayo M, et al. Design of Antibody−Maytansinoid Conjugates Allows for Efficient Detoxification via Liver Metabolism. *Bioconjug Chem*. 2011;22:728-735.
13. Erickson HK, Park PU, Widdison WC, et al. Antibody-maytansinoid conjugates are activated in targeted cancer cells by lysosomal degradation and linker-dependent intracellular processing. *Cancer Res*. 2006;66:4426-4433.
14. Younes A, Gopal AK, Smith SE, et al. Results of a Pivotal Phase II Study of Brentuximab Vedotin for Patients With Relapsed or Refractory Hodgkin's Lymphoma. *J Clin Oncol*. 2012;30:2183-2189.

15. Verma S, Miles D, Gianni L, et al. Trastuzumab Emtansine for HER2-Positive Advanced Breast Cancer. *N Engl J Med*. 2012;367:1783-1791.

16. Kantarjian HM, DeAngelo DJ, Stelljes M, et al. Inotuzumab Ozogamicin versus Standard Therapy for Acute Lymphoblastic Leukemia. *N Engl J Med*. 2016;375:740-753.

17. Beck A, Reichert JM. Antibody-drug conjugates present and future. *MAbs*. 2014;6:15-17.

18. Castaigne S, Pautas C, Terré C, et al. Effect of gemtuzumab ozogamicin on survival of adult patients with de-novo acute myeloid leukaemia (ALFA-0701): a randomised, open-label, phase 3 study. *Lancet*. 2012;379:1508-1516.

19. Junutula JR, Raab H, Clark S, et al. Site-specific conjugation of a cytotoxic drug to an antibody improves the therapeutic index. *Nat Biotechnol*. 2008;26:925-932.

20. Shen B-Q, Xu K, Liu L, et al. Conjugation site modulates the in vivo stability and therapeutic activity of antibody-drug conjugates. *Nat Biotechnol*. 2012;30:184-189.

21. Singh SK, Luisi DL, Pak RH. Antibody-Drug Conjugates: Design, Formulation and Physicochemical Stability. Vol 32.; 2015.

22. Jain N, Smith SW, Ghone S, Tomczuk B. Current ADC Linker Chemistry. *Pharm Res*. 2015;32:3526-3540.

23. Lyon RP, Setter JR, Bovee TD, et al. Self-hydrolyzing maleimides improve the stability and pharmacological properties of antibody-drug conjugates. *Nat Biotechnol*. 2014;32:1059-1062.

24. Lyon RP, Bovee TD, Doronina SO, et al. Reducing hydrophobicity of homogeneous antibody-drug conjugates improves pharmacokinetics and therapeutic index. *Nat Biotechnol*. 2015;33:733-735.

25. Li F, Emmerton KK, Jonas M, et al. Intracellular released payload influences potency and bystander-killing effects of antibody-drug conjugates in preclinical models. *Cancer Res*. 2016;76:2710-2719.

26. Pillow TH, Schutten M, Yu S, et al. Modulating Therapeutic Activity and Toxicity of Pyrrolobenzodiazepine Antibody–Drug Conjugates with Self-Immolative Disulfide Linkers. *Mol Cancer Ther*. 2017;16:871-878.

27. Miller ML, Fishkin NE, Li W, et al. A new class of antibody-drug conjugates with potent DNA alkylating activity. *Mol Cancer Ther*. 2016;15:1870-8.

28. Hamblett KJ, Senter PD, Chace DF, et al. Effects of drug loading on the antitumor activity of a monoclonal antibody drug conjugate. *Clin Cancer Res*. 2004;10:7063-70.

29. Sun X, Ponte JF, Yoder NC, et al. Effects of Drug-Antibody Ratio on Pharmacokinetics, Biodistribution, Efficacy, and Tolerability of Antibody-Maytansinoid Conjugates. *Bioconjug Chem*. 2017;28:1371-1381.

30. Oldham RK, Foon KA, Morgan AC, et al. Monoclonal antibody therapy of malignant melanoma: in vivo localization in cutaneous metastasis after intravenous administration. *J Clin Oncol*. 1984;2:1235-1244.

31. Schroff RW, Woodhouse CS, Foon KA, et al. Intratumor localization of monoclonal antibody in patients with melanoma treated with antibody to a 250,000-dalton melanoma-

associated antigen. *J Natl Cancer Inst*. 1985;74:299-306.

32. Schroff RW, Morgan AC, Woodhouse CS, et al. Monoclonal antibody therapy in malignant melanoma: factors effecting in vivo localization. *J Biol Response Mod*. 1987;6:457-72.

33. Del Vecchio S, Reynolds JC, Carrasquillo JA, et al. Local distribution and concentration of intravenously injected ^{131}I-9. 2. 27 monoclonal antibody in human malignant melanoma. *Cancer Res*. 1989;5:2783-2789.

34. Elias DJ, Hirschowitz L, Kline LE, et al. Phase I clinical comparative study of monoclonal antibody KS1/4 and KS1/4-methotrexate immunconjugate in patients with non-small cell lung carcinoma. *Cancer Res*. 1990;50:4154-9.

35. Scott AM, Lee F, Jones R, et al. Cancer Therapy : Clinical A Phase I Trial of Humanized Monoclonal Antibody A33 in Patients with Colorectal Carcinoma : Biodistribution , Pharmacokinetics , and QuantitativeTumor Uptake. *Clin Cancer Res*. 2005;11:4810-4817.

36. Baker JHE, Lindquist KE, Huxham L a., Kyle AH, Sy JT, Minchinton AI. Direct visualization of heterogeneous extravascular distribution of trastuzumab in human epidermal growth factor receptor type 2 overexpressing xenografts. *Clin Cancer Res*. 2008;14:2171-2179.

37. Thurber GM, Schmidt MM, Wittrup KD. Antibody tumor penetration: Transport opposed by systemic and antigen-mediated clearance. *Adv Drug Deliv Rev*. 2008;60:1421-1434.

38. Jain RK, Baxter LT. Mechanisms of heterogeneous distribution of monoclonal antibodies and other macromolecules in tumors: significance of elevated interstitial pressure. *Cancer Res*. 1988;48:7022-32.

39. van Osdol W, Fujimori K, Weinstein JN. An Analysis of Monoclonal Antibody Distribution in Microscopic Tumor Nodules: Consequences of a “Binding Site Barrier.” *Cancer Res*. 1991;51:4776 LP-4784.

40. Thurber GM, Schmidt MM, Wittrup KD. Factors determining antibody distribution in tumors. *Trends Pharmacol Sci*. 2008;29:57-61.

41. Rhoden JJ, Wittrup KD. Dose Dependence of Intratumoral Perivascular Distribution of Monoclonal Antibodies. *J Pharm Sci*. 2012;101:860-867.

42. Schmidt MM, Wittrup KD. A modeling analysis of the effects of molecular size and binding affinity on tumor targeting. *Mol Cancer Ther*. 2009;8:2861-2871.

43. Thurber GM, Zajic SC, Wittrup KD. Theoretic criteria for antibody penetration into solid tumors and micrometastases. *J Nucl Med*. 2007;48:995-999.

44. Minchinton AI, Tannock IF. Drug penetration in solid tumours. *Nat Rev Cancer*. 2006;6:583-592.

45. Welt S, Divgi CR, Real FX, et al. Quantitative analysis of antibody localization in human metastatic colon cancer: a phase I study of monoclonal antibody A33. *J Clin Oncol*. 1990;8:1894-1906.

46. Cilliers C, Menezes B, Nessler I, Linderman J, Thurber GM. Improved tumor penetration and single-cell targeting of antibody–drug conjugates increases anticancer efficacy and

host survival. *Cancer Res*. 2018;78:758-768.

47. Donaghy H. Effects of antibody, drug and linker on the preclinical and clinical toxicities of antibody-drug conjugates. *MAbs*. 2016;8:659-671.

48. Krop IE, Beeram M, Modi S, et al. Phase I study of trastuzumab-DM1, an HER2 antibody-drug conjugate, given every 3 weeks to patients with HER2-positive metastatic breast cancer. *J Clin Oncol*. 2010;28:2698-2704.

49. Leyland-Jones B, Colomer R, Trudeau ME, et al. Intensive loading dose of trastuzumab achieves higher-than-steady-state serum concentrations and is well tolerated. *J Clin Oncol*. 2010;28:960-966.

50. Chari RVJ. Expanding the Reach of Antibody–Drug Conjugates. *ACS Med Chem Lett*. 2016;7:974-976.

51. Bouchard H, Viskov C, Garcia-Echeverria C. Antibody–drug conjugates—A new wave of cancer drugs. *Bioorg Med Chem Lett*. 2014;24:5357-5363.

52. Vugmeyster Y. Pharmacokinetics and toxicology of therapeutic proteins: Advances and challenges. *World J Biol Chem*. 2012;3:73.

53. Oliveira S, Cohen R, Walsum M, et al. A novel method to quantify IRDye800CW fluorescent antibody probes ex vivo in tissue distribution studies. *EJNMMI Res*. 2012;2:50.

54. Adams GP, Schier R, McCall a. M, et al. High affinity restricts the localization and tumor penetration of single-chain Fv antibody molecules. *Cancer Res*. 2001;61:4750-4755.

55. Smaglo BG, Aldeghaither D, Weiner LM. The development of immunoconjugates for targeted cancer therapy. *Nat Rev Clin Oncol*. 2014;11:637-648.

56. Brand C, Abdel-Atti D, Zhang Y, et al. In Vivo Imaging of GLP-1R with a Targeted Bimodal PET/Fluorescence Imaging Agent. *Bioconjug Chem*. 2014;25:1323-1330.

57. Kimura RH, Cheng Z, Gambhir SS, Cochran JR. Engineered knottin peptides: a new class of agents for imaging integrin expression in living subjects. *Cancer Res*. 2009;69:2435-42.

58. Seibold U, Wängler B, Schirrmacher R, Wängler C. Bimodal Imaging Probes for Combined PET and OI: Recent Developments and Future Directions for Hybrid Agent Development. *Biomed Res Int*. 2014;2014:1-13.

59. Press OW, Shan D, Howell-Clark J, et al. Comparative Metabolism and Retention of Iodine-125, Yttrium-90, and Indium-111 Radioimmunoconjugates by Cancer Cells. *Cancer Res*. 1996;56:2123-9.

60. Ferl GZ, Kenanova V, Wu AM, DiStefano JJ. A two-tiered physiologically based model for dually labeled single-chain Fv-Fc antibody fragments. *Mol Cancer Ther*. 2006;5:1550-8.

61. Griffiths GL, Govindan S V., Sgouros G, Ong GL, Goldenberg DM, Mattes MJ. Cytotoxicity with Auger electron-emitting radionuclides delivered by antibodies. *Int J Cancer*. 1999;81:985-992.

62. Knowles SM, Zettlitz KA, Tavare R, et al. Quantitative ImmunoPET of Prostate Cancer Xenografts with 89Zr- and 124I-Labeled Anti-PSCA A11 Minibody. *J Nucl Med*.

2014;55:452-459.

63. Williams S-P. Tissue Distribution Studies of Protein Therapeutics Using Molecular Probes: Molecular Imaging. *AAPS J*. 2012;14:389-399.

64. Thurber GM, Dane Wittrup K. A mechanistic compartmental model for total antibody uptake in tumors. *J Theor Biol*. 2012;314:57-68.

65. Gioux S, Choi HS, Frangioni J V. Image-Guided Surgery Using Invisible Near-Infrared Light: Fundamentals of Clinical Translation. *Mol Imaging*. 2010;9:237-255.

66. Laughney AM, Kim E, Sprachman MM, et al. Single-cell pharmacokinetic imaging reveals a therapeutic strategy to overcome drug resistance to the microtubule inhibitor eribulin. *Sci Transl Med*. 2014;6:261ra152.

67. Thurber GM, Yang KS, Reiner T, et al. Single-cell and subcellular pharmacokinetic imaging allows insight into drug action in vivo. *Nat Commun*. 2013;4:1504.

68. Thurber GM, Reiner T, Yang KS, Kohler RH, Weissleder R. Effect of Small-Molecule Modification on Single-Cell Pharmacokinetics of PARP Inhibitors. *Mol Cancer Ther*. 2014;13:986-995.

69. Resch-Genger U, Grabolle M, Cavaliere-Jaricot S, Nitschke R, Nann T. Quantum dots versus organic dyes as fluorescent labels. *Nat Methods*. 2008;5:763-775.

70. Pansare VJ, Hejazi S, Faenza WJ, Prud'homme RK. Review of Long-Wavelength Optical and NIR Imaging Materials: Contrast Agents, Fluorophores, and Multifunctional Nano Carriers. *Chem Mater*. 2012;24:812-827.

71. Jose J, Burgess K. Benzophenoxazine-based fluorescent dyes for labeling biomolecules. *Tetrahedron*. 2006;62:11021-11037.

72. Kessel D. Photodynamic Therapy of Neoplastic Disease. CRC Press, Inc.; 1990.

73. Arden-Jacob J, Frantzeskos J, Kemnitzer NU, Zilles A, Drexhage KH. New fluorescent markers for the red region. *Spectrochim Acta - Part A Mol Biomol Spectrosc*. 2001;57:2271-2283.

74. Olafsen T, Wu AM. Antibody Vectors for Imaging. *Semin Nucl Med*. 2010;40:167-181.

75. Luo FR, Yang Z, Dong H, et al. Correlation of pharmacokinetics with the antitumor activity of Cetuximab in nude mice bearing the GEO human colon carcinoma xenograft. *Cancer Chemother Pharmacol*. 2005;56:455-464.

76. Conner KP, Rock BM, Kwon GK, et al. Evaluation of Near Infrared Fluorescent Labeling of Monoclonal Antibodies as a Tool for Tissue Distribution. *Drug Metab Dispos*. 2014;42:1906-1913.

77. Rosania GR, Lee JW, Ding L, Yoon HS, Chang YT. Combinatorial approach to organelle-targeted fluorescent library based on the styryl scaffold. *J Am Chem Soc*. 2003;125:1130-1131.

78. Poulin P, Theil FP. A priori prediction of tissue:plasma partition coefficients of drugs to facilitate the use of physiologically-based pharmacokinetic models in drug discovery. *J Pharm Sci*. 2000;89:16-35.

79. Warther D, Bolze F, Léonard J, et al. Live-Cell One- and Two-Photon Uncaging of a Far-RedEmitting Acridinone Fluorophore. *J Am Chem Soc*. 2010;132:2585-2590.

80. Maxwell JL, Terracio L, Borg TK, Baynes JW, Thorpe SR. A fluorescent residualizing label for studies on protein uptake and catabolism in vivo and in vitro. *Biochem J*. 1990;267:155-62.

81. Bhatnagar S, Deschenes E, Liao J, Cilliers C, Thurber GM. Multichannel Imaging to Quantify Four Classes of Pharmacokinetic Distribution in Tumors. *J Pharm Sci*. 2014;103:3276-3286.

82. Berezin MY, Guo K, Akers W, et al. Rational Approach To Select Small Peptide Molecular Probes Labeled with Fluorescent Cyanine Dyes for in Vivo Optical Imaging. *Biochemistry*. 2011;50:2691-2700.

83. Yang X, Shi C, Tong R, et al. Near IR Heptamethine Cyanine Dye-Mediated Cancer Imaging. *Clin Cancer Res*. 2010;16:2833-2844.

84. Shapiro AB, Corder AB, Ling V. P-Glycoprotein-Mediated Hoechst 33342 Transport Out of the Lipid Bilayer. *Eur J Biochem*. 1997;250:115-121.

85. Thorpe SR, Baynes JW, Chroneos ZC. The Design and Application of Residualizing Labels for Studies of Protein Catabolism. *FASEB J*. 1993;7:399-405.

86. Hamann FM, Brehm R, Pauli J, et al. Controlled Modulation of Serum Protein Binding and Biodistribution of Asymmetric Cyanine Dyes by Variation of the Number of Sulfonate Groups. *Mol Imaging*. 2011;10:258-269.

87. Choi HS, Gibbs SL, Lee JH, et al. Targeted zwitterionic near-infrared fluorophores for improved optical imaging. *Nat Biotechnol*. 2013;31:148-153.

88. Thurber GM, Figueiredo J-L, Weissleder R. Detection limits of intraoperative near infrared imaging for tumor resection. *J Surg Oncol*. 2010;102:758-764.

89. Adams KE, Ke S, Kwon S, et al. Comparison of visible and near-infrared wavelength-excitable fluorescent dyes for molecular imaging of cancer. *J Biomed Opt*. 2007;12:24017.

90. Thurber GM, Weissleder R. A Systems Approach for Tumor Pharmacokinetics. Boswell CA, ed. *PLoS One*. 2011;6:e24696.

91. Reichert JM. Antibodies to watch in 2016. *MAbs*. 2016;8:197-204.

92. Boswell CA, Bumbaca D, Fielder PJ, Khawli L a. Compartmental Tissue Distribution of Antibody Therapeutics: Experimental Approaches and Interpretations. *AAPS J*. 2012;14:612-618.

93. Zhang L, Navaratna T, Thurber GM. A Helix-Stabilizing Linker Improves Subcutaneous Bioavailability of a Helical Peptide Independent of Linker Lipophilicity. *Bioconjug Chem*. 2016;27:1663-1672.

94. Goldenberg DM, Larson SM. Radioimmunodetection in cancer identification. *J Nucl Med*. 1992;33:803-14.

95. Boswell CA, Tesar DB, Mukhyala K, Theil F-P, Fielder PJ, Khawli L a. Effects of Charge on Antibody Tissue Distribution and Pharmacokinetics. *Bioconjug Chem*. 2010;21:2153-2163.

96. Boswell CA, Mundo EE, Zhang C, et al. Impact of Drug Conjugation on Pharmacokinetics and Tissue Distribution of Anti-STEAP1 Antibody–Drug Conjugates in Rats. *Bioconjug Chem*. 2011;22:1994-2004.

97. Hoppin J, Orcutt KD, Hesterman JY, et al. Assessing Antibody Pharmacokinetics in Mice with In Vivo Imaging. *J Pharmacol Exp Ther*. 2011;337:350-358.

98. Natarajan A, Türkcan S, Gambhir SS, Pratx G. Multiscale Framework for Imaging Radiolabeled Therapeutics. *Mol Pharm*. 2015;12:4554-4560.

99. Weissleder R, Ntziachristos V. Shedding light onto live molecular targets. *Nat Med*. 2003;9:123-128.

100. Vahrmeijer AL, Hutteman M, van der Vorst JR, van de Velde CJH, Frangioni J V. Image-guided cancer surgery using near-infrared fluorescence. *Nat Rev Clin Oncol*. 2013;10:507-518.

101. de Vries EGE, Munnink THO, van Vugt MATM, Nagengast WB. Toward Molecular Imaging–Driven Drug Development in Oncology. *Cancer Discov*. 2011;1:25-28.

102. Maeda A, Bu J, Chen J, Zheng G, DaCosta RS. Dual in vivo Photoacoustic and Fluorescence Imaging of HER2 Expression in Breast Tumors for Diagnosis, Margin Assessment, and Surgical Guidance. *Mol Imaging*. 2015;14:7290.2014.00043.

103. Zhang L, Navaratna T, Liao J, Thurber GM. Dual-Purpose Linker for Alpha Helix Stabilization and Imaging Agent Conjugation to Glucagon-Like Peptide-1 Receptor Ligands. *Bioconjug Chem*. 2015;26:329-337.

104. Sato K, Nagaya T, Nakamura Y, et al. Impact of C4′- O -Alkyl Linker on in Vivo Pharmacokinetics of Near-Infrared Cyanine/Monoclonal Antibody Conjugates. *Mol Pharm*. 2015;12:3303-3311.

105. Darne C, Lu Y, Sevick-Muraca EM. Small animal fluorescence and bioluminescence tomography: a review of approaches, algorithms and technology update. *Phys Med Biol*. 2014;59:R1-R64.

106. Cilliers C, Guo H, Liao J, Christodolu N, Thurber GM. Multiscale Modeling of Antibody-Drug Conjugates: Connecting Tissue and Cellular Distribution to Whole Animal Pharmacokinetics and Potential Implications for Efficacy. *AAPS J*. 2016;18:1117-1130.

107. Cohen R, Vugts DJ, Stigter-van Walsum M, Visser GWM, van Dongen G a MS. Inert coupling of IRDye800CW and zirconium-89 to monoclonal antibodies for single- or dual-mode fluorescence and PET imaging. *Nat Protoc*. 2013;8:1010-1018.

108. Rogers BE, Franano FN, Edwards WB, et al. Identification of Metabolites of 111In-Diethylenetriaminepentaacetic Acid Monoclonal Antibodies and Antibody Fragments in Vivo. *Cancer Res*. 1995;55:5714s-5720s.

109. Sands H. Experimental studies of radioimmunodetection of cancer: an overview. *Cancer Res*. 1990;50:809s-813s.

110. Brechbiel MW, Gansow OA, Atcher RW, et al. Synthesis of 1-(p-isothiocyanatobenzyl) derivatives of DTPA and EDTA. Antibody labeling and tumor-imaging studies. *Inorg Chem*. 1986;25:2772-2781.

111. Cohen R, Stammes M a, de Roos IH, Stigter-van Walsum M, Visser GW, van Dongen GA. Inert coupling of IRDye800CW to monoclonal antibodies for clinical optical imaging of tumor targets. *EJNMMI Res*. 2011;1:31.

112. Sato K, Gorka AP, Nagaya T, et al. Role of Fluorophore Charge on the In Vivo Optical Imaging Properties of Near-Infrared Cyanine Dye/Monoclonal Antibody Conjugates. *Bioconjug Chem*. 2016;27:404-413.

113. Cilliers C, Liao J, Atangcho L, Thurber GM. Residualization Rates of Near-Infrared Dyes for the Rational Design of Molecular Imaging Agents. *Mol Imaging Biol*. 2015;17:757-762.

114. Zhang L, Bhatnagar S, Deschenes E, Thurber GM. Mechanistic and quantitative insight into cell surface targeted molecular imaging agent design. *Sci Rep*. 2016;6:25424.

115. Harris LJ, Skaletsky E, McPherson A. Crystallographic structure of an intact IgG1 monoclonal antibody. *J Mol Biol*. 1998;275:861-872.

116. Wishart DS, Knox C, Guo AC, et al. DrugBank: a comprehensive resource for in silico drug discovery and exploration. *Nucleic Acids Res*. 2006;34:D668-D672.

117. Ogawa M, Regino CAS, Choyke PL, Kobayashi H. In vivo target-specific activatable near-infrared optical labeling of humanized monoclonal antibodies. *Mol Cancer Ther*. 2009;8:232-239.

118. Aldrich MB, Wang X, Hart A, et al. Assessment of Free Dye in Solutions of Dual-Labeled Antibody Conjugates for In Vivo Molecular Imaging. *Mol Imaging Biol*. 2011;13:32-42.

119. Sako Y, Minoghchi S, Yanagida T. Single-molecule imaging of EGFR signalling on the surface of living cells. *Nat Cell Biol*. 2000;2:168-172.

120. Kim MT, Chen Y, Marhoul J, Jacobson F. Statistical Modeling of the Drug Load Distribution on Trastuzumab Emtansine (Kadcyla), a Lysine-Linked Antibody Drug Conjugate. *Bioconjug Chem*. 2014;25:1223-1232.

121. Goldmacher VS, Amphlett G, Wang L, Lazar AC. Statistics of the Distribution of the Abundance of Molecules with Various Drug Loads in Maytansinoid Antibody–Drug Conjugates. *Mol Pharm*. 2015;12:1738-1744.

122. Zhang L, Thurber GM. Quantitative Impact of Plasma Clearance and Down-regulation on GLP-1 Receptor Molecular Imaging. *Mol Imaging Biol*. 2016;18:79-89.

123. Paudyal B, Paudyal P, Oriuchi N, Hanaoka H, Tominaga H, Endo K. Positron emission tomography imaging and biodistribution of vascular endothelial growth factor with 64Cu-labeled bevacizumab in colorectal cancer xenografts. *Cancer Sci*. 2011;102:117-121.

124. Austin CD, De Mazière AM, Pisacane PI, et al. Endocytosis and Sorting of ErbB2 and the Site of Action of Cancer Therapeutics Trastuzumab and Geldanamycin. *Mol Biol Cell*. 2004;15:5268-5282.

125. Ito S, Muguruma N, Hayashi S, et al. Development of agents for reinforcement of fluorescence on near-infrared ray excitation for immunohistological staining. *Bioorg Med Chem*. 1998;6:613-8.

126. Yamasaki Y, Sumimoto K, Nishikawa M, et al. Pharmacokinetic analysis of in vivo

disposition of succinylated proteins targeted to liver nonparenchymal cells via scavenger receptors: importance of molecular size and negative charge density for in vivo recognition by receptors. *J Pharmacol Exp Ther*. 2002;301:467-77.

127. van der Bilt ARM, van Scheltinga AGTT, Timmer-Bosscha H, et al. Measurement of Tumor VEGF-A Levels with 89Zr-Bevacizumab PET as an Early Biomarker for the Antiangiogenic Effect of Everolimus Treatment in an Ovarian Cancer Xenograft Model. *Clin Cancer Res*. 2012;18:6306-6314.

128. Kelly RL, Sun T, Jain T, et al. High throughput cross-interaction measures for human IgG1 antibodies correlate with clearance rates in mice. *MAbs*. 2015;7:770-777.

129. Geng SB, Cheung JK, Narasimhan C, Shameem M, Tessier PM. Improving Monoclonal Antibody Selection and Engineering using Measurements of Colloidal Protein Interactions. *J Pharm Sci*. 2014;103:3356-3363.

130. Hötzel I, Theil F-P, Bernstein LJ, et al. A strategy for risk mitigation of antibodies with fast clearance. *MAbs*. 2012;4:753-760.

131. Chan AC, Carter PJ. Therapeutic antibodies for autoimmunity and inflammation. *Nat Rev Immunol*. 2010;10:301-316.

132. Kaur S, Venktaraman G, Jain M, Senapati S, Garg PK, Batra SK. Recent trends in antibody-based oncologic imaging. *Cancer Lett*. 2012;315:97-111.

133. Miller MA, Weissleder R. Imaging of anticancer drug action in single cells. *Nat Rev Cancer*. 2017;17:399-414.

134. Wu AM. Engineered antibodies for molecular imaging of cancer. *Methods*. 2014;65:139-147.

135. Marshall M V, Rasmussen JC, Tan I-C, et al. Near-Infrared Fluorescence Imaging in Humans with Indocyanine Green: A Review and Update. *Open Surg Oncol J*. 2010;2:12-25.

136. Urano Y, Asanuma D, Hama Y, et al. Selective molecular imaging of viable cancer cells with pH-activatable fluorescence probes. *Nat Med*. 2009;15:104-109.

137. Cilliers C, Nessler I, Christodolu N, Thurber GM. Tracking Antibody Distribution with Near-Infrared Fluorescent Dyes: Impact of Dye Structure and Degree of Labeling on Plasma Clearance. *Mol Pharm*. 2017;14:1623-1633.

138. Wiley HS. Anomalous binding of epidermal growth factor to A431 cells is due to the effect of high receptor densities and a saturable endocytic system. *J Cell Biol*. 1988;107:801-810.

139. Ackerman ME, Chalouni C, Schmidt MM, et al. A33 antigen displays persistent surface expression. *Cancer Immunol Immunother*. 2008;57:1017-1027.

140. Ackerman ME, Pawlowski D, Wittrup KD. Effect of antigen turnover rate and expression level on antibody penetration into tumor spheroids. *Mol Cancer Ther*. 2008;7:2233-40.

141. Fan Z, Lu Y, Wu X, Mendelsohn J. Antibody-induced epidermal growth factor receptor dimerization mediates inhibition of autocrine proliferation of A431 squamous carcinoma cells. *J Biol Chem*. 1994;269:27595-27602.

142. Flynn AA, Pedley RB, Green AJ, et al. The Nonuniformity of Antibody Distribution in the Kidney and its Influence on Dosimetry. *Radiat Res*. 2003;159:182-189.

143. Vegt E, van Eerd JEM, Eek A, et al. Reducing Renal Uptake of Radiolabeled Peptides Using Albumin Fragments. *J Nucl Med* . 2008;49:1506-1511.

144. Barok M, Joensuu H, Isola J. Trastuzumab emtansine: mechanisms of action and drug resistance. *Breast Cancer Res*. 2014;16:3378.

145. Hazin J, Moldenhauer G, Altevogt P, Brady NR. A novel method for measuring cellular antibody uptake using imaging flow cytometry reveals distinct uptake rates for two different monoclonal antibodies targeting L1. *J Immunol Methods*. 2015;423:70-77.

146. Wang Y, Pennock S, Chen X, Wang Z. Endosomal Signaling of Epidermal Growth Factor Receptor Stimulates Signal Transduction Pathways Leading to Cell Survival. *Mol Cell Biol* . 2002;22:7279-7290.

147. Jain RK. Physiological barriers to delivery of monoclonal antibodies and other macromolecules in tumors. *Cancer Res*. 1990;50:814s-819s.

148. Lewis Phillips GD, Li G, Dugger DL, et al. Targeting HER2-positive breast cancer with trastuzumab-DM1, an antibody-cytotoxic drug conjugate. *Cancer Res*. 2008;68:9280-9290.

149. Izumi Y, Xu L, di Tomaso E, Fukumura D, Jain RK. Tumour biology: herceptin acts as an anti-angiogenic cocktail. *Nature*. 2002;416:279-280.

150. Pastuskovas C V., Mundo EE, Williams SP, et al. Effects of Anti-VEGF on Pharmacokinetics, Biodistribution, and Tumor Penetration of Trastuzumab in a Preclinical Breast Cancer Model. *Mol Cancer Ther*. 2012;11:752-762.

151. Kate CI ten, Fischman A, Rubin RH, et al. Effect of isoelectric point on biodistribution and inflammation imaging with indium-111-labelled IgG. *Eur J Nucl Med*. 1990;17:305-309.

152. Kamath A V., Iyer S. Preclinical Pharmacokinetic Considerations for the Development of Antibody Drug Conjugates. *Pharm Res*. 2015;32:3470-3479.

153. Panowski S, Bhakta S, Raab H, Polakis P, Junutula JR. Site-specific antibody drug conjugates for cancer therapy. *MAbs*. 2014;6:34-45.

154. Mullard A. Maturing antibody–drug conjugate pipeline hits 30. *Nat Rev Drug Discov*. 2013;12:329-332.

155. Baxter LT, Zhu H, Mackensen DG, et al. Biodistribution of monoclonal antibodies: scale-up from mouse to human using a physiologically based pharmacokinetic model. *Cancer Res*. 1995;55:4611-4622.

156. Baxter LT, Zhu H, Mackensen DG, Jain RK. Physiologically Based Pharmacokinetic Model for Specific and Nonspecific Monoclonal Antibodies and Fragments in Normal Tissues and Human Tumor Xenografts in Nude Mice. *Cancer Res*. 1994;54:1517-1528.

157. Davda JP, Jain M, Batra SK, Gwilt PR, Robinson DH. A physiologically based pharmacokinetic (PBPK) model to characterize and predict the disposition of monoclonal antibody CC49 and its single chain Fv constructs. *Int Immunopharmacol*. 2008;8:401-413.

158. Garg A, Balthasar JP. Physiologically-based pharmacokinetic (PBPK) model to predict IgG tissue kinetics in wild-type and FcRn-knockout mice. *J Pharmacokinet Pharmacodyn*. 2007;34:687-709.

159. Nestorov I. Whole body pharmacokinetic models. *Clin Pharmacokinet*. 2003;42:883-908.

160. Rowland M, Peck C, Tucker G. Physiologically-Based Pharmacokinetics in Drug Development and Regulatory Science. *Annu Rev Pharmacol Toxicol*. 2011;51:45-73.

161. Shah DK, Betts AM. Towards a platform PBPK model to characterize the plasma and tissue disposition of monoclonal antibodies in preclinical species and human. *J Pharmacokinet Pharmacodyn*. 2012;39:67-86.

162. Germani M, Crivori P, Rocchetti M, et al. Evaluation of a basic physiologically based pharmacokinetic model for simulating the first-time-in-animal study. *Eur J Pharm Sci*. 2007;31:190-201.

163. Poulin P, Chen YH, Ding X, et al. Prediction of drug distribution in subcutaneous xenografts of human tumor cell lines and healthy tissues in mouse: application of the tissue composition-based model to antineoplastic drugs. *J Pharm Sci*. 2015;104:1508-1521.

164. Poulin P, Theil F-P. Prediction of Pharmacokinetics Prior to In Vivo Studies. II. Generic Physiologically Based Pharmacokinetic Models of Drug Disposition. *J Pharm Sci*. 2002;91:1358-1370.

165. Li Z, Krippendorff B-F, Sharma S, Walz AC, Lavé T, Shah DK. Influence of molecular size on tissue distribution of antibody fragments. *MAbs*. 2016;8:113-119.

166. Ferl GZ, Wu AM, DiStefano JJ. A Predictive Model of Therapeutic Monoclonal Antibody Dynamics and Regulation by the Neonatal Fc Receptor (FcRn). *Ann Biomed Eng*. 2005;33:1640-1652.

167. Fronton L, Pilari S, Huisinga W. Monoclonal antibody disposition: a simplified PBPK model and its implications for the derivation and interpretation of classical compartment models. *J Pharmacokinet Pharmacodyn*. 2014;41:87-107.

168. Krogh A. The number and distribution of capillaries in muscles with calculations of the oxygen pressure head necessary for supplying the tissue. *J Physiol*. 1919;52:409-415.

169. Levitt DG. Capillary-tissue exchange kinetics: An analysis of the krogh cylinder model. *J Theor Biol*. 1972;34:103-124.

170. Tepper RS, Lee HL, Lightfoot EN. Transient convective mass transfer in Krogh tissue cylinders. *Ann Biomed Eng*. 1978;6:506-530.

171. Baxter LT, Jain RK. Transport of fluid and macromolecules in tumors. IV. A microscopic model of the perivascular distribution. *Microvasc Res*. 1991;41:252-272.

172. Shorten PRR, McMahon CDD, Soboleva TKK. Insulin Transport within Skeletal Muscle Transverse Tubule Networks. *Biophys J*. 2007;93:3001-3007.

173. Venkatasubramanian R, Arenas RB, Henson MA, Forbes NS. Mechanistic modelling of dynamic MRI data predicts that tumour heterogeneity decreases therapeutic response. *Br J Cancer*. 2010;103:486-497.

174. Eikenberry S. A tumor cord model for Doxorubicin delivery and dose optimization in solid tumors. *Theor Biol Med Model*. 2009;6:16.

175. Bertuzzi A, Fasano A, Gandolfi A, Sinisgalli C. Tumour Cords and Their Response to Anticancer Agents.; 2008.

176. Shah DK, Haddish-Berhane N, Betts A. Bench to bedside translation of antibody drug conjugates using a multiscale mechanistic PK/PD model: A case study with brentuximab-vedotin. *J Pharmacokinet Pharmacodyn*. 2012;39:643-659.

177. Vasalou C, Helmlinger G, Gomes B. A Mechanistic Tumor Penetration Model to Guide Antibody Drug Conjugate Design. *PLoS One*. 2015;10:e0118977.

178. Blumenthal RD, Fand I, Sharkey RM, Boerman OC, Kashi R, Goldenberg DM. The effect of antibody protein dose on the uniformity of tumor distribution of radioantibodies: An autoradiographic study. *Cancer Immunol Immunother*. 1991;33:351-358.

179. Fujimori K, Covell DG, Fletcher JE, Weinstein JN. A Modeling Analysis of Monoclonal Antibody Percolation Through Tumors: A Binding-Site Barrier. *J Nucl Med*. 1990;31:1191-1198.

180. Baxter LT, Jain RK. Transport of fluid and macromolecules in tumors. II. Role of heterogeneous perfusion and lymphatics. *Microvasc Res*. 1990;40:246-263.

181. Wittrup KD, Thurber GM, Schmidt MM, Rhoden JJ. Practical Theoretic Guidance for the Design of Tumor-Targeting Agents. In: Wittrup KD, Verdine GLBT-M in E, eds. Protein Engineering for Therapeutics, Part B. Vol 503. Academic Press; 2012:255-268.

182. Singh AP, Shin YG, Shah DK. Application of Pharmacokinetic-Pharmacodynamic Modeling and Simulation for Antibody-Drug Conjugate Development. *Pharm Res*. 2015;32:3508-3525.

183. Sukumaran S, Gadkar K, Zhang C, et al. Mechanism-Based Pharmacokinetic/Pharmacodynamic Model for THIOMAB^{TM} Drug Conjugates. *Pharm Res*. 2015;32:1884-1893.

184. Bender B, Leipold DD, Xu K, Shen B-Q, Tibbitts J, Friberg LE. A mechanistic pharmacokinetic model elucidating the disposition of trastuzumab emtansine (T-DM1), an antibody-drug conjugate (ADC) for treatment of metastatic breast cancer. *AAPS J*. 2014;16:994-1008.

185. Yuan F, Dellian M, Fukumura D, et al. Vascular Permeability in a Human Tumor Xenograft : Molecular Size Dependence and Cutoff Size Advances in Brief Vascular Permeability in a Human Tumor Xenograft : Molecular Size Dependence and Cutoff Size1. *Cancer Res*. 1995;55:3752-3756.

186. Bostrom J, Haber L, Koenig P, Kelley RF, Fuh G. High affinity antigen recognition of the dual specific variants of herceptin is entropy-driven in spite of structural plasticity. *PLoS One*. 2011;6:e17887.

187. Jackson TL, Lubkin SR, Siemers NO, Kerr DE, Senter PD, Murray JD. Mathematical and experimental analysis of localization of anti-tumour antibody–enzyme conjugates. *Br J Cancer*. 1999;80:1747-1753.

188. Hilmas DE, Gillette EL. Morphometric analyses of the microvasculature of tumors during growth and after x-irradiation. *Cancer*. 1974;33:103-110.

189. Yamashita-Kashima Y, Shu S, Harada N, Fujimoto-Ouchi K. Enhanced antitumor activity of trastuzumab emtansine (T-DM1) in combination with pertuzumab in a HER2-positive gastric cancer model. *Oncol Rep*. 2013;30:1087-1093.

190. Jackson D, Atkinson J, Guevara CI, et al. In Vitro and In Vivo Evaluation of Cysteine and Site Specific Conjugated Herceptin Antibody-Drug Conjugates. Ho M, ed. *PLoS One*. 2014;9:e83865.

191. McLarty K, Cornelissen B, Scollard DA, Done SJ, Chun K, Reilly RM. Associations between the uptake of 111In-DTPA-trastuzumab, HER2 density and response to trastuzumab (Herceptin) in athymic mice bearing subcutaneous human tumour xenografts. *Eur J Nucl Med Mol Imaging*. 2009;36:81-93.

192. Khera E, Cilliers C, Bhatnagar S, Thurber GM. Computational transport analysis of antibody-drug conjugate bystander effects and payload tumoral distribution: implications for therapy. *Mol Syst Des Eng*. 2018;3:73-88.

193. J. KM, C. SA, Wikke P, et al. Experimental radioimmunotherapy of small peritoneal metastases of colorectal origin. *Int J Cancer*. 2003;106:965-972.

194. Fujimori K, Covell DG, Fletcher JE, Weinstein JN. Modeling analysis of the global and microscopic distribution of immunoglobulin G, F(ab')2, and Fab in tumors. *Cancer Res*. 1989;49:5656-63.

195. Fenwick JR, Philpott GW, Connett JM. Biodistribution and histological localization of anti-human colon cancer monoclonal antibody (MAb) 1A3: The influence of administered MAB dose on tumor uptake. *Int J Cancer*. 1989;44:1017-1027.

196. Schroff RW, Morgan ACJ, Woodhouse CS, et al. Monoclonal Antibody Therapy in Malignant Melanoma: Factors Effecting In Vivo Localization. *J Immunother*. 1987;6.

197. Junutula JR, Flagella KM, Graham RA, et al. Engineered thio-trastuzumab-DM1 conjugate with an improved therapeutic index to target human epidermal growth factor receptor 2-positive breast cancer. *Clin Cancer Res*. 2010;16:4769-4778.

198. Pillow TH, Tien J, Parsons-reponte KL, et al. Site-Specific Trastuzumab Maytansinoid Antibody?Drug Conjugates with Improved Therapeutic Activity through Linker and Antibody Engineering. *J Med Chem*. 2014;57:7890-7899.

199. Goldenberg DM, Cardillo TM, Govindan S V, Rossi EA, Sharkey RM. Trop-2 is a novel target for solid cancer therapy with sacituzumab govitecan (IMMU-132), an antibody-drug conjugate (ADC). *Oncotarget*. 2015;6:22496-512.

200. Schoeberl B, Eichler-Jonsson C, Gilles ED, Müller G. Computational modeling of the dynamics of the MAP kinase cascade activated by surface and internalized EGF receptors. *Nat Biotechnol*. 2002;20:370-375.

201. Tang Y, Lou J, Alpaugh RK, Robinson MK, Marks JD, Weiner LM. Regulation of Antibody-Dependent Cellular Cytotoxicity by IgG Intrinsic and Apparent Affinity for Target Antigen. *J Immunol*. 2007;179:2815 LP-2823.

202. Rudnick SI, Lou J, Shaller CC, et al. Influence of affinity and antigen internalization on the uptake and penetration of anti-HER2 Antibodies in Solid Tumors. *Cancer Res*. 2011;71:2250-2259.

203. Thurber GM, Wittrup KD. Quantitative spatiotemporal analysis of antibody fragment diffusion and endocytic consumption in tumor spheroids. *Cancer Res*. 2008;68:3334-3341.

204. Spector NL, Blackwell KL. Understanding the Mechanisms Behind Trastuzumab Therapy for Human Epidermal Growth Factor Receptor 2–Positive Breast Cancer. *J Clin Oncol*. 2009;27:5838-5847.

205. Ozcelik C, Erdmann B, Pilz B, et al. Conditional mutation of the ErbB2 (HER2) receptor in cardiomyocytes leads to dilated cardiomyopathy. *Proc Natl Acad Sci*. 2002;99:8880-8885.

206. Boswell CA, Mundo EE, Firestein R, et al. An integrated approach to identify normal tissue expression of targets for antibody-drug conjugates: case study of TENB2. *Br J Pharmacol*. 2013;168:445-457.

207. Hernandez MC, Knox SJ. Radiobiology of radioimmunotherapy: Targeting CD20 B-cell antigen in non-Hodgkin's lymphoma. *Int J Radiat Oncol*. 2004;59:1274-1287.

208. Perrino E, Steiner M, Krall N, et al. Curative properties of noninternalizing antibody-drug conjugates based on maytansinoids. *Cancer Res*. 2014;74:2569-2578.

209. Hamblett KJ, Jacob AP, Gurgel JL, et al. SLC46A3 is required to transport catabolites of noncleavable antibody maytansine conjugates from the lysosome to the cytoplasm. *Cancer Res*. 2015;75:5329-5340.

210. Bryant P, Pabst M, Badescu G, et al. In vitro and in vivo evaluation of cysteine rebridged trastuzumab-MMAE antibody drug conjugates with defined drug-to-antibody ratios. *Mol Pharm*. 2015;12:1872-1879.

211. Müller P, Kreuzaler M, Khan T, et al. Trastuzumab emtansine (T-DM1) renders HER2 + breast cancer highly susceptible to CTLA-4/PD-1 blockade. *Sci Transl Med*. 2015;7:315ra188.

212. Gerhard L. Pharmacologic target-mediated drug disposition. *Clin Pharmacol Ther*. 1994;56:248-252.

213. Mager DE, Jusko WJ. General Pharmacokinetic Model for Drugs Exhibiting Target-Mediated Drug Disposition. *J Pharmacokinet Pharmacodyn*. 2001;28:507-532.

214. Mager DE. Target-mediated drug disposition and dynamics. *Biochem Pharmacol*. 2006;72:1-10.

215. Polakis P. Antibody Drug Conjugates for Cancer Therapy. Esbenshade TA, ed. *Pharmacol Rev*. 2015;68:3-19.

216. Singh AP, Sharma S, Shah DK. Quantitative characterization of in vitro bystander effect of antibody-drug conjugates. *J Pharmacokinet Pharmacodyn*. 2016;43:567-582.

217. Kovtun Y V., Audette CA, Ye Y, et al. Antibody-Drug Conjugates Designed to Eradicate Tumors with Homogeneous and Heterogeneous Expression of the Target Antigen. *Cancer*

Res. 2006;66:3214-3221.

218. Cilliers C, Thurber GM. "Standing by" for Bystander Effects: Dual Isotope Imaging of Antibody-Drug Conjugate and Payload Distribution. *J Nucl Med*. July 2018.

219. Barok M, Tanner M, Köninki K, Isola J. Trastuzumab-DM1 is highly effective in preclinical models of HER2-positive gastric cancer q. *Cancer Lett*. 2011;306:171-179.

220. Fujimoto-Ouchi K, Sekiguchi F, Yasuno H, Moriya Y, Mori K, Tanaka Y. Antitumor activity of trastuzumab in combination with chemotherapy in human gastric cancer xenograft models. *Cancer Chemother Pharmacol*. 2007;59:795-805.

221. Yamashita-Kashima Y, Iijima S, Yorozu K, et al. Pertuzumab in combination with trastuzumab shows significantly enhanced antitumor activity in HER2-positive human gastric cancer xenograft models. *Clin Cancer Res*. 2011;17:5060-5070.

222. Singh R, Kim WJ, Kim P, Hong HJ. Combined blockade of HER2 and VEGF exerts greater growth inhibition of HER2-overexpressing gastric cancer xenografts than individual blockade. *Exp Mol Med*. 2013;45:e52-e52.

223. Barok M, Isola J, Palyi-Krekk Z, et al. Trastuzumab causes antibody-dependent cellular cytotoxicity-mediated growth inhibition of submacroscopic JIMT-1 breast cancer xenografts despite intrinsic drug resistance. *Mol Cancer Ther*. 2007;6:2065-2072.

224. Chang AJ, DeSilva R, Jain S, Lears K, Rogers B, Lapi S. 89Zr-Radiolabeled Trastuzumab Imaging in Orthotopic and Metastatic Breast Tumors. *Pharmaceuticals*. 2012;5:79-93.

225. Thurber GM, Weissleder R. Quantitating Antibody Uptake In Vivo: Conditional Dependence on Antigen Expression Levels. *Mol Imaging Biol*. 2011;13:623-632.

226. Oude Munnink TH, Dijkers EC, Netters SJ, et al. Trastuzumab Pharmacokinetics Influenced by Extent Human Epidermal Growth Factor Receptor 2–Positive Tumor Load. *J Clin Oncol*. 2010;28:e355-e356.

227. Pabst M, McDowell W, Manin A, et al. Modulation of drug-linker design to enhance in vivo potency of homogeneous antibody-drug conjugates. *J Control Release*. 2017;253:160-164.

228. Hong EE, Erickson H, Lutz RJ, et al. Design of coltuximab ravtansine, a CD19-targeting antibody-drug conjugate (ADC) for the treatment of B-cell malignancies: Structure-activity relationships and preclinical evaluation. *Mol Pharm*. 2015;12:1703-1716.

229. de Goeij BECG, Lambert JM. New developments for antibody-drug conjugate-based therapeutic approaches. *Curr Opin Immunol*. 2016;40:14-23.

230. Reddy N, Ong GL, Behr TM, Sharkey RM, Goldenberg DM, Mattes MJ. Rapid blood clearance of mouse IgG2a and human IgG1 in many nude and nu/+ mouse strains is due to low IgG2a serum concentrations. *Cancer Immunol Immunother*. 1998;46:25-33.

231. Loganzo F, Sung M, Gerber H-P. Mechanisms of Resistance to Antibody–Drug Conjugates. *Mol Cancer Ther*. 2016;15:2825-2834.

232. Starodub AN, Ocean AJ, Shah MA, et al. First-in-human trial of a novel anti-trop-2 Antibody-SN-38 conjugate, sacituzumab govitecan, for the treatment of diverse metastatic solid tumors. *Clin Cancer Res*. 2015;21:3870-3878.

233. Williams S-P, Ogasawara A, Tinianow JN, et al. ImmunoPET helps predicting the efficacy of antibody-drug conjugates targeting TENB2 and STEAP1. *Oncotarget*. 2016;7:25103-25112.

234. Gebhart G, Lamberts LE, Wimana Z, et al. Molecular imaging as a tool to investigate heterogeneity of advanced HER2-positive breast cancer and to predict patient outcome under trastuzumab emtansine (T-DM1): The ZEPHIR trial. *Ann Oncol*. 2016;27:619-624.

235. Ulaner GA, Hyman DM, Ross DS, et al. Detection of HER2-Positive Metastases in Patients with HER2-Negative Primary Breast Cancer Using 89Zr-Trastuzumab PET/CT. *J Nucl Med*. 2016;57:1523-1528.

236. Trotter M, Chaplin D, Olive P. Use of a carbocyanine dye as a marker of functional vasculature in murine tumours. *Br J Cancer*. 1989;59:706-709.

237. West MJ. Introduction to Stereology. *Cold Spring Harb Protoc*. 2012;2012.

238. Chalkley HW, Cornfield J, Park H. A Method for Estimating Volume-Surface Ratios. *Science (80-)*. 1949;110:295-7.